VENEZUELA-MEM/USA-DOE FOSSIL ENERGY REPORT IV-12

DOE/BC-00/6/SP
OSTI ID: 768404

SUPPORTING TECHNOLOGY FOR ENHANCED OIL RECOVERY

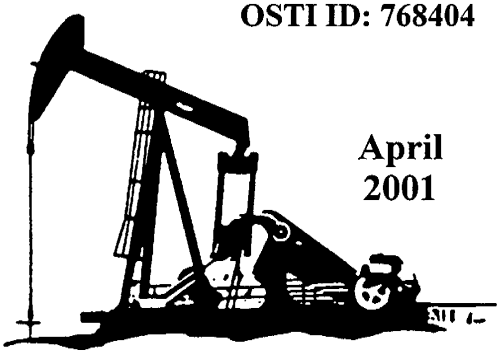

April
2001

EOR THERMAL PROCESSES

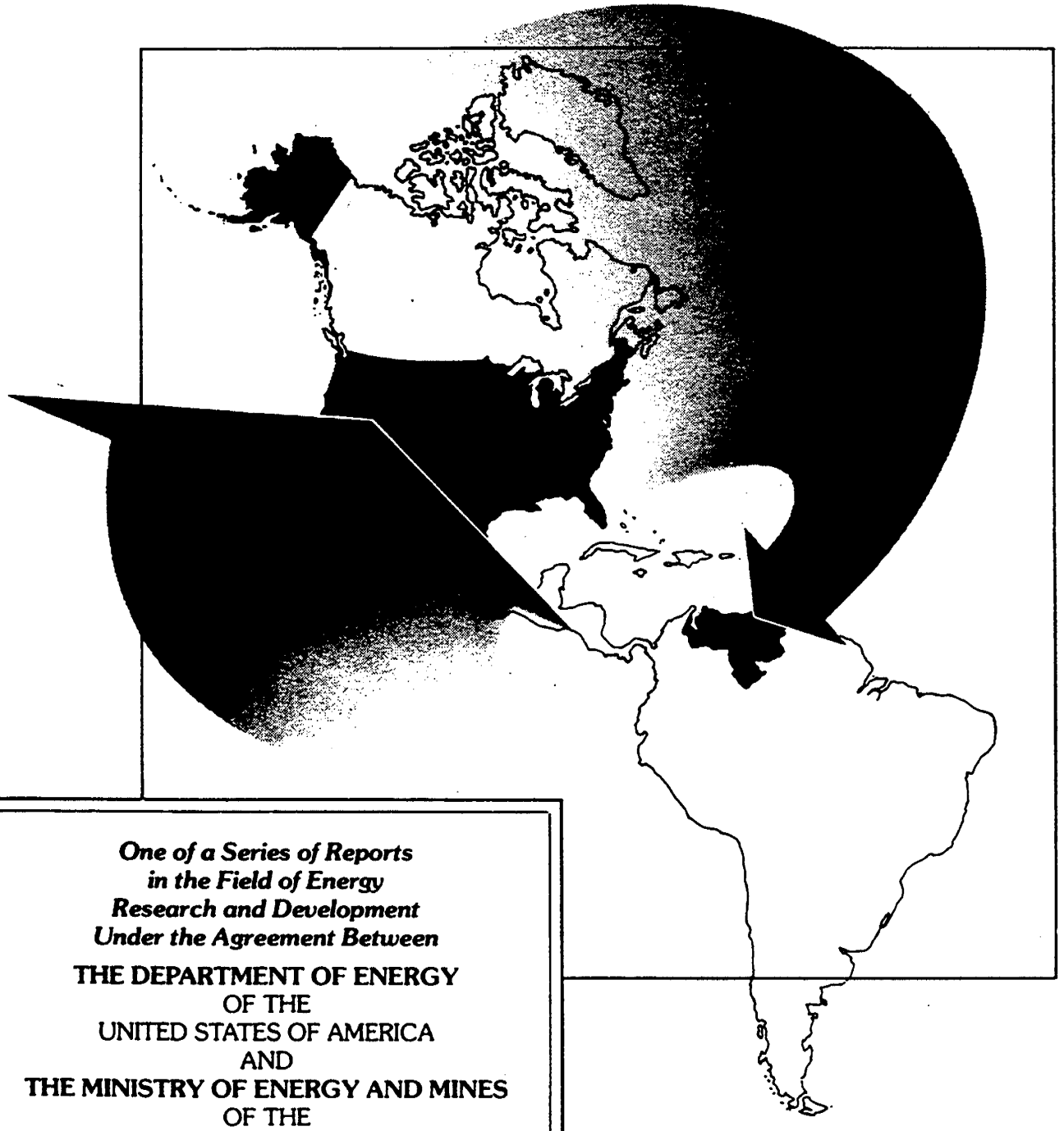

One of a Series of Reports
in the Field of Energy
Research and Development
Under the Agreement Between

THE DEPARTMENT OF ENERGY
OF THE
UNITED STATES OF AMERICA
AND
THE MINISTRY OF ENERGY AND MINES
OF THE
REPUBLIC OF VENEZUELA

DOE/BC-00/6/SP
OSTI ID: 768404
Distribution Category UC-122

ELEVENTH AMENDMENT AND EXTENSION TO

Annex IV-ENHANCED OIL RECOVERY THERMAL PROCESSES

THE DEPARTMENT OF ENERGY OF THE UNITED STATES OF AMERICA

And

THE MINISTRY OF ENERGY AND MINES OF THE REPUBLIC OF VENEZUELA

Submitted By:

Thomas B. Reid, Project Manager
Thermal Recovery/Novel Technology
National Petroleum Technology Office
U.S. Department of Energy

Tulio Colmenares Torrealba
Exploration of Heavy/Extra Heavy Crude Manager
PDVSA INTEVEP, S.A.
Filial de Petroleos de Venezuela, S.A.

Approved By:

Donald A. Juckett
U.S. Department of Energy
1000 Independence Avenue
Washington, DC 20585

Francisco Simonpietri
Minister of Energy and Mines
Caracas 1010A, Venezuela

United States Department of Energy

PREFACE

An Agreement between the Department of Energy of the United States of America and the Ministry of Energy and Mines of the Republic of Venezuela to cooperate in Energy Research and Development was signed March 6, 1980. The object of cooperation under the DOE/MEM Agreement was to promote a balanced exchange of energy technologies and to conduct joint projects in the area of Petroleum, Solar Energy, Hydroelectric Energy, and Coal.

This Agreement supported the Agreement for Scientific and Technological Cooperation between the two countries which was signed by the Secretary of State of the U.S.A. and the Minister of Foreign Relations of Venezuela on January 11, 1980.

On October 13, 1997, a second Agreement was signed by the Secretary of Energy of the U.S.A. and the Minister of Energy and Mines of the Republic of Venezuela to expand the information exchange to include energy efficiency, renewable energy, and policy matters. This Agreement encompassed the original Agreement.

The original DOE/MEM Agreement was supplemented by six annexes to describe specifically the work to be done. Over the past twenty years, additional annexes have been signed, resulting in a total of seventeen annexes to date. The Agreement has been extended to October 12, 2007. The annexes are:

I. Joint Characterization of Heavy Crude Oils
II. Supporting Research in the Area of Enhanced Oil Recovery
III. Evaluation of Past and Ongoing Enhanced Oil Recovery Projects in the U.S. and Venezuela
IV Enhanced Oil Recovery Thermal Processes
V. Oil Drilling, Coring, and Telemetry
VI. Residual Oil Saturation
VII. Petroleum Products Utilization and Evaluation
VIII. Coal Preparation, Combustion, and Related Technology
IX. Subsidence Due to Fluid Withdrawal
X. On-Site Training of Petroleum Engineers
XI. Energy Conservation
XII. Geochemistry (Oil Generation, Migration, and Accumulation)
XIII. Microbial Enhanced Oil Recovery
XIV. Exchange of Energy Related Personnel
XV. Oil Recovery Information and Technology Transfer
XVI. Oil and Petrochemical Ecology and Environmental Research
XVII. Drilling Technology

Each of these annexes has a document describing the work to be done as part of the cooperation. Amendments and Extensions to the Annexes are provided for in the Agreement.

Currently, seven annexes are active (Annexes I, IV, X, XIV, XV, XVI, and XVII) and ten annexes have been completed (Annexes II, III, V, VI, VII, VIII, IX, XI, XII, and XIII). The Agreement is in force until October 12, 2007.

CONTENTS

	Page
PREFACE	iii
ABSTRACT	vii
Task 74 DOE/SUPRI - Laboratory Research and Computer Modeling to Determine the Mechanisms of Heavy Oil Recovery	74-1
Task 75 INTEVEP - Field Results and Computer Simulation of the SAGD Process	75-1
Task 76 DOE/TRW PT - Research Results on Developing Methods to Economically Recover Heavy Crude in an Arctic Environment	76-1
Task 77 INTEVEP - Development of Guidelines and Procedures to Determine the Geomechanical Properties of Unconsolidated Sands	77-1
Task 78 DOE/LLNL - Resistivity Imaging from Cross-Bore and Surface-to-Borehole Electromagnetic Induction Methods and the Use of this Technology in Steel Cased Wells	78-1
Task 79 INTEVEP - Using Seismic Methods for Monitoring Reservoir Production	79-1

APPENDIX A - Short text of the Eleventh Amendment to Annex IV of the Implementing Agreement Between the Department of Energy of the United States of America and the Ministry of Energy of the Republic of Venezuela in the Area of Enhanced Oil Recovery Thermal Processes signed on September 30, 1998.

APPENDIX B - Full text of the Agreement Between the Department of Energy of the United States of America and the Ministry of Energy of the Republic of Venezuela in the Area of Enhanced Oil Recovery Thermal Processes signed on October 13, 1997.

ABSTRACT

This report contains the results of the research information exchanged under the six Tasks of the Eleventh Amendment and Extension of Annex IV - Enhanced Oil Recovery Thermal Processes of the Venezuela/USA R&D Energy Agreement.

This report is presented in Sections (for each of the six Tasks) and each Section contains one or more reports that were prepared to describe the results of the effort under each of the Tasks.

A statement of each Task, taken from the Agreement Between Project Managers, is presented on the first page of each Section. The Tasks are numbered 74 through 79.

The first through eleventh report on the research results exchanged under Annex IV are numbered Venezuela MEM/USA DOE Fossil Energy Report Number IV-1, IV-2, IV-3, IV-4, IV-5, IV-6, IV-7, IV-8, IV-9, IV-10, and IV-11. These reports are dated April 1983, August 1984, March 1986, July 1987, November 1988, December 1989, October 1991, February 1993, March 1995, December 1997, and April 2000.

Task 74 - DOE shall provide PDVSA-Intevep with results of the SUPRI heavy oil mechanisms research program. This work includes studies of the flow properties studies at heavy oil reservoirs conditions, in-situ combustion, steam with additives, formation evaluation and support of specific field experiments. Among the axis of research for the duration of this task are investigation of the "foamy oil" mechanism, studies of heat and fluid transfers in fractured media, better determination of flow parameters such as relative permeability and capillary pressure and effects of catalysts on in-situ combustion. In-situ upgrading methods will be investigated. Experiments will be conducted in micromodels and cores, with saturations measured by an X ray CT scanner.

Executive Summary

The United States continues to rely heavily on petroleum fossil fuels as a primary energy source, while domestic reserves dwindle. However, so-called heavy oil (10 to 20 °API) remains an underutilized resource of tremendous potential. Heavy oils are much more viscous than conventional oils. As a result, they are difficult to produce with conventional recovery methods such as pressure depletion and water injection. Thermal recovery is especially important for this class of reservoirs because adding heat, usually via steam injection, generally reduces oil viscosity dramatically. This improves displacement efficiency. The research described here was directed toward improved understanding of thermal and heavy-oil production mechanisms and is categorized into:

(i) flow and rock properties,
(ii) in-situ combustion
(iii) additives to improve mobility control
(iv) reservoir definition, and
(v) support services

The scope of activities extended over a three-year period.

Significant work was accomplished in the area of flow properties of steam, water, and oil in consolidated and unconsolidated porous media, transport in fractured porous media, foam generation and flow in homogeneous and heterogeneous porous media, the effects of displacement pattern geometry and mobility ratio on oil recovery, and analytical representation of water influx. Significant results are now described briefly.

In the area of flow properties, Akin *et al* conducted experiments using a computed tomography (CT) scanner and also a simulation study to examine the temperature dependence of water/oil relative permeability curves (Akin *et al.* 1999). In the dynamic mode of relative permeability measurement and at temperatures from about 20 to 80 °C, viscous instabilities dominate the displacement pattern. Interpretations based on assumption of one-dimensional flow are, thus, invalid. Simulations confirm that input relative permeability curves differ greatly from the apparent curves obtained using standard interpretation techniques based on a one-dimensional flow assumption.

An experimental apparatus for investigating relative permeability, capillary pressure, and fluid flow characteristics of low permeability rocks was designed specifically for use in CT scanners (Schembre *et al.* 1998). Experiments and interpretation of results were completed for spontaneous water imbibition experiments in diatomite, chalk, and sandstone. Air/water and oil/water systems were studied with differing initial water saturations.

To better understand multiphase flow and matrix to fracture fluid transfer, experiments on a fractured Berea sandstone system were conducted (Rangel-German *et al.* 1998). The progress of fluid movement was measured with CT scanning, as in the previous experimental studies. Multiphase flow in the fracture system was observable with the CT scanner. Fractures with the narrowest apertures showed the most stable displacement fronts, largest effects of capillary pressure within the fracture, and fastest breakthrough times. Using fine-grid simulations and a commercial simulator, fracture relative permeability and capillary pressure curves were obtained.

Several projects studied aspects of gas mobility in porous media and the effect of steam on porous media. In regard to foam for the control of gas mobility in porous media, Bertin *et al* studied foam generation and transient displacement in heterogeneous porous media (Bertin *et al.* 1998). A composite heterogeneous porous medium was created by centering a nearly homogeneous sandstone within a cylindrical tube and filling the annular space with a more permeable homogeneous sand. Capillary communication between the two zones of the composite core was prevented by the placement of a teflon jacket around the sandstone. Removal of the jacket allowed the heterogeneities to communicate. Using the CT scanner, it is concluded that displacement by foam can be efficient in both cases. Foam can control gas mobility in a manner that helps to equalize gas flow resistance in media with different permeabilities.

Research into foam properties was also conducted by Sagar *et al* (1998). The aim of this work was to visualize and understand the deleterious effects of oil on some foaming agents. A silicon micromodel etched with an accurate representation of the pore network of a Berea sandstone allowed direct observation of foam generation, flow, and destruction. It was found that fluorosurfactants produce strong, static, gas-blocking foams while alpha-olefin sulfonates do not in the presence of crude oil. All experiments were conducted close to atmospheric pressure.

Another area of recent research is the dissolution of a siliceous rock matrix when it is subjected to hot steam condensate (Bhat and Kovscek 1998). For low permeability porous media where oil recovery occurs by steam injection, dissolution of small amounts of rock mineral, transport of the dissolved rock, and reprecipitation in cooler regions of the reservoir could alter the distribution of porosity and permeability. Network models have been employed to understand how permeability shifts with evolving pore topology. This modeling effort has explained previous experimental results where a very strong power-law relationship between permeability and porosity was noted for hot fluid injection into fine-grained diatomite.

In the area of reservoir definition, study has focused on the shape of displacement patterns as a function of mobility ratio and water encroachment into oil and gas reservoirs. Wang et al dispelled the common notion that areal sweep efficiency from a staggered-line-drive pattern is always better than that from a five-spot pattern (Wang *et al.* 1999). Using a streamline based simulator, it was found that the five-spot pattern results in superior recovery efficiency compared to other patterns when the mobility ratio is very favorable. Also in this area, Brigham developed an analytical solution to diagnose the effects of water influx from the perimeter of an oil reservoir (Brigham 1998). Essentially, the exact infinite series solutions for various geometries were transformed into very accurate closed form approximations for ease of calculation. Linear, radial, and spherical systems were examined.

References

Akin, S., Castanier, L. M. and Brigham, W. E. (1999). Effect of Temperature on Heavy Oil/Water Relative Permeabilities. SPE 54120, 1999 SPE International Thermal Operations Symposium, Bakersfield, CA, 17-19 Mar. 1999.

Bertin, H. J., Apaydin, O. G., Castanier, L. M. and Kovscek, A. R. (1998). Foam Flow in Heterogeneous Porous Media: Effect of Crossflow. SPE 39678, 1998 SPE/DOE Improved Oil Recovery Symposium, Tulsa, OK, April 19-22, 1998.

Bhat, S. K. and Kovscek, A. R. (1998). Permeability Modification of Diatomite During Hot Fluid Injection. SPE 46210, 1998 Western Regional Meeting of the Society of Petroleum Engineers, Bakersfield, CA, May 10-13, 1998.

Brigham, W. E. (1998). "Water Influx, and Its Effect on Oil Recovery: Part 1. Aquifer Flow." SUPRI Technical Report 103, Stanford University, Stanford, CA.

Rangel-German, E., Akin, S. and Castanier, L. M. (1998). "Multiphase Flow Properties of Fractured Porous Media", presented at the SPE Western Regional Meeting, 26-27 May 1999, Anchorage, AK.

Sagar, N., Castanier, L. M. and E., B. W. (1998). Pore-Level Visualization of Oil/Foam Interactions in a Silicon Micromodel. SPE India Oil and Gas Conf. and Exhibition, New Dehli, India, 17-19 Feb 1998.

Schembre, J. M., Akin, S., Castanier, L. M. and Kovscek, A. R. (1998). Spontaneous Water Imbibition into Diatomite. SPE 46211, 1998 Western Regional Meeting of the Society of Petroleum Engineers, Bakersfield, CA, May 10-13, 1998 SPE.

Wang, Y., Kovscek, A. R. and Brigham, W. E. (1999). "Effect of Mobility Ratio on Pattern Behavior of a Homogeneous Porous Medium." In Situ **23**(1): p. 1-20 (1999).

1. Introduction and Objectives

The Stanford University Petroleum Research Institute (SUPRI) studied heavy-oil production mechanisms with the ultimate goal of increasing oil reservoir recovery efficiency. Additional aspects of the research effort covered a broad range of techniques that are useful for all improved oil recovery targets.

The research was organized into five topical areas:

- **Flow and Rock Properties.** The objectives of flow and rock properties were to assess the effect of reservoir parameters, such as temperature and pressure, on relative permeability and capillary pressure. Included in this effort were improvements to existing laboratory techniques to better study heat and fluid transport in porous media at reservoir temperature and pressure. Ultimately, this results in better data for use in predictive numerical models.

- **In-Situ Combustion.** In the area of in-situ combustion, goals were to study parameters affecting combustion field projects such as catalytic metallic salt additives, to study the effect of oxygen concentration on combustion parameters, to model accurately reaction kinetics and flow behavior of combustion processes.

- **Additives to Improve Mobility Control.** Objectives were to study and model the foam process for improving mobility control of injected gases including gravity override and channeling, with emphasis on steam injection. Objectives also included elucidation and modeling of the mechanisms of foam flow in porous media with oil present.

- **Reservoir Definition.** The main goal of reservoir definition was to develop techniques for evaluating the response of oil reservoirs to fluid injection. Reservoir geology and flow processes were studied in concert and this leads to interpretation procedures that allow us to better understand oil reservoirs.

- **Support Services.** In this category, objectives were to provide technical support, economic evaluation, and design and monitoring of field tests. Included here were technology transfer efforts aimed at sharing technology developed in all of the research areas with industry and other researchers.

The following sections summarize our accomplishments, present our technical results in detail, and chronicle our technology transfer efforts.

2. Accomplishments

Accomplishments during the contract period take the form of technical reports, papers presented at technical meetings, and manuscripts submitted to journals. A universally accessible world wide web site was also created to aid in the rapid distribution of technical information.

During this period of research SUPRI also held three Industrial Advisory Committee reviews and participated at DOE's request in 3 memorandum of understanding (MOU) meetings with Venezuela. Next accomplishments are summarized by category.

2.1 Industrial Outreach

- SUPRI Industrial Advisory Committee Review Meeting, Hartley Conference Center, Stanford University, April 15-16, 1999.

- SUPRI Industrial Advisory Committee Review Meeting, Hartley Conference Center, Stanford University, April 16-17, 1998.

- University Research Forum, held jointly with Petroleum Technology Transfer Council, University of Southern California, and the University of California, Berkeley, Los Angeles, CA, May 15, 1997.

- SUPRI Industrial Advisory Committee Review Meeting, room 450 Durand Building, Stanford University, April 4-5, 1997.

- Horizontal Wells and Enhanced Oil Recovery, meeting following the International Thermal Operations and Heavy Oil Symposium, Bakersfield, CA February 12, 1997.

- Establishment of a world wide web site describing our work and providing online distribution of research reports and papers at http://ekofisk.stanford.edu/supria.html.

2.2 Technical Reports

- SUPRI TR-119: "Computer Simulation of Single-Well Steam Assisted Gravity Drainage (SW-SAGD)" by K. E. Elliot and A. R. Kovscek (July 1999).
- SUPRI TR-118: "An Analytical Model for Simulating Heavy-Oil Recovery by Cyclic Steam Injection Using Horizontal Wells" by U. K. Diwan and A. R. Kovscek (July 1999).
- SUPRI TR-116: "An Experimental and Theoretical Investigation of Multi- Phase Flow in Fractured Porous Media" by E. R. Rangel-German, L. M. Castanier, and S. Akin (June 1999).
- SUPRI TR-115: "A Study of the Effect of Mobility Ratios on Pattern Displacement Behavior" by Y. Wang, A. R. Kovscek, and W. E. Brigham (December 1998).
- SUPRI TR-114: "Spontaneous Imbibition in Low Permeability Porous Media" by J. M. Schembre, S. Akin, and A. R. Kovscek (December 1998).
- SUPRI TR-113: "Modeling Permeability Alteration in Diatomite Reservoirs During Steam Drive" by S. K. Bhat and A. R. Kovscek (July 1998).
- SUPRI TR-112: "An Experimental Investigation of Foam Flow in Homogeneous and Heterogeneous Porous Media" by O. G. Apaydin, H. J. Bertin, L. M. Castanier, and A.R. Kovscek (July 1998).
- SUPRI TR-110: "Oil-Foam Interactions in a Micromodel" by N. S. Sagar and L. M. Castanier (November 1997).
- SUPRI TR-108: "A Comparison of Mass Rate and Steam Quality Reductions to Optimize Steamflood Performance" by G. L. Messner (April 1997).
- SUPRI TR-107: "CT Imaging Techniques for Two-Phase and Three-Phase In-Situ Saturation Measurements", by B. C. Sharma, W. E. Brigham, and L. M. Castanier (September 1996).

- SUPRI TR-104: "CT Measurments of Two-Phase Flow in Fractured Porous Media", by R.G. Hughes, W. E. Brigham, and L. M. Castanier. (June 1997).

2.3 Annual Reports

- SUPRI TR-117: "SUPRI Heavy Oil Research Program Twenty Second Annual Report" by W. E. Brigham, A. R. Kovscek, and L. M. Castanier (May 1999).
- SUPRI TR-111:"SUPRI Heavy Oil Research Program Twenty First Annual Report" by W. E. Brigham, A. R. Kovscek, and L. M. Castanier (May 1998).
- SUPRI TR-109: "SUPRI Heavy Oil Research Program Twentieth Annual Report" by W. E. Brigham, A. R. Kovscek, and L. M. Castanier (May 1997).

2.4 Conference Presentations

- "Simulation of Early-Time Response of Single-Well Steam-Assisted Gravity Drainage", SPE 54618, by K. T. Elliot and A. R. Kovscek, presented at the SPE Western Regional Meeting, 26-27 May 1999, Anchorage, AK.
- "Multiphase Flow Properties of Fractured Porous Media", SPE 54591, by E. Rangel-German, S. Akin and L. M. Castanier, presented at the SPE Western Regional Meeting, 26-27 May 1999, Anchorage, AK.
- "Imbibition Studies of Low-Permeability Porous Media", SPE 54590, by S. Akin and A. R. Kovscek, presented at the SPE Western Regional Meeting, 26-27 May 1999, Anchorage, AK.
- "Effect of Temperature on Heavy Oil/Water Relative Permeabilities", SPE54120, by S. Akin, L. M. Castanier, and W. E. Brigham presented at the 1999 SPE International Thermal Operations Symposium, 17-19 March 1999, Bakersfield, CA.
- "Reservoir Simulation of Foam Displacement Processes", UNITAR 1998.186, by A. R. Kovscek presented at the 7th Unitar International Conference on Heavy Crude and Tar Sands, 27-31 October 1998, Beijing, China.
- Messner, G.I., L.M. Castanier, and W.E. Brigham: "A Comparison of Mass Rate and Steam Quality Reductions to Optimize Steamflood Performance," presented at the Unitar Symposium, October 27-30, 1998, Beijing, China.
- "Effect of Mobility Ratio on Areal Sweep Efficiency and Pattern Flood Behavior", by Y. Wang, A. R. Kovscek, and W. E. Brigham presented at the 19th Annual International Energy Agency Workshop and Symposium, 4-7 October 1998, Carmel, CA.
- "Experimental and Theoretical Investigation of Multiphase Flow in Fractured Media", by E. R. German, S. Akin, and L. M. Castanier presented at the Geothermal Resources Council Meeting 1998 Annual Meeting, 20-23 September 1998, San Diego, California, USA.
- "Foam Flow in Heterogeneous Porous Media: Effect of Crossflow", SPE 39678, by H. J. Bertin, O. G. Apaydin, L. M. Castanier, and A. R. Kovscek presented at the SPE/DOE Improved Oil Recovery Symposium, 19-22 April 1998, Tulsa, OK, USA.
- Joshi, Sameer, L.M. Castanier, and W.E. Brigham: "Techno-Economic and Risk Evaluation of an EOR Project," SPE 39578, paper presented at the 1998 SPE India Oil and Gas Conference and Exhibition, February 17-19, 1998, New Delhi.

2.5 Journal Publications

- Wang, Y., A. R. Kovscek, and W. E. Brigham, " Effect of Mobility Ratio on Pattern Behavior of a Homogeneous Porous Medium," *In Situ*, **23(1),** p. 1-20 (1999).
- Bhat, S. K. and A. R. Kovscek, "Statistical Network Theory of Silica Deposition and Dissolution in Diatomite," *In Situ*, **23(1),** p. 21-54 (1999).
- Bertin, H. J., O. G. Apaydin, L. M. Castanier, and A. R. Kovscek, "Foam Flow in Heterogeneous Porous Media: Effect of Crossflow," *Society of Petroleum Engineers Journal*, **4(2)**, p. 75-82 (1999).
- Bertin, H.J., Quintard, M.Y, and Castanier, L.M.: " Development of a Bubble-Population Correlation for Foam-Flow Modeling in Porous Media," *Society of Petroleum Engineers Journal* **3(4)**, 356-362 (1998).
- Kovscek, A. R., T. W. Patzek, and C. J. Radke. "Mechanistic Foam Flow Simulation in Heterogeneous and Multidimensional Porous Media," *Society of Petroleum Engineers Journal*, **2(4)**, p. 511-526 (1997).
- Castanier, L.M. and W.E. Brigham: "Modifying In-situ Combustion with Metallic Additives," *In Situ* **21 (1)**, 27-45 (1997).
- Akin, S., J. M. Schembre, S. K. Bhat, and A. R. Kovscek, "Spontaneous Imbibition Characteristics of Diatomite," *Journal of Petroleum Science and Engineering*, to appear 2000.

SPE International
Society of Petroleum Engineers

SPE 54591

Multiphase-Flow Properties of Fractured Porous Media

E. Rangel-German, S. Akin, and L. Castanier, Stanford University

Copyright 1999, Society of Petroleum Engineers Inc.

This paper was prepared for presentation at the 1999 SPE Western Regional Meeting held in Anchorage, Alaska, 26–28 May 1999.

This paper was selected for presentation by an SPE Program Committee following review of information contained in an abstract submitted by the author(s). Contents of the paper, as presented, have not been reviewed by the Society of Petroleum Engineers and are subject to correction by the author(s). The material, as presented, does not necessarily reflect any position of the Society of Petroleum Engineers, its officers, or members. Papers presented at SPE meetings are subject to publication review by Editorial Committees of the Society of Petroleum Engineers. Electronic reproduction, distribution, or storage of any part of this paper for commercial purposes without the written consent of the Society of Petroleum Engineers is prohibited. Permission to reproduce in print is restricted to an abstract of not more than 300 words; illustrations may not be copied. The abstract must contain conspicuous acknowledgment of where and by whom the paper was presented. Write Librarian, SPE, P.O. Box 833836, Richardson, TX 75083-3836, U.S.A., fax 01-972-952-9435.

Abstract

The fluid transfer parameters between matrix and fracture are not well known. Consequently, simulation of fractured reservoirs uses, in general, very crude and unproved hypothesis such as zero capillary pressure in the fracture and/or relative permeability functions that are linear with saturation. In order to improve the understanding of flow in fractured media, an experimental study was conducted and numerical simulation used to interpret experimental results.

A laboratory flow apparatus was built to obtain data on water-air imbibition and oil-water drainage displacements in fractured sandstone systems. During the experiments, porosity and saturation were measured along the core utilizing a Computerized Tomography (CT) scanner. Saturation images were reconstructed in 3-D to observe how matrix-fracture interaction occurred. Differences in fluid saturations and relative permeabilities caused by changes of fracture width have also been analyzed.

In the case of water-air imbibition, fracture systems with narrower fracture apertures showed more stable fronts and slower water breakthrough than the wide fracture systems. However, the final water saturation was higher in wide fracture systems, thus showing that capillary pressure in the narrow fracture has more effect on fluid distribution in the matrix. During oil-water drainage, oil saturations were higher in the blocks near the thin fracture, again showing the effect of fracture capillary pressure. Oil fingering was observed in the wide fracture.

Fine-grid simulations of the experiments using a commercial reservoir simulator were performed. Relative permeability and capillary pressure curves were obtained by history matching the experiments. The results showed that the assumption of fracture relative permeability equal to phase saturation is incorrect. We found that both capillary and viscous forces affect the process. The matrix capillary pressure obtained by matching an experiment showed lower values than reported in the literature.

Introduction

Flow equations describing fractured porous media are usually written assuming that reservoir behavior is dominated by the transfer of fluid from the matrix to high conductivity fractures, that are often entirely responsible for flow between blocks and flow to wells.

Conventional representation of these equations assumes the knowledge of both rock and fluid properties, capillary pressure, and relative permeabilities. Any of these parameters can be obtained for the matrix by laboratory work, but not for the fractures. To obtain more data on properties such as fracture capillary pressure, fracture relative permeabilities and/or saturation distributions, an experimental and numerical study was conducted

In general, several authors (Kazemi and Merrill (1979), Beckner (1990), Gilman et al. (1994)) have assumed that fracture capillary pressure is negligible. Others have shown experimentally that capillary continuity becomes important when gravity provides a driving force (Horie et al. (1988), Firoozabadi and Hauge (1990), Labastie (1990), Firoozabadi and Markeset (1992). Kazemi (1990) states his belief that capillary continuity is prevalent in the vertical direction and has suggested that, to reduce the number of equations to solve, fractured reservoir simulators should use the dual-permeability formulation for the z direction and the dual-porosity formulation for the x and y directions.

For this work, detailed measurements of pressure, rate, and saturation distribution were performed, and attempts to measure phase distribution inside the fracture were also made using a (CT) scanner. This research resulted in a much better understanding of the physical processes that occur when two or three phases flow in a fractured system, compared to previous reported studies (Guzman and Aziz (1993), Hughes (1995)). Our first step was constructing an experimental apparatus capable of reproducing the results obtained by that by Hughes(1995). Thus, we conducted similar experiments using two of the core holders developed by him in order to verify that this new experiment gives consistent results. Once the apparatus was tested, we conducted multiphase flow

experiments using an 8% NaBr brine solution as the wetting phase, and decane as the nonwetting phase. Three stages in each experiment were completed: study of water imbibing into a dry core, decane displacing water in a water-saturated core, and water displacing oil. Differences in fluid saturations and relative permeabilities caused by changes in fracture width were also analyzed.

Simulations of the experiments using a commercial reservoir simulator were performed. Fracture relative permeability and capillary pressure curves were obtained by history matching the experiments. A sensitivity analysis of parameters such as fracture relative permeability, capillary pressure in the fracture, and fracture width was also completed.

Experiment Design

The experiments presented in this work were made using an apparatus similar to the one designed, constructed and used by Hughes (1995). The following subsections give a description of the material and methods used to build the experimental set-up.

Cores. For this work, we used two of the three rectangular blocks of Boise sandstone cores constructed and used by Hughes(1995). Both core holders consist of two 2 15/16 x 1 1/2 x 11 inch blocks. The first core holder is system of the two blocks together, i.e. with no spacer in between the blocks. The second one is a similar configuration, but has a 1-mm thick spacer fastened in place with Epoxy 907 to provide separation between the blocks to simulate a fracture.

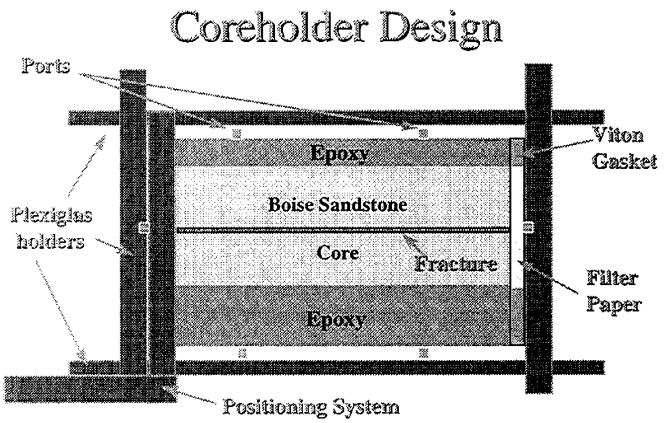

Fig. 1- The Core Holder.

Core holders. Due to the rectangular shape and the desire to measure in-situ saturations through the use of the CT scanner, conventional core holders could not be used. A core holder similar to the one designed by Guzman and Aziz (1993), and later developed by Hughes (1995) was used. An epoxy resin surrounds the core, as well as plexiglas end plates and a piece of 3/8 inch Viton that acts as a gasket between the core and the plexiglas end plates as shown in **Fig. 1.**

Positioning System. The positioning system consists of a moving table with 0.01 mm accuracy that is positioned electronically by means of a control panel. Basically, any flat surface can be attached to this table using screws. This system was one of the major improvements to previous designs (Guzman, 1993; Hughes, 1995). In this way, we can obtain cross-sectional images of the core at the same location at any desired time of the experiment. This could not be performed in other studies because the standard patient table of a CT Scanner of this type lacks comparable accuracy.

Flow System. The flow system (**Fig. 2**) allows fluids to be directed to any port or combination of ports in the experiment such that: 1)It can be directed to calibrate the pressure transducers, 2)It can be used to inject from one end and to produce from the opposite end, 3) It can be used to inject into one or more of the ports on the top and bottom of the core holder, or 4) To bypass the core holder completely. It also consists of two pumps that inject 0.01 to 9.99 cm^3/min in 0.01 increments. Plumbing downstream of the pumps allows mixing of the fluids being discharged by each pump. This setup allows injection pressure to be monitored with a test gauge and recirculation to measure pump output rates.

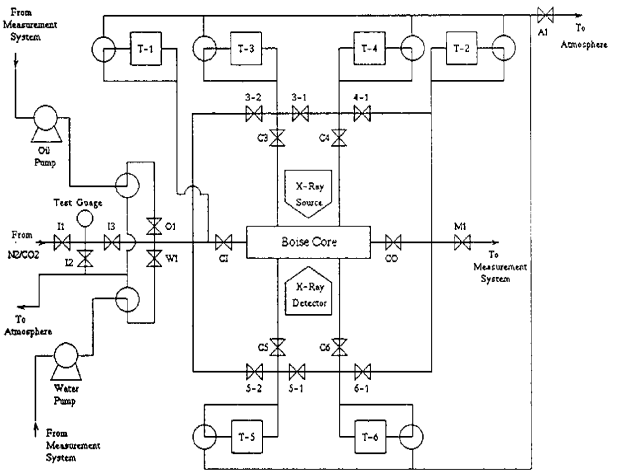

Fig. 2- Flow System (After Hughes, 1995.)

Production Measurement System. The production measurement system is an adaptation of a design given by Ameri and Wong (1985). **Fig. 3** shows this system. The electronic balances are connected to the serial communication ports of a personal computer (PC).

Pressure Measurement System. Pressure drop along the core can be measured between any of the six different positions on the core labeled as T-x. In **Fig. 2,** one can see that two of the transducers are connected to the inlet and outlet of the core holder. Each transducer is connected to a carrier demodulator which produces a DC signal in the range from -10 to +10 V that is proportional to the pressure drop. The output signals were recorded on a chart recorder and also captured in digital form.

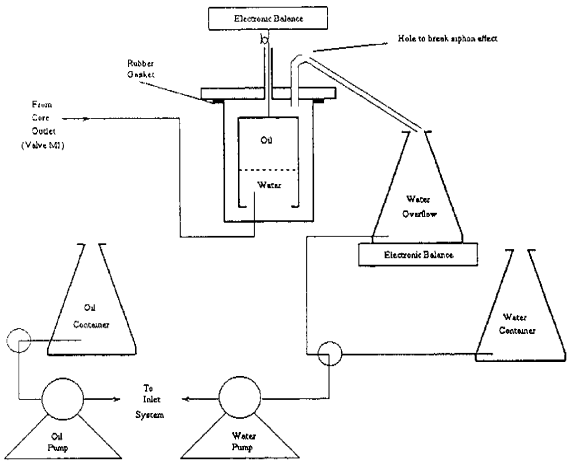

Fig. 3- Production system (after Hughes, 1995.)

CT Scanner. A CT Scanner can be used to calculate porosity, saturation and in some cases, concentration distribution and to track advancing fronts. It can also be used to measure fracture aperture. We use a Picker 1200SX Dual Energy CT scanner.

Fluids. CT numbers are proportional to their densities. A selection of fluids and dopants were employed in order to obtain the best contrast in CT numbers and, hence, most accurate in terms of phase saturation. Decane was used to represent the oil phase, and 8% NaBr, by weight, water solution was used as the water phase.

Experimental Procedure

The first core used had a fracture with no spacer in between the blocks. The total travel distance of the positioning system (accuracy ± 0.01 mm) was then 25.5 cm, resulting in 13 slices including two located at the pressure ports (fourth and eleventh, for the first experiment; and fourth and tenth, for the second experiment.) The second experiment was conducted using a core holder that contained a similar system with two Boise sandstone blocks with a 1 mm thick fracture in between. **Fig. 4** shows the CT scan locations.

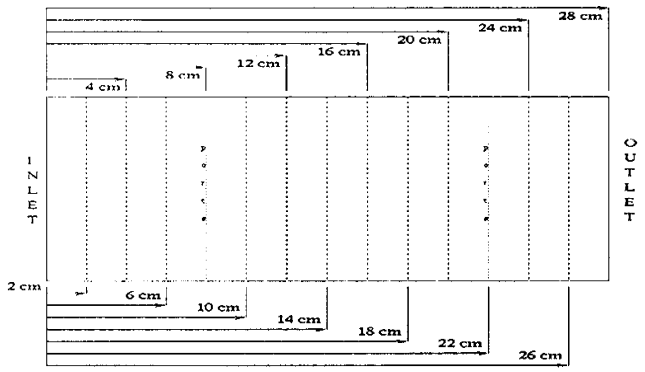

Fig. 4- CT Scan locations.

The first step in the experimental procedure was to scan the dry core. This step was very important to verify that the apparatus and the set-up were working properly. For instance, there were some problems with the core holder in a first trial for the dry scan. We could not keep its position horizontal, because it was quite heavy and held only by one of the sides. Two C clamps were used to strengthen the attachment to the positioning system and, thus, to keep the core holder in the same horizontal position during the experiment. After these improvements, the dry scans were conducted successfully.

The second step was to evaluate how water imbibed into an unsaturated core. This part of the experiment gave us results that can be compared with those obtained by Hughes (1995), and eventually used to evaluate how well the new experiment worked. Starting with a flow rate of 2 cm^3/min, CT images of the core were taken every 5 minutes for the first 20 minutes of water injection (0.15 PV); after this, images were taken at 30 min (0.22 PV), 45 min (0.33 PV), 1 hr. (0.45 PV), 1hr 30 min (0.67 PV), 2 hr (0.89 PV), 3 hr (1.34 PV), and 4 hours (1.78 PV) after water injection started. Next, the top and bottom ports were opened since we wanted to fill up the core to the maximum water saturation (S_w=1.) Common to all time steps, we tried to take images up to one location ahead of the position of the water front.

After 5 hours of water injection (2.25 PV), the flow rate was changed to 0.5 cm^3/min in order to inject water for 14 more hours to reach steady state. After 19 hours (8.55 PV), reference 100% water saturated images were taken. Then, at 19 hours and 45 min (8.9 PV) the water rate was changed back to 2 cm^3/min, and the top and bottom ports were closed. At 21 hours (9.45 PV) a final set of slices was taken to find any possible change in CT numbers. Negligible changes in CT numbers were observed. At 23 hours of water injection, the third step of the experiment started. Table 1 summarizes the flow rates used.

The third step of the experiment involved injecting decane at 2 cm^3/min. The scanning frequency was intended to be the same as the water injection process. Thus, images of the core were taken every five minutes until the first 20 minutes of oil injection (0.15 PV). After that, more images were taken at 30 min (0.22 PV), 45 min (0.33 PV), 1 hr. (0.45 PV), 1hr 30 min (0.67 PV), 2 hr 30 min (1.13 PV), and 3 hr 45 min. (1.69 PV) after oil injection started. Then, the top and bottom ports were opened at 4 hours (1.79 PV) since we wanted to fill the core up to the maximum possible point. At 4 hr 30 min of oil injection, one more set of images was taken. After 5 hours (2.25 PV) of oil injection, the flow rate was changed to 1 cm^3/min for 16 hours (7.2 PV) to reach higher possible oil saturations (1-S_{wc}). After 21 hours of oil injection (9.45 PV), a new set of slices was taken, and the ports were closed. Then, at 21 hours and 39 min the oil injection was stopped, and water injection at the maximum pump rate (9.99 cm^3/min) was started.

The fourth step of the experiment was the water displacing oil stage. Injecting 9.99 cm^3/min of water, images were taken at 5 min (0.04 PV), 15 min (0.13 PV), and 30 min (0.23 PV). At 1hr 10 min (0.53 PV), water injection was stopped, the inlet and outlet lateral ports were also closed, leaving all of the core holder's ports closed. One more set of images was taken after two days of closing the core holder to observe if capillary

equilibrium had been reached. Table 1 summarizes the flow rates used and the timing of each.

The second experiment was performed using the core holder that contained a system with two Boise sandstone blocks with a 1 mm thick fracture in between. The same experimental procedure was followed. Essentially, we wanted to obtain CT images, and then saturation values for equivalent times, so we could compare the differences between the two systems. The rates and timing for the case of two blocks with a wider fracture are shown in Table 2.

Data Analysis

Using the CT numbers obtained from the experiments, porosity and saturation distributions along the core were determined. The most common way to calculate porosity from CT Scanner images is by using the following expression (Withjack, 1988):

$$\phi = \frac{CT_{cw} - CT_{cd}}{CT_w - CT_a} \quad \text{.....(1)}$$

where CT_{cw} is the CT number for a 100% water saturated core at a matrix location, CT_{cd} is the CT number for a dry core at a matrix location, CT_w is the CT number for water, and CT_a is the CT number for air. The CT number for water (8%NaBr solution, for this work) is around 360, while the CT number for air is -1000.

The water and oil saturations were also calculated from the CT images. The following equations show how to evaluate water saturation for the water displacing air case, and for the oil displacing water or water displacing oil case.

$$S_w = \frac{CT_{aw} - CT_{cd}}{CT_{cw} - CT_{cd}} \quad \text{.....(2)}$$

where CT_{aw} is the CT number for water and air saturated core at a matrix location. Similarly, for the case of oil-water systems:

$$S_w = \frac{CT_{ow} - CT_{cw}}{\phi(CT_o - CT_w)} \quad \text{.....(3)}$$

where CT_{ow} is the CT number for a water and oil saturated core at a matrix location, and CT_o is the CT number for oil. The CT number for oil (decane, for this work) is around -272.

Experimental Results

First, we computed the values of porosity using Eq. 1 at each location indicated in **Fig. 4**. The porosity images for both systems are shown in **Fig. 5**, where the values below each square correspond to the mean and the standard deviation, respectively, of the porosity values obtained from CT numbers. This step was essential for both experiments because from these images and their corresponding values we differentiated the regions with higher or lower porosity. The range of values is shown in the color bar in the right hand side in **Fig. 4**. There, we can also see that the system with the thin fracture has a little higher porosity than the system with the wide fracture, especially in the top block, where values up to 0.13 were observed. We found that the average value for porosity calculated from the scans was 14.5% which matches with the average value 14.35% reported by Hughes (1995); however, this value differs from the average porosity measurements of 25.4% obtained by Guzman and Aziz (1993) and 29.3% obtained by Sumnu (1995). All of these previous studies have also shown areas in the rocks, which have lower permeability.

Water-Air Imbibition. Following the aforementioned procedure, and the flow rates, times and water injection conditions listed in Table 1, several sets of images like those shown in **Fig. 6** corresponding to 1.5 hours of water injection (0.67 PV) were obtained. Similar to the porosity images, each square corresponds to water saturation values obtained at one location. The pair of values presented below each square corresponds to the mean and standard deviation of the top, bottom, and both blocks, respectively. The gray scale on the right hand side shows the range of water saturation values. Different profiles, corresponding to different pore volumes of water injected were plotted. The profiles are more or less stable and they appear to be quasi one dimensional. The same procedure was followed for the wide fracture system and CT saturations were obtained. **Fig. 7** gives water the saturation distribution at 0.67 PV of water injected. Different profiles, corresponding to different pore volumes of water injected were also plotted. The profiles are less stable than those for the thin fracture system as observed from the 8^{th} through 12^{th} slices. We observed similar profiles for all times.

Oil-Water Drainage. Similar images were obtained for the second stage of the experiments (oil injection). **Fig. 8** shows a set of images corresponding to 2.5 hours (1.13 PV) of oil injection. Here, the pairs of values below each square indicate the mean and the standard deviation of oil saturation, respectively. Shades were also assigned to the oil saturation values. Thus, the gray scale on the right hand side shows the range of values and their corresponding lightness or darkness. In all the images shown in **Fig. 8** darker shades indicate lower oil saturation. For instance, black means zero oil saturation. This stage was finished after 4 hours of oil injection when we opened the lateral ports of the core holder to reach the maximum possible oil saturation. The corresponding images for the wide fracture system are shown in **Fig. 9**.

Water-Oil Displacement. Images for the third stage of the experiment (water displacing oil) were also obtained. Due to problems with one of the pumps, we could not analyze properly the rest of the data for the case of thin fracture system. Images for the third stage of the second experiment (water displacing oil in the wide fracture system) were also obtained. The most interesting sets are shown in **Fig. 10** and

Fig. 11 corresponding to 16 hours (7.2 PV) and 17 hours (7.7 PV) of water injection, respectively. One can see that the displacement of oil is completed almost perfectly.

Analysis of Experimental Results

Due to the fact that the experiments ended differently, we were able to compare the results up to the second stage of both experiments. This section shows the comparison graphically.

Three-dimensional (3-D) reconstructions of the sets of water saturation images were calculated. All these images were obtained using a color map for values above 50% of water or oil saturation, respectively. These 3-D images show more clearly how the fluids actually flow through the fractured porous media. This work was intended to show the differences between the flow patterns for different fracture thicknesses. The reconstructed images are shown in **Fig. 12**. Each image corresponds to a specific time. Thus, the first image on the left-hand side of Fig. 12 is compared to the first one of the right hand side of the same Fig. 12. The second image on the left hand side was computed for the same time as the second image on the right hand side, and so on. There, we can see that the water front for the wider fracture system moves at almost at the same speed as the water front for the narrow fracture system does. For instance, one can see that after 1.5 hours of water injection, the water front of the narrow fracture system seems to be ahead of the front for the wide fracture system; however, after two hours of water injection water has filled up both systems.

Similarly, the 3-D oil injection history was also reconstructed. Since the oil saturations were low for both cases, it is a bit harder to see the differences. It is possible to see that the thinner fracture system has higher oil saturation close to the fracture. This is shown in **Fig.13**. One can see that the narrow fracture system has lighter colors close to the injection surface. We can also see that for the case of the wide fracture system, the oil does not penetrate. Furthermore, oil flows almost completely through the fracture. This is shown in all the images on the right hand side of Fig. 13 by the almost white horizontal line that corresponds to the fracture. Remember that for the case of oil injection stages, darker means lower oil saturation.

Numerical Simulation Results

Numerical simulations of the experiments using a commercial reservoir simulator were conducted to study fracture relative permeability and matrix/fracture interaction, to match previous experimental results, and to provide experimental-numerical based suggestions how to simulate multiphase flow in fractured porous media.

A cubic Cartesian gridding proportional to the cores was designed in such a way that we had three different "boxes". Two of them simulate the top and bottom blocks with matrix rock properties; i.e., matrix capillary pressure curves, matrix relative permeability curves, matrix absolute permeability, porosity, and the other set of blocks simulate the horizontal fracture with fracture properties; i.e., large absolute permeability, fracture capillary pressure curves, and fracture relative permeability curves. It was assumed that relative permeability and capillary pressure in the matrix are constant.

For the water-air cases, we used the curves presented by Persoff et. al. (1991) for matrix relative permeability and the ones measured by Sanyal (1972) for matrix capillary pressure. For the oil-water cases, we used the matrix capillary pressure curves presented by Sanyal (1972). Unfortunately, no relative permeability curves for oil-water system in Boise sandstone have been reported, so we followed the procedure presented by Purcell(1949) to obtain the matrix relative permeability curves.

Fracture relative permeability and capillary pressure curves were obtained by history matching the experiments. Sensitivity analysis of parameters such as fracture relative permeability, capillary pressure in the fracture, and fracture width have been completed. We considered each parameter independently.

First, we studied capillary pressure in the fracture under the assumption that it is a linear function of water saturation. Different cases for capillary pressure curves and relative permeability curves for the fracture are shown in **Fig. 14**. It is important to note that for fracture relative permeability curves, the lower the slope of the straight line, the higher the resistance to flow through the fracture. Starting with a high capillary pressure in the fracture, we observed that the matrix front matched well, but the breakthrough time was faster compared to our experimental results. We decreased the slope of the straight line capillary pressure in the fracture up to a point in which the breakthrough time as well as the matrix front matched the experiments. For the sake of completeness, we also studied extreme cases that are often used in real practice such as very low and no capillary pressure in the fracture, although neither one resembled experimental data. The no capillary pressure case showed us that the blocks worked independently, so the capillary continuity that we had seen in the experiments did not occur in the numerical studies.

After obtaining the proper description of capillary pressure in the fracture, we continued by studying the effect of fracture relative permeability curves. The assumption of fracture relative permeability equal to phase saturation is often used in numerical simulation. This assumption suggests, no resistance, ideal flow of fluids in the fractures, such that inside the fracture the phases can move past each other without hindrance. However, if relative permeabilities with a slope less than 1.0 are used, the effective total mobility is reduced. Pan and Wang (1996) discussed that higher resistance in the fractures must be used, such as 0.75 and 0.6 slope straight lines instead. Our results show that the best matches are achieved when an 0.6 slope is used. This indicates that the presence of a small amount of one phase interferes significantly with the flow of the other phase.

In order to obtain the best match, we also examined the heterogeneities present in the systems, especially in the wide fracture system. We ran different heterogeneous cases until we obtained better matches. We achieved this goal by assigning higher porosity (14%) to the bottom block and lower porosity (13%) to the top block. The results for this case are shown in

Fig. 15 which proves that, capillary pressure in the fracture can not be neglected and the heterogeneity must also be considered.

Similarly, we followed the same analysis for the system with no spacer in between the blocks. An interesting observation was that neither the capillary pressure in the fracture nor the relative permeability curves affected the results. That led us to the conclusion that the fracture is so thin that there is almost perfect continuity, and it acts like a solid block. **Fig. 15** also shows the comparison of the experimental results with the numerical simulation results for the system with no spacer. The fracture system without a spacer showed a more stable front and faster breakthrough than the other, as we had seen in the experimental results.

Similarly, we followed the same procedure for the oil injection stages. The matches for the thin fracture system were not very good, but the results for the wide fracture system, where we had seen in the experiments that most of the oil flowed though the fracture, are better. In this case, the assumption of zero capillary pressure in the fracture worked properly. These results are shown in **Fig. 16**.

Discussion and Recommendations

An apparatus that can be used to obtain detailed measurements of pressure, rate and saturation distribution was built and tested. It consists of a fractured core in an epoxy core holder, with six different locations for pressure measurements. Phase distribution in the matrix and inside the fracture were also determined by means of a (CT) scanner.

Multiphase flow runs were performed, and data were obtained. The experimental results were matched well by numerical simulation. Numerical simulations were also used to estimate the influence of variables such as fracture relative permeability, matrix/fracture capillary pressure, and fracture width. The results show that capillary pressure is a dominant parameter in this type of water displacement. Knowledge of the capillary pressure function is then critical.

The combined experimental and simulation study resulted in a much better understanding of the physical processes that occur when two or three phases flow in a fractured system, compared to previous reported studies (Guzman and Aziz (1993), Hughes (1995)).

This work allowed us to find areas with lower permeability and porosity, and then use them in the numerical simulations to obtain the best matches as shown in **Fig. 15**, for instance. All the CT images and the three-dimensional reconstructions obtained from them made the understanding of multiphase flow and the comparison with simulation results much easier, as shown in **Fig. 15** and **Fig. 16**.

Several authors (Kazemi and Merrill (1979), Beckner (1990), Gilman et al. (1994)) have assumed that fracture capillary pressures are negligible. Others have shown experimentally that capillary continuity becomes important when gravity provides a driving force (Horie et al. (1988), Firoozabadi and Hauge (1990), Labastie (1990), Firoozabadi and Markeset (1992). Kazemi (1990) stated that capillary continuity is prevalent in the vertical direction and has suggested that, to reduce the number of equations to solve, fractured reservoir simulations should use the dual permeability formulation for the z direction and the dual porosity formulation for the x and y directions.

This work showed that capillary continuity can occur in any direction, depending on the relative strengths of the capillary and Darcy terms in the flow equations; the thin fracture systems have a more stable front and slower breakthrough compared to wide fracture systems, and that capillary pressure has more effect when the fracture is narrow. We observed that neither the capillary pressure nor the relative permeability curves in the fracture affected the results for the narrow fracture system. That led us to the conclusion that the fracture is so thin and/or each half mated so well that there is almost perfect capillary continuity, and it acts very similar to a solid block.

With this work we were able to verify that larger recoveries can be obtained when fractures are wider, and that the assumption of zero capillary pressure in the fracture is incorrect especially for air and water. The assumption of fracture relative permeabilities equal to the phase saturation was tested. This work shows that straight-line fracture relative permeability can be used, but it is not necessarily equal to the phase saturation. X-type relative permeability curves can be used for fractured system using larger flow resistances in the fractures, such as 0.75 or 0.6 sloped straight lines instead. Our results show that the best matches are achieved when a slope of 0.6 is used.

This work has shown that both capillary and viscous forces dominate the flow in fractures. Moreover, a procedure for determining the parameters involved in transmissibility and the transfer terms that appear in the flow equations in finite difference form was established.

The reader should realize that experiments presented in this work were performed only once. We assumed that our results were correct because they were comparable to Hughes (1995) results, and we could reproduce the experiments very accurately by numerical simulations. However a repeatability test should be performed on these experiments to achieve a higher certainty of the conclusions presented here.

Conclusions

The results of the combined experimental and the simulation study show:

1.Areas with lower permeability and porosity can be identified and used in numerical simulation.

2. Thin fractures systems showed more stable fronts and slower breakthrough compared to wide fracture systems.

3. Capillary pressure has more effect when the fractures are narrow.

4. Larger recoveries can be obtained when the fractures are wider.

5. Assuming zero capillary pressure in the fracture is incorrect.

6. X-type relative permeability curves can be used for fractured systems using high resistance through fractures, but relative permeability is not equal to phase saturation.

Nomenclature

CT = CT scanner number
S = saturation
ϕ = porosity

Subscripts

a = air
aw = air and water saturated
cd = dry core
cw = 100% water saturated
ow = oil and water saturated
w = water

Acknowledgments

This work is supported by U.S. Department of Energy under contract No. DE-FG22-96BC14994, SUPRI-A Industrial Affiliates and Consejo Nacional de Ciencia y Tecnología (CONCACyT), México.
We thank Anthony Kovseck, Richard Hughes and William Brigham of Stanford University for valuable discussions and advice.

References

1. Ameri, H. and Wang, J.: "Effect of Temperature on Oil-Water Relative Permeability," SUPRI Heavy Oil Research Program, Eighth Annual Report, SUPRI TR-47, (April 1985), 11-24.
2. Beckner, B.L.: Improved Modeling of Imbibition Matrix/Fracture Fluid Transfer in Double Porosity Simulators, PhD dissertation, Stanford University (July 1990)
3. Buckley, S.E. and Leverett, M.C.: "Mechanisms of Fluid Displacement in Sands," Transactions American Institute of Mining and Metallurgical Engineers, 146 (1942), 107-116.
4. Eclipse 100 User's Manual, Intera Information Technology Limited, Oxfordshire, England, 1994.
5. Firoozabadi, A. and Hauge, J.: "Capillary Pressure in Fractured Porous Media," JPT (June 1990) 784-791.
6. Firoozabadi, A. and Markeset, T.: "An Experimental Study of Capillary and Gravity Crossflow in Fractured Porous Media," SPE 24918, presented at the 67th SPE Annual Technical Conference and Exhibition, Washington, D.C., October 4-7, 1992.
7. Gilman, J.R., Bowzer, J.L. and Rothkopf, B.W.: "Application of Short-Radius Horizontal Boreholes in the Naturally Fractured Yates Field," SPE 28568, presented at the 69th SPE Annual Technical Conference and Exhibition, New Orleans, LA, September 25-28, 1994.
8. Guzman, R.E. and Aziz, K.: Design and Construction of an Experiment For Two-Phase Flow in Fractured Porous Media, SUPRI TR-95, Stanford Petroleum Research Institute, Stanford, CA, (June 1993).
9. Horie, T., Firoozabadi, A. and Ishimoto, K.: "Capillary Continuity in Fractured Reservoirs," SPE 18282, presented at the 63rd SPE Annual Technical Conference and Exhibition, Houston, TX, October 2-5, 1988.
10. Hughes, R.G.: CT Measurements of Two-Phase Flow in Fractured Porous Media, Masters Report, Stanford University (December 1995).
11. Kazemi, H. and Merrill, L.S.: "Numerical Simulation of Water Imbibition in Fractured Cores," SPEJ (June 1979) 175-182.
12. Kazemi, H.: Naturally Fractured Reservoirs, Third International Forum on Reservoir Simulation, Baden, Austria (1990).
13. Labastie, A.: "Capillary Continuity Between Blocks of a Fractured Reservoir," SPE 20515 presented at the 65th SPE Annual Technical Conference and Exhibition, New Orleans, LA, September 23-26, 1990.
14. Pan, X. and Wong, R.C.: "Steady State Two-phase in a Smooth Parallel Fracture," presented at the 47th Annual Technical Meeting of The Petroleum Society in Calgary, Alberta, Canada, June 10-12, 1996.
15. Persoff, P., Pruess, K., and Myer, L.: "Two-Phase Flow Visualization and Relative Permeability Measurement in Transparent Replicas of Rough-Walled Rock Fractures," Sixteenth Workshop on Geothermal Reservoir, Stanford University (January 1991).
16. Purcell, W. R.: "Capillary Pressures - Their Measurement Using Mercury and the Calculation of Permeability Therefrom," *Trans, AIME, 186, 39* (1949).
17. Rangel-German, E.: Experimental and Theoretical Investigation of Multiphase Flow in Fractured Porous Media, Masters Report, Stanford University (June 1998).
18. Sanyal, S.K.: The Effect of Temperature on Electrical Resistivity and Capillary Pressure Behavior of Porous Media, Ph.D. dissertation, Stanford University (December 1971).
19. Withjack, E.M.: "Computed Tomography for Rock-Property Determination and Fluid-Flow Visualization", SPEFE (December 1988) 696-704.

TABLE 1. RATES AND TIMING FOR THE CORE WITH NARROW FRACTURE

Fluid Injected	Time (hrs)	Flow Rate (cm^3/min)	Ports
Water	0.0 - 4.0	2.0	Top and bottom closed, lateral open.
Water	4.0 - 5.0	2.0	Top and bottom open, lateral closed.
Water	5.0 - 19.8	0.5	Top and bottom open, lateral closed.
Water	19.8 - 23.0	2.0	Top and bottom closed, lateral open.
Decane	23.0 - 27.0	2.0	Top and bottom closed, lateral open.
Decane	27.0 - 28.0	2.0	Top and bottom open, lateral closed.
Decane	28.0 - 44.7	1.0	Top and bottom open, lateral closed.
Water	44.7 - 46.0	9.99	Top and bottom closed, lateral open.
	46		Shut down everything

TABLE 2. RATES AND TIMING FOR THE CORE WITH WIDE FRACTURE

Fluid Injected	Time (hrs)	Flow Rate (cm^3/min)	Ports
Water	0.0 - 5.0	2.0	Top and bottom closed, lateral open.
	5.0 - 21.0	0.0	Top and bottom closed, lateral closed.
Water	21.0 - 22.5	2.0	Top and bottom open, lateral closed.
Water	22.5 - 25.6	2.0	Top open, bottom closed, and lateral closed.
	25.6 - 45.0	0.0	Top and bottom closed, lateral closed.
Decane	45.0 - 48.0	2.0	Top and bottom closed, lateral open.
Decane	48.0 - 49.2	4.0	Top and bottom closed, lateral open.
Decane	49.2 - 51.0	4.0	Top and bottom open, lateral closed.
	51.0 - 52.0	0.0	Top and bottom closed, lateral closed.
Water	52.0 - 54.3	4.0	Top and bottom closed, lateral open.
Water	54.3 - 68.8	0.5	Top and bottom closed, lateral open.
Water	68.8 - 71.0	4.0	Top and bottom open, lateral closed.
	71		Shut down everything

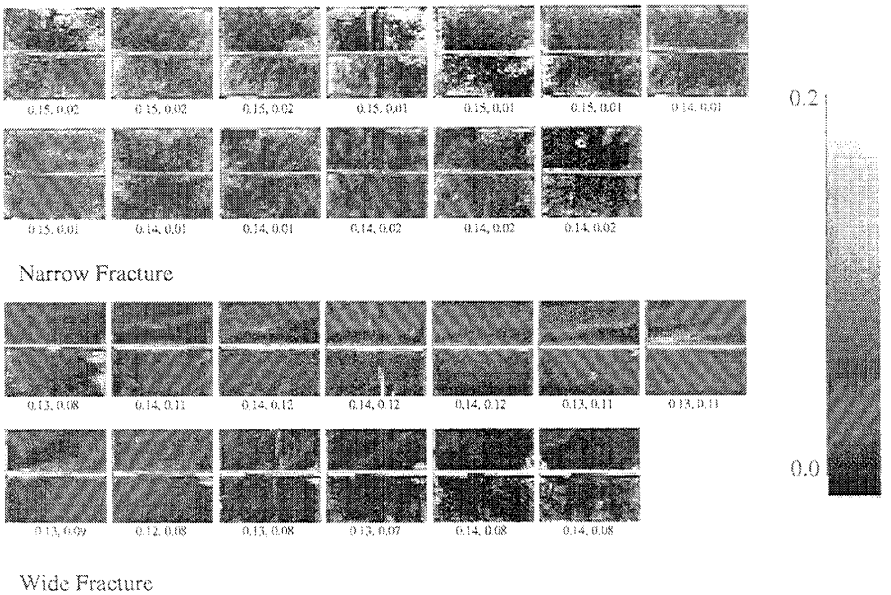

Fig. 5- Porosity distribution for the experimental system.

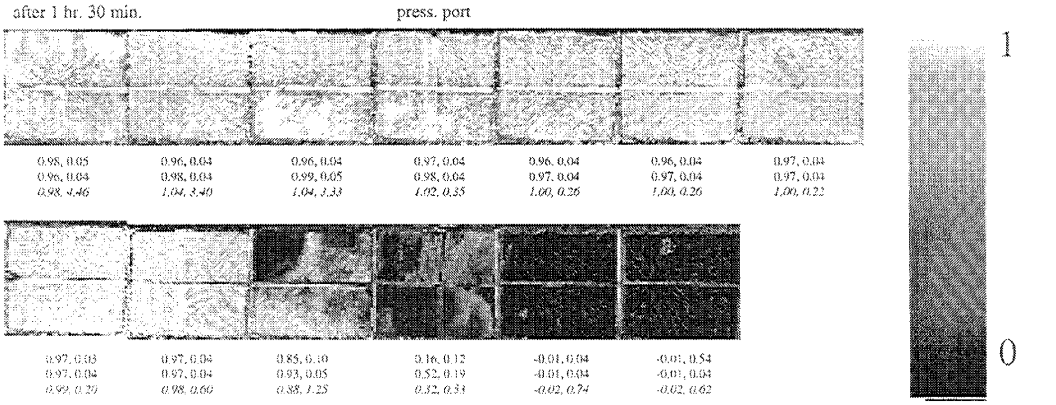

Fig. 6- CT Saturation images for the thin fracture system after 1 hr 30 min of water injection (0.67 PV.)

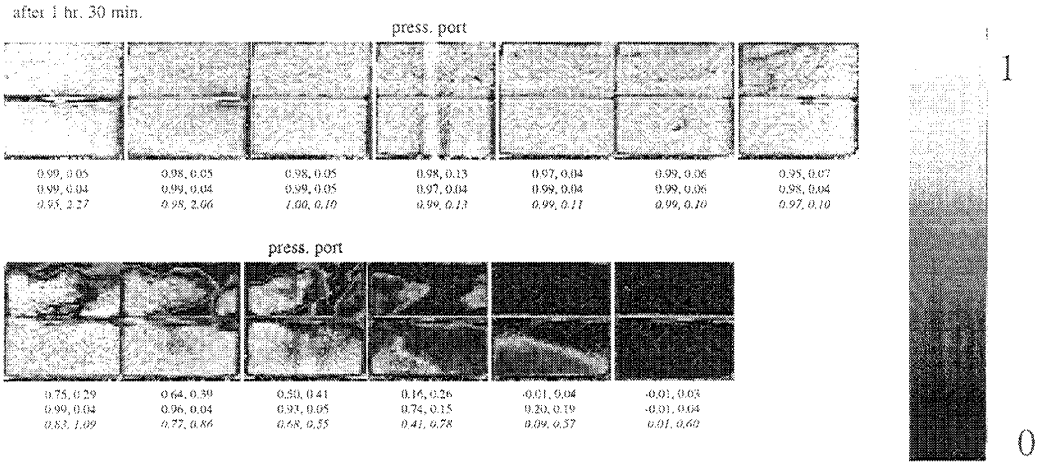

Fig. 7- CT Saturation images for the wide fracture system after 1 hr 30 min of water injection (0.67 PV.)

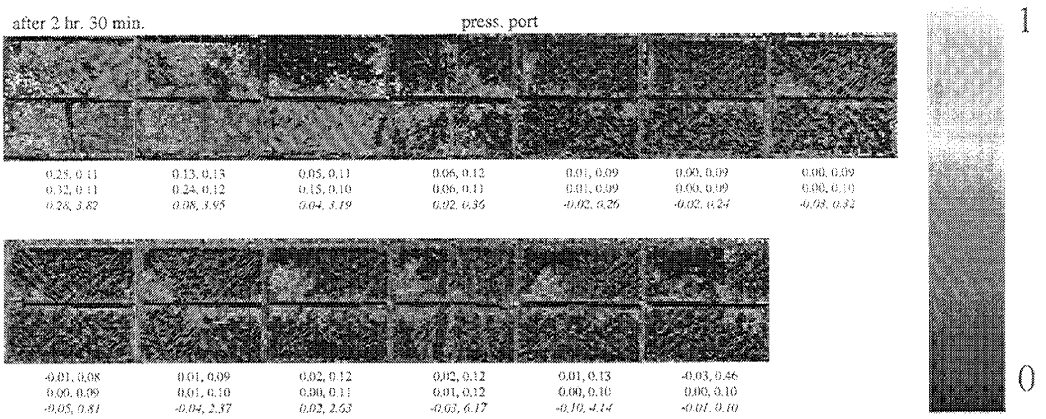

Fig. 8- CT Saturation images for the narrow fracture system after 2 hr 30 min of oil injection (1.13 PV.)

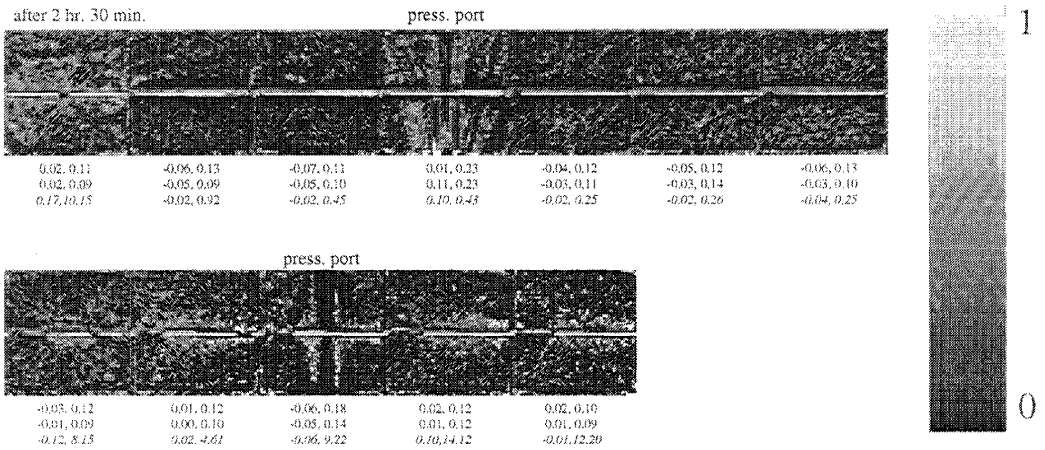

Fig. 9- CT Saturation images for the wide fracture system after 2 hr 30 min of oil injection (1.13 PV.)

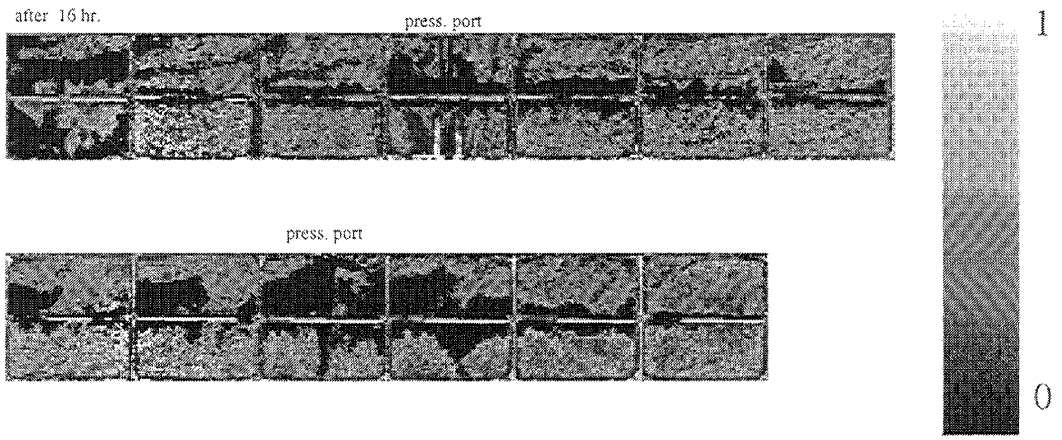

Fig. 10- CT Saturation images for the wide fracture system after 16 hours of water injection (7.2 PV.)

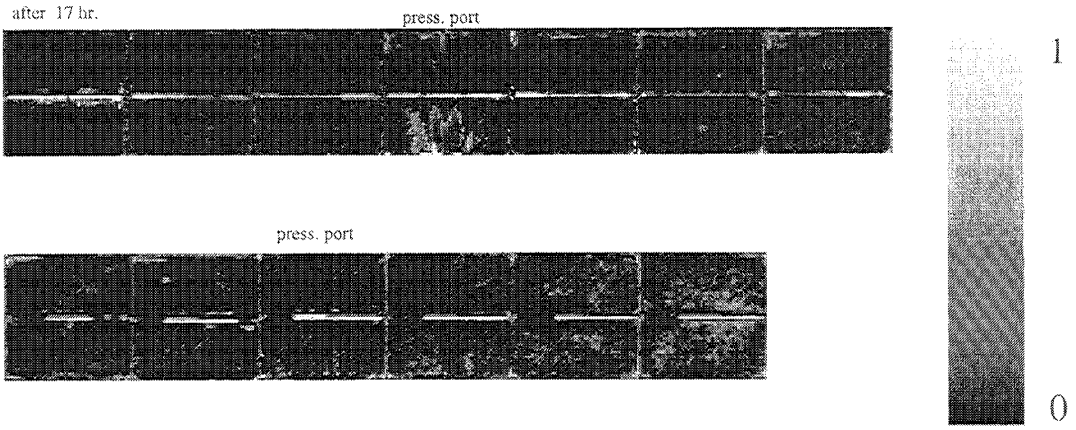

Fig. 11- CT Saturation images for the wide fracture system after 17 hours of water injection (7.7 PV.)

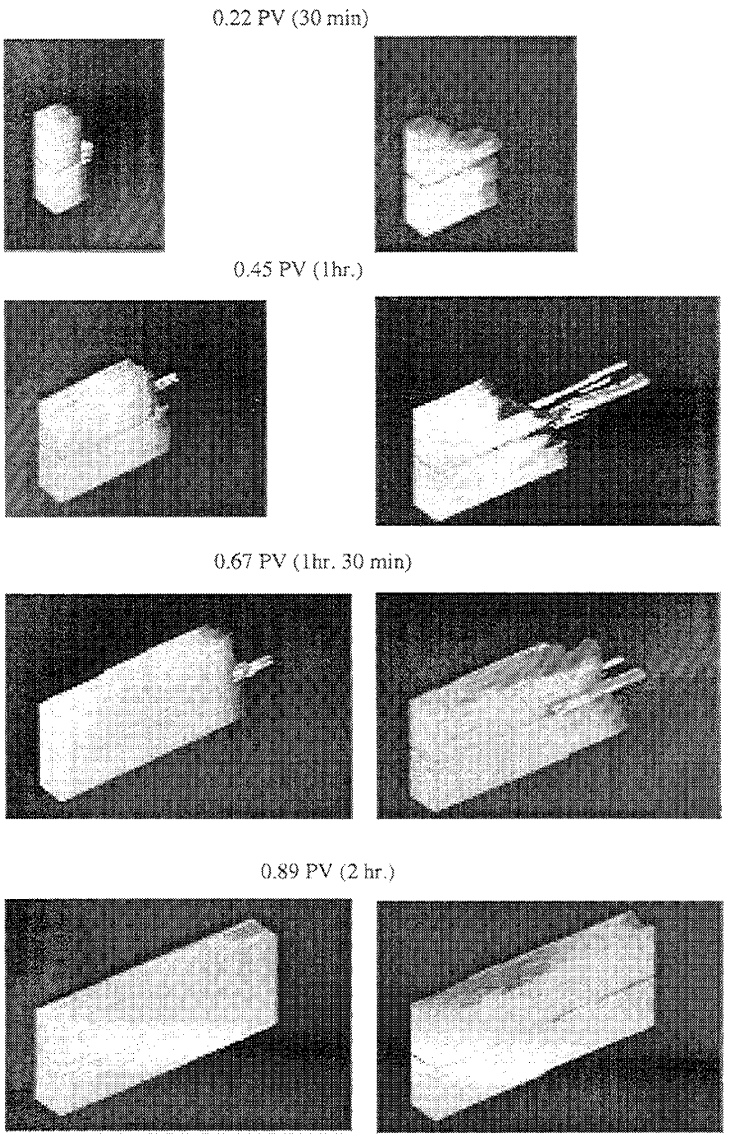

Fig. 12- 3-D Reconstruction for both systems for water injection.

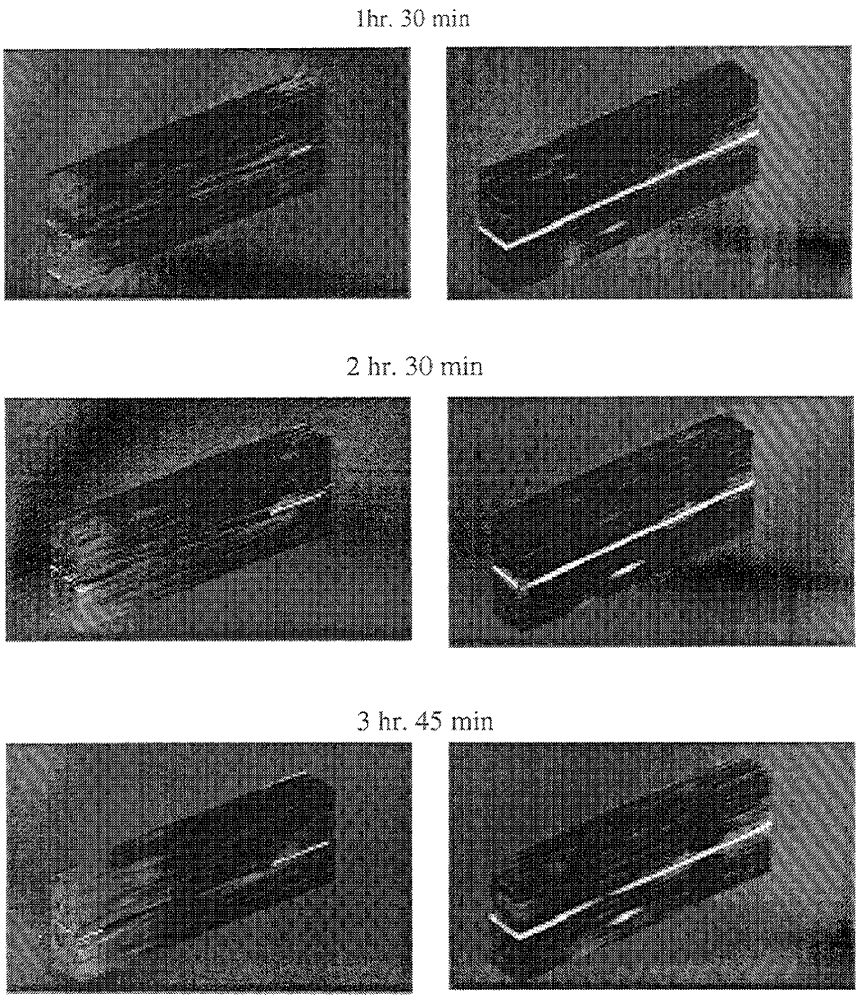

Fig. 13- 3-D Reconstruction for both systems for oil injection.

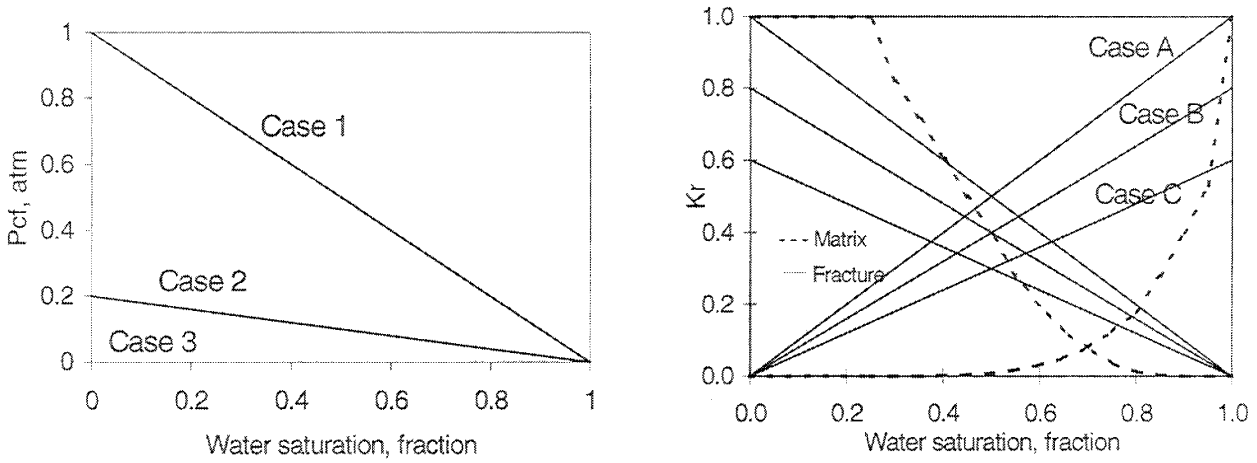

Fig. 14- Capillary pressure curves and relative permeability curves for the fracture.

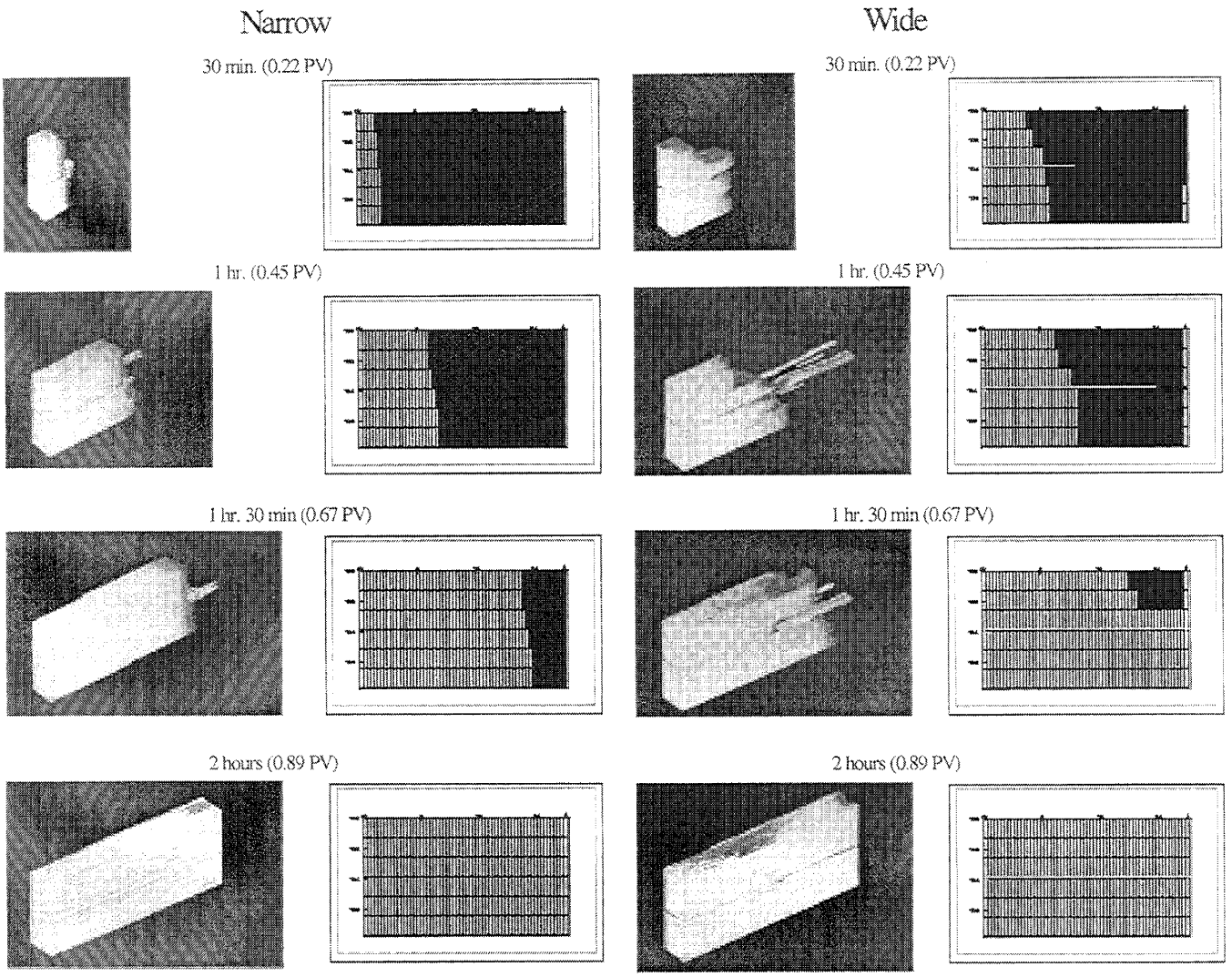

Fig. 15- Comparison between experiments and numerical simulations for narrow and wide fracture systems for different PV of water injection.

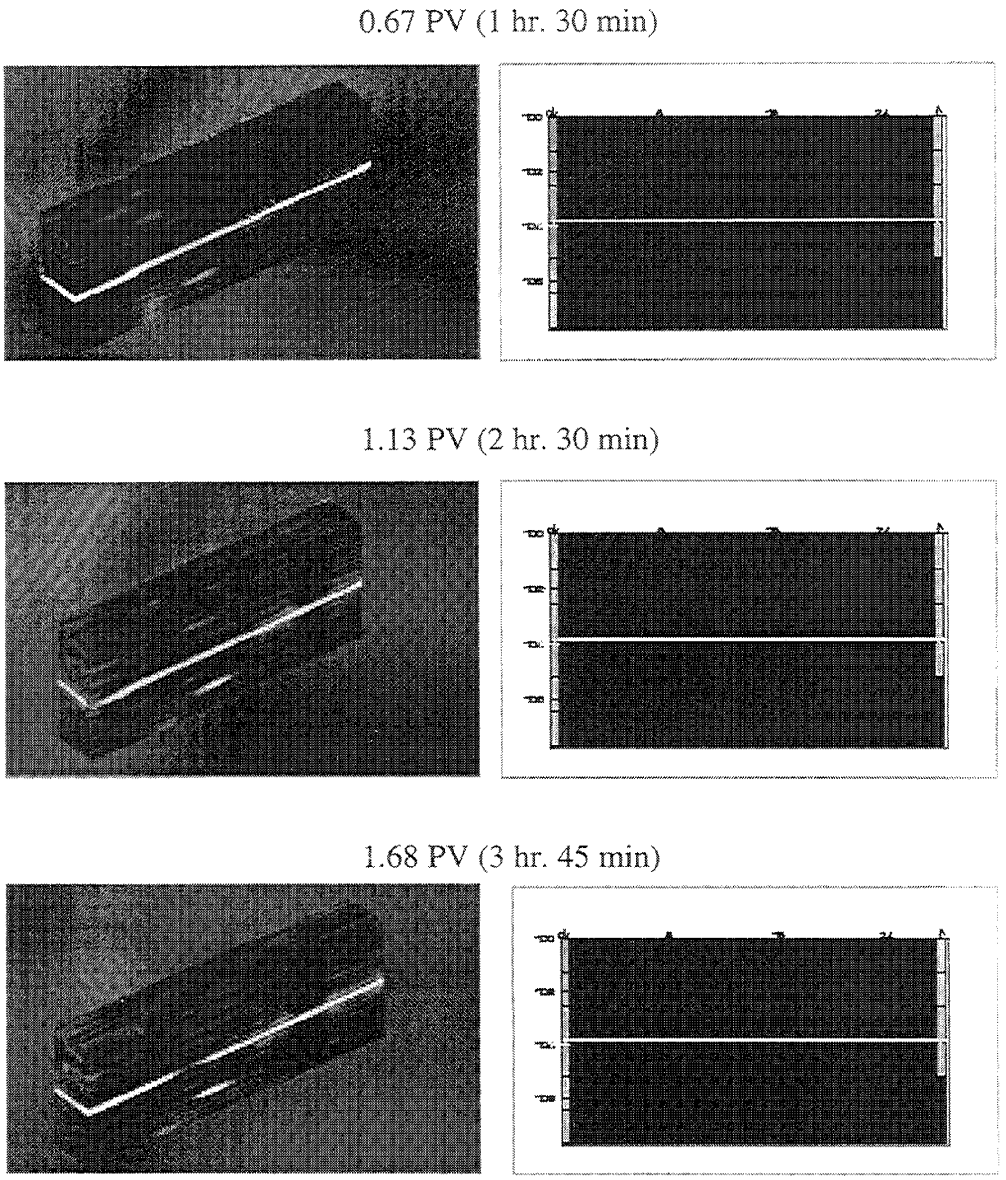

Fig. 16- Comparison between experiments and numerical simulations for narrow and wide fracture systems for different PV of water injection.

2.1 INSITU COMBUSTION

(Louis Castanier)

During the period of performance of the contract, in-situ combustion research was initially focused towards the effect of metallic additives on the reactions of combustion. Equipment failures lead to a complete rebuilding of the experimental set up which is still ongoing. As a result, no significant new experimental data were obtained. The following is a summary of why we continue to research in-situ combustion and an example of application of this method to unusual (e.g., offshore, arctic) or difficult reservoirs. We are currently studying the feasibility of a combination of solvent and in-situ combustion techniques and will continue this work in the future.

NEED FOR IN-SITU COMBUSTION

The traditional recovery techniques for heavy oils can be classified in two categories: thermal methods, which aim at decreasing the crude viscosity by increasing temperature and non-thermal methods, which in heavy oil reservoirs generally suffer from the high mobility contrast between the oil and injected fluids. By far the most widely used recovery method for heavy oils is steam injection, either cyclic or as a drive. Steam injection, however, is not applicable to many reservoirs. Among the parameters affecting the success of steam injection are:

- Depth: If the reservoir depth is over 3,000 ft. (1,000 m) the heat losses in the injection well will make the steam injection inefficient. Insulated tubing can be used as a partial remedy, but it is expensive and difficult to install properly in the field. Downhole steam generators have been tried without success in the last twenty years. They suffer from reliability problems.
- Pressure: At high pressure, the latent heat of water drastically decreases and high pressure also means high injection temperature causing less efficient heat transport and added heat losses.
- Permeability: Clays present in the reservoir may swell in presence of the fresh water produced by steam condensation. This can reduce injectivity and impair the process.
- Oil saturation and porosity: These two parameters are very important. If not enough oil is in place, the energy used to heat the reservoir will be more than the energy obtained by the oil produced. Steam injection is generally impossible in reservoir where the product of porosity by oil saturation is less than 0.1.

From the above discussion, it is clear that despite its usefulness, steam injection is limited to a select group of reservoirs. Let us now turn our attention to in-situ combustion. In-situ combustion is not limited by reservoir depth. It is also applicable where wellbore heat transfer would severely limit steam injection. Two possible cases are offshore fields and the presence of permafrost where steam is not applicable but combustion would be feasible. Combustion is more energy efficient and less polluting than steam. It has been field proven in a number of countries. Combustion, however, suffers from poor sweep efficiency caused by the mobility contrast between the injected air (or oxygen) and the reservoir fluids. It also requires careful engineering and is less flexible and forgiving of errors than steam.

SOLVENT USE

Solvents can be used to reduce the oil viscosity and facilitate production. The solvents can be gases used in miscible or non-miscible mode, or liquids at reservoir conditions. Liquid solvents are usually expensive and the price of the oil recovered low. Consequently, the economics of liquid solvent injection are usually not favorable. Gases are used in miscible or non-miscible modes. Miscibility of gases with heavy oils requires very high pressures. Again the economics of miscible flooding of heavy oils are not good. Non-miscible gas injection has been tried with some success, especially in a cyclic fashion. Some of the technical problems involved with solvent injection arise from precipitation of asphaltene or other compounds during the mixing of the oil and the solvent. This phenomenon is well known and described in a number of publications. It leads to reduction in permeability, especially near the wells, and can, in some cases be very severe and cause technical failure of the process. We expect this problem to be acute in the case of heavy oils.

PROPOSED WORK FOR DIFFICULT RESERVOIRS

None of the existing enhanced oil recovery methods is applicable to difficult or unusual heavy oil reservoirs such as deep, high pressure, offshore, or arctic fields. The rest of this section proposes a combination of several of the existing techniques that is designed to solve this problem. The economic aspects have been taken into account in our preliminary study and we feel that the proposed improved oil recovery ideas can be field applied with existing technology.

METHOD DESCRIPTION

The following description should be considered as a possible outline to be followed. Although the concepts will remain the same, local technical and economic conditions will dictate numerous variations and changes in methods. Cyclic oil recovery has advantages, both technical and in terms of economics. It can also be easily optimized in a given oil reservoir. We propose cyclic injection of solvents, either gas or liquid, followed by in-situ combustion of a small part of the reservoir to increase the temperature near wellbore, and also to clean the wellbore region of the residues left by the solvents. Alternate slugs of solvent and air will be injected and production will occur after each solvent slug injection and after each combustion. The process can be repeated until the economic limit is reached. One important fact to note is that both solvent injection and in-situ combustion have been proven to be effective in a variety of reservoirs, the combination of the two methods has, to our knowledge, never been tried.

First Cycle: Solvent Injection

A slug of solvent (liquid or a gas) should be injected. The amount to be injected needs to be determined by reservoir simulation or from calculations. We expect that in most cases, the amount to be injected will be a small fraction of the pore volume of the reservoir considered. By mixing with the oil, the solvent will decrease the viscosity of the mixture as compared to the viscosity of the original oil. This viscosity reduction can be evaluated if the solvent is a liquid by using Eq. 1 from Burger, *et al.*, page 41. The improvement in oil production can be estimated using an approach similar to the one used by Boberg for steam cyclicing and taking into account only the change of viscosity caused by the solvent. Production after the injection

of the first slug of solvent can thus be easily calculated. If the solvent is a gas, Eq. 1 does not apply, instead, the dissolved gases will induce swelling of the oil and also viscosity reduction as the gas saturated oil will be less viscous than the original oil . Of course, these parameters are best established by laboratory measurements on the crude/solvent system to be studied. Numerical simulation can now predict the expected improvement in production from the solvent injection part of the process. The VAPEX process in Canada is a good example of application of such methods to heavy oils.

At the end of the first solvent cycle, one can expect some damage to the near wellbore area. Most significant will be the precipitation and/or deposition of heavy hydrocarbons such as asphaltenes or paraffins. The produced oil is expected to be upgraded by the solvent cycle.

First Cycle: Combustion

Unlike the classic well-to-well in-situ combustion, we will only try to improve near wellbore conditions by burning the solid residues left after the solvent cycle. The amount of air (or oxygen) to be injected can be easily determined by laboratory experiments and numerical simulation or simple calculations. The benefits of using combustion at this stage are expected to include:

- Productivity improvement through removal of the solids percipitated from the solvent cycle.
- Possible deactivation of the near wellbore clays caused by the high temperature of the combustion
- Reduced viscosity of the oil due to temperature increase.
- Effect of CO_2 production causing swelling and viscosity reduction of the oil.
- Pressure maintenance.

One must note that combustion burns only the heaviest part of the crude, and hence the upgrading already observed during the solvent cycle should be maintained, and even improved. A soak period will probably be necessary at the end of the air/oxygen injection to ensure that all of the oxygen injected has reacted in the reservoir and will not be produced during the subsequent production cycle. The recovery predictions at this stage of the process will be difficult and probably require a fine grid thermal/compositional simulation. It is, however, possible to obtain some estimates based on simple correlations similar to the well-known steam cyclic models.

Repeat Cycles:

The process can be repeated by alternating solvent injection and near well in-situ combustion as long as the economics warrant it. Optimization of slug sizes and duration needs to be made to ensure maximum economic efficiency. Reservoir conditions will, of course, dictate these parameters.

DISCUSSION OF POSSIBLE PROBLEMS: PRELIMINARY WORK REQUIRED:

During the solvent injection, the main problem will be the efficient use of a limited amount of expensive injected fluid. Reservoir heterogeneities and density and mobility differences between solvent and reservoir oil will cause sweep efficiency problems. This in turn can cause concentration gradients and hence large viscosity differences among the fluids to be produced. As in any improved recovery technique, proper reservoir definition is needed. The fact that the

process is cyclic in nature should ensure no waste of solvent. The other problems to be encountered in the solvent part of the process are well-known and described in the literature. The type of work required prior to field application involves PVT studies and creation in the laboratory of various oil/solvent mixtures. Deposition of asphaltenes or other residues on rocks similar to reservoir rocks should also be studied. The following describes some simple tests that can be used as screening techniques for the method.

FEASIBILITY STUDY

Heavy crudes, such as Cold Lake or Hamaca, will be mixed with liquid solvents and viscosities of the mixtures will be measured. Filtration of the mixtures should determine whether or not solid precipitation or formation damage will occur. This first step has been done with Cold Lake Bitumen and has shown both significant viscosity reduction and the presence of solid precipitate. This work is still preliminary and will be continued. During the second step, the mixtures will be injected into a sandpack of permeability and pore structure close to the field sands. Permeability versus injected volume of the mixtures will be recorded. When (and if) the ratio of the permeability, before and after passage of the mixtures reach a given value, the sand pack will be subjected to an in-situ combustion tube run. Fuel concentration and composition as well as an estimate of the air requirements will be obtained. At this stage, simple calculations will give estimates on the production in the field.

Economic evaluation should start at this level. Laboratory tests for gas in solution may be more difficult to implement. The literature is poor in PVT data for heavy oils and more complex experiments may be required. A significant research effort is being made on the "foamy oil" problem, and data from those experiments can probably be used in our project. The database of heavy oil with CO_2 projects should also be used.

OPTIMIZATION AND PRACTICAL APPLICATION

Although reservoir and economic conditions will dictate the directions to be followed for optimization of the process, some general comments are warranted at this point. It would appear that cycle size should increase if the reservoir is thick. One would expect the combustion area to move toward the top of the reservoir in this case. Gravity drainage will be an important part of the recovery mechanism and should be taken into account in the implementation of any field test. Position of the injection/production intervals should be calculated to optimize the process. Numerical simulations will probably be needed to fully optimize the recovery.

As previously mentioned, a soak period will be needed at the end of the combustion portion of each cycle. Its duration can be determined by kinetics studies giving the reactivity of the oil with air. As temperatures near wellbore at the end of the air injection will be high, there should be no problem of oxygen backflush into the well as it will react with the oil. Careful monitoring of the produced gases will be needed for added safety.

REFERENCES

Burger, J., Sourieau, P. and Combarnous, M.: Thermal Recovery Techniques, Ed. Technip, Paris (1984).

Prats, M.: Thermal Recovery, SPE Monograph, Vol. 7 (1982).

2.2 IN-SITU COMBUSTION USING WATER SOLUBLE METALLIC ADDITIVES

(U. Diwan and L. Castanier)

2.2.1 INTRODUCTION

Crude oils are often grouped into three categories based on specific gravity range:

1. Heavy Oil (10°-20°API)
2. Intermediate Oil (20°-30°API)
3. Light Oil (greater than 30°API)

Heavy oils consist mainly of high density naphthenes, aromatics and heteroatoms that are poor in alkanes, while light oils consist mainly of alkanes (Boduszynski, 1987; Boduszynski, 1988). Bitumen or tar are extremely dense hydrocarbons (about 10°API or less), and are non-volatile liquids, semi-solids or solids.The deposits are often referred to as oil sands or tar sands.

2.2.2 IN-SITU COMBUSTION

In-situ combustion is a thermal recovery technique in which a part of the heavy oil in place is burned to generate heat. This heat brings about a reduction in viscosity of the crude oil to get improved mobility and hence oil production rate and recovery. In a laboratory the process of ignition is initiated by using electric heaters while a stream of air is injected into a combustion tube to initiate and sustain combustion. Pure oxygen may also be used, but for economy sake air is popular. The fuel that is burned is the unrecoverable carbon rich residue of that is left on the reservoir matrix behind the steam front as a result of steam distillation, thermal cracking and some catalytic cracking. The heat that is generated partially distills the crude oil. The lighter ends are distilled off, and they condense in the cooler regions ahead of the combustion front along with the vaporized connate water and water produced as a combustion byproduct. The region ahead of the combustion front is heated by conduction, by convection of combustion gases, and by the condensation of volatiles (light ends) and steam. The oil ahead of the combustion front is displaced toward the production well by gas drive provided by the combustion gases, by hot water and steam steam drive, and by miscible drive provided by the condensed light hydrocarbons (Alexander *et al.*, 1962; Holt, 1992)

A typical combustion front moves through the reservoir matrix by consuming the fuel as it moves ahead, thereby leaving no oil behind the burning front. As the combustion front approaches the volume element, the temperature of the element rises and water and light ends are vaporized. These vapors are carried in the gas stream and condense in the cooler regions ahead of the combustion front. The water vapors condense to form a water bank (E), following a bank of light hydrocarbons (F). A steam plateau (D) comprises of the steam-liquid, two-phase region. As the temperature in the volume element exceeds $350^{o}C$ the oil undergoes thermal cracking to form a volatile fraction and a low volatility heavy residue (represented by C). The volatile fraction gets carried in the gas stream and the heavy residue constitutes the fuel which gets burned in the combustion zone (B). The heat generated in the combustion zone gets transported ahead of the front by conduction and convection by the vapors and liquids. The combustion zone is often only a few inches in thickness and has a temperature in the range 350^{o}

- 650°C. As the combustion front moves past this volume element it leaves behind a zone of clean sand (A) which serves as a preheater for the incoming air.

2.2.2.1 Applicability, Merits and Demerits of In-situ Combustion

In-situ combustion is applicable to a wide range of reservoir fluid characteristics. The absence of well bore heat losses in the injection well allows in-situ combustion to be carried out in deeper reservoirs having thinner, tighter sand sections which are not amenable to steam injection. The oil that is produced is also lighter than the oil in place as a result of cracking and distillation.

This technique is amongst the most energy efficient of improved oil recovery methods available today for heavy oils. However, one major constraint that limits its practical application is the amount of fuel formation in the matrix. If a sufficient amount of fuel is not deposited, as is often the case for light oils, the combustion front will not sustain itself. Conversely, if the quantity of fuel deposited is large, as is often the case with very heavy oils, the rate of advance of the front tends to be slower, with an uneconomically high demand for compressed air to sustain combustion (Alexander *et al.*, 1962).

As a result it would be desirable to find substances that alter the reaction kinetics of oil oxidation during in-situ combustion. There are a number of factors affecting the rates of these reactions, among which are the composition and concentration of the catalyst, surface of the catalyst available for reaction temperature. Combustion tube studies with metallic additives (Baena *et al.*, 1990; Castanier *et al.*, 1992; Holt, 1992) have shown that the addition of water soluble metallic salts can change the reaction kinetics of combustion. These indicate an increased fuel deposition in runs which carried salts of iron or tin. It has not been established for certain how the presence of theses substances affect the fuel deposition mechanism, but it may be due to the reduction in the temperature required for cracking reactions.

Kinetic tube studies with metallic additives (de los Rios *et al.*, 1988; Shallcross, 1989) indicate that aqueous solutions of certain metallic salts like zinc, iron and tin increased the fuel concentrations. All these studies indicate that the overall oxidation mechanism of crude oils in porous media is the result of an overlap of several reactions that occur at different ranges of temperature. These have been classified as low temperature, medium temperature and high temperature reactions.

In a properly designed combustion process there should be minimal amount of low temperature oxidation (Agrawal and Sidqi, 1996). Therefore, the presence of metallic additives, which affect reaction kinetics, would affect the overall performance of the combustion process. It is believed that low temperature oxidation reactions affect fuel formation, therefore the alteration of this reaction would affect fuel deposition characteristics.

Earlier work done by De Los Rios (1987), has shown, on a quantitative basis, that the use of metallic additives affects the nature of the fuel formed; this, in turn, will affect the heat of combustion, the air-oil ratio, the air requirements, the front velocity and the oil recovery rate.

2.2.2.2 Metallic Additives in In-situ Combustion

Studies on the effect of metallic additives (salts) on in-situ combustion date back to the early nineteen seventies. It was observed that reservoirs having mineral contents with high metallic content in the rock matrix had increased fuel deposition (Burger and Sahuquet, 1972). Early attempts at understanding the mechanics of oil oxidation reactions was done through kinetic tube experiments in the presence of metallic additives.

A brief description to explain how the oxidation reactions take place is given on the following page.

2.2.2.3 Kinetic Studies with Metals and Metallic Additives

Several studies have been performed to determine the influence of metals and metallic additives on the oxidation characteristics of crude oils. The work performed and observations made during these experiments are described below.

1. Of particular importance to the current study are the kinetic studies performed by De Los Rios (1988) and Shallcross (1989) at Stanford University. De Los Rios performed kinetic experiments on Huntington Beach Oil and various metallic additives. Shallcross performed kinetic experiments on Huntington Beach and Venezuelan oils with various metallic additives. Both studies analyzed oxygen consumption data by decoupling the total oxygen consumption data into three parts. This was done to represent the oxygen consumed by the three competing groups of reactions. The found that metallic additives iron and tin increased oxygen consumption. They also reported that iron and tin increased the reaction rates for the oxidation reactions. They found that zinc did not produce the effects reported for iron and tin. From the results of these studies it was expected that iron and tin may be useful agents in catalyzing combustion reactions (Mamora, 1993).

2. Burger and Sahuquet (1981) report on two kinetic runs using 2000 ppm copper performed on a 27°API oil. The activation energy for the LTO was found to be lowered due to the copper additive (Holt, 1992).

3. Fassihi *et al.* (1981) report on kinetic experiments with 2000 ppm copper says that the activation energy of the LTO was unaffected, but itís reaction rate was increased. Fassihi also reported that the activation energy for the high temperature portion of the reaction was reduced (Baena *et al.*, 1990; Mamora, 1993).

Reactions taking place:

1. Low temperature oxidation (LTO)	Result in formation of peroxides, hydroperoxides, aldehydes, ketones, carboxylic acids and alcohols (Burger and Sahuquet, 1972). Alexander *et al.*(1962) and Al-Saadon (1970) showed that fuel availability was increased when LTO of crude oil took place. Dabbous and Fulton (1974) corroborated this and also found that LTO causes a substantial decline in recoverable oil from the distillation and cracking zones, an increase in the fuel deposition and marked changes in the fuel characteristics and coked sand properties. Weijdema (1968) and Fassihi (1981) found that the order for the LTO reaction, in terms of the partial pressure of oxygen, was close to unity.
2. Medium temperature oxidation (MTO)	Involve distillation, visbreaking and coking of the fuel along with partial oxidation of the products formed (Bardon and Gadelle, 1977; Fassihi, 1981; Sidqi *et al.*, 1985). The amount of coking and atomic H/C ratio of the fuel were found to decrease with increasing coking temperature (Bousaid, 1967). Increasing pressure was found to increase the amount of hydrocarbon residue formed; but the fuel deposited has a lesser hydrogen content (Sidqi *et al.*, 1985).
3. High temperature oxidation (HTO)	Involve oxidation of the cracked hydrocarbon residue. HTO takes place according to the following equation:

$$CH_n + \left(\frac{2m+1}{2m+2} + \frac{n}{4}\right) O_2 \rightarrow \left(\frac{m}{m+1}\right) CO_2 + \left(\frac{1}{m+1}\right) CO + \left(\frac{n}{2}\right) H_2O$$

m: ratio of carbon dioxide to carbon monoxide formed upon oxidation of the fuel
n: atomic hydrogen to carbon ratio of fuel burned
The reaction rate has been found to be first order with respect to the fuel concentration and was found to have an order of 0.5 to 1.0 with respect to the oxygen partial pressure (Dabbous and Fulton, 1974).

To recap:

- It has been found by previous researchers that the presence of certain metals can affect the kinetic parameters used to model combustion reactions.
- These kinetic experiments can give estimates of activation energies and reaction rates for combustion reactions.

2.2.2.4 Tube Studies with Metallic Additives

Observations that the physical and chemical properties of the core material can affect the combustion performance in tube runs was made by several researchers. Some of them are mentioned below.

1. Vossoughi *et al.*, 1982, Hardy *et al.*, 1972, Alexander *et al.*, 1962 observed that, for a particular oil, more fuel can be expected from a native core than from a clean sand pack. This is believed to result from both physical and chemical processes. Fine grained material

in native cores provides more surface area for combustion reactions while metals in natural minerals act as catalysts (Baena *et al.*, 1990; Bardon and Gadelle, 1977).

2. Baena *et al.*, 1990 report on experiments with 22°API Huntington Beach Oil. They observed that tin and iron additives increased oxygen utilization efficiency, burning front velocity, and fuel concentration. The zinc additive showed lesser effect (Baena *et al.*, 1990).

3. Castanier *et al.*, 1992 report on thirteen metallic additive combustion tube runs. The runs made with 10°API Hamaca oil show that tin and iron increased the fuel deposition, oxygen utilization efficiency, and front velocity while zinc was less effective (Bardon and Gadelle, 1977).

2.2.3 PRESENT STUDY

The present study shall involve a series of combustion tube experiments performed with the Wilmington Oil (~15°API) and a couple of aqueous metallic additives.

2.2.4 WORK COMPLETED

- Thermocouple testing
- Calibration of mass flow meter
- Calibration of mass flow controller
- Calibration of carbon monoxide gas analyzer
- Calibration of carbon dioxide gas analyzer

2.1.5 FUTURE WORK

- Calibration of oxygen analyzer
- Checking apparatus for leakages
- Checking data logger
- Transducer calibration to measure pressure drop along tube
- Conduct a trial run using no packing, just air
- Observe temperature profiles
- Pack the combustion tube with the crude oil
- Perform runs

2.2.6 REFERENCES

1. Agrawal, V.K. and Sidqi, A.: "A Study of In-situ Combustion on Saudi Tar," Stanford University Petroleum Research Institute, SUPRI-TR-105 [DE-FG22-93BC14899], Stanford University, Stanford (April 1996).

2. Alexander, J.D., Martin, W.L., and Dew, J.N.: "Factors Affecting Fuel Availability and Composition During In-Situ Combustion," *J. Pet. Tech.* (October 1962) 1154-1162.

3. Baena, C.J., Brigham, W.E., and Castanier, L. M.: "Effect of Metallic Additives on In-Situ Combustion of Huntington Beach Crude Experiments," Stanford University Petroleum Research Institute, SUPRI-TR-78 [DE-FG19-87BC14126], Stanford University, Stanford (August 1990).
4. Boduszynski, M. M.,: "Composition of Heavy Petroleums. 1. Molecular Weight, Hydrogfen Deficiency, and Heteroatom Concentration as a Function of Atmospheric Equivalent Boiling Point upto 1400°F (760°C)," *Energy & Fuels* (1987) **1**.

5. Boduszynski, M. M.: "Composition of Heavy Petroleums. 2.Molecular Characterization," *Energy & Fuels* (1988) **2**.

6. Bardon, C. And Gadelle, C.: ìEssai de Laboratoire Pour LíEtude de la Combustion In-Situ,î Institute Francais du Petrole, Paris (May 1977).

7. Bousaid, I.S. and Ramey, H.J. Jr.: "Oxidation of Crude Oil in Porous Media," *Soc. of Pet. Eng. J.* (June 1968) 137-148.

8. "Combustion Kinetics," *Soc. Pet. Eng. J.* (October 1972) 410-420.

9. Castanier, L. M., Baena, C.J., Tavares, C., Holt, R. J., and Brigham, W.E.: "In-Situ Combustion with Metallic additives," No. SPE 23708, paper presented at the SPE-AIME Latin American Petroleum Engineering Conference, Caracas (March 1992).

10. Dabbous M.K. and Fulton, P.F.: "Low-Temperature Oxidation Reaction Kinetics and Effects on the In-Situ Combustion Process," *Soc. of Pet. Eng. J.* (June 1974) 253-262.

11. De Los Rios, C. F., Brigham, W. E., and Castanier, L. M.: "The Effect of Metallic Additives on the kinetics of Oil Oxidation Reactions in In-Situ Combustion," Stanford University Petroelum Research Institute, SUPRI-TR-63 [DE-FG19-87BC14126] Stanford University, Stanford, (November 1988).

12. Fassihi, M. R.: "Analysis of Fuel Oxidation in In-Situ Combustion Oil Recovery," PhD disertation, Stanford University, Stanford (May 1981).

13. Gureyev, A. A., and Sablena, Z. A.: "The Role of Metals in Oxidation of Hydrocarbon Fuels in the Liquid Phase," Scientific Research Institute of Fuel and Lubricating Materials, Pergamon Press (1965).

14. Holt, R. J.: "In-Situ Combustion with Metallic Additives," Stanford University Petroleum Research Institute, SUPRI-TR-87 [DE-FG22-90BC14600], Stanford University, Stanford (July 1992).

15. Mamora, D. D.: "Kinetics of In-Situ Combustion," PhD dissertation, Stanford University, Stanford, California (May 1993).

16. Shallcross, D. C.: "Modifying In-Situ Combustion Performance by the use of Water-Soluble Metallic Additives," No. SPE 19485, paper presented at the SPE-AIME Aia-Pacific Conference, Sydney, Australia (September 1989).

17. Sidqi, A., Ramey, H. J. Jr.,Pettit, P., and Brigham, W. E.: "The Reaction Kinetics of Fuel Formation for In-Situ Combustion," Stanford University Petroleum Research Institute, Stanford, CA, SUPRI-TR-46 [DE-AC03-81SF 11564] (May 1985).

18. Weijdema, J.: "Determination of the Oxidation Kinetics of the in-Situ Combustion Process," Report from Koninklijke/Shell Exploratie En Producktie Laboratorium, Rijswijk, The Netherlands (1968).

3.5 AN ANALYTICAL MODEL FOR SIMULATING HEAVY-OIL RECOVERY BY CYCLIC STEAM INJECTION USING HORIZONTAL WELLS

(U. Diwan and A.R. Kovscek)

Abstract

In this investigation, existing analytical models for cyclic steam injection and oil recovery are reviewed and a new model applicable to horizontal wells is proposed. A new flow equation for oil production during cyclic steaming of horizontal wells is developed. The model accounts for the gravity-drainage of oil along the steam-oil interface and through the steam zone. Oil viscosity, effective permeability, geometry of the heated zone, porosity, mobile oil saturation, and thermal diffusivity of the reservoir influence the flow rate of oil in the model. The change in reservoir temperature with time is also modeled, and it results in the expected decline in oil production rate during the production cycle as the reservoir cools. Wherever appropriate, correlations are incorporated to minimize data requirements. A limited comparison to numerical simulation results agrees well indicating that essential physics are successfully captured.

Cyclic steaming appears to be a systematic method for heating a cold reservoir provided that a relatively uniform distribution of steam is obtained along the horizontal well during injection. A sensitivity analysis shows that the process is robust over the range of expected physical parameters.

Contents

			List of Tables	2
			List of Figures	2
			Nomenclature	3
1.			Introduction	5
	1.1		Horizontal Wells	5
	1.2		Cyclic Steam Injection	5
	1.3		Existing Models	6
2.			Model Development	7
	2.1		Introduction	7
	2.2		Injection and Soak Periods	8
	2.3		Heat Remaining in the Reservoir	9
	2.4		Production Period	11
		2.4.1	Development of Flow Equation	12
	2.5		Property Correlations	13
		2.5.1	Oil and Water Viscosities	13
		2.5.2	Fluid Saturations and Relative Permeabilities	14
	2.6		Algorithm for Calculation Scheme	14
		2.6.1	Computer Code	15
		2.6.2	Program Structure	15
3.			Validation of Model, Results and Discussions	15
	3.1		Sensitivity Analysis	16
		3.1.1	Base Case	16
		3.1.2	Sensitivity to Steam Quality	17
		3.1.3	Sensitivity to Formation Thickness	17
		3.1.4	Sensitivity to Steam Injection Rate	18
		3.1.5	Sensitivity to Down-Hole Steam Pressure	18
		3.1.6	Sensitivity to Steam Soak Interval	18
	3.2		Discussion	19
4.			Conclusions	19
			References	19
			Tables	21
			Figures	23
			Appendix A	37

List of Tables

Table 1: Data for Model Validation 21
Table 2: Input Data 22

List of Figures

Fig.1(a) Schematic diagram of heated area geometry 23
Fig.1(b) differential element of the heated area 23

Fig.2 Schematic diagram of area of cross section of heated area 23
Fig.3 Base case 24
Fig.4 Sensitivity to steam quality 25
Fig.5 Sensitivity to formation thickness 28
Fig.6 Sensitivity to steam injection Rate 30
Fig.7 Sensitivity to bottom-hole pressure (BHP) 32
Fig.8 Sensitivity to soaking interval 34
Fig.9 Sensitivity to soaking interval 36

Nomenclature

A	=	Cross sectional area	ft^2 (m^2)
A_L	=	Dimensionless factor for linear flow	
C_w	=	Specific heat of water	Btu/lb.°F (kJ/kg°K)
f_{HD}	=	Dimensionless factor that accounts for horizontal heat losses	
f_{VD}	=	Dimensionless factor that accounts for vertical heat losses	
f_{PD}	=	Dimensionless factor that accounts for heat lost by produced fluids	
f_{sdh}	=	Steam quality at down-hole conditions (mass fraction)	
F_l	=	Ratio of heat lost to heat injected	
g	=	Gravitational acceleration	32.17 ft/s^2 or 9.81 m/s^2
h	=	Formation thickness	ft (m)
h_{st}	=	Steam zone thickness	ft (m)
$h_w(T)$	=	Enthalpy of liquid water	Btu/lb (kJ/kg)
H_{inj}	=	Amount of heat injected during a cycle	Btu (kJ)
H_{lost}	=	Amount of heat remaining in the reservoir at the end of a cycle	Btu (kJ)
K_R	=	Reservoir thermal conductivity	Btu/ft.D.°F (kJ/m.d.°K)
k_o	=	Effective permeability of oil	Darcy
k_{st}	=	Effective permeability of steam	Darcy
k_w	=	Effective permeability of water	Darcy
k_{ro}	=	Relative permeability to oil	fraction
k_{rw}	=	Relative permeability to water	fraction
ΔH_{lvdh}	=	Latent heat of vaporization at down-hole conditions	Btu/lb (kJ/kg)
L	=	Length of horizontal well	ft (m)
M_o	=	Volumetric oil heat capacity	Btu/ft^3.°F (kJ/m^3.°K)
M_w	=	Volumetric water heat capacity	Btu/ft^3.°F (kJ/m^3.°K)
M_{SH}	=	Volumetric shale (overburden / underburden) heat capacity	Btu/ft^3.°F (kJ/m^3.°K)
M_T	=	Total volumetric heat capacity	Btu/ft^3.°F (kJ/m^3.°K)
M_σ	=	Volumetric rock heat capacity (M_{rr})	Btu/ft^3.°F (kJ/m^3.°K)
N_p	=	Cumulative oil production	bbl (m^3)
OIP	=	Volume of oil in place	bbl (m^3)
p_s	=	Down-hole steam pressure	psia, (kPa)
p_{wf}	=	Bottom hole flowing pressure	psia, (kPa)
q_o	=	Oil production rate	BPD (m^3/d)
q_w	=	Water production rate	BPD (m^3/d)
$\overline{Q_i}$	=	Amount of heat injected per unit mass of steam	Btu/lb (kJ/kg)
Q_i	=	Cumulative heat injected	Btu/lb (kJ/kg)

Q_{MAX}	=	Maximum heat entering in the reservoir in one cycle	Btu (kJ)
Q_l	=	Heat loss to reservoir	Btu (kJ)
w_s	=	Steam injection rate (cold water volume)	BPD (m^3/d)
Q_p	=	Rate of heat withdrawal from reservoir with produced fluids	Btu/D (kJ/d)
r_w	=	Well radius	ft (m)
R_h	=	Heated zone horizontal range	ft (m)
R_x	=	Distance along hot oil zone interface	ft (m)
S_{ors}	=	Residual oil saturation in the presence of steam	
S_{orw}	=	Residual oil saturation in the presence of water	
S_{wi}	=	Initial water saturation	
$\overline{S}_w$	=	Average water saturation	
t_{DH}	=	Dimensionless time for horizontal heat loss	
t_{DV}	=	Dimensionless time for vertical heat loss	
t_{inj}	=	Injection period	days
t_{prod}	=	Production time	days
t_{soak}	=	Soak time	days
T_{avg}	=	Average temperature of heated zone	°F (°K)
T_R	=	Original reservoir temperature	°F (°K)
T_S	=	Down-hole steam temperature	°F (°K)
T_{SOAK}	=	Temperature at the end of soaking period	°F (°K)
T_{STD}	=	Temperature at standard conditions	°F (°K)
u	=	Velocity of the steam-oil interface growth downwards	ft/sec (cm/sec)
v	=	Darcy velocity	ft/sec (cm/sec)
V_s	=	Steam zone volume	ft^3 (m^3)
w_i	=	Total injection rate	BPD (m^3/d)
WIP	=	Volume of water in place	bbl (m^3)
W_p	=	Cumulative water production	BPD (m^3/d)
α	=	Reservoir thermal diffusivity	ft^2/D (m^2/d)
α_{SH}	=	Shale thermal diffusivity	ft^2/D (m^2/d)
Δp	=	Pressure drawdown	psi (kPa)
Δt	=	Time step size	days
φ	=	Porosity	
ϕ	=	Potential	ft^2/sec^2 (m^2/sec^2)
μ_o	=	Oil viscosity	cp
μ_{st}	=	Steam viscosity	cp
μ_w	=	Water viscosity	cp
ν	=	Kinematic oil viscosity	cs
ν_{avg}	=	Kinematic oil viscosity at average temperature	cs
ν_s	=	Kinematic viscosity of oil at steam temperature	cs
ν_{ws}	=	Kinematic viscosity of water at steam temperature	cs
ρ_o	=	Oil density	lb/ft^3 (gm/ml)
ρ_{oSTD}	=	Oil density at standard conditions	lb/ft^3 (gm/ml)
ρ_{st}	=	Steam density	lb/ft^3 (gm/ml)
ρ_w	=	Water density	lb/ft^3 (gm/ml)
θ	=	Angle between steam-oil interface and reservoir bed	degrees (radians)
ξ	=	Hot oil zone thickness	cm

Chapter 1

1. Introduction

Shell discovered the process of steam stimulation by accident in Venezuela during production of heavy crude by steamflooding the Mene Grande field near the eastern shore of Lake Maracaibo (Butler et al., 1980). During the flood, a breakthrough of steam to the ground surface occurred and, in order to reduce the steam pressure in the reservoir, the injection well was allowed to flow back. Copious quantities of oil were produced; from this accidental discovery in 1959 came the cyclic steam stimulation process, which also goes by the name of *steam soak* and *huff and puff*. Since then, there have been several mathematical models describing the phenomenon. These range from complex numerical simulators to simple analytical expressions.

This work concerns the application of horizontal wells to thermal oil recovery. It consists of an analytical model developed to calculate oil recovery and reservoir heating during cyclic steam injection. It holds for heavy-oil, pressure-depleted reservoirs where the main driving force for production is gravity. Our objective is to present a relatively simple model taking into account gravity-drainage along the sides of the steam-oil interface, the pressure draw down driving force and the drainage of oil through the steam zone. A brief overview of the analytic and semi-analytic models for response to steam injection follows next.

1.1 Horizontal Wells

Horizontal wells are applied increasingly in steam injection projects for recovering heavy-oil (Basham et al., 1998). In the well-known steam assisted gravity-drainage (SAGD) process, a horizontal injector is located above a horizontal producer (Butler et al., 1980). The producer below collects and drains away the mobilized oil and water (condensed steam). Often the injector contains tubing for delivering steam to the well toe, while the annulus directs the steam to the formation and produces the excess for circulation. Recently, there has been interest in heavy-oil reservoirs in the application of a single dual-stream horizontal well, where the annulus assumes the role of the producer, and the tubing, the injector. Cyclic steaming using a single horizontal well could be considered a variant of SW-SAGD and should be useful for efficient initial heating of the reservoir volume.

The performance of such wells may be predicted from empirical correlations, simple analytical models, or thermal reservoir simulation. Empirical correlations can be extremely useful for correlating data within a field and for predicting performance of new wells in that and similar fields. However, use of such correlations for situations much different from those that led to their development might be subject to large errors. On the other hand, one can use a compositional or black-oil thermal model to predict the performance of cyclic steam operations. Thermal models are based on the fundamental laws of conservation of mass and heat. Fluid flow is related to pressure gradient through the concept of relative permeability. In addition, a thermal model is sensitive to rock properties, fluid properties and geological features. Much of this information is often unknown and must be estimated from limited data and experience in similar situations. Furthermore, because of the complexity of the SAGD recovery process, the equations of a thermal simulator could be difficult and expensive to solve depending upon the exact scenario. Simply, an analytical model of cyclic steam injection might be useful to expose the first-order mechanisms of reservoir heating and oil production.

1.2 Cyclic Steam Injection

There are two important reasons to study cyclic steam injection with horizontal wells. Firstly, the thermal efficiency of cyclic operation is high, and it is thus attractive. Secondly, cyclic steaming to promote effective initial reservoir heating might precede continuous steam injection

during a SW-SAGD recovery process (Elliott and Kovscek, 1999). The steam is usually injected at a fixed rate and known wellhead quality for a short period of time. After some heat loss in the wellbore, the steam enters the reservoir. Uniform steam distribution along the well is an important factor in the success of cyclic operations with a horizontal well (Mendonza, 1998). The bottom-hole quality and pressure may be predicted from a wellbore model of the type discussed by Fontanilla and Aziz (1982). After injection for a specified period of time, the well is shut-in and the steam is allowed to "soak" into the reservoir for another specified period. To complete the cycle, the well is produced until the oil production rate reaches a minimum rate. This cyclic process is repeated until the recovery per cycle drops below an economic limit. Generally, the length of cycles increases as recovery matures. Given the bottom-hole conditions during the production cycle, the wellhead conditions may be predicted.

In principle, the reservoir simulator yields the most accurate answer, but it is only possible to generalize after many different simulations (Aziz and Gontijo, 1984). Further, the reservoir simulator is sensitive to data that are often not known or unreliable. It is natural to develop simpler analytical models (Boberg and Lantz, 1966) that account for the important mechanisms involved in this process from which we may draw general conclusions about performance. This indeed has been the case and several models and correlations of varying degree of complexity are available in the literature for cyclic operation of vertical wells and continuous steam injection in dual horizontal wells (Butler et al., 1980).

1.3 Existing Models

Briefly, let us touch upon the models that have been created so far. Marx and Langenheim (1959) describe a method for estimating thermal invasion rates, cumulative heated area, and theoretical economic limits for sustained hot-fluid injection at a constant rate into an idealized reservoir. Full allowance is made for non-productive reservoir heat losses. In all cases, the heat conduction losses to the overburden and the underburden impose an economic limit upon the size of the area which can be swept out from any one injection point, for a given set of reservoir conditions, at any given heat injection rate.

Jones (1977) presented a simple cyclic steam model for heavy-oil, pressure-depleted, gravity-drainage reservoirs. The Boberg and Lantz (1966) procedure was used as the basis for the reservoir shape and temperature calculations versus time. Here, the only driving force assumed is gravity, and hence, the model tends to calculate lower initial oil rates than observed in the field. For matching, certain empirical parameters are employed.

Van Lookeren(1977) has presented calculation methods for linear and radial steam flow in reservoirs. He assumes immediate gravity overlay of the steam zone and presented analytical expressions to describe interface locus. The steam zone shape is governed by factors A_{LD} and A_{RD} which are dimensionless parameters that characterize the degree of steam override for linear and radial flow, respectively. A simplistic formulation is given to calculate the average steam zone thickness.

Myhill and Stegemeier (1978) presented a model for steam drive correlation and prediction. Assuming a piston like displacement, they modified Mandl and Volek's (1969) method to calculate the steam zone volume. It identifies a critical time beyond which the zone downstream of the advancing front is heated by the water moving through the condensation front. Also, a thermal efficiency of the steam zone is calculated as a function of the dimensionless time and the ratio of the latent heat to the total energy injected.

Butler *et al.* (1979) presented theoretical equations for gravity-drainage of heavy-oils during in-situ steam heating. The method described consists of an expanding steam zone as a result of steam injection and production of oil via the mechanism of gravity-drainage along the interface of the steam chamber. The oil is produced through a horizontal well located at the bottom of the steam chamber. Oil flow rate is derived starting from Darcy's law. Heat transfer takes into account the thermal diffusivity of the reservoir and it is proportional to the square root of the driving force. In the case of an infinite reservoir, an analytical dimensionless expression describing the position of the interface is derived. When the outer boundary of the reservoir is considered, the position of the interface and the oil rate are calculated numerically. A simple second order polynomial is found to fit dimensionless oil production versus time. An equation describing the growth of the steam chamber is also presented. The method is limited to gravity-drainage and linear flow of heavy-oil from horizontal wells.

Jones (1981) presented a steam drive model that is basically a combination of Van Lookeren's (1977) and Myhill and Stegemeier's (1978) methods. It is limited to continuous steam drive and it uses empirical factors to match calculated rates with measured values.

Vogel (1982) considered heat calculations for steam floods. Similar to Van Lookeren (1977), this model works on the basic assumption of instantaneous steam rise to the top of the reservoir. After this happens, the steam chamber grows downward at a very low velocity. Heat losses to the adjacent formations are calculated by solving the heat conduction problem from an infinite plane. The model characterizes two main driving forces affecting oil production: gravity-drainage and steam drag. In his conclusions, Vogel says that, above a certain limit, injection rates have little influence on oil production.

Finally, Aziz et al. (1984) presented a model that considers the flow potential to be a combination of pressure drop and gravity forces. The flow equation for oil and water production derived is based on the method illustrated by Butler et al. (1979). They solve a combined Darcy flow and a heat conduction problem. The structure of the model is based on Jones' (1981) method.

Chapter 2
2. Model Development

Cyclic steam injection, commonly referred to as "Huff-n-Puff" involves steam injection into a pressure-depleted reservoir, followed by soaking, and finally the oil production period. As stated earlier, oil production is governed by the gravity driving force. The model developed in the following section incorporates gravity as a prime driving force for oil flow towards the well and thereby predicts the oil production flow rate per unit length of the horizontal well in the production period. Heat losses from the heated zone to the overburden and the adjacent unheated oil-bearing formation are also included.

2.1 Introduction

Steam introduced at the bottom of the formation through a horizontal well, displaces the oil and rises to the top of the formation where it is trapped if an impermeable cap rock exists. We assume that the steam zone adopts a triangular shape in cross section as shown in Fig.1. The steam injection rate around the well remains constant over the entire injection interval. Therefore, the steam injection pressure generally remains constant over the injection process if the reservoir is pressure-depleted. Steam heats up the colder oil sand near the condensation surface and oil drains along the condensation surface by a combination of gravity and pressure difference into the production well. Steam condensate also drains toward the well. In addition, oil drains through the steam chamber into the production well. The mechanisms involved in oil production during cyclic steam injection are diverse and intricate. Reduction of oil viscosity as a

result of an increase in the temperature greatly improves the production response. Gravity-drainage and pressure drawdown are the major mechanisms of oil production in the case of cyclic steaming.

The model is divided into three periods: the injection period, the soaking period and the production period. Each will be described in detail. In what follows, correlations and equations are given in field units (°F, psi, ft, BTU, BPD, etc), unless otherwise noted.

2.2 Injection and Soak Periods

During the injection interval, heat losses from the steam zone to the reservoir are considered negligible although heat losses to the overburden must be considered. The oil sand near the wellbore is assumed to be at steam temperature T_s, the saturated steam temperature at the sand face injection pressure. Pressure fall-off away from the well during injection is neglected during this analysis. In the soaking period, heat is lost to the overburden and the reservoir. The temperature of the steam zone thus decreases while soaking

There are certain important variables such as the steam zone volume and the zone horizontal range that need to be addressed. The steam zone volume, V_s, during injection is calculated using the approach of Myhill and Stegemeier (1978) as

$$V_s = \frac{Q_i E_{h,s}}{M_T \Delta T} \tag{1}$$

where, $E_{h,s}$ is the thermal efficiency, ΔT is the temperature rise of the steam zone above the initial reservoir temperature (assumed to be same as the temperature rise at down-hole condition, ΔT_i), and M_T is the total volumetric heat capacity of the reservoir. Heat capacity is the sum of the rock and fluid contributions and is written

$$M_T = (1-\phi)M_{rr} + \sum_{\beta=w,o,g} \phi S_\beta M_\beta \tag{2}$$

where, ϕ is the porosity, S is the phase saturation, and the subscript β refers to the individual phases. The quantity Q_i is the cumulative heat injected including any remaining heat from the previous cycles. The heat injection rate is given by

$$\dot{Q}_i = w_i (C_w \Delta T + f_{sdh} \Delta H_{vdh}) \tag{3}$$

where, w_i is the mass rate of steam injection in the reservoir, C_w is the average specific heat of water over the temperature range corresponding to ΔT, f_{sdh} and ΔH_{vdh} are the steam quality and the latent heat of vaporization both at down-hole conditions, respectively.

The thermal efficiency is calculated from the function given by Myhill and Stegemeier (1978) as

$$E_{h,s} = \frac{1}{t_D}\left\{ G(t_D) + (1-f_{hv})\frac{U(t_D - t_{cD})}{\sqrt{\pi}}\left[2\sqrt{t_D} - 2(1-f_{hv})\sqrt{t_D - t_{cD}} - \int_0^{t_{cD}} \frac{e^x erfc(\sqrt{x})}{\sqrt{t_D - x}} dx - \sqrt{\pi} G(t_D) \right] \right\} \tag{4a}$$

In the expression above, the heat losses to both, the overburden as well as the underburden are included. In the model proposed, the triangular cross sectional shape of the steam chamber is such that heat loss occurs only to the overburden. Thus, $E_{h,s}$ needs to be modified to be consistent with our model. Now, $E_{h,s}$ is defined as the ratio of the heat remaining in the zone to the total heat injected. Thus, the quantity $(1-E_{h,s})$ is the ratio of the heat lost to the total heat injected

$$F_l = 1 - E_{h,s} \tag{4(b)}$$

Neglecting loss to the underburden, heat losses are approximately one-half of the value predicted by Eq.4(b). Therefore, the modified thermal efficiency is

$$(E_{h,s})_{mod} = 1 - \tfrac{1}{2} F_l = \tfrac{1}{2}(1.0 + E_{h,s}) \quad 4(c)$$

In Eq.(4a), $G(t_D)$ is

$$G(t_D) = 2\sqrt{\frac{t_D}{\pi}} - 1 + e^{t_D} erfc\left(\sqrt{t_D}\right) \quad (5)$$

The symbols t_D and t_{cD} represent dimensionless times given by

$$t_D = 4\left(\frac{M_{SH}}{M_T}\right)^2 \frac{\alpha_{SH}}{h_t^2} t \quad (6)$$

where, α_{SH} is the shale thermal diffusivity, t is the time, h_t is the total reservoir thickness and M_{SH} is the shale volumetric heat capacity. The dimensionless critical time (Myhill and Stegemeier, 1978) is defined by

$$e^{t_{cD}} erfc(t_{cD}) \equiv 1 - f_{hv} \quad (7)$$

The quantity f_{hv}, the fraction of heat injected in latent form, is given by

$$f_{hv} = \left(1 + \frac{C_w \Delta T}{f_{sdh} \Delta H_{vdh}}\right)^{-1} \quad (8)$$

The step-function U in Eq.(4) is defined as

$$U(x) = 0 \quad for \quad x < 0 \quad (9a)$$

$$U(x) = 1 \quad for \quad x > 0 \quad (9b)$$

We assume that the steam zone shape has a triangular cross section with a *y*-directional length equal to the length of the horizontal well, L (Fig.1). The volume is written as

$$V_s = R_h L h_{st} \quad (10a)$$

where R_h is one-half of the base of the triangular heated zone and h_{st} is the steam zone thickness also referred to as "Zone Horizontal Range".

Rearranging Eq.(10a), it follows that,

$$R_h = \frac{V_s}{L h_{st}} \quad (10b)$$

2.3 Heat Remaining in the Reservoir

Boberg and Lantz (1966) give the average temperature of the steam zone, T_{avg}, as

$$T_{avg} = T_R + (T_s - T_R)[f_{HD} f_{VD}(1 - f_{PD}) - f_{PD}] \quad (11)$$

The dimensionless parameters f_{VD}, f_{HD} and f_{PD} are functions of time and represent horizontal loss, vertical loss and energy removed with the produced fluids, respectively. Aziz and Gontijo (1984) define them according to the following expressions.

The horizontal heat losses are expressed as (Aziz and Gontijo, 1984):

$$f_{HD} = \frac{1}{1 + 5t_{DH}} \tag{12a}$$

where,

$$t_{DH} = \frac{\alpha(t - t_{inj})}{R_h^2} \tag{12b}$$

An alternate treatment for the calculation of f_{HD} is presented in Appendix B. The quantity f_{HD} is the average unit solution for the one-dimensional heat conduction problem in the horizontal direction:

$$\alpha \frac{\partial^2 f}{\partial x^2} = \frac{\partial f}{\partial t} \tag{12c}$$

where $f = \left(\frac{T - T_o}{T_s - T_o} \right)$ is the dimensionless temperature.

The averaged solution for this equation after making use of the appropriate boundary conditions consistent with the geometry chosen for our model is:

$$f_{HD} = \frac{1}{2} + \sqrt{\frac{t_{DH}}{\pi}} \left\{ -2.0 + \exp\left(-\frac{1}{t_{DH}} \right) \right\} + erf\left(\frac{1}{\sqrt{t_{DH}}} \right) \left\{ \left(\frac{2}{\sqrt{\pi}} - 1 \right) t_{DH} + \frac{1}{2} \right\} \tag{12d}$$

Similarly, the vertical heat losses are expressed as (Aziz and Gontijo, 1984):

$$f_{VD} = \frac{1}{\sqrt{1 + 5t_{DV}}} \tag{13a}$$

where,

$$t_{DV} = \frac{4\alpha(t - t_{inj})}{h_t^2} \tag{13b}$$

In the equations above, α is the reservoir thermal diffusivity.

Note that for the first cycle, the initial amount of heat in the reservoir is set to zero. For all following cycles, the initial amount of energy is calculated based on steam zone volume and the average temperature at the end of the previous cycle. The average temperature at any time during the cycle is calculated using Eq.(11) (Boberg and Lantz, 1966). Since Boberg and Lantz's equation assumes a cylindrical shape for the heated zone, this equation is just an approximation for the triangular shape being considered. However, we use the approximations for f_{HD} and f_{VD} as employed by Aziz and Gontijo (1984) who assume a conical shape with triangular cross section. This is identical to the cross sectional shape that we have considered. The only difference is that they rotate the triangular shape through π radians whereas our coordinate system is Cartesian.

The term that accounts for the energy removed with produced fluids is given by

$$f_{PD} = \frac{1}{2Q_{MAX}} \int_0^t Q_p \, dt \tag{14}$$

where,

$$Q_p = 5.615(q_o M_o + q_w M_w)(T_{avg} - T_R) \tag{15}$$

where Q_{MAX} is the maximum heat supplied to the reservoir. It is calculated at the end of the soak period as the amount of heat injected plus the heat remaining in the reservoir from the previous cycle minus the losses to the over burden (Vogel, 1982)

$$Q_{MAX} = Q_{inj} + Q_{last} - 2R_h LK_R(T_s - T_R)\sqrt{\frac{t_{soak}}{\Pi\alpha}} \tag{16a}$$

$$Q_{inj} = 350.376\overline{Q_i}w_s t_{inj} \tag{16b}$$

$$Q_{last} = V_s M_T (T_{avg} - T_R) \tag{16c}$$

where, L is the length of the horizontal well, K_R is the thermal conductivity of the reservoir, t_{soak} is the soak time, α is the reservoir thermal diffusivity, t_{inj} is the length of the injection cycle, Q_{last} is the heat remaining from the previous cycle, $\overline{Q_i}$ is the amount of heat injected per unit mass of steam, and w_s is the steam injection rate (cold water equivalent).

The steam pressure is calculated from the following approximate relationship (Prats, 1982):

$$p_s = \left[\frac{T_s}{115.95}\right]^{4.4545} \tag{17}$$

The volumetric heat capacities of oil and water are given as (Prats, 1982):

$$\begin{aligned} M_o &= (3.065 + 0.00355T)\sqrt{\rho_o} \\ M_w &= \rho_w C_w \end{aligned} \tag{18}$$

As the integral for f_{PD} is not easy to calculate, it is approximated by the following expression (Aziz and Gontijo, 1984),

$$\Delta f_{PD} = \frac{5.615(q_o M_o + q_w M_w)(T_{avg}^{n-1} - T_R)\Delta t}{2Q_{MAX}} \tag{19}$$

where, Δt is the time step, n is the time step number, q_o and q_w are the oil and water production rates, respectively. The average temperature of the steam zone in the 'n-1'th cycle is T_{avg}^{n-1}.

2.4 Production Period

In this period, the well is opened for oil flow from the reservoir. Presented in the following section is a model to predict oil production rates during the production period.

Butler et al. (1980) presented a series of publications related to the gravity-drainage of heavy-oil reservoirs subjected to steam injection in which the theory was directed to linear flow from horizontal wells. In this development, a similar approach is used. However, the steam zone shape has been assumed to be a prism with triangular cross section and the horizontal well lies at the bottom edge. Fig.1 shows the cross sectional shape of the zone.

It is assumed in the derivation of the flow equation that the reservoir is initially saturated with oil and water, and it is pressure-depleted. After steam flooding, the steam chamber occupies a prismatic shape. Steam distribution along the well is assumed to be uniform. Heat transfer from

the steam chamber to the neighboring oil zone is via conduction. During the injection period, the average temperature of the steam chamber is assumed to be the saturation temperature of the steam. The oil is heavy enough to permit the injected steam to go to the top of the reservoir as suggested by Van Lookeren (1977). The reservoir is assumed to be initially pressure-depleted and is only negligibly re-pressurized when steam is injected. Finally, the potential that causes flow of oil into the same well that acts as a production well is a combination of gravity forces and pressure drive.

2.4.1 Development of Flow Equation

In this approach, we assume that gravity-drainage takes place through the entire steam chamber. Thus, integration is over the entire steam chamber and proceeds angularly with the appropriate approximation for the area. Gravity and pressure drive are taken as the forces causing production. The steam zone growth is estimated in terms of the decrease in the angle of inclination of the zone with the horizontal, θ. The thickness of the steam zone is assumed to be equal to the reservoir thickness. The heated-zone geometry used to derive the flow equation is given in Fig.1. The maximum heated dimension in the horizontal direction is R_h, while the maximum heated dimension in the vertical direction is the reservoir thickness h.

According to Darcy's law, the flow rate through an incremental area, dA, normal to the direction of flow [Fig.1(b)], is written

$$dq_o = -\frac{k_o}{\mu_o}(\rho_o - \rho_s)\nabla\phi dA \tag{20}$$

where, $\nabla\phi$ is the gradient of potential in the direction of flow, μ_o is the dynamic viscosity of oil, k_o is the effective permeability to oil, and $\rho_o - \rho_s$ is the density difference between the oil and steam. According to Hubbert (1956), the potential is expressed as

$$\Delta\phi = \frac{p_s - p_{wf}}{\rho_o} + g\sin\theta\ \Delta h$$

Here, g is the acceleration due to gravity. The differential area depends upon distance, r, above the well:

$$dA = 2r\sin\left(\frac{1}{2}d\theta\right) \approx rd\theta \tag{21}$$

The oil-phase effective permeability, k_o is the product of the absolute permeability, k, and relative permeability, k_{ro}. With r equal to $h_{st}\text{cosec}(\theta)$ and applying the approximation suggested in Eq.(21), the differential area reduces to

$$dA = Lh_{st}\cos ec\theta d\theta \tag{22}$$

It follows upon substitution of Eq.(22) into Eq.(20) that the flow rate becomes

$$dq_o = -\frac{k_o}{\mu_o}(\rho_o - \rho_s)\left(\frac{p_s - p_{wf}}{\rho_o} + gh_{st}\sin(\theta)\right)h_{st}L\cos ec\theta d\theta \tag{23}$$

Integration over one-half of the heated area and multiplication by 2 yields

$$\frac{q_o}{L} = -\frac{2k_o}{\mu_o}(\rho_o - \rho_s)\left[144.0\frac{p_s - p_{wf}}{\rho_o}\log\left\{\frac{1}{\tan\left(\frac{\theta}{2}\right)}\right\} + gh_{st}(\pi - 2\theta)\right] \tag{24}$$

2.5 Property Correlations

The steam viscosity, μ_{st}, and density, ρ_{st}, are calculated by correlations given by Farouq Ali (1982).

$$\rho_{st}(lb/ft^3) = \frac{p_s^{0.9588}}{363.9}, \quad p_s \ \ in \ \ psia \tag{25}$$

$$\mu_{st}(cp) = 10^{-4}(0.2T_s + 82), \quad T_s \ \ in \ ^oF \tag{26}$$

The average specific heat of water is given by:

$$C_w = \frac{h_w(T_s) - h_w(T_R)}{T_s - T_R} \tag{27}$$

The water enthalpy correlation of Jones (1977) and the steam latent heat correlation of Farouq Ali (1982) are used:

$$h_w = 68\left[\frac{T_s}{100}\right]^{1.24}, T_s \ \ in \ ^oF \tag{28a}$$

$$\Delta H_{vdh} = 94(705 - T_s)^{0.55}, T_s \ \ in \ ^oF \tag{28b}$$

where T_s is the steam saturation temperature at the given bottom-hole pressure. The oil and water densities are approximated by (Aziz, 1984):

$$\rho_o = \rho_{o_{STD}} - 0.0214(T - T_{STD}) \tag{29a}$$

$$\rho_w = 82.4 - 11\ln\left[\frac{705 - T_{STD}}{705 - T}\right] \tag{29b}$$

where the subscript STD refers to standard conditions.

The oil density correlation holds for oils with gravity less than 20°API and temperature less than 500°F.

2.5.1 Oil and Water Viscosities

Fluid viscosities as a function of temperature are obtained from relations given by Jones (1977)

$$\mu_o(cp) = 0.001889047e^{\frac{8956.257}{T+460}} \tag{30a}$$

$$\mu_w(cp) = 0.66\left[\frac{T}{100}\right]^{-1.14} \tag{30b}$$

The correlation for oil viscosity is applicable to oils with specific gravity less than 30° API.

2.5.2 Fluid Saturations and Relative Permeabilities

After the soak period and before the production begins, it is assumed that the only mobile phase around the well is water.

$$\overline{S}_w = 1 - S_{orw} \tag{31}$$

Once the well is opened for production, it is assumed that the oil saturation around the well increases. Also, the water saturation is given by

$$S_w = \overline{S}_w - (\overline{S}_w - S_{wi})\frac{W_p}{WIP} \tag{32}$$

where W_p is the water production during the cycle and WIP is the amount of mobile water in place at the beginning of the cycle (Aziz and Gontijo, 1984). The normalized water saturation expression is

$$S_w^o = \frac{S_w - S_{wi}}{1 - S_{wi} - S_{orw}} \tag{33}$$

The analytical expressions presented by Farouq Ali (1982) for the relative permeabilities suggested by Gomaa (1980) are as follows:

$$k_{rw} = -0.002167S_w^o + 0.024167(S_w^o)^2 \tag{34a}$$

$$k_{ro} = -0.9416 + \frac{1.0808}{S_w^o} - \frac{0.13856}{(S_w^o)^2} \tag{34b}$$

with,

$$k_{ro} = 1.0 \quad if \quad S_w^o \le 0.2 \tag{34c}$$

2.6 Algorithm for Calculation Scheme

These equations and ideas are translated into a seven-step algorithm:

1. Initialize the model by inputting reservoir, fluid, and operational properties.
2. Calculate steam zone geometry (volume, height, and thickness), temperature, and saturations during injection and at the start of the production cycle.
3. Calculate oil and water production flow rates at small time steps within the production interval. Also, calculate the cumulative volume of fluids produced and check against original fluids in place.
4. Calculate the average temperature of the heated zone during production and at the end of the production cycle.
5. If additional steps are needed for cycle completion, go to stage 3, else proceed.
6. Calculate the amount of fluids and heat remaining in the reservoir at the termination of the cycle, and thereby calculate recovery and oil-steam ratio (OSR).
7. If a new cycle is required, repeat steps, else terminate calculations.

2.6.1 Computer Code

A C++ computer program was written to implement the proposed analytical model. The prime objective of this code is to validate the physical applicability of the model described in Chapter 2. The code outputs the oil production rate versus time. For calculating the oil production, there are many preceding steps that include calculation of thermal properties of the reservoir matrix and fluids, temperature calculations based on heat losses as well as change in rheological behavior of the fluids. The correlations used are simple and easy to apply. The program also calculates the temperature decline of the steam zone with time as well as the water production rate with time. The calculations are made for each cycle that is comprised of three periods: the "injection interval", the "soak interval" and the "production interval". Note that production does not begin until the production interval starts. However, the temperature decline of the heated zone begins from the soaking interval. At the end of each such cycle, the heat remaining in the reservoir is calculated based on the temperature. This heat becomes the initial heat due to steam injection for the next cycle.

2.6.2 Program Structure

The program is structured in the following order:

1. Input data
2. Begin cycle calculations
3. Calculate fluid properties
4. Calculate steam zone geometry at the end of injection
5. Calculate average temperature of steam zone at end of soak
6. Calculate thermal properties of reservoir and fluids at each time step as a function of average temperature
7. Calculate saturations and relative permeabilities of oil and water
8. Calculate pressure gradient acting as driving force
9. Calculate oil and water flow rate until the end of production
10. Calculate cumulative fluids production
11. Check to see if the end of production or beginning of a new cycle has been reached

The input data is illustrated in Table 1. The complete code is provided in Appendix B.

Chapter 3

3. Validation of Model, Results and Discussions

The proposed model is appropriate for predicting the oil production from pressure-depleted reservoirs where oil gravity is less than 30° API and steam injection temperatures not more than 450°F. If the input data are not within these limits, the correlations for fluid properties and flow behavior are inaccurate.

The model was validated and results were compared with those presented by Elliot and Kovscek (1999) for cyclic steaming prior to single-well SAGD. The data and the oil viscosity correlation employed were also taken from Elliot and Kovscek (1999), as shown in Table 1. Fig.3 depicts the comparison made. It is a plot of recovery factor versus time. The recovery factor is the ratio of cumulative oil produced to the original oil in place. As observed, the recovery factor obtained using the analytical model proposed matches quite closely with the recovery factor data presented by Elliot et al (1999) at early times. At later times, it is slightly greater, but within reasonable limits.

Runs were made for an example base case and illustrated are the temperature, steam zone volume, angle of inclination of the steam zone with respect to the vertical, and the cumulative oil production versus time. A sensitivity analysis is performed in order to understand

better where cyclic steaming with a horizontal well works best and to verify the limitations of the model.

3.1 Sensitivity Analysis

The sensitivity of the model was tested for the following parameters:

1. down-hole steam quality
2. formation thickness
3. steam injection rate
4. down-hole pressure
5. soaking interval
6. production interval

3.1.1 Base Case

This case was run using the properties and input data shown in Table 2. Briefly, the oil gravity is 14 °API, reservoir permeability is 1.5 D, and the pay thickness is 80 ft. The curves for the oil and water production versus time, average temperature of the steam zone versus time and the steam zone volume versus time are given in Fig.4(a) – Fig.4(d).

Fig4(a) shows the cumulative oil production per foot of the well in STB/ft versus cumulative time in days. All production and injection information is per foot of the horizontal well as are steam zone volumes. The three regions correspond to three cycles. Each cycle has distinct flat zones, which are the injection and soak intervals. After the soak interval in a given cycle is the production interval. During steam injection and soak there is no production. The instantaneous oil rate increases rapidly at early times in the production interval, as witnessed by steep gradients in cumulative production because the oil is hot and its viscosity is low. At later times, oil production decreases as the temperature declines. The production at late times is primarily due to gravity-drainage of cool oil.

A similar explanation applies to Fig.4(b) for the cumulative water production versus time curve. Here, during steam injection and soak there is no production. The instantaneous water rate increases rapidly at early times in the production interval, accounting for condensed steam around the well. But at later times water production declines. The production at late times is primarily due to gravity-drainage of condensed water.

Fig.4(c) depicts the average heated zone temperature versus time. The temperature is at the steam saturation temperature during the injection interval. During the soaking period it decreases due to conduction heat losses to the adjacent reservoir and overburden. Since the rate of heat loss is proportional to the temperature gradient, the temperature decline is greatest at the beginning of the soak period. At the beginning of the production period, temperature decline increases rapidly because hot fluids are produced. At later times, the rate of decline decreases.

Fig.4(d) shows the volume of the heated zone versus time. The volume of the heated zone increases continuously during the injection interval. This is because the amount of injected heat increases. This trend is in agreement with Eq.16, which gives the volume of the heated zone. In the soak and production intervals, it remains constant at the value it reached at the end of the injection period. At the end of the production interval the volume of the heated zone collapses to a finite value, Eq.16(c), that accounts for the heat remaining in the hot zone. Therefore, the volume of the heated zone starts at this finite value at the beginning of the next cycle.

Fig.4(e) shows the cumulative oil-steam ratio (OSR) versus the cumulative time. During the first injection and soaking intervals, there no production and the ratio is zero. In the first

production interval, the OSR increases as oil is produced. At the beginning of the second injection interval, steam is injected and therefore the OSR decreases as no oil is produced. In the ensuing soaking interval, there is no steam injection nor any oil production. Hence, the OSR remains constant. In the production interval, as there is oil production, OSR increases and reaches a peak at the end of the production interval. As k_{rw} is very small, the water flow rate, which is directly proportional to the water relative permeability is also small.

Next, the various sensitivity runs are described.

3.1.2 Sensitivity to Steam Quality

This case was run using four different values, 50%, 70%, 85% and 95%, of down-hole steam quality at an identical mass injection rate. The results are depicted in Fig.5(a) – Fig.5(d). Arrows are drawn to indicate the trends with increasing steam quality.

In Fig.5(a), as the steam quality increases from 50% to 95%, the cumulative oil production increases. As steam quality increases at constant mass flow rate, the total heat carried by the vapor increases. Hence, there is a greater volume heated as the quality increases, thereby increasing the quantity of heated oil flowing towards the horizontal production well. An increase in the steam quality from 50% to 85% almost doubles the cumulative oil produced at the end of three cycles.

Cumulative water production is not affected much by the increase in steam quality as seen in Fig.5(b). This is because the total mass of water injected is the same for all four cases.

The temperature of heated zone shown in Fig.5(c) reaches a uniform steam saturation temperature in the injection intervals and decreases with similar trends in the soak and production intervals for all the steam quality values.

The volume of the heated zone shown in Fig.5(d) increases for increasing steam quality. As steam quality increases, the heat carried by the vapor increases, thereby causing an enhanced contacted heated volume.

3.1.3 Sensitivity to Formation Thickness

This case was run using three different values, 80 ft, 200 ft and 300 ft, of the formation thickness holding all other parameters and variables constant. The results are depicted in Fig.6(a) – Fig.6(d). Again, arrows indicate increasing pay thickness.

As the formation thickness increases, the cumulative oil and water production decreases as the volume of the reservoir contacted by the steam relative to the total volume decreases. Equation (24) predicts that gravity drainage from within the heated zone increases as the base of the heated zone, R_h, increases and θ, likewise, decreases. Hence, for identical steam volume, a short, squat heated zone produces more oil than a taller, narrower heated zone. This is shown in Fig6(a) and Fig6(b), respectively.

Figure 6(c) demonstrates that the temperature of the heated zone decreases more rapidly for smaller formation thickness. Essentially, the lesser the formation thicknesses, the larger are the heat losses to the overburden. One can visualize this by comparing it with a situation where we have a concentrated heat source in contact with a heat sink. The higher concentration heat source can be treated analogously to the heated zone with a smaller formation thickness, but with a higher energy (thermal) density. It is quite straightforward that the higher intensity heat source

emits more energy. Hence, the smaller the formation thickness, the greater are the losses and the steeper are the temperature gradients.

Fig.6(d) is self-explanatory. The larger the formation thickness, the larger the volume of the heated zone due to lesser heat losses.

3.1.4 Sensitivity to Steam Injection Rate

This case was run using three different values, 1 B/D-ft, 5 B/D-ft, and 10 B/D-ft, of the steam injection rate per foot of well. The results are depicted in Fig.7(a) – Fig.7(d).

Figure 7(a) and Fig.7(b) depict the cumulative oil and water production versus time, respectively. As the steam injection rate is increased, the oil and water production increases significantly, as greater amount of heat and water is injected and a greater volume of the reservoir is contacted, as shown in Fig.7(d).

Figure 7(c) shows the temperature of the heated zone. With increasing steam injection rates the net temperature decreases over a cycle is comparatively less. This behavior is attributed to the fact that higher injection rates lead to greater thermal energy in the reservoir volume, and this energy is slow to dissipate. Although the corresponding heated zone volumes for higher injection rates are larger, thermal energy dissipation rates are lower. The surface area for heat transfer does not increase as rapidly as the heated volume.

3.1.5 Sensitivity to Down-hole Steam Pressure

This case was run using three different values, 150 psia, 200 psia, and 300 psia, of the down-hole steam pressure. Hence, the injection temperature increases and the mass injection rate and quality are constant. The results are depicted in Fig.8(a) – Fig.8(d).

A slight increase is observed in the cumulative oil and water production as we increase down-hole steam pressure. The effects are not very large because of the following reasons. The steam quality was kept constant at 0.7. As the down-hole pressure is increased, the latent heat of vaporization decreases, thereby causing more heat to be injected as sensible heat. This fact causes the amount of heat injected to be low for that temperature. Also, the heat losses are more sensitive to the temperature than to the amount of heat injected since the temperature is high and the amount of heat injected is relatively low causing a large fraction of the injected heat to be lost quickly to the adjacent layers. Another important reason could be that higher temperatures tend to cause higher initial fluid production and a lot of heat is removed at the beginning of the cycle.

As shown in Fig.8(c), the temperature of the heated zone drops rapidly during soak and production for higher injection pressures. Larger initial fluid production results due to higher saturated steam temperatures, and larger heat loss at the beginning of each cycle occurs also. Heat losses are large because the temperature gradient is large.

3.1.6 Sensitivity to Steam Soak Interval

This case was run using four different values, 15 days, 25 days, 30 days and 50 days, of the soaking interval. Arrows indicate the lengthening soak interval. The results are depicted in Fig.9(a) – Fig.9(b).

As shown in Fig.9(a), as the soaking interval is increased, the cumulative oil production decreases. Increase in the soaking interval implies a greater time for energy dissipation. In our case, the cumulative heat losses increase due to larger soaking periods. Therefore, the temperature of the heated zone at the end of the soaking interval is predictably lesser. As a consequence the oil viscosity is larger and mobility of oil toward the horizontal production well

in the production period is reduced. Hence, cumulative oil production decreases with increased soaking time. A similar explanation can be put forth to explain the behavior of the cumulative water production depicted in Fig.9(b). However, as the viscosity of oil is not a strong function of temperature, the change in water production observed is small. Quite obviously, the production is delayed as we have longer soaking time.

3.2 Discussion

As observed, an increase in steam quality results in higher oil production, as there is more energy per unit mass of the reservoir matrix due to a greater fraction of energy injected as latent heat of vaporization. This means that a given mass of steam carries more heat due to heat in the latent form, and hence, a greater oil rate is observed. Therefore, a higher steam quality is recommended for greater oil production.

For thicker pay zones, the energy density in the reservoir rock matrix is lesser. This is because of greater volume of the reservoir rock to be contacted by steam. Also, the reservoir fluid acts as a heat sink. Therefore, too large a pay zone might lead to very low oil rates. On the other hand, if the pay thickness is too low, then the energy density within the zone is extremely large, resulting in large losses to the surrounding matrix. A way to get around this problem is to reduce the energy carried per unit mass of the steam i.e. either decreasing the mass flow rate of steam or reducing the steam quality.

Higher steam injection rates enhance heat delivery, thereby increasing oil production. Excessively high injection rates cause over heating of the reservoir matrix that results in larger heat losses, and thus causing a decrease in the thermal efficiency of the process. The optimum steam injection rate is the one that results in minimal heat losses and maximum heated volume.

Increasing down-hole steam pressure has a negligible effect on the oil production. Even though the injection temperature is higher, the excess heat gets dissipated in the soaking interval, thereby making the process thermally inefficient.

Chapter 4
4. Conclusions

A simple model for the cyclic steam process with a horizontal well has been developed. It incorporates a new flow equation for gravity drainage of heavy oil. Important factors such as pressure drive, gravity drive, and shape of the steam zone are incorporated into the model. Limited comparison of the model to numerical simulation results indicate that the model captures the essential physics of the recovery process. Cyclic steaming appears to be effective in heating the near-well area and the reservoir volume. A sensitivity analysis shows that the process is relatively robust over the range of expected physical parameters.

References

Aziz, K. and Gontijo J.E.: "A Simple Analytical Model for Simulating Heavy-oil Recovery by Cyclic Steam in Pressure-Depleted Reservoirs", paper SPE 13037 presented at the 59th Annual Technical Conference and Exhibition, Houston, September 16-19, 1984.

Basham, M., Fong, W.S. and Kumar, M.: "Recent Experience in Design and Modeling of Thermal Horizontal Wells", paper 119, presented at the 9th UNITAR International Conference in Heavy Crude and Tar Sands, Beijing, China, October 27-30, 1998.

Boberg, T.C. and Lantz, R.B.: "Calculation of the Production Rate of a Thermally Stimulated Well", J.Pet.Tech. (Dec. 1966).

Butler, R.M. and Stephens, D.J.,: "The Gravity-drainage of Steam-Heated Heavy-Oil to Parallel Horizontal Wells", paper presented at the 31st Annual Technical Meeting of The Petroleum Society of CIM in Calgary, May 25-28, 1980.

Carlslaw, H.S. and Jaeger, J.C.,: "Conduction of Heat in Solids", 2nd ed., Oxford Science Publications, 1992.

Elliot, K.E. and Kovscek, A.R.: "Simulation of Early-Time Response of Single-Well Steam Assisted gravity-drainage (SW-SAGD)", SPE 54618, presented at the Western Regional Meeting of the SPE, Anchorage, Alaska, May 26-28, 1999.

Farouq Ali, S.M.: "Steam Injection Theories – A Unified Approach", paper SPE 10746 presented at the California Regional Meeting of the SPE, San Francisco, March 24-26, 1982.

Fontanilla, J.P. and Aziz, K.: "Prediction of Bottom-Hole Conditions for Wet Steam Injection Wells", J.Can.Pet.Tech., March-April 1982.

Gomaa, E.E.: "Correlations for Predicting Oil Recovery by Steamflood", J.Pet.Tech. (Feb. 1980) 325-332.

Hubbert, M.K. "Darcy's Law and the Field Equations of the Flow of Underground Fluids", Shell Development Cp., J.Pet.Tech., Sept.12, 1956.

Jones, J.: "Cyclic steam Reservoir Model for Viscous Oil, Pressure-depleted, Gravity-drainage Reservoirs", SPE 6544, 47th annual California Regional Meeting of the SPE of AIME, Bakersfield, April 13-15, 1977.

Mandl, G. and Volek, C.W.: "Heat and Mass Transport in Steam-Drive Processes", *Soc. Pet. Eng. J.* (March 1969) 59-79; *Trans.*, AIME, **246**.

Marx, J.W. and Langenheim, R.H.: "Reservoir Heating by Hot-Fluid Injection", Trans. AIME (1959) 216, 312-315.

Mendonza, H.: "Horizontal Well Steam Stimulation: A Pilot Test in Western Venezuela", paper 129, presented at the 9th UNITAR International Conference in Heavy Crude and Tar Sands, Beijing, China, October 27-30, 1998.

Myhill, N.A. and Stegemeier, G.L.: "Steam Drive Correlation and Prediction", J. Pet. Tech. (Feb. 1978) 173-182.

Prats, M.: "Thermal Recovery", Monograph – Volume 7, SPE of AIME, Henry L. Doherty Memorial Fund of AIME, 1982.

Van Lookeren: "Calculation Methods for Linear and Radial Steam Flow in Oil Reservoirs", J.Pet.Tech. (June, 1983) 427-439.

Vogel, V.: "Simplified Heat Calculation of Steamfloods", paper SPE 11219 presented at the 57th SPE Annual Fall Technical Conference and Exhibition, New Orleans, LA, September 26-29, 1982.

Tables

Table 1: Data for validation of proposed analytical model with results of Elliot et al (1999).

Grid System	
3D Cartesian System	
Total Number of Blocks	5568
X-Dimension (ft)	4592.0
Y-Dimension (ft)	209.92
Z-Dimension (ft)	64.288
Well Length (ft)	2624.0
Reservoir Properties	
Initial Pressure (psia)	385.132
Initial Temperature (°F)	60.8
Initial S_o (%)	85.0
Initial S_w (%)	15.0
Rock Properties	
Porosity (%)	33.0
Operating Conditions	
Injection Rate (B/D)	1.57

Table 2: Input Data

Variable	Value
Reservoir permeability (Darcy)	1.5
Reservoir porosity	0.2
Initial water saturation	0.25
Connate water saturation	0.1
Well radius (ft)	0.31
Residual oil saturation to steam	0.05
Residual oil saturation to water	0.25
Initial reservoir temperature (°F)	110
Saturated steam temperature (°F)	365
Reservoir thermal conductivity (Btu/ft D. °F)	24.0
Reservoir thermal diffusivity (ft^2/D)	0.48
Time step size (days)	1.0
Injected steam quality	0.67
Steam injection rate (B/D)	1.0
API gravity of oil (°API)	14.0
Injection pressure (psi)	150.0
Pay thickness (ft)	80.0

Figures

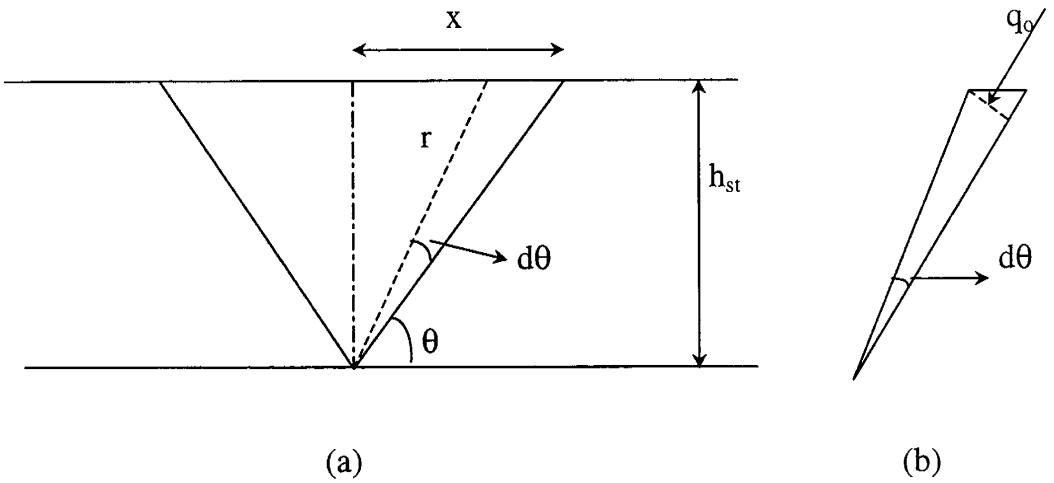

Fig.1(a) Schematic diagram of heated area geometry; (b) differential element of the heated area.

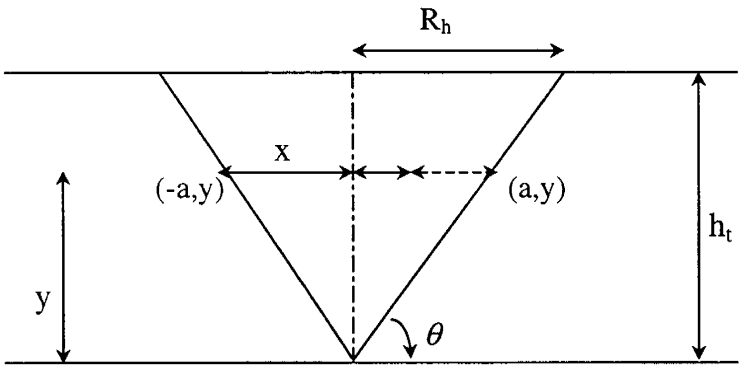

Fig.2 Schematic diagram of area of cross section of heated area

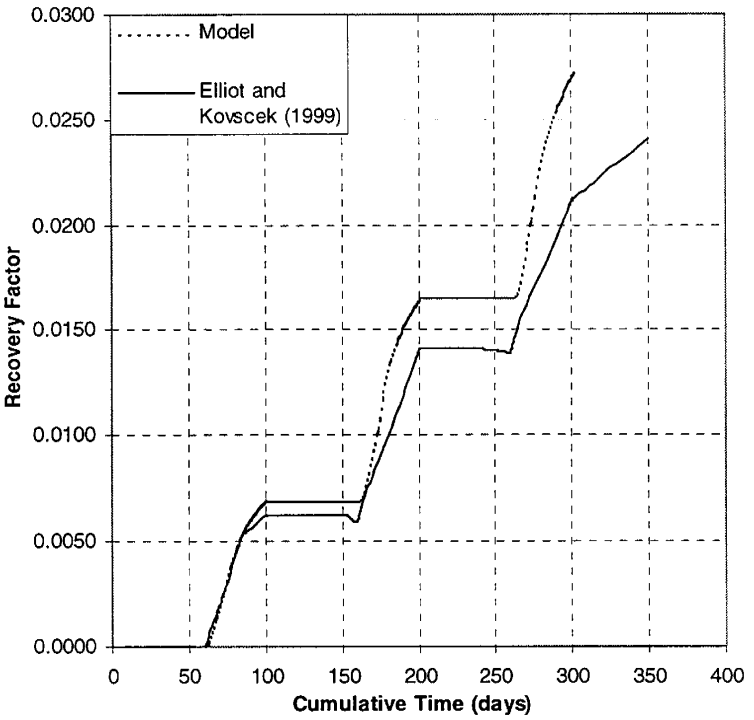

Fig.3 Recovery factor versus cumulative time (Comparison with results Elliot and Kovscek, 1999)

4 (a)

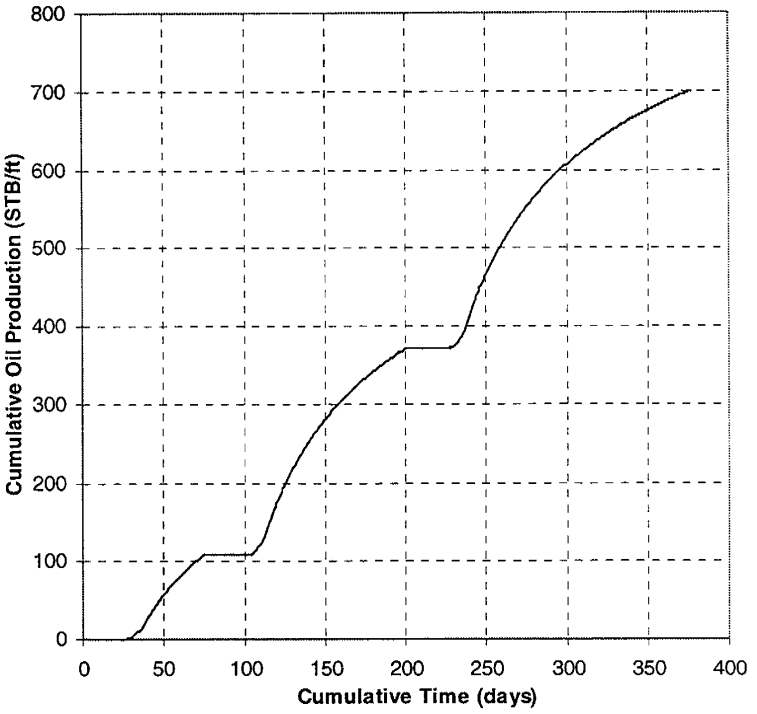
Cumulative Oil Production (STB/ft)
800
700
600
500
400
300
200
100
0
0
50
100
150
200
250
300
350
400
Cumulative Time (days)

4 (b)

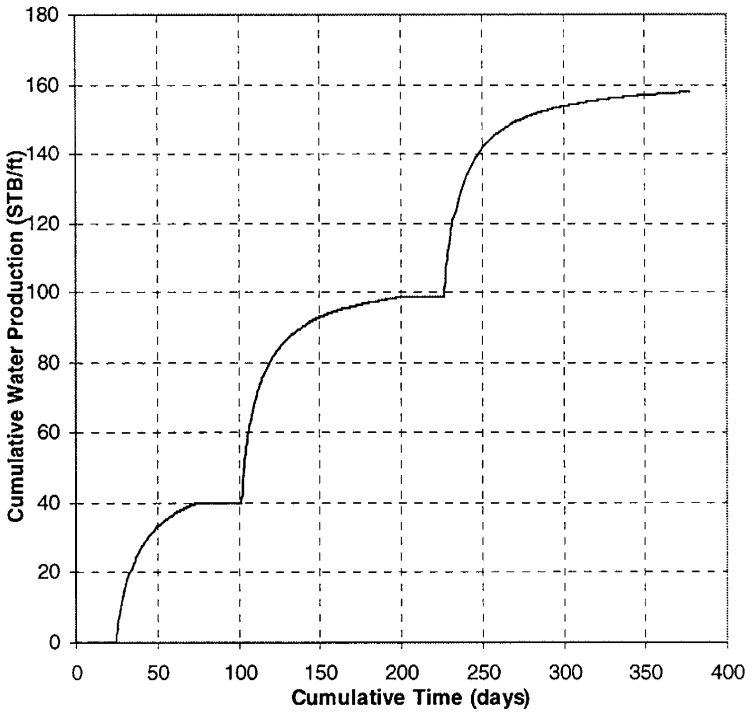
Cumulative Water Production (STB/ft)
180
160
140
120
100
80
60
40
20
0
0
50
100
150
200
250
300
350
400
Cumulative Time (days)

4 (c)

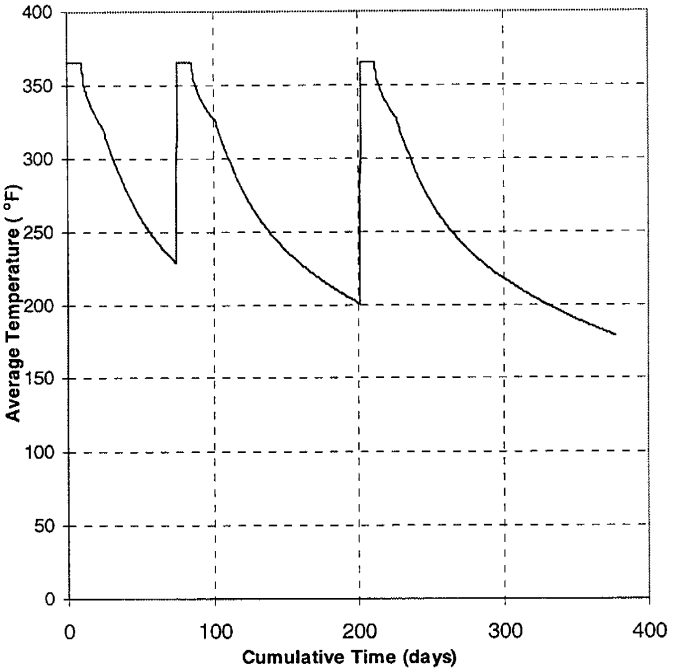
Average Temperature (°F)
400
350
300
250
200
150
100
50
0
0
100
200
300
400
Cumulative Time (days)

4(d)

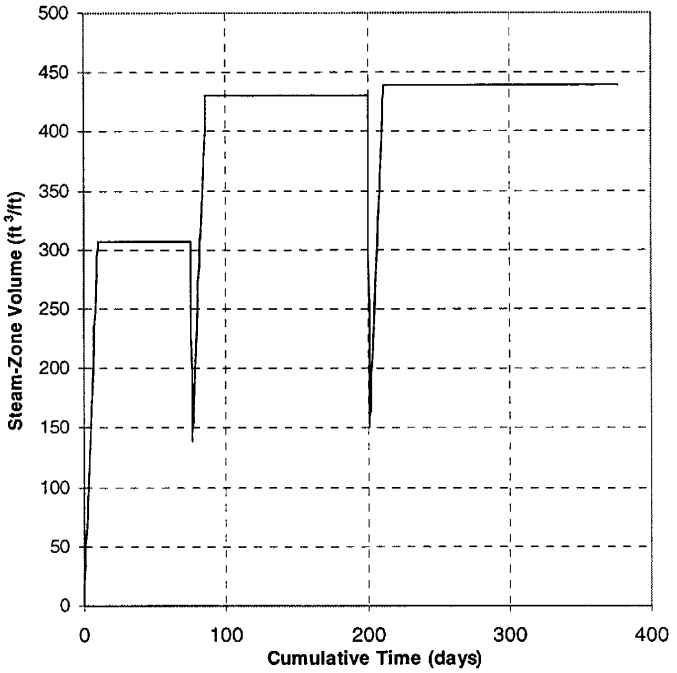
Steam-Zone Volume (ft 3/ft)
500
450
400
350
300
250
200
150
100
50
0
0
100
200
300
400
Cumulative Time (days)

4(e)

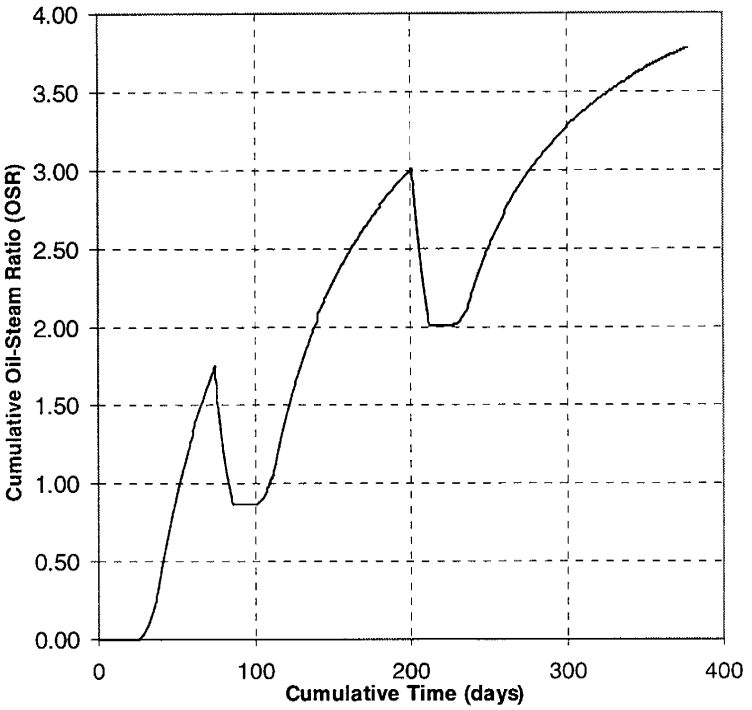

Fig.4 Base case: (a) cumulative oil production versus cumulative time, (b) cumulative water production versus cumulative time, (c) average steam zone temperature versus cumulative time, (d) steam zone volume versus cumulative time, (e) oil-steam ratio versus cumulative time.

5(a)

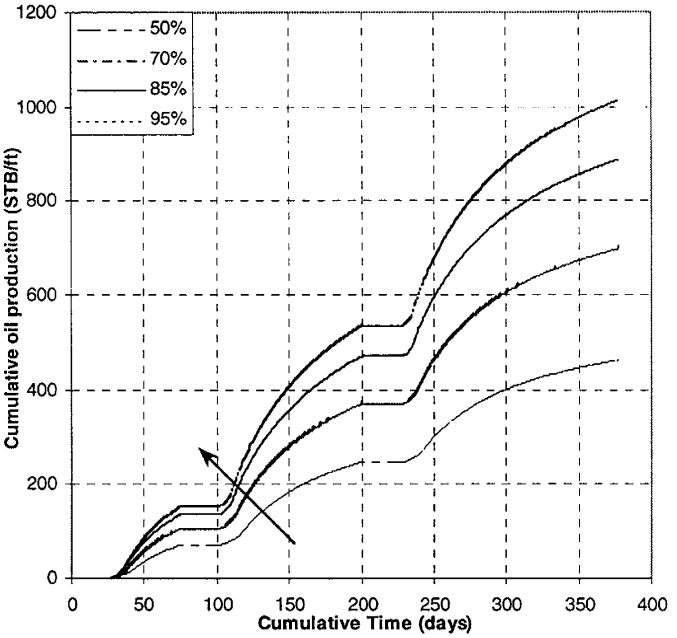
50%
70%
85%
95%
Cumulative oil production (STB/ft)
Cumulative Time (days)
0
200
400
600
800
1000
1200
0
50
100
150
200
250
300
350
400

5(b)

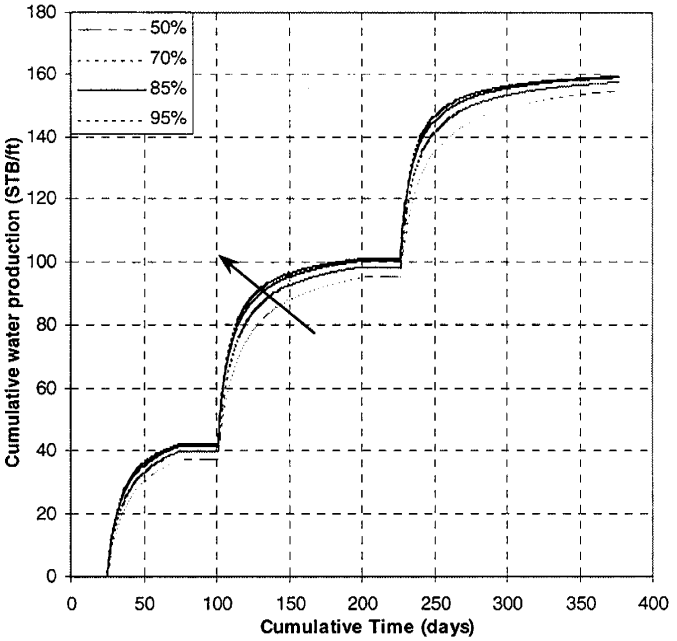
50%
70%
85%
95%
Cumulative water production (STB/ft)
Cumulative Time (days)
0
20
40
60
80
100
120
140
160
180
0
50
100
150
200
250
300
350
400

5(c)

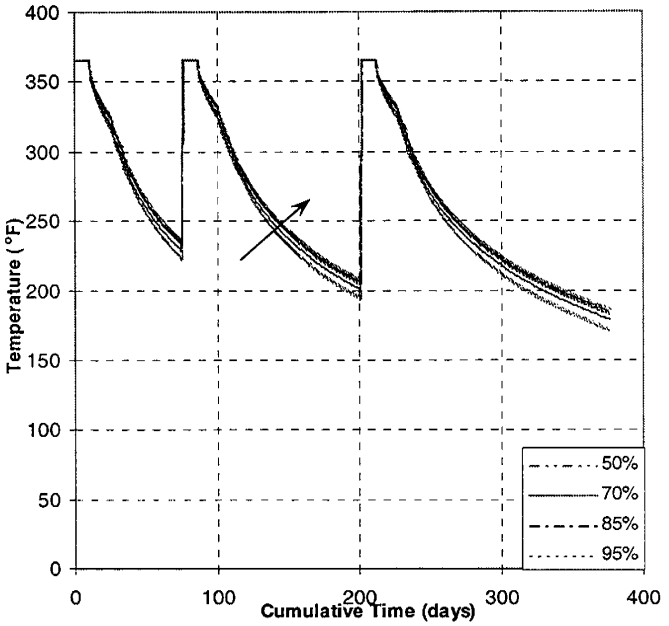

5(d)

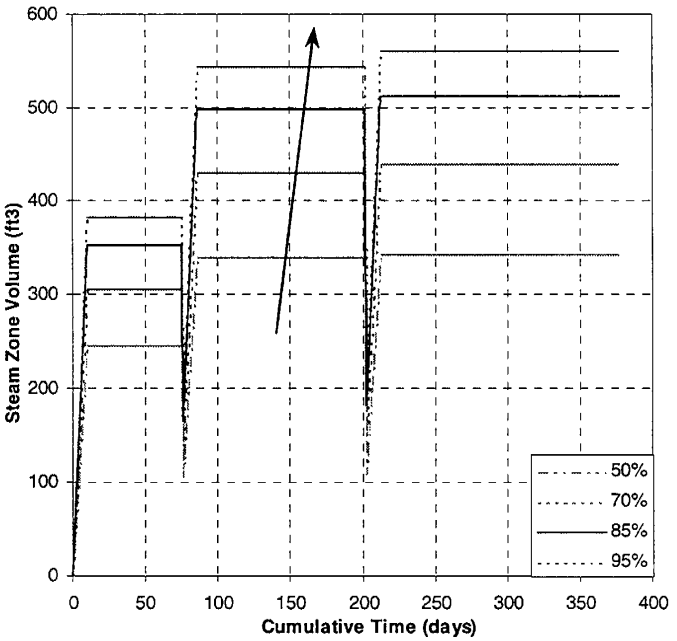

Fig.5 Sensitivity to steam quality: (a) cumulative oil production versus cumulative time, (b) cumulative water production versus cumulative time, (c) average steam zone temperature versus cumulative time, (d) steam zone volume versus cumulative time.

6(a)

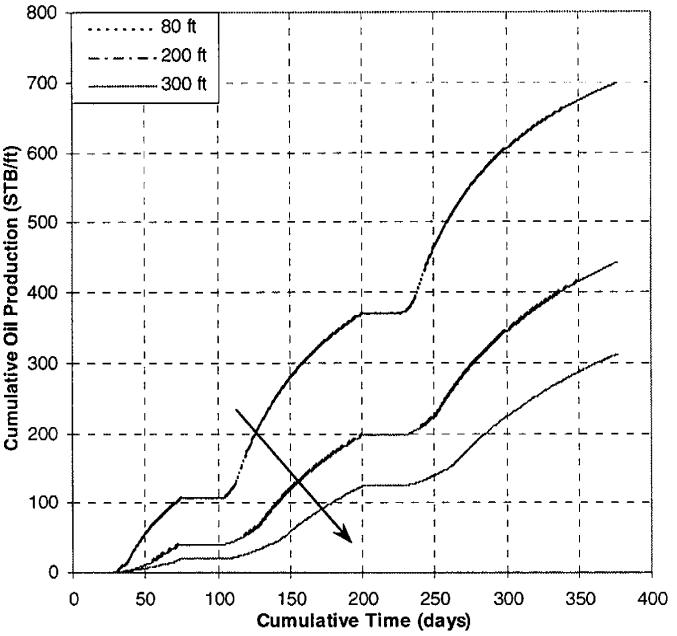
80 ft
200 ft
300 ft
Cumulative Oil Production (STB/ft)
Cumulative Time (days)
0
100
200
300
400
500
600
700
800
0
50
100
150
200
250
300
350
400

6(b)

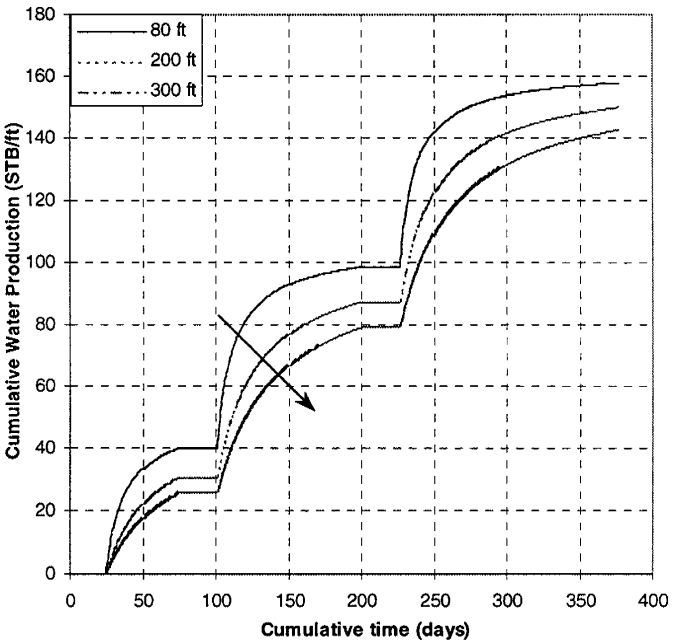
80 ft
200 ft
300 ft
Cumulative Water Production (STB/ft)
Cumulative time (days)
0
20
40
60
80
100
120
140
160
180
0
50
100
150
200
250
300
350
400

6(c)

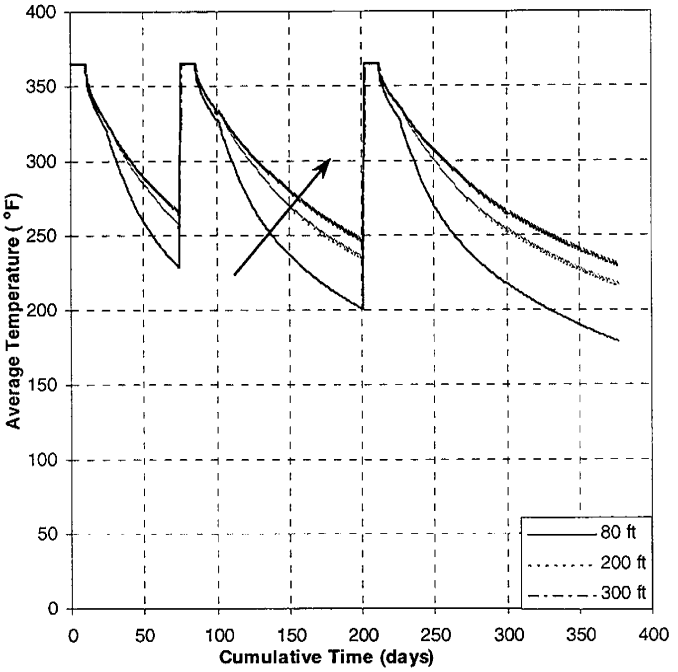

6(d)

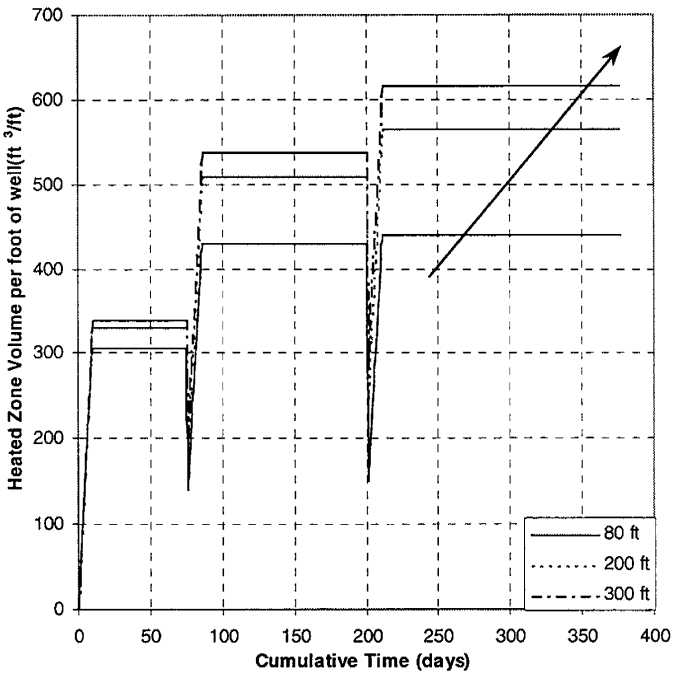

Fig.6 Sensitivity formation thickness: (a) cumulative oil production versus cumulative time, (b) cumulative water production versus cumulative time, (c) average steam zone temperature versus cumulative time, (d) steam zone volume versus cumulative time.

7(a)

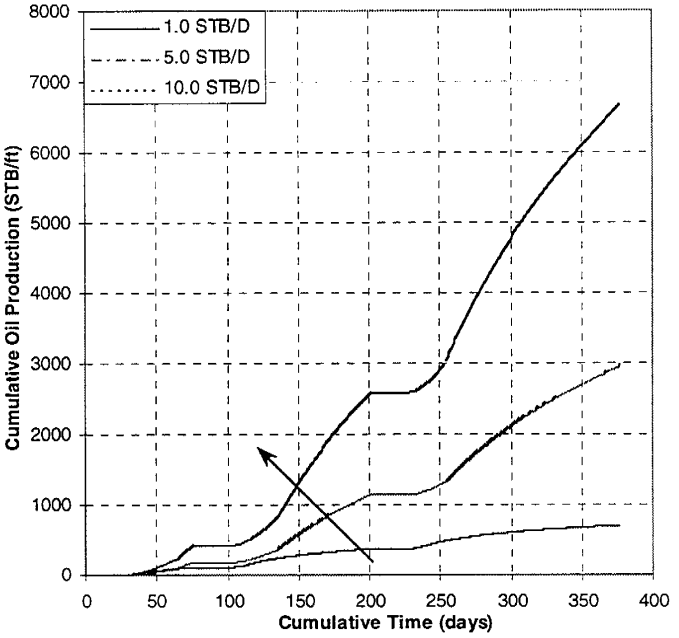
1.0 STB/D
5.0 STB/D
10.0 STB/D
Cumulative Oil Production (STB/ft)
Cumulative Time (days)
0
1000
2000
3000
4000
5000
6000
7000
8000
0
50
100
150
200
250
300
350
400

7(b)

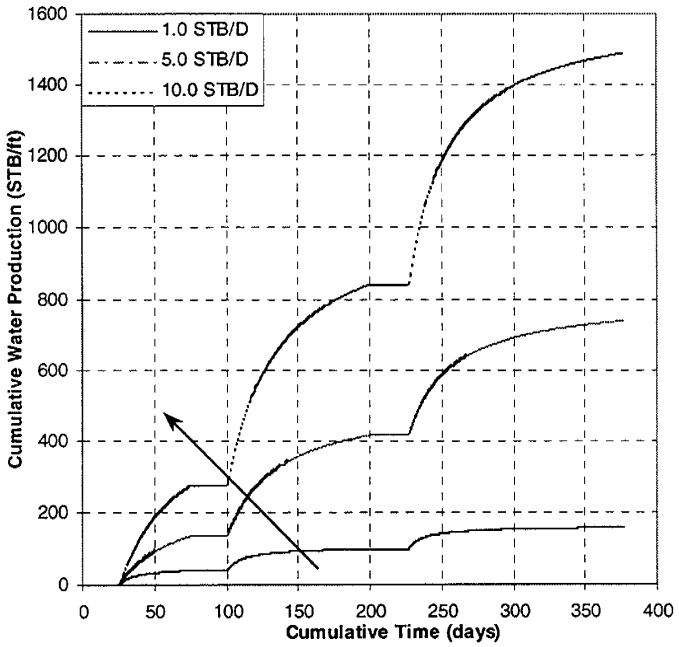
1.0 STB/D
5.0 STB/D
10.0 STB/D
Cumulative Water Production (STB/ft)
Cumulative Time (days)
0
200
400
600
800
1000
1200
1400
1600
0
50
100
150
200
250
300
350
400

7(c)

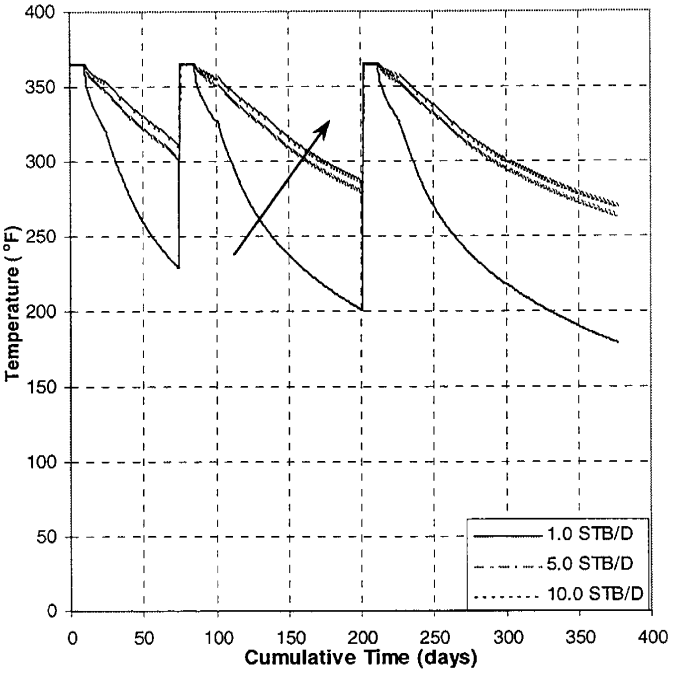

7(d)

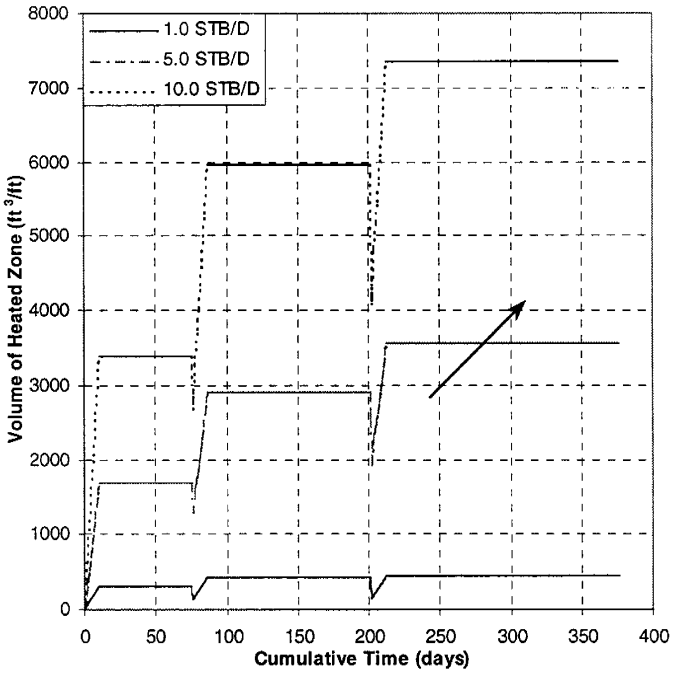

Fig.7 Sensitivity to steam injection rate: (a) cumulative oil production versus cumulative time, (b) cumulative water production versus cumulative time, (c) average steam zone temperature versus cumulative time, (d) steam zone volume versus cumulative time

8(a)

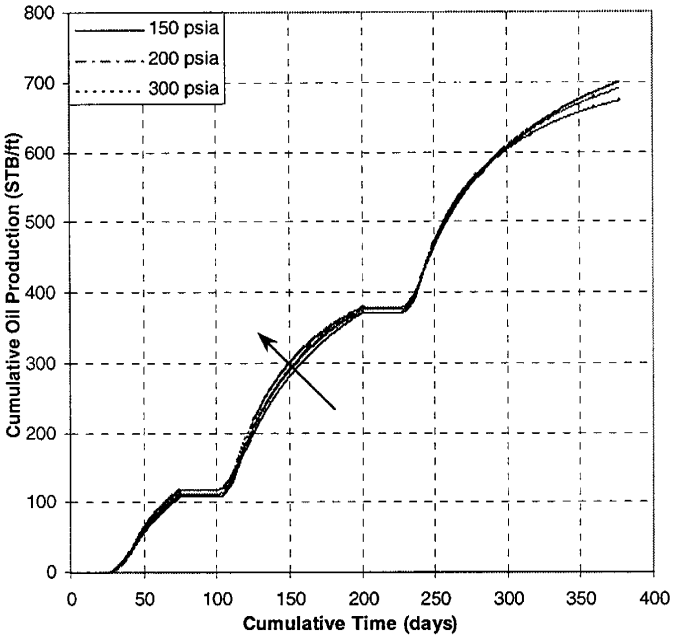
150 psia
200 psia
300 psia
Cumulative Oil Production (STB/ft)
Cumulative Time (days)
0
100
200
300
400
500
600
700
800
0
50
100
150
200
250
300
350
400

8(b)

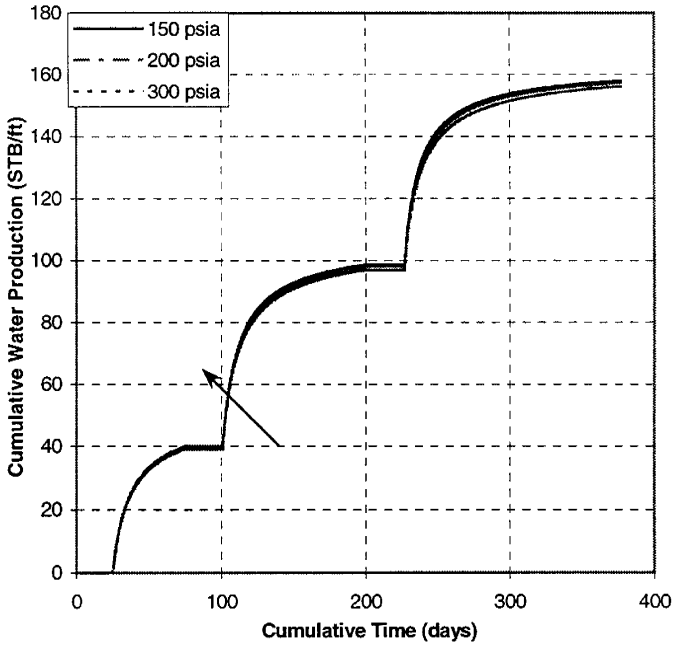
150 psia
200 psia
300 psia
Cumulative Water Production (STB/ft)
Cumulative Time (days)
0
20
40
60
80
100
120
140
160
180
0
100
200
300
400

8(c)

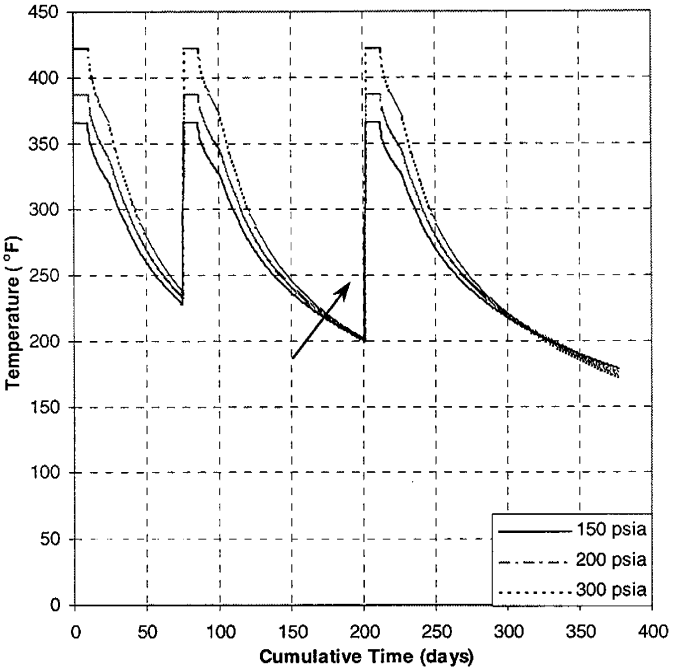

8(d)

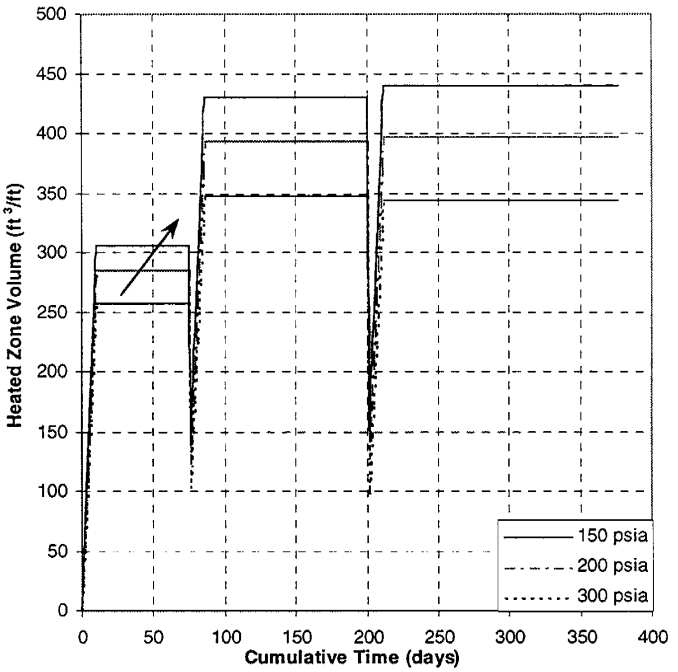

Fig.8 Sensitivity to bottom-hole pressure: (a) cumulative oil production versus cumulative time, (b) cumulative water production versus cumulative time, (c) average steam zone temperature versus cumulative time, (d) steam zone volume versus cumulative time

9(a)

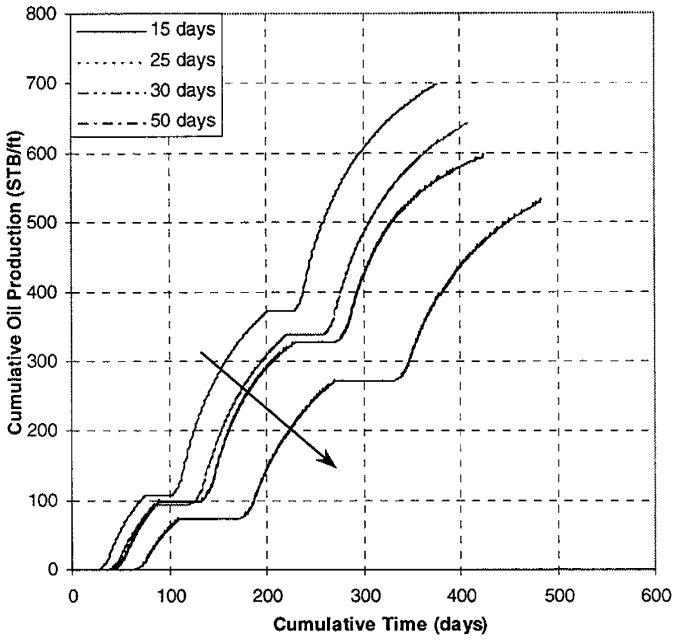

9(b)

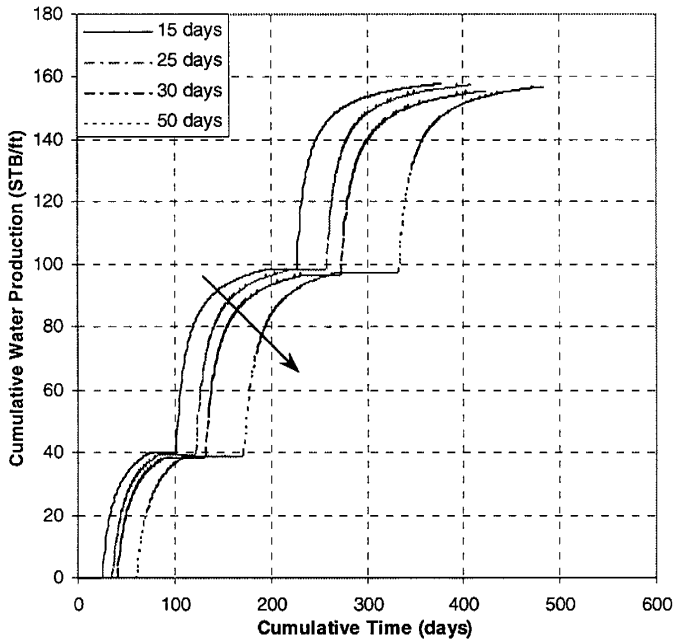

Fig.9 Sensitivity to soaking interval: (a) cumulative oil production versus cumulative time (b) cumulative water production versus cumulative time

Appendix A

Derivation for calculating f_{HD}

The heat transfer model for conduction cooling of the heated zone can be solved for the horizontal and vertical conduction mechanisms. We have solved the horizontal heat transfer mechanism problem. When conduction occurs as described, the temperature at any point within the heated geometry can be expressed as the product:

$$v = V v_x v_z$$
$$V = T_s - T_R \tag{A-1}$$

where, v_x and v_z are unit solutions of component conduction problems in the x and z directions, respectively. Similarly, an integrated average temperature for the heated regions may be computed as:

$$\bar{v} = V \bar{v}_x \bar{v}_z \tag{A-2}$$

The average unit solution for $\bar{v}_x$ is obtained by solving the one-dimensional heat conduction problem in the horizontal direction:

$$\alpha \frac{\partial^2 v_x}{\partial x^2} = \frac{\partial v_x}{\partial t} \tag{A-3}$$

Initial and Boundary conditions:

1. $v_x = 1$; $t = t_{init}$; $0 < x < a$
2. $v_x = 0$; $t = t_{init}$; $|x| > a$
3. $v_x = 0$; $t \geq t_{init}$; $x \rightarrow \infty$
4.

Carlslaw and Jaeger have given the solution for the problem at hand with the boundary condition specified as:

$$v_x = \frac{1}{2}\left\{ erfc\left(\frac{a-x}{2\sqrt{\alpha t}}\right) + erfc\left(\frac{a+x}{2\sqrt{\alpha t}}\right)\right\} \tag{A-4}$$

This solution holds at any vertical distance ' y ' upwards from the horizontal well as shown in the figure. To find the average $\bar{v}_x$ over the entire triangular heated area, we have,

$$\bar{v}_x = \frac{\int_0^A v_x dA}{\int_0^A dA} \tag{A-5}$$

If we take an elementary strip parallel to the x-axis, we will be integrating the given function with respect to x. The ends of this strip are bounded by the lines $x = (b/h_t).y$ and $x = -(b/h_t).y$; so that

these are the limits of integration with respect to x. Next, we integrate with respect to y from y = 0 to y = h_t. This, therefore, covers the whole area of the triangle.
Thus, the integral reduces to:

$$\overline{V}_x = \frac{\int_{-\frac{b}{h_t}y}^{\frac{b}{h_t}y}\int_0^{h_t} v_x dxdy}{\int_{-\frac{b}{h_t}y}^{\frac{b}{h_t}y}\int_0^{h_t} dxdy} \tag{A-6}$$

The final integration result is:

$$\overline{V}_x = \frac{1}{2} + \sqrt{\frac{t_{DH}}{\pi}}\left\{-2.0 + \exp\left(-\frac{1}{t_{DH}}\right)\right\} + erf\left(\frac{1}{\sqrt{t_{DH}}}\right)\left\{\left(\frac{2}{\sqrt{\pi}} - 1\right)t_{DH} + \frac{1}{2}\right\} \tag{A-7}$$

where,

$$t_{DH} = \frac{\alpha\left(t - t_{inj}\right)}{R_h^2} \tag{A-8}$$

R_h is the horizontal range of the extent of the steam zone and is given by,

$$R_h = h_t \cot(\theta) \tag{A-9}$$

5.1 A COMPARISON OF MASS RATE AND STEAM QUALITY REDUCTIONS TO OPTIMIZE STEAMFLOOD PERFORMANCE

(Gregory Messner and William Brigham)

Abstract

Many operators of steamdrive projects will reduce the heat injection rate as the project matures. The major benefit of this practice is to reduce the fuel costs and thus extend the economic life of the project. However, there is little industry consensus on whether the heat cuts should take the form of; (1) mass rate reductions while maintaining the same high steam quality, or (2) steam quality decreases while keeping the same mass rate. Through the use of a commercial three-phase, three-dimensional simulator, the oil recovery schedules obtained when reducing the injected steam mass rate or quality with time were compared under a variety of reservoir and operating conditions. The simulator input was validated for Kern River Field conditions by using the guidelines developed by Johnson, *et al.* (1989) for four steamflood projects in Kern River.

The results indicate that for equivalent heat injection rates, decreasing the steam injection mass rate at a constant high quality will yield more economic oil than reducing the steam quality at a constant mass rate. This conclusion is confirmed by a sensitivity analysis which demonstrates the importance of the gravity drainage/steam zone expansion mechanism in a low-pressure, heavy oil steamflood with gravity segregation. Furthermore, the impact of discontinuous silts and nonuniform initial temperatures within the steamflood zone was studied, indicating again that a decreasing mass rate injection strategy is a superior operating practice.

1. Introduction

It is routine to reduce the heat injection rate in a steamflood project as it approaches the economic limit. The major benefit of this practice is to reduce the fuel costs and thus extend the economic life of the project. Furthermore, there is evidence that frequent reductions in the heat injection rate are both theoretically sound and economically advantageous in steamflooding operations (Vogel, 1984). There are two general approaches to accomplishing these reductions: (1) cutting the mas rate of the injected steam while maintaining the same high quality; and (2) reducing the steam quality while keeping the same rate. Interestingly, there appears to be no industry consensus on which heat reduction process should be applied under a given set of reservoir conditions, and operators will often follow different steam injection rate or quality strategies within the same field.

The purpose of this study is to examine the recovery consequences of reducing mass rates or steam qualities using a thermal reservoir simulation program. In addition to the insights gained, it was hoped that general guidelines could be developed which would help determine which heat reduction scheme should be applied under a given set of steamflood conditions.

2. Literature Review

Several investigators have studied the effect of varying the heat injection rate with time in thermal recovery projects. Chu and Trimble (1975) conducted a reservoir simulation study using a three-dimensional, three-phase numerical model (Coats, *et al.*, 1974). After history matching the oil recovery performance for a single pattern in the Kern River Field, they investigated the influence of varying the steam injection schedule. By using the concept of cumulative discounted net oil (CDNO) as the optimizing criterion, they found that the economic performance of a steamflood could be improved over the constant rate injection case by increasing the initial steam rate and then decreasing the steam rate with time. In all these cases, the steam quality was held constant at 70%. While they mentioned that further work was needed to determine the optimal variations of steam rates, a hyperbolic decline was superior to a linear variation. They also concluded that the improvements increased with sand thickness.

The work of Vogel (1984) provides a more theoretical foundation for placing the Chu and Trimble results in perspective. By assuming that steam override is instantaneous, he derived an analytical descending steam chest model using the equations for linear heat flow from an infinite plane. Inspection of his equations showed that the heat rate requirements in a steamflood should start high and then decline with time. Figure 1, reproduced from Vogel's paper, illustrates typical steam injection rate requirements using his method. These steam requirements decline in a somewhat hyperbolic manner. Although not explicitly expressed, Vogel appeared to assume that mass rates rather than steam qualities should be cut, because the key to his method involved estimating the rate of downward growth of the steam zone.

In a similar study, Neuman (1985) developed equations to predict steamflood performance with steam override. His approach enabled calculation of steam zone growth, oil displaced, and consequences of reduced heat injection. With these equations, a reasonable match of oil production was made for Chevron's 10-pattern steamflood in the Kern River Field, California (Oglesby, *et al.*, 1982 and Blevins and Billingsley, 1975). Like Vogel, Neuman also showed the benefits of decreased heat injection with time, but he stated that a reduction in steam quality is the preferred method. However, he did not present any field or theoretical evidence to support this assertion.

Other studies have supported reduced injection rates with time in steamfloods. Using scaled physical laboratory models and field data, Myhill and Stegemeier (1978) found that high initial steam injection rates were desirable to promote faster heating around the producers. After breakthrough, however, large amounts of heat were produced, indicating that injection rates should be reduced. Also, from a mathematical heat balance model, they demonstrated that oil-steam ratios were improved with increased steam quality. Farouq Ali and Meldau (1979) expanded upon these findings.

Spivak and Muscatello (1987) performed a reservoir simulation study of steamflooding in the South Belridge Field, Kern County, California. After peak oil production, they found that tapering the mass injection rate at constant quality, increased the oil-steam ratio over a constant injection rate case. The optimum taper rate was 10% per year. Furthermore, they showed that, for equivalent heat injection, tapering the steam quality was much less effective than tapering the mass rate. However, these comparisons were made for a layered reservoir model with no vertical communication, so steam override was not a factor.

In the field, reduced injection rates have been reported to be successful in several steamflood projects. In Kern River, Bursell and Pittman (1975) saw improved steam-oil ratios resulting from reduced steam injection rates in three steamflood pilots, presumably with steam

at a constant high quality. Ault, *et al.* (1985) also reported economic success in reducing heat injection rates in two Kern River projects, but they accomplished these reductions by cutting the steam quality to approximately 10%.

There seems to be common agreement that the heat injection rate should be reduced with time. However, contradictory evidence exists over whether heat cuts should take the form of reduced rate at constant quality or reduced quality at constant rate. Since fuel consumption is the highest operating cost item in a steamflood, deciding how best to use that fuel is of great importance. The purpose of this work is to answer that question.

3. Methodology

This study relies heavily on a commercial three-phase, three-dimensional thermal simulation program (THERM) developed by Scientific Software-Intercomp (SSI). This program is capable of simulating steamflood, hot waterflood, cyclic steam and in-situ combustion processes and is fully implicit in the pressure, temperature, saturation and concentration terms. All simulation runs used a 9-point finite difference scheme which accurately handles reservoir heterogeneities and unequal grid spacings, and considerably reduces any grid orientation effect (SSI, 1988). All runs were made on a CRAY supercomputer.

For model input, the general guidelines developed for the Kern River Field by Johnson, *et al.* (1989) were incorporated. These include:

1. Kern River oil can be represented by a single-component, non-distillable heavy oil.
2. To induce the rapid steam overlay observed in the field, the vertical transmissibility at the injector is multiplied by 100 until 0.4 pore volumes (PV) of steam are injected.
3. A uniform set of relative permeability curve shapes and endpoints can be used.

Reservoir input data used in all of the following models are listed in Table 1. All cases comparing either mass rate or steam quality reductions have identical heat injection schedules.

One further point should be stressed here. The Johnson, *et al.* (1989) study successfully history matched the performance of high and low quality steamfloods using a uniform set of input guidelines. Not only were oil and water production rates and cumulatives matched; but also satisfactory predictions were achieved for steam breakthrough times, oil saturation profiles and temperature profiles. Successful history matching of several types of field data reduces the problem of non-uniqueness and indicates that the model is properly simulating the recovery mechanisms in low-pressure, heavy oil steamfloods. In a similar vein, this study will use several different operating scenarios and initial reservoir conditions to arrive at general conclusions regarding the preference of rate or quality reductions.

4. Discussion of Results

Several different types of reservoir settings and production schemes were studied to assess their effects on the economics of heat reduction operations. Each of these will be discussed in some detail.

4.1 One-Eighth of a Five-Spot Model

The first segment of this study involved using a one-eighth pattern element of symmetry to model a five-spot steamflood configuration. A $7 \times 4 \times 5$ parallel grid (Fig. 2) was set up for two homogeneous sand thicknesses, 40 and 80 feet. Table 2 lists input assumptions for these cases. The first set of runs assumed a 24% heat injection rate cut for two timing scenarios: (1) after two years of high quality, constant rate injection; and (2) at the high quality, constant rate economic limit, which was set to occur at a steam-oil ratio of 10.5. "High quality" in these cases means 52.5% of the steam mass is vapor at the sandface, a good average for Kern River operations. Key results from these simulation runs are shown in Figs. 3 and 4.

In brief, the recovery results for the 40 ft. reservoirs show that rate cuts at constant quality are superior to quality cuts at constant rate, no matter when the reduction in heat rate begins. Clearly comparing Figs. 3 and 4, it is better to start heat reduction sooner. The resulting total recoveries are about the same, but the operating costs would be significantly less.

For the 80 ft. reservoir case, the recoveries are also better for rate reduction compared to quality reduction. But clearly these differences are minor. In terms of practicality, we should recognize that we seldom see steam floods in sands that have as much as 80 ft. of homogeneous section. Later results will include cases where the systems are not homogeneous, but first we will discuss the effects of assumed relative permeability relationships and residual oil saturations.

4.2 Recovery Mechanisms and Sensitivity to Residual Oil Saturation and Relative Permeability Assumptions

From examining these simulation runs, it is clear that tapering mass rates promotes more rapid steam zone expansion. For example, in the 40 ft. example, the average steam saturation in the entire reservoir was 9.7% at the end of four years in the rate cut case. This is 34% higher than the quality cut case (7.1%). Furthermore, the rate case had 10% greater volumetric sweep of the steam zone.

These differences in steam zone expansion rates should be expected, since more steam vapor is injected in the rate cut case. However, the oil recovery differences suggest that steam zone expansion/gravity drainage is a more efficient recovery mechanism than hot water displacement. Looking at our input data, this idea is reasonable, given that at 225°F the residual oil saturation to liquid water (S_{orw}) is assumed to be 0.233, while the residual oil saturation to steam vapor (S_{org}) is only 0.05. These endpoint residual oil saturation (ROS) assumptions are extremely important in determining whether to reduce steam mass rates or qualities.

Since economic limits are built into the recovery comparisons, the shapes of the relative permeability curves should also have some influence on the recovery efficiencies. Changing the shapes and endpoints of these curves did have some effect on the results. The endpoint effect was the stronger of the two.

4.3 Validity of ROS and Relative Permeability Input Assumptions

A key factor influencing the recovery comparisons is the residual oil saturation to water and steam vapor. The ROS endpoint values used here are the same as those used by Johnson *et al.* (1989). The S_{orw} values were based on laboratory coreflood experiments, and the S_{org} endpoints were determined from both post-steamflood coring and laboratory corefloods. The low ROS to steam (0.05 PV) agrees with field results presented by other authors (Bursell and Pittman, 1975; and Blevins and Billingsley, 1975).

There are two major mechanisms by which steam vapor reduces oil saturation to very low values: (1) distillation, and (2) three-phase film flow with gravity (Hirasaki, 1989). These two phenomena were visually observed by Bruining, *et al.* (1984) during gravity-stable coreflood experiments. For longer flood times their residual oil saturations were below 0.10. These studies explain the low ROS's observed in steam-swept field cores, and tend to validate the S_{org} endpoint values used herein.

As previously mentioned, the S_{orw} endpoints were determined from laboratory measurements (Johnson, *et al.*, 1989). For 225°F, the S_{orw} averaged 0.234, but the laboratory measurement scatter was significant. Other experimental work discussed by Prats (1982, Chapter 6) indicates that the S_{orw} endpoint at higher temperatures tends to remain above 0.20. Thus the ROS endpoints to hot water used in this study appear to be realistic.

The relative permeability curves used in any reservoir simulation study are always subject to question, as recently explained by Saleri and Toronyi (1988). However, the chosen curves have been successfully used in history matching several steamflood projects (Johnson, *et al.*, 1989) and thus are within a reasonable uncertainty range.

In summary, the input assumptions which have the greatest impact on the comparison of rate and quality cuts, i.e., the ROS endpoints and the oil relative permeability curve to water, are considered to be quite reasonable. Thus, the conclusions regarding rate and quality reductions, appear to be valid. The behavior is consistent with observations by Vogel (1984) and Myhill and Stegemeier (1978). The primary recovery mechanism after steam breakthrough, is downward steam zone expansion with gravity drainage of heated oil. Cutting the rate but keeping the steam quality high will promote this effect. Cutting steam quality, and maintaining rate, depends on less efficient hot water displacement.

4.4 Multiple Pattern Model

In the previous model, it was implicitly assumed that all fluid flow was confined within the five-spot pattern. In an actual steamflood project, there will usually be some inter-pattern communication. For example, in the Kern River 10-pattern steamflood pilot, approximately 10% of the increased production came from hot production wells outside of the original project area (Blevins and Billingsley, 1975). Thus a multiple pattern model was constructed to incorporate asymmetric conditions. With less pattern confinement, it was thought that the recovery mechanisms identified in the confined model, might change in their relative importance.

The multiple pattern model consisted of a $16 \times 16 \times 3$ triangular grid representing one-eighth of 50 patterns covering 125 acres in a 60 ft. sand, and is similar to the model set-up described by Chu (1987). The reservoir conditions were identical to those of the single pattern model, except that the grid thicknesses were now 9, 18 and 33 ft, from top to bottom, with the injection wells completed only in the bottom layer. To initialize asymmetrical conditions the

exterior 34 patterns were steamflooded for six years while the interior 16 patterns remained idle (Fig. 5). After steam stimulating the interior producers (Wells 1, 2 and 7), a steamflood was started in the interior 16 patterns, with steam injection rates of 331 BPD/well.

First, a test case of constant rate injection was run, and immediately apparent was the low oil recovery in the multiple pattern flood. Recovery was 48,000 bbl/pattern compared with 88,000 bbl from the single pattern after five years. Nevertheless, several years of economic oil production were attained in this model set-up. Figure 6 illustrates the oil recovery versus time for tapering the mass rates and steam qualities at two different decline rates. It is apparent that tapering the rate is significantly better than tapering the quality.

Interestingly, the recovery differences between the rate and quality cases are more pronounced than those in the confined model. At least part of this effect is due to the lower pressures in the multipattern model, which allow more steam zone expansion.

4.5 Comparison of Rate and Quality Reductions in Silty Sands

Both the single and multiple pattern models discussed so far have assumed homogeneous rock properties for the entire flood area. However, most steamflood projects are conducted in reservoirs with some degree of heterogeneity. For example, several Kern River steamfloods have been shown to have discontinuous shale layers within the displacement interval (Bursell and Pittman, 1975; and Blevins and Billingsley, 1975).

For this segment of the study, a $7 \times 4 \times 7$ grid was used to model one-eighth of a 2.5 acre, 60 ft. thick pattern. Input data are listed in Table 3. The presence of silts was simulated by altering the vertical fluid transmissibilities to correspond to a 2 ft. thick, 5 millidarcy shale layer. The first set of runs assumed one silt interbedded between grid layers 4 and 5, corresponding to a position 24 ft. below the top of the formation. Also, no shale was placed in the vicinity of the injection well, as illustrated in Fig. 7. This was done to create the maximum opportunity for steam override above the silt layer, as might result from a poor quality cement bond in the injector, and thus counteract the rate cut's main advantage seen in the clean sand cases: the downward steam zone expansion/gravity drainage recovery mechanism.

Figure 8 shows oil recovery vs. time for 10% and 30% per year taper rates beginning at 548 days into the project. Instead of the modest differences in recovery seen in Fig. 4, the mass rate reductions recover far more economic oil. Furthermore both the 10% and 30% per year taper cases are still producing economically after eight years of steamflooding, with a recovery over 60% of the OOIP indicated for the 10% case. The oil recoveries are well above those in the clean sand model. The reasons for these results will be discussed later.

For the second discontinuous silt model, three silt interbeds were placed in positions corresponding to 9, 24, and 48 ft. from the top of the 60 ft.. thick sand. The areal extent of the silts was assigned using a random number generator (Figs. 9-11). Like the one silt case, Fig. 12 shows that mass rate cuts are far more efficient in this model. Again, high economic oil recoveries are indicated.

These high recoveries need further discussion. Comparing Figs. 8 and 12 with Fig. 4, it is apparent that the sand/silt models recover significantly more oil than the homogeneous sand case. The saturation and temperature distributions show that the silt layers improve the vertical sweep of the steamflood by trapping steam below them. Figure 13 illustrates this phenomenon for the one silt model. On this cross-section, an additional steam zone lies under

the silt layer. Thus, the silt layers accelerate the downward heating of the formation and extend the economic production time. Furthermore, high steam quality promotes this effect.

4.6 Preheated Reservoir Sands

Restine (1983) has pointed out that the productive section of the Kern River Field consists of a sequence of sands averaging 60 ft. in thickness and separated by continuous silt or clay layers. While these shaly layers may be impermeable to steam, the sands immediately above a steamflooded interval are heated by conduction. Restine discussed field results and simulation work, and he concluded that this preheating effect of upper sands is an important consideration in a steamflood operation.

To see the impact of reservoir preheating on the comparison of rate and quality cuts, a one-eighth pattern model with a $7 \times 4 \times 7$ grid was again used to simulate a steamflood in a 60 ft. thick sand. The reservoir conditions were identical to the discontinuous silts model (Table 3) except that the initial reservoir temperature varied with depth. This temperature relationship is illustrated in Fig. 14 and is similar to the field data presented by Restine (1983).

Table 4 summarizes the production results for clean and silty sand cases, and we see again that for the equivalent heat injection rate, one should cut the mass rate at constant quality. Note, however, that while the 30% per year tapers show large differences between rate and quality reductions, the 10% rate decreases yielded only modest inprovement (3-6% of OOIP). It is likely that the 10% rate cases were relatively overinjected with heat. Evidence of overinjection can be seen in the almost identical final oil recoveries for the 10% and 30% cases.

Another interesting result is the high ultimate oil recoveries seen in the clean sand cases with tapered injection rates. In the last section it was noted that the presence of discontinuous silts could increase recovery, in sands of uniform temperature, by hindering the gravity override of the steam and thus accelerating the downward heating of the formation. However, when a zone has already been heated by underlying conduction, this effect is minor; in fact, discontinuous silts in preheated sand steamfloods could actually reduce oil recovery by hindering gravity drainage due to reduced vertical permeabilities. This concept is suggested in the Table 4 data, where the clean sands produced slightly more oil than the silty sand cases when the mass rates were tapered.

5. Conclusions

Under a variety of reservoir and operating conditions, the oil recovery consequences of reducing the injected steam mass rate or quality with time have been compared with the help of a thermal simulator. Examination of the simulation results combined with the literature review leads us to the following conclusions:

1. Under the conditions assumed in this study, declining the steam injection mass rate at a constant high quality will recover more economic oil than reducing the steam quality at a constant mass rate. This result assumes equivalent heat injection for the two cases.
2. This constant steam quality strategy agrees with some researchers' observations that in heavy oil, low-pressure steamfloods with gravity segregation, the dominant recovery mechanism is gravity drainage of heated oil accompanied by downward steam zone expansion. High steam quality will promote this effect more than reducing steam quality, which depends on the less effective hot water displacement.

3. Based on cumulative discounted net oil (CDNO), steam injection should start at a high rate than taper with time for the most economic operating strategy. This observation is consistent with the results of Chu and Trimble (1975) and Vogel (1984).
4. Discontinuous silts within an otherwise uniform interval can enhance oil recovery by accelerating the downward heating of the formation. Furthermore, a reduced mass rate approach will be far superior to reducing the quality under these reservoir conditions.
5. If a reservoir sand has been preheated by an underlying steamflood, steam injection rate cuts with time appear to be even more effective than the same strategy in non-preheated reservoirs.

Recommendations

These general conclusions do not answer the question of the best strategy for a given reservoir. The question is: "When should rate reductions occur, and at what decline rate?" Clearly this question can only be answered by making runs for the specific field case of interest. Such calculations would be quite important economically.

Nomenclature

CDNO	=	Cumulative discounted net oil, bbl
CWE	=	Cold water equivalent volume of steam
k_{rg}	=	Gas relative permeability, dimensionless
$(k_{rg})_{ro}$	=	Gas (steam) relative permeability at residual oil saturation, dimensionless
$(k_{ro})_{iw}$	=	Oil relativbe permeability at irreducible water saturation, dimensionless
k_{rog}	=	Oil relative permeability in a gas (steam/oil system, dimensionless
k_{row}	=	Oil relative permeability in a gas (steam/oil system, dimensionless
k_{rw}	=	Water relative permeability, dimensionless
$(k_{rw})_{ro}$	=	Water relative permeability at residual oil saturation, dimensionless
n_g	=	Exponent for gas relative permeability calculation, dimensionless
n_{og}	=	Exponent for oil relative permeability calculation in a gas (steam)/oil system, dimensionless
n_{ow}	=	Exponent for oil relative permeability calculation in a water/oil system, dimensionless
n_w		Exponent for water relative permeability calculation, dimensionelss
OOIP	=	Original oil in place, bbl
ROS	=	Residual oil saturation
S_{iw}	=	Irreducible water saturation, fraction PV
S_{org}	=	Residual oil saturation to steam fraction
S_{orw}	=	Residual oil saturation to steam, fraction pv
T	=	Temperature, degrees Fahrenheit

References

1. Ault, J.W., Johnson, W.M. and Kamilos, G.N.: "Conversion of Mature Steamfloods to Low-Quality Steam and/or Hot-water Injection Projects," SPE 13604, paper presented at the SPE California Regional Meeting, Bakersfield (March 27-29, 1985).
2. Blevins, T.R. and Billingsley, R.H.: "The Ten-Pattern Steamflood, Kern River Field, California," *JPT* (December 1975), 1505-1514.
3. Bruining, J., Dietz, D.N., Heijnen, W.H.P.M., Metselaar, G., Scholten, J.W. and Emke, A.: "Enhancement of Distillation Effects During Steamflooding of Heavy Oil Reservoirs," Proceedings of the Second E.C. Symposium, Luxembourg (December 5-7, 1984).
4. Bursell, C.G. and Pittman, G.M.: "Performance of Steam Displacement in the Kern River Field," *JPT* (August 1975) 997-1004.
5. Coats, K.H., George, W.D., Chu, C. and Marcum, B.E.: "Three-Dimensional Simulation of Steamflooding," *SPEJ* (December 1974) 573-592.
6. Chu, C.: "Examination of the Confined-Pattern Concept in Steamflood Simulation," *SPERE* (November 1987) 559-564.
7. Chu, C. and Trimble, A.E.: "Numerical Simulation of Steam Displacement - Field Performance Applications," *JPT* (June 1975), 765-776.
8. Farouq Ali, S.M. and Meldau, R.F.: "Current Steamflood Technology," *JPT* (October 1979) 1332-1342.
9. Hirasaki, G.J.: "The Steam-Foam Process," *JPT* (May 1989), 449-456.
10. Johnson, R.S., Chu, C., Mioms, D.S. and Haney, K.L.: "History Matching of High- and Low-Quality Steamfloods in Kern River Field, California," SPE 18768, paper presented at the SPE California Regional Meeting, Bakersfield (April 5-7, 1989).
11. Myhill, N.A. and Stegemeier, G.L.: "Steam Drive Correlation and Prediction," *JPT* (February 1978), 173-182.
12. Neuman, C.H.: "A Gravity Override Model of Steamdrive," *JPT* (January 1985) 163-169.
13. Oglesby, K.D., Blevins, T.R., Rogers, E.E. and Johnson, W.M.: "Status of the 10-Pattern Steamflood, Kern River Field, California," *JPT* (October 1982) 2251-2257.
14. Prats, M.: Thermal Recovery. SPE Monograph Vol. 7, SPE OF AIME, New York (1982).
15. Restine, J.L.: "Effect of Preheating on Kern River Field Steam Drive," *JPT* (March 1983) 523-529.
16. Saleri, N.G. and Toronyi, R.M.: "Engineering Control in Reservoir Simulation: Part I," SPE 18305, paper presented at the 63rd SPE Annual Technical Meeting, Houston (October 2-5, 1988).
17. SSI: THERM User's Manual, Release 2.4. Scientific Software-Intercomp (1988).
18. Spivak, A. and Muscatello, J.A.: "Steamdrive Performance in a Layered Reservoir - A Simulation Sensitivity Study," *SPERE* (August 1987) 324-334.
19. Vogel, J.V.: "Simplified Heat Calculations for Steamfloods," *JPT* (July 1984) 1127-1136.

Acknowledgements

Financial aid for this work was provided by Department of Energy Grant DE-FG22-96BC-14994 and by SUPRI-A Industrial Affiliates. This support is gratefully acknowledged. We also thank Texaco for permission to publish the data in this report.

TABLE 1

RESERVOIR DATA USED IN ALL SIMULATION RUNS

20.

Reservoir Description

Rock heat capacity, Btu/ft^3-°F	35.0
Rock thermal conductivity, Btu/ft-D-°F	25.6
Overburden heat capacity, Btu/ft^3-°F	39.0
Overburden thermal conductivity, Btu/ft-D-°F	27.6
Rock compressibility, psi^{-1}	0.000735
Initial pressure at top of reservoir, psia	40

Oil Properties

Heat capacity, Btu/lbm-°F	.50
Thermal Expansion, °F^{-1}	.00039
Compressibility, psi^{-1}	.5 X 10^{-5}

Relative Permeability Curve Shape and End Point Data (See Appendix A)

n_w = 1.94
n_{ow} = 2.24
n_{og} = 1.20
n_g = 2.58

$(k_{rg})_{ro}$ = 0.46 (all temperatures)

TEMP, °F	S_{iw}	S_{orw}	S_{org}	$(k_{rw})_{ro}$	$(k_{ro})_{iw}$
50	0.515	0.400	0.400	0.0486	0.751
225	0.590	0.234	0.050	0.0558	0.575
400	0.665	0.229	0.050	0.0630	0.400

TABLE 2

RESERVOIR DATA USED IN ONE-EIGHTH PATTERN MODEL

Model and grid	1/8 of 5-spot X x Y x Z: 7 x 4 x 5	
Vertical Grid Thickness	40′ Sand	80′ Sand
Z = 1	5 ft	5 ft
Z = 2	5 ft	10 ft
Z = 3	10 ft	15 ft
Z = 4	10 ft	20 ft
Z = 5	10 ft	30 ft
Distance between injector and producer, ft	233.35 (2.5 Acre Pattern)	
Initial reservoir temperature °F	85	
Porosity, %	31	
Initial water saturation, %	55	
Initial oil saturation, %	45	
Initial gas saturation, %	-0-	
Horizontal permeability, md	3,000	
Vertical permeability, md	2,700	
Oil viscosity @ 80°F, cp	7,500	
Oil viscosity @ 300°F, cp	8.38	

Injectors completed in the bottom 30′ of zone
Producers completed throughout thickness

P_{wf} = 25 psia

P_{inj} varies according to injectivity
Injected fluid enthalpies set at 366°F

TABLE 3

RESERVOIR DATA USED IN MODEL WITH DISCONTINUOUS SILTS

Model: grid		1/8 of 5-spot pattern 2.5 acres X x Y x Z: 7 x 4 x 7
Distance between injection and producer, ft		233.35
Initial Reservoir Temperature, °F		85
Porosity, %		31.0
Initial Water Saturation, %		55
Initial Oil Saturation, %		45
Initial Gas Saturation, %		0
Horizontal Permeability, md		3500
Vertical Permeability, md		3150
Oil Viscosity, cp	80°F	7175
	300°F	7.40

Vertical Grid Thickness

Z = 1	3′
Z = 2	6′
Z = 3	6′
Z = 4	9′
Z = 5	12′
Z = 6	12′
Z = 7	12′
	60′ Total

Injector completed in bottom 3 layers
Producer completed in all layers

TABLE 4

COMPARISON OF OIL RECOVERIES
FOR TAPERING INJECTION RATES/QUALITIES
IN PREHEATED 60' SANDS

CASE	OIL RECOVERY AT THE E. L., % OOIP	LIFE, YEARS
Clean Sand		
1. 10%/Yr Taper		
Rate	63.4	4.25
Quality	57.4	3.50
2. 30%/Yr Taper		
Rate	63.3	5.75
Quality	46.2	3.00
One Shale		
1. 10%/Yr Taper		
Rate	62.5	3.75
Quality	59.7	3.75
2. 30%/Yr Taper		
Rate	61.8	5.0
Quality	46.7	3.4
3 Random Shales		
1. 10%/Yr Taper		
Rate	61.9	4.0
Quality	58.3	3.75
2. 30%/Yr Taper		
Rate	61.1	5.5
Quality	45.0	3.15

TAPERING INJECTION SCHEDULE
FOR PREHEATED SAND CASES

TIME, DAYS	10%/YR RATE TAPER BPD	10%/YR QUALITY TAPER %	30%/YR RATE TAPER BPD	30%/YR QUALITY TAPER %
0-183	331	52.5	331	52.5
183-548	300	43.885	245	28.59
548-913	271	35.82	182	11.07
913-1278	245	28.59	142.17	0
1278-1643	222	22.20	142.17	0
1643-2008	201	16.36	142.17	0
2008-2373	182	11.08	142.17	0
2373-2738	164	6.07	142.17	0

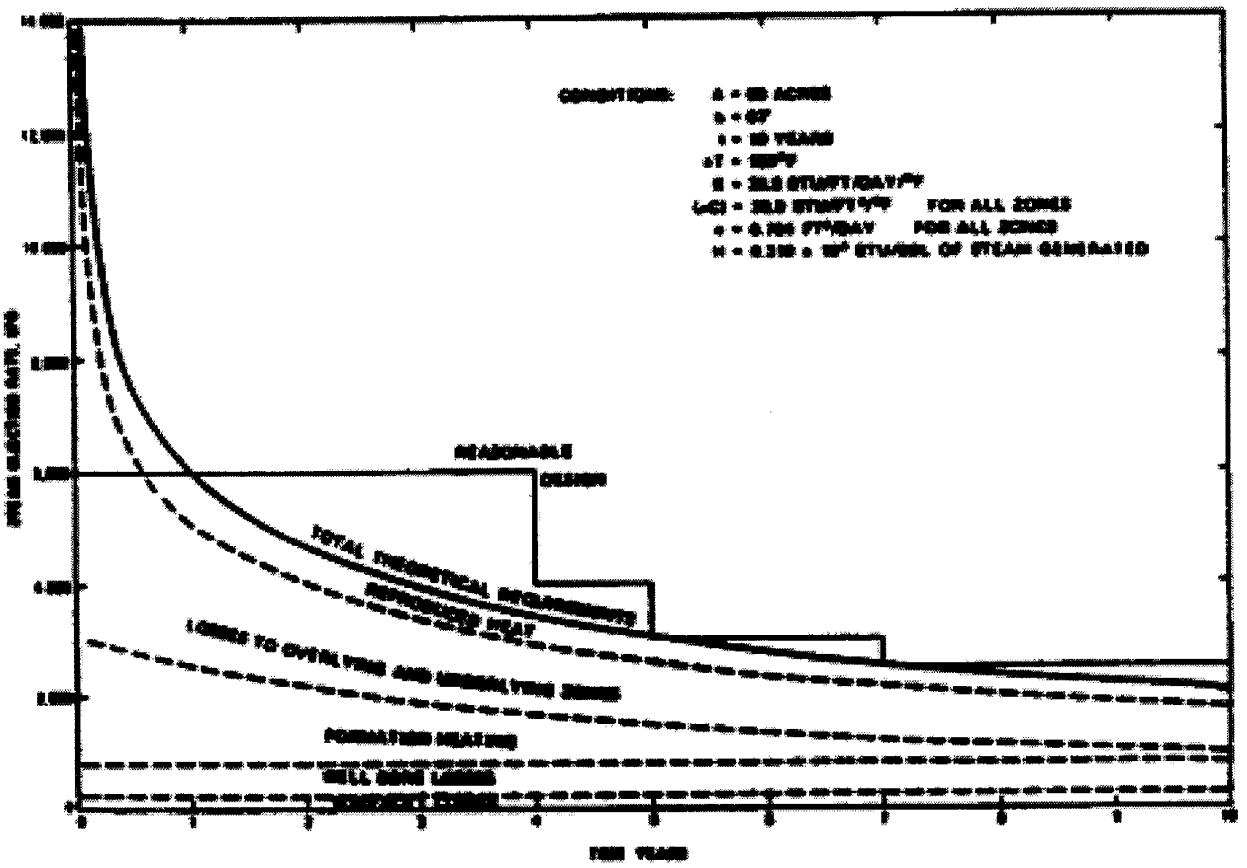

Figure 1. Theoretical steam requirements using planar heat flow model (Vogel, 1984).

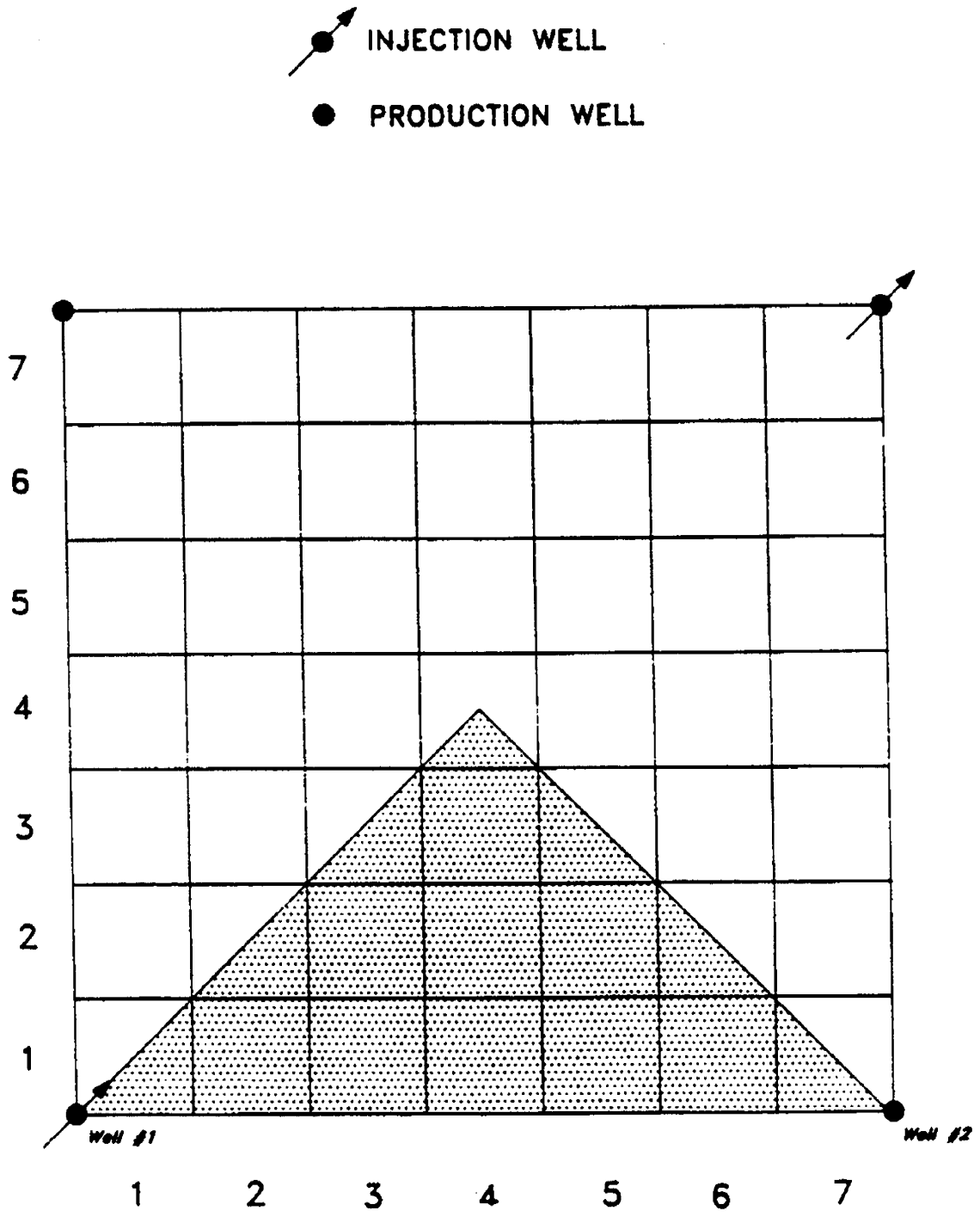

Figure 2. One-eighth of a five-spot pattern, areal view of parallel grid.

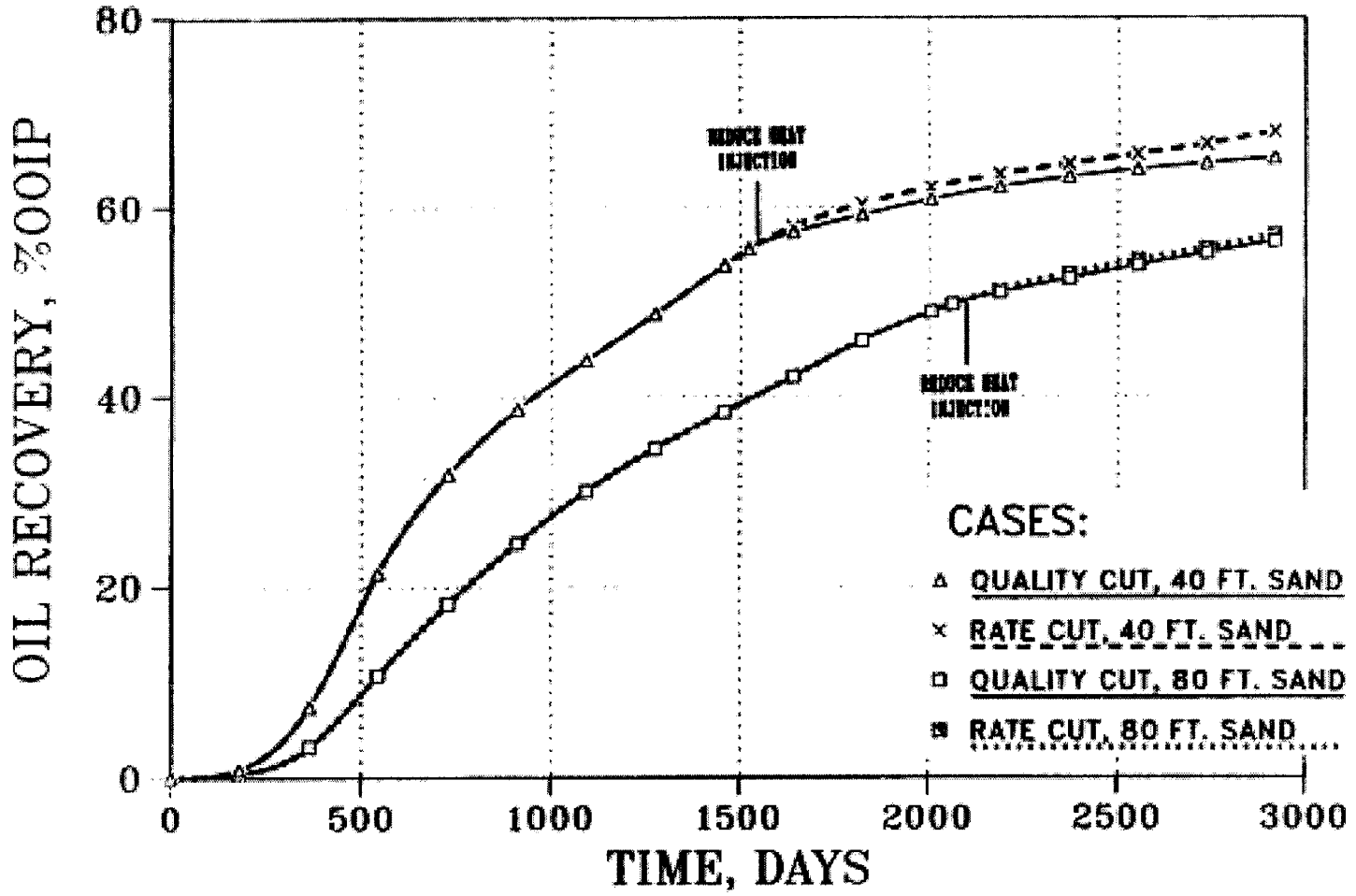

Figure 3. Oil recovery vs. time. One-eighth pattern model. Heat injection reduction at the E.L.

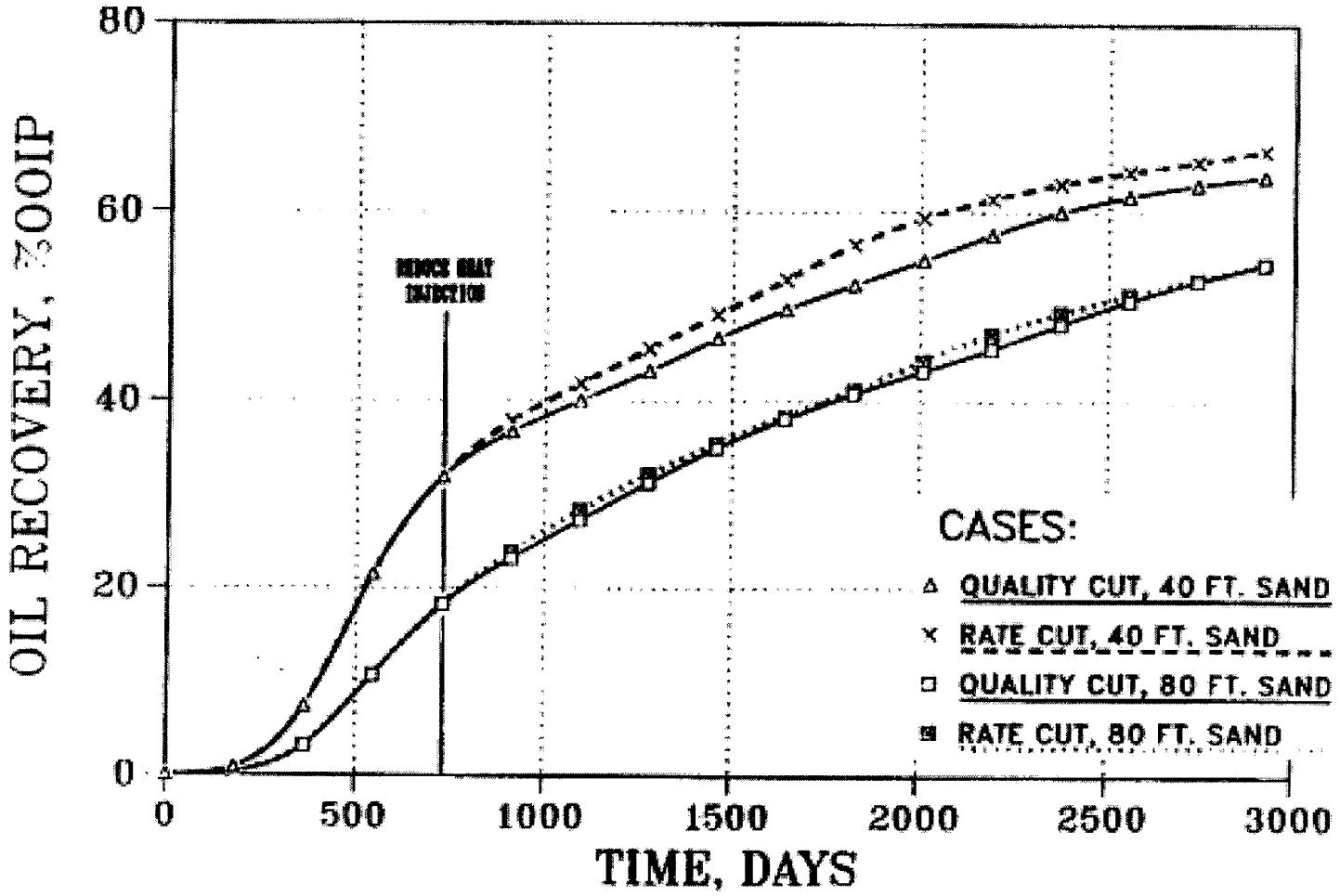

Figure 4. Oil recovery vs. time. One-eighth pattern model. Heat injection in Year 3.

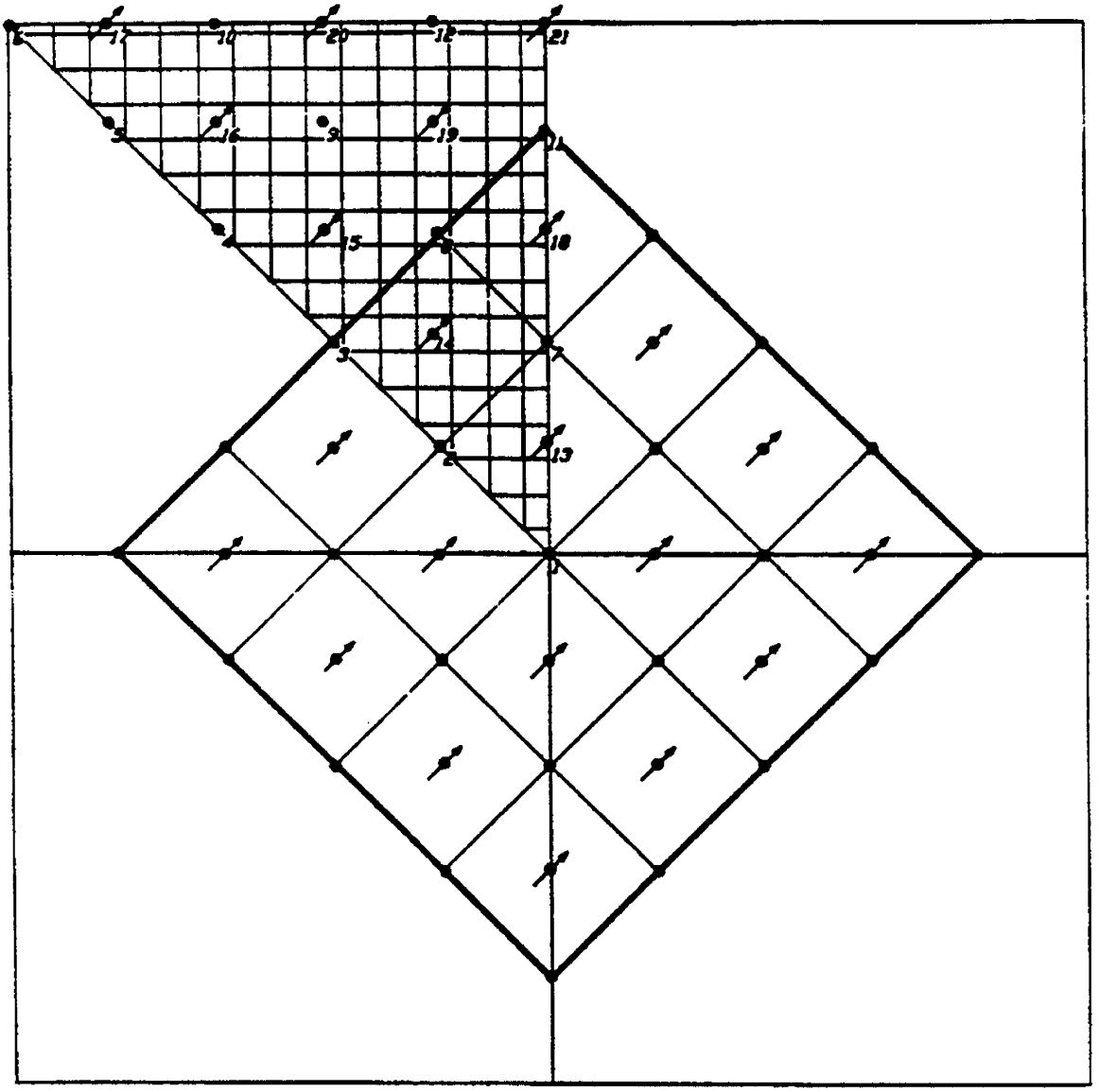

Figure 5. Multipattern model configuration sixteen patterns surrounded by previously steamflooded reservoir.

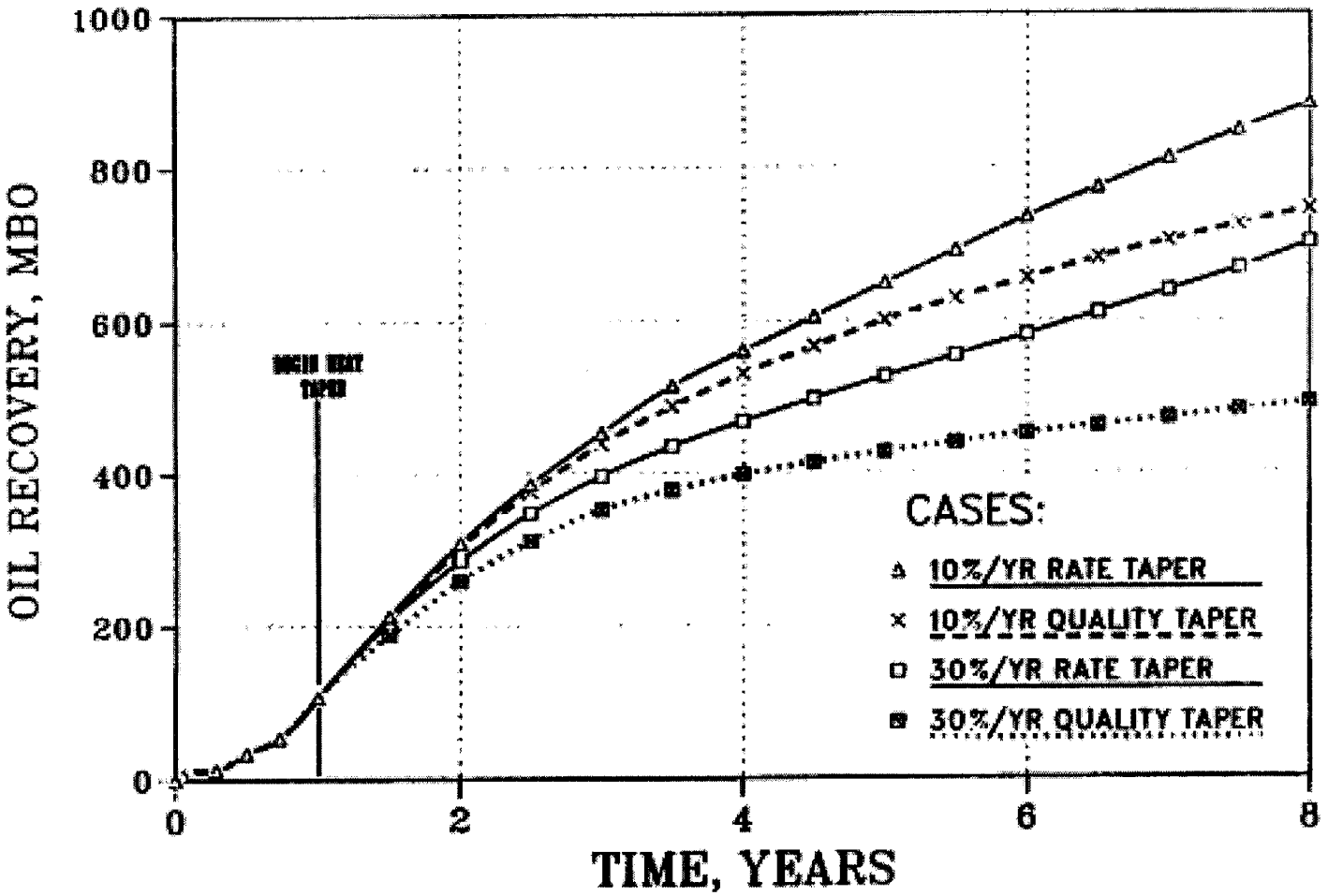

Figure 6. Oil recovery vs. time numerical model -- field case (sixteen) patterns. Heat injection taper starting in Year 2.

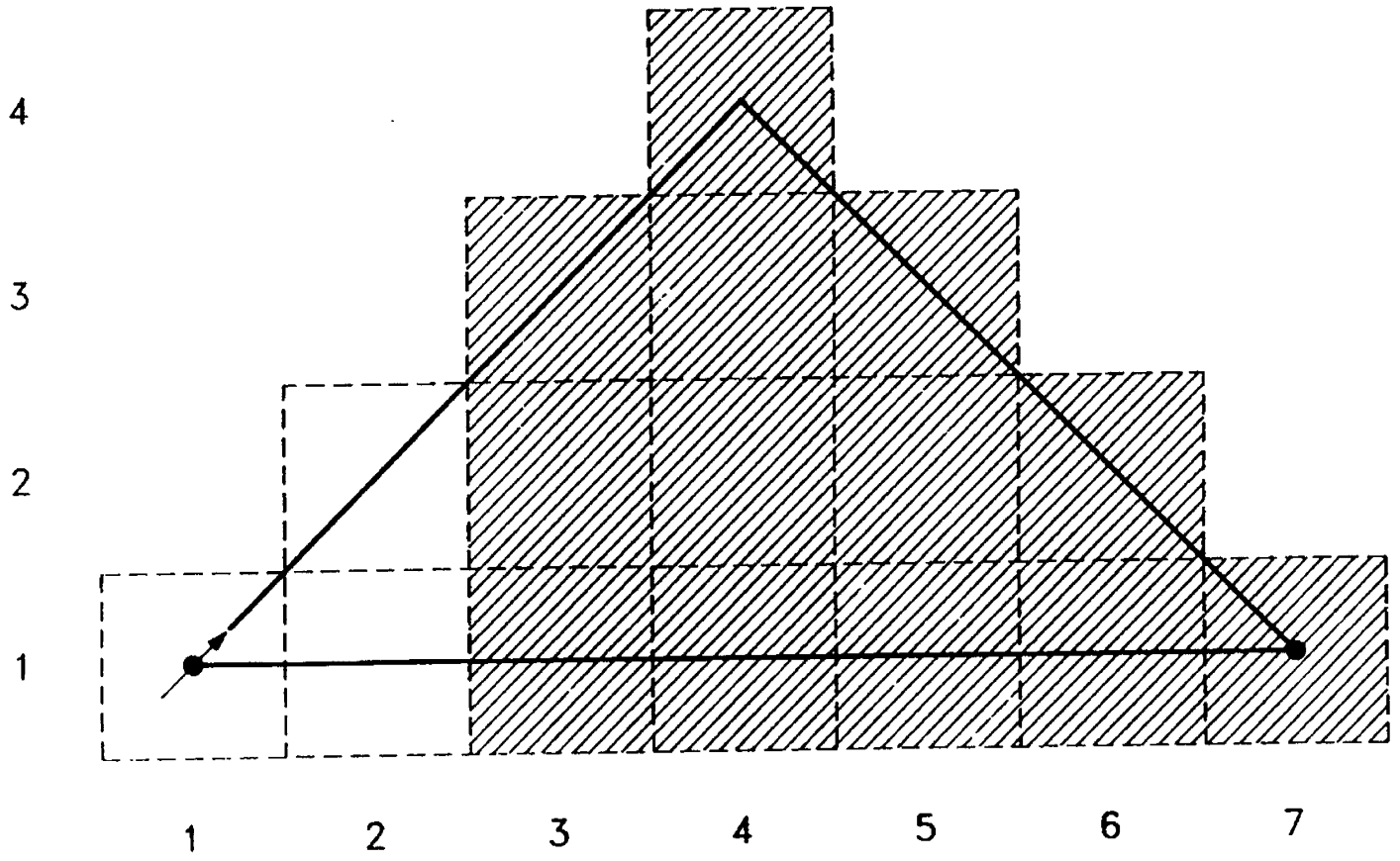

Figure 7. Location of silt between Layers 4 and 5, one silt model (24 ft. from top, 36 ft. from bottom).

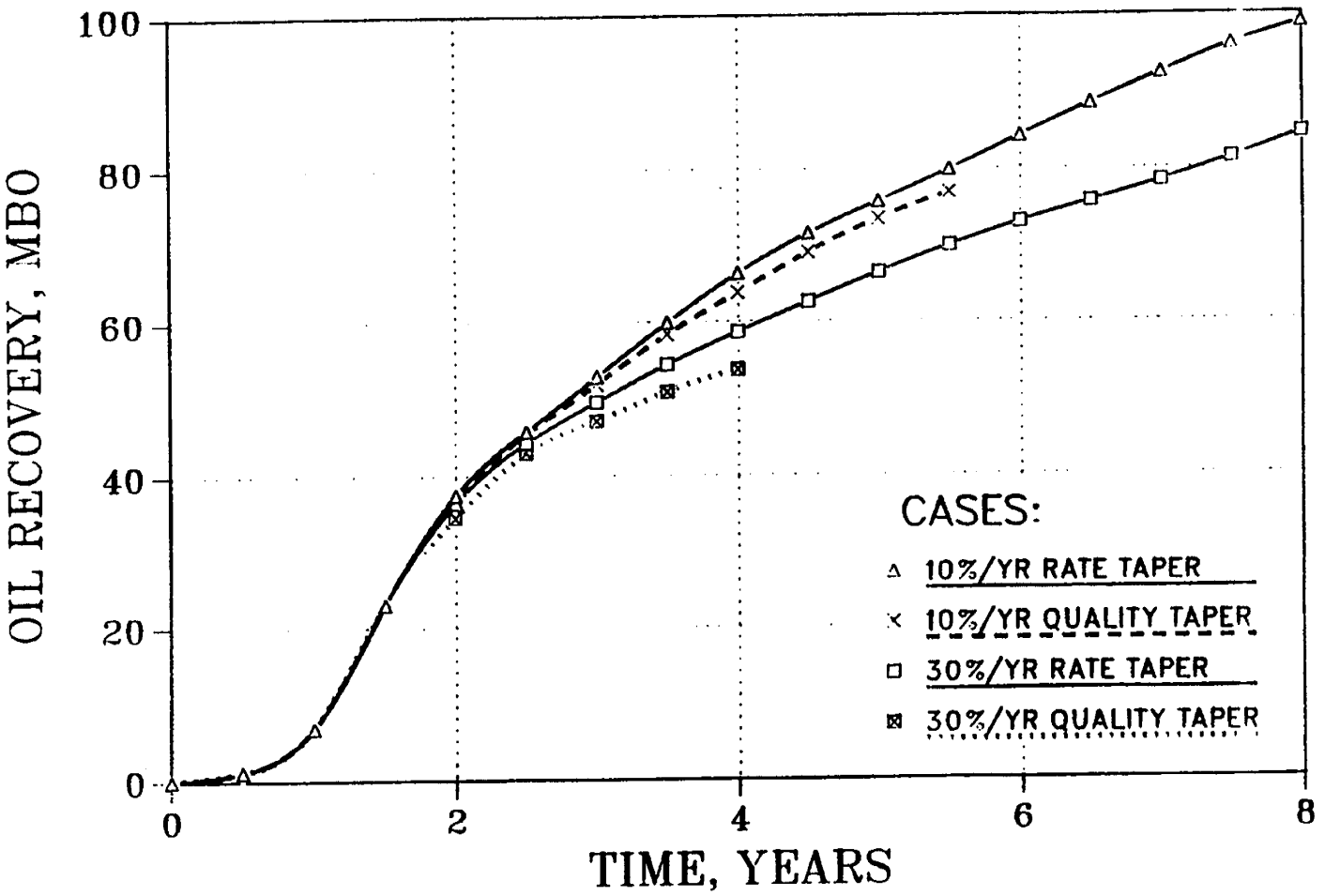

Figure 8. Oil recovery vs. time to the E.L. One-eighth pattern model. Heat injection taper starting at 548 days. One discontinuous silt in the 60 ft. sand.

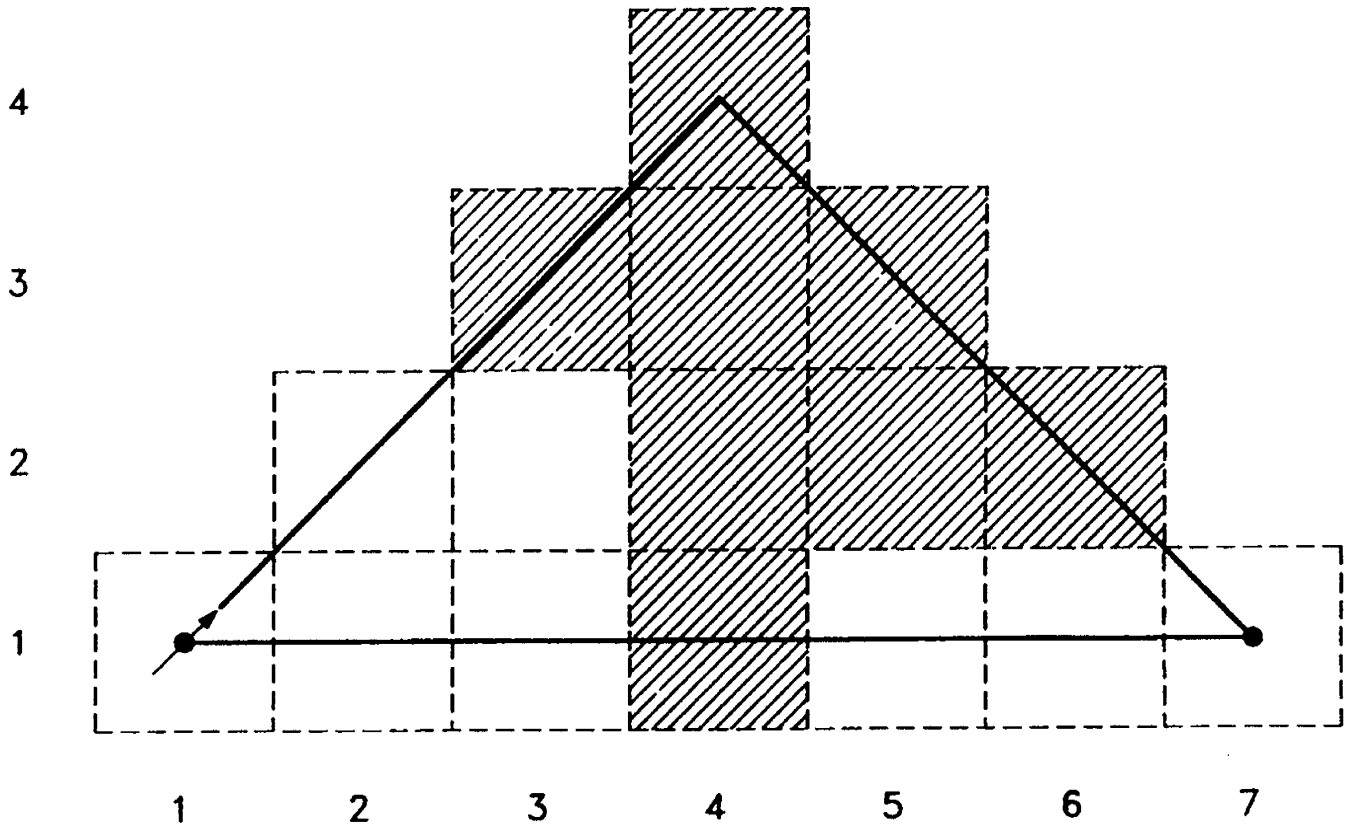

Figure 9. Location of silts between Layers 2 and 3, three-silt model (9 ft. from top).

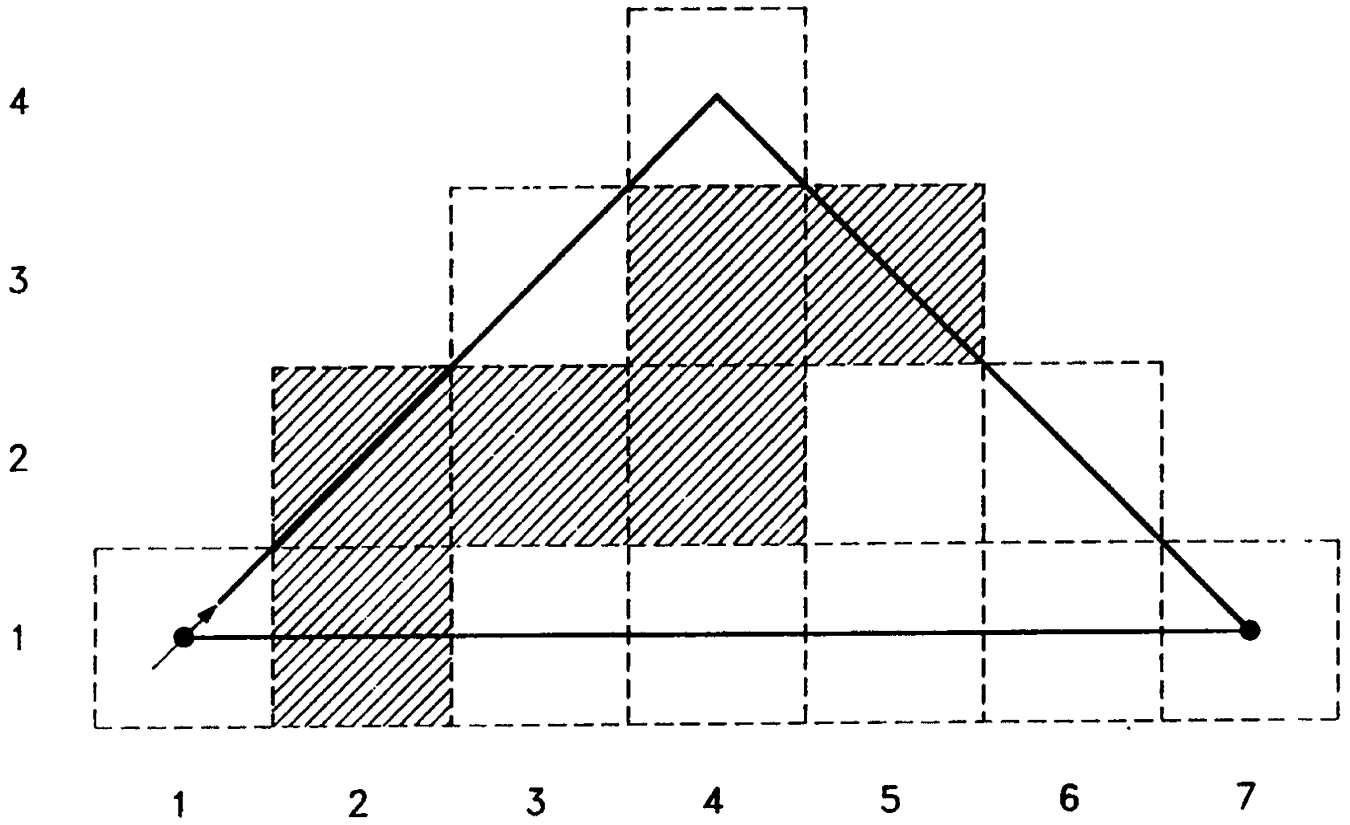

Figure 10. Location of silt between Layers 4 and 5, three-silt model (24 ft. from top).

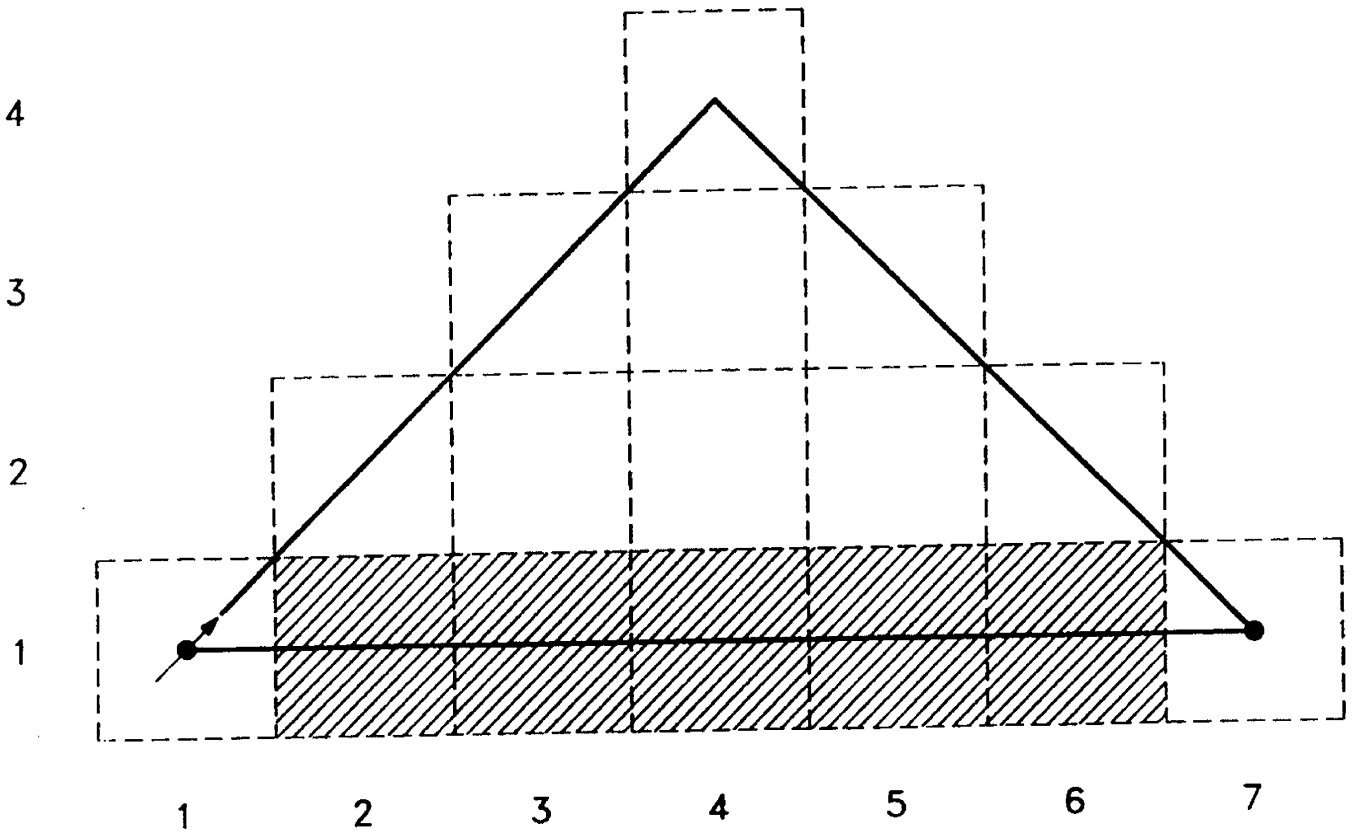

Figure 11. Location of silt between Layers 6 and 7, three-silt model (48 ft. from top).

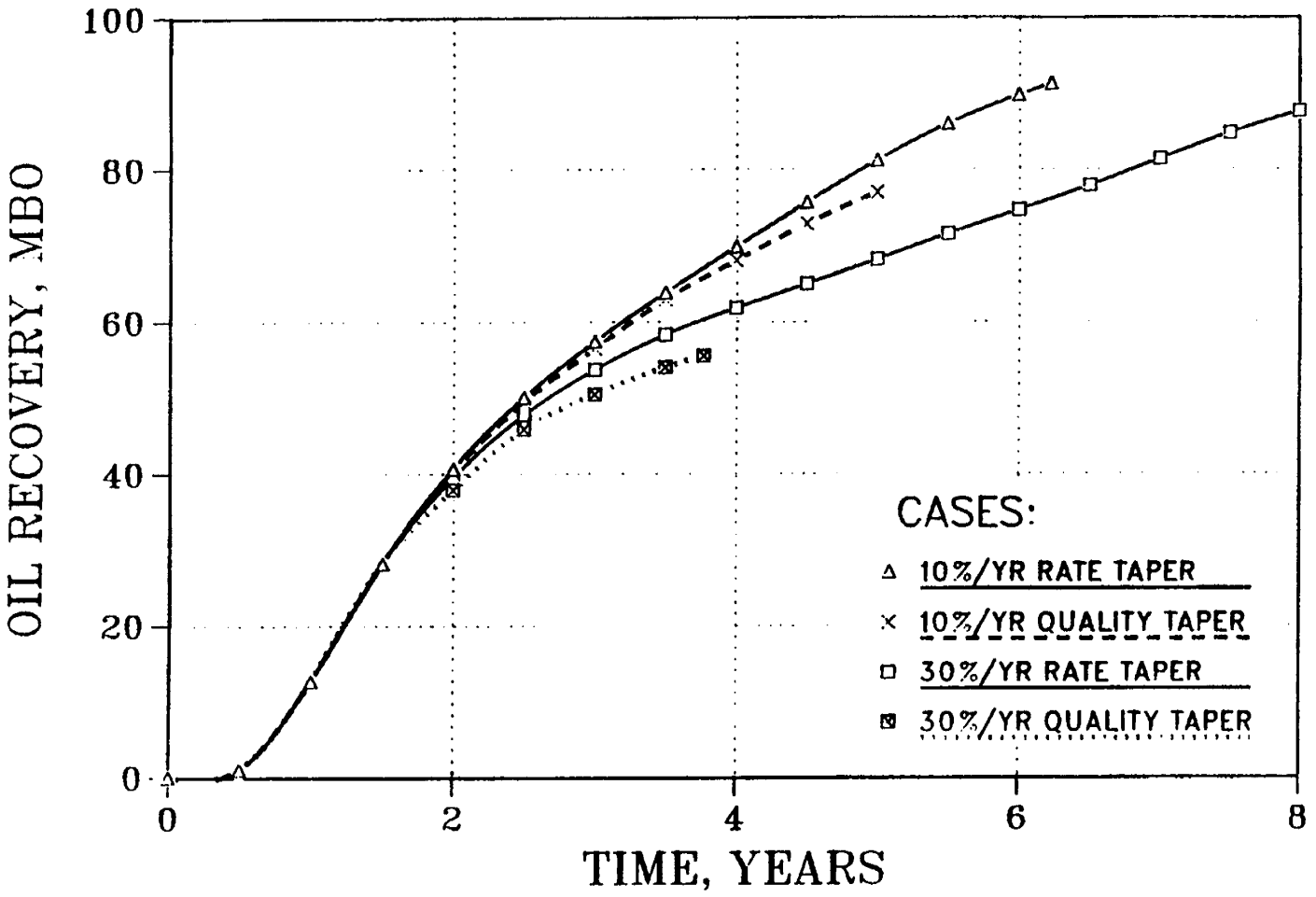

Figure 12. Oil recovery vs. time to the E.L. One-eighth pattern model. Heat injection taper starting at 548 days, 3 random silt layers, 60 ft. sand.

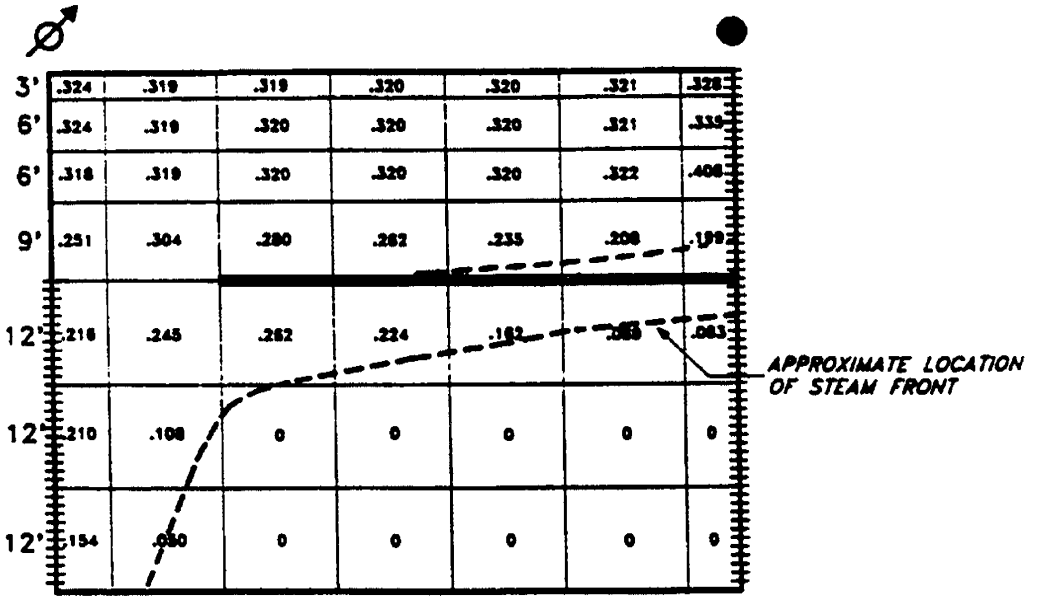

STEAM SATURATIONS @ 2190 DAYS
ONE DISCONTINUOUS SILT CASE
INJECTION RATE=331 BPD CWE
STEAM QUALITY=52.5%

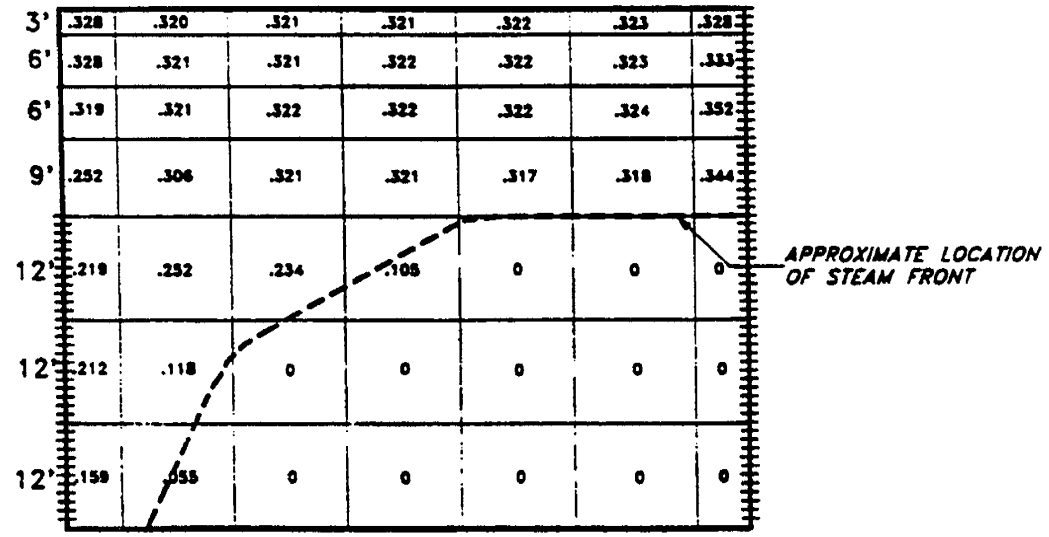

STEAM SATURATIONS @ 2190 DAYS
CLEAN SAND CASE
INJECTION RATE=331 BPD CWE
STEAM QUALITY=52.5%

I=1-7, J=1

Figure 13. Comparison of steam saturation profiles for clean and silty sands.

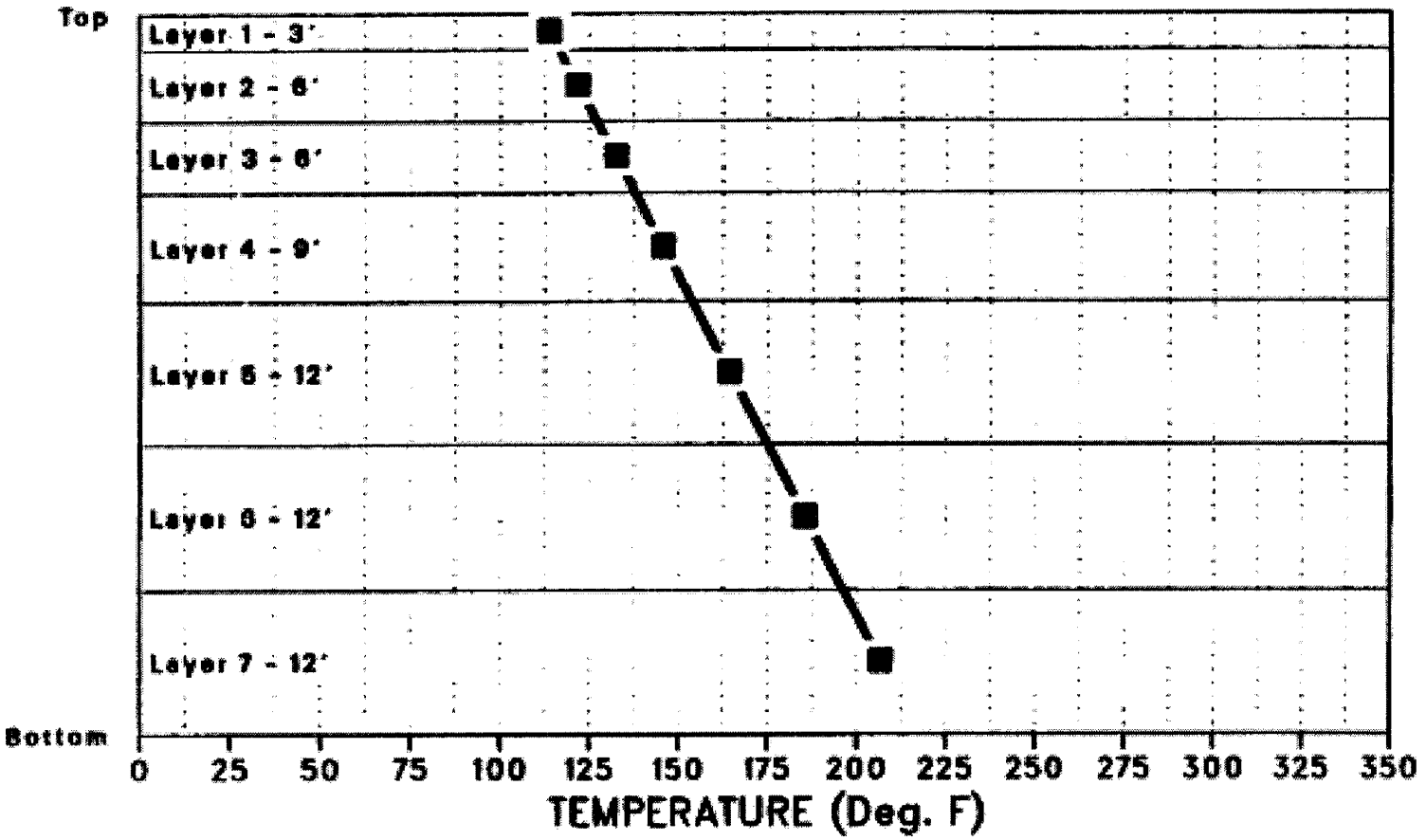

Figure 14. Initial temperature profile for 60 ft. preheated sand.

Task 75 – PDVSA Intevep will provide DOE with information on the field results of monitoring the temperature profile along one pair of SAGD horizontal wells, as well as the modeling of the SAGD process using this information.

STEAM ASSISTED GRAVITY DRAINAGE IN PDVSA

Saul Buitrago, Alexis Gammiero
PDVSA-Intevep

Abstract

The thermal processes represent 70% of the enhanced oil recovery methods, due to the high recovery obtained from them. Among the thermal recovery processes one of the newest is the steam assisted gravity drainage (SAGD) technique. This process reports several advantages as steam-oil ratio of 2 to 3 and recoveries as high as 60% of the original oil in place. It makes the modeling of this process very important, in order to understand and enhance its operational conditions. In this work, a three dimensional analytical model for steam assisted gravity drainage process for a pair of closely spaced, parallel horizontal wells has been developed, based on the temperature profile and pressure meassured along the wells. The model predictions are found to be in good agreement with field data for a resevoir in Venezuela. Also a new system for monitoring and control of the SAGD process is described.

1 Introduction

The quantity of heavy oil and bitumen in place in Venezuelan reservoirs is approximately 1.8 trillion barrels from a total of 3 trillion barrels worldwide (see Fig.1). Thus, the challenge of developing suitable methods for recovery is of very great practical importance. One of the main characteristics of the heavy oil and bitumen are their high viscosity and low API gravity. This characteristics limit the application of primary and secondary recovery methods for extraction of this type of oil. Heavy oil in situ recovery methods generally depend upon heating this type of oil in order to reduce its viscosity; both heating with steam and in situ combustion have been used.

This work is concerned only with the technique of heating the heavy oil or bitumen with steam to reduce its viscosity and increase its mobility. One approach is the cyclic steam stimulation technique. In this method, steam is first injected into the reservoir through the production well, the reservoir region adjacent to the well becomes heated and, subsequently, the flow is reversed to allow production. This continues until the flow has declined to uneconomical values and then the cycle is repeated. One of the problem with this methodology is the gravity drainage around the well, i.e. the conventional wells

which are employed (near vertical) have a rather limited contact with the reservoir, and the need for radial flow provides a considerable resistance.
Another approach is the steam assisted gravity drainage (SAGD from now on) method. It employs gravity drainage to move the crude to the production well, and with the advantage that the contact with the reservoir is much greater, because horizontal wells are employed (see Fig.2). Also, adequate flows can be achieved with heads equivalent to that obtained from gravity. The process allows the oil to remain hot as it drains downwards, and there is a systematic coverage of the reservoir so that high recovery can be achieved.
The production of heavy oil and bitumen reservoirs by gravity drainage, from a horizontal well with the continuous injection of steam from the upper well makes the process very attractive. Fig.3 shows a comparison of the cumulative production of several wells under cyclic steam injection and SAGD process. It can be seen that the production reached by the SAGD pair denoted 5085 is comparable with the vertical well 4258, even though the second well has been producing for 17 years and the SAGD pair only for 2.5 years.
In this study, a three dimensional analytical model for steam assisted gravity drainage process for a pair of closely spaced, parallel horizontal wells has been developed. The model predictions are found to be in good agreement with field data from a resevoir in Venezuela. Also a new system for monitoring and control of the SAGD process is described.

2 Steam assisted gravity drainage

In horizontal SAGD process (see [1-4]), steam is injected along the length of a horizontal injector well which is closely spaced above a horizontal producer at the base of the reservoir and parallel to it. The injected steam rises to the top of the reservoir due to gravity difference between the steam and the reservoir fluid and condenses at the steam-oil interface. The heat liberated from the condensing steam is transfered by thermal conduction into the cold reservoir and heats the oil and reduces its viscosity. The water condensates from the steam and the heated oil flows, driven by gravity, to the production well located below. As the oil flows away and is produced, the steam chamber expands. It can expand both upwards and sideways.
The nature of the process is such that there is a systematic displacement of the cold oil by the steam and the oil remains hot as it flows to the lower production well. If fluids are removed too quickly from horizontal production well then the steam chamber will be draw down to the well and bypassing will occur. Essentially the only driving force available to move the oil to the well comes from the effect of gravity and the mobile oil is just the one

relatively close to the steam chamber.

In general by knowing the distributed temperature profile along the well lenght allows reservoir engineers and operators to anticipate which horizons are being swept by steam and which are not. Proper actions on the injection profile can be made in order to improve spatial steam distribution and heat management. Non-uniform temperature profile along the production interval may anticipate any inefficient steam flood process, in which case remedial action may be taken on time. Temperature monitoring can help to extend project life and increase recovery factor.

This distributed temperature sensing can be achived by the use of fiber optic systems or thermocouple bundles. Thermocuples have been used extensively in Canadian SAGD projects.

For the case of fiber optic system, temperature monitoring is performed by deploying specially covered fiber cable into a 1/4 in coiled stainless steeel tubing. The tubing is previously attached along the producing tubing or casing. The measurement of distributed temperature is achieved by sending a laser light pulse down through a multimode optical fiber waveguide. As this pulse of light travels along the waveguide, specific molecular vibration caused by temperature along the waveguide generates a very weak reflected signal to travel back up the fiber towards the source. This weak signal is filtered out and measured using a detector. The detector compares the emision time of that light pulse to the time taken for the reflected light to get back. This determine the point of the temperature measurement as the speed of light in the fiber is constant and is known. The amplitude of the returned light is a function of the molecular vibration. As the molecular vibration rises with temperature, the increased amplitude of light gives temperature at the point of reflection. The laser sends out a pulse of light every 10ns and the detector examines all of the returned signals to give temperature reading at 1 meter intervals along the whole length of the fiber.

Thermocouples bundles are availables in lengths up to 5000 ft with up to 36 thermocouples, whereas comercial fiber length are produced up to 32,000 ft. There are many more data points available with fiber optic systems that measure a temperature every meter. The fiber optic line dimensions are usually much smaller than multiple thermocouple lines. The fiber optic sensor can be removed and replaced without disturbing the outer control cable. Because the fiber optic sensor measures data all along the wellbore, pre-positioning the cable in the well in unnecessary. This will be the case with a thermocouple bundle, where it is vital to place a thermocouple at a particular point in the well. In general, optical sensors do not require down-hole electronics, they are inmune to shock/vibration and electromagnetic interference, they are highly reliable, extremely small, easily deployed

and have multiplexing capabilities.

Also, a system for monitoring and control the wells was developed in house [5-6]. The system is based on state-of-the-art technologies, and it guarantees a robust and reliable mean of gathering as much data as possible coming from the oil well sites. The system architecture has been designed taking into account the ways of collecting, organizing, and transfering both surface and sub-surface measured well data to the main SCADA (Supervisory Control And Data Acquisition system). The system has also the capability to post all information to intranet corporate users, by incorporating an optional communications link (either via radio comunications or a plug-in ethernet card) using web-based techniques.

2.1 SAGD pilot well

The area selected for the pilot test was the Tia Juana Field, at Western Venezuela. It contains heavy oil with a relatively high viscosity (10.000 to 45.000 cp at 110° F) which has historically shown low recovery (10%) under cyclic steam stimulation. Heavy oil deposits in the Tia Juana Field occur in the Lower Lagunillas Member of the Lagunillas Formation (see [7-8]).

The reservoir is composed of channel deposits, with the top of the reservoir varyng from 450 to 1000 ft (TVD). The reservoir structure is a monoclynal 3° dipping to the south west with no faults in or around the pilot area. The total thickness of the lower Lagunillas formation averages 280 ft and is divided into 2 main layers. The 40 to 85 ft top layer was selected for the pilot test because of the homogeneous condition of the rock (99% quartz). The pilot wells consisted of 2 pairs of infill wells within an original 7 spot pattern with a well spacing of 231 m. For the first pair, 5085 and 5088, the planning and implementation of the test was done between June and December 1997, and production started on Dicember 15, 1997. Thermocouples were installed the heel, middle and toe of the horizontal section of each well for monitoring the temperature. Capillary tubing was installed from the heel to the toe of the wells to monitor pressure at the same time.

The second pair, 5091 and 5092, was drilled in the same zone, but this time a fiber optic system was used for monitoring the temperature. The Installation work for the wells was as follows:

- Install a fiber optic temperature profiling system into two 2900 feet horizontal injector and producer. The wells have a horizontal section of 1700 feet and will be furnished with a 7 inches production liner. A 3-1/2 inches hydrill tubing will run to the toe of each of the wells.

- For each of the system, the control line will be clamped to the 3-1/2 inches hydrill tubing as a doble ended U-tube with turnaround sub placed at the toe of the 3-1/2 inches tubing.

- The high temperature optical fiber that will measure temperature at every 1 meter interval along its length will be rated for continuous operation at 550° F.

- Install 2 pressure chambers with theirs capillary tubing containing nitrogen connected to a gauge at the surface, into two 2900 feet horizontal injector and producer.

This methodology was chosen to evaluate both the technology itself and enable monitoring of steam channeling into the producer and progressive growth of the steam chamber with time.

2.2 Analytical model

The three dimensional SAGD model presented here builds upon the original concepts derived by Butler et al [2,4], and the improvements proposed by Reis [9], Closmann [10], and Vikas & Kamath [11]. The model considers a pair of closely spaced, parallel horizontal wells located at the bottom of the pay zone in a homogeneous heavy oil or bitumen reservoir. The steam is injected continuously through the top horizontal injector and heated oil which flows to the bottom producer by gravity drainage is produced (see Fig.2).
For the development of the new model several basic criteria are taken into account:

- The system is divided in several sections: the steam chamber, the produced fluids, the overburden and the reservoir (farther to the steam-oil interface). For each section the associated heat is determined.

- From experimental observation the steam zone shape can be approximated as an inverted triangle with the lower vertex fixed at the production well.

- The temperature in the steam chamber is essentially that of the injected steam.

- The temperature profile is assumed to decline exponentially with distance from the interface.

- An empirically based temperature profile to determine the oil viscosity ahead of the steam zone is assumed.

In the model, the cumulative oil production is estimated as the sum of the contributions per unit length of the well producer and the conditions established for the well and around it.

The model for estimating the oil production per unit length of the well is based on:

1. The Butler [2] and Reis [9] models for the steam chamber growing
2. A correlation for the viscosity behavior as a function of the temperature
3. The temperature profile and pressure measured along the wells

Initially, the steam rises upward to the top of the reservoir and this process is called rising chamber phase. The production rate increases with time in this phase. Once the steam chamber reaches the top of the reservoir, the steam chamber grows sideways and production rate starts to decline. The steam chamber forms an inverted triangle shape (two dimensional transversal section to the length of well) and the heated oil in the vecinity of the steam chamber flows parallel to steam-oil interface due to gravity drainage. The heat penetration rate is proportional to the oil drainage rate indicating the replacement nature of this process.

From these considerations, the model calculations are divided into two phases: the vertical growing of the steam chamber and the lateral expansion of the steam chamber.

The cumulative production for phase 1, vertical growing of the steam chamber, is as follows:

$$Np_1 = 2.25\sqrt[3]{(\frac{k_o\ g\ \alpha}{m\ \nu_s})^2\ \phi\ (S_o - S_{or})\ ((t_f)^4 - (t_i)^4)\ \delta}$$

In case of phase 2, lateral expansion of the steam chamber, the following formula gives a way to calculate the cumulative production,

$$Np_2 = 2\sqrt{\frac{1.3\ k_o\ g\ \alpha\ \phi\ (S_o - S_{or})\ H}{m\ \nu_s}}\ (t_f - t_i)\ \delta\ .$$

For phases 1 and 2 m is calculated as follows

$$m = \frac{\log(\frac{\nu_{os}}{\nu})}{\log(\frac{T - T_r}{T_s - T_r})},$$

K_o the oil effective permeability, g the gravity, α the thermal diffusivity of reservoir, ϕ the porosity, S_o and S_{or} the initial and residual oil saturation, t_i and t_f the initial and final time of the process, ν_{os} and ν the kinematic viscosity at temperatures T_s and T, T_r the reservoir temperature, H the reservoir thickness and δ the distance between temperature measurements.

The model for estimating the steam injection rate is based on:

- Heat losses to the different components of the system
- Performing of the heat balance
- Considering latent and sensible heat

The heat losses to the different components of the system taken into account in this work are the following:

- Heat accumulated in the steam chamber which is calculated as

$$Q_{CV} = M_{r1} (T_s - T_r) \frac{V_{op}}{\phi (S_o - S_{or})}$$

where M_{r1} is the volumetric formation heat capacity of the rock including the residual fluids, V_{op} is the volume of cumulative oil production, ϕ the porosity, S_o and S_{or} are the initial and residual oil saturations, T_s and T_r are the steam and reservoir temperatures.

- Heat lost through produced fluids. It will be given by

$$Q_{fp} = Q_o + Q_{wi} + Q_{wc}$$

because the produced fluid is a mixture of oil, connate water and steam condensate. Q_o represents the heat lost with the produced oil and it is calculated as

$$Q_o = \rho_o C_o V_{op} (T_{fp} - T_r),$$

with ρ_o the oil density and C_o the specific heat of oil. Q_{wi} is the heat lost with the produced formation water and it is given by

$$Q_{wi} = \frac{\rho_w C_w V_{op} (S_w - S_{wr}) (T_{fp} - T_r)}{S_o - S_{or}},$$

with ρ_w the water density, C_w the specific heat of water, S_w and S_{wr} the formation and residual water saturations in the reservoir (not the steam condensated). Q_{wc} is the heat lost with the produced condensed water, and it is produced as water to the produced fluid temperature. It is evaluated as

$$Q_{wc} = \rho_w C_w (T_{fp} - T_r) (RAC - \frac{S_w - S_{wr}}{S_o - S_{or}}) V_{op},$$

where RAC is water-oil ratio.

- Heat to the overburden. It is estimated as

$$Q_L = \frac{8\ \lambda_{ob}\ (T_s - T_r)\ dL}{3\sqrt{\pi}\sqrt[4]{\alpha^3}} \sqrt[4]{\frac{a\ \nu_{os}\ m\ V_{op}^6}{(\phi H(S_o - S_{or}))^5\ 128\ k_o\ g\ dL^6}}$$

with α the thermal diffusivity of reservoir, k_o oil effective permeability, H the reservoir thickness, $a = 0.4$, ν_{os} the oil kinematic viscosity at steam temperature, t time, dL unit length of the horizontal well, λ_{ob} thermal conductivity of the overburden, and m adimensional viscosity coefficient.

- Heat to the reservoir (farther to the steam-oil interface). It is given by the following expresion

$$Q_{MI} = \frac{M_r\ (T_s - T_r)\ \alpha}{2\sqrt{2}\ H^3\ a\phi^2(S_o - S_{or})^2\ dL} \sqrt{\frac{a\ \phi\ (S_o - S_{or})\ \nu_{os}\ m\ H}{\alpha\ K_o\ g}} V_{op}^2$$

The heat balance is given by the following equation

$$Q_t = Q_{CV} + Q_{fp} + Q_L + Q_{MI}$$

where Q_T is the total heat introduced to the system (bottom hole) as steam.
To calculate the total heat injected at the sand face the following equation will be used (see Prats [12])

$$Q_t = Q_s \rho_w t[(h_{ws} - h_{wr}) + xL_s]$$

where Q_s is steam injection rate, ρ_w is the water density, h_{ws} is the sensible heat to the steam temperature, h_{wr} is the sensible heat to the reservoir temperature, x is the steam quality, L_s is the latent heat of the steam, and t is the time for the steam injection.
The data needed to run the analytical model is presented in Table 1. The cumulative production is 173047 barrels of oil for a period of 222 days and the average temperature for the injector and producer well are 214.3 and 186.6° C respectively. Table 2 reports the heat losses to the different components of the system. The average injection rate to the reservoir is 865 B/d, which is lower than the calculated by the analytical model. The heat stored in the steam chamber is the highest in the system, this fact agrees with the results reported by Butler [2] in his analysis of thermal efficiency, however the quantities are different. Also the heat to the overburden and the heat to the reservoir are quantities of the same order, which is also reported by Butler in his model. Figs. 4, 5 and 6 show a comparison of the field and model data for the cumulative oil production, oil production rate and steam injection rate for the first pair of SAGD wells.

3 Conclusions and Recomendations

- A SAGD pilot test has been successfully implemented in Tia Juana Field. Initial production rate was better than expected (700 vs 300 BOPD). Steam injection needed to keep the producer well under "natural flow". Steam trap and producing at low water cut (50%) was in the order of 120 to 140 T/D. This is close to 70% less steam than expected which provides an OSR of 0.8.

- Fiber optic technology is ideally suited for permanent down-hole sensing applications. Distributed temperature monitoring is a reliable real time method of monitoring reservoirs and provides time vs depth data every meter along the wells.

- An analytical model for estimating the oil production rate was developed based on the observation that the steam zone can be approximated as an inverted triangle, and also on the measurements of the temperature and pressure profiles along the wells.

- An analytical model was developed for estimating the steam injection rate required to produce at a predetermined oil rate through an energy balance, based on the heat losses to the different components of the system.

- A new system for the monitoring and control the SAGD process to achieve optimal ways of automating their production operations was implemented.

4 References

1. Butler, R.M.; Stephens, D.J.:The Gravity Drainage of Steam-heated Heavy Oil to Parallel Horizontal Wells, Journal of Canadian Petroleum Technology, pp 90-96, April-June 1981.

2. Butler, R.M.: "A New Approach to the Modelling of Steam-Assisted Gravity Drainage", Journal of Canadian Petroleum Technology, pp. 42-51, May-June 1985.

3. Scott Ferguson, F.R.; Butler, R.M.: "Steam-assisted gravity drainage model incorporating energy recovery from a cooling steam chamber", Journal of Canadian Petroleum Technology, Vo. 27 No. 5, pp. 75-83, September-Octuber 1988.

4. Butler, R. M.: " Thermal Recovery of Oil and Bitumen. Englewood Cliffs: Prentice Hall, pp. 307-312, 1991.

5. Mora, G; Rodríguez, J.J.; Rotzer, I.; De Sousa, D.: "Definición de arquitecturas de automatizacin para la transferencia confiable de datos, PDVSA-Intevep, Informe Técnico INT-6413, Los Teques, Venezuela1999, 1999.

6. Mora, G.; De Sousa, D.; Zapico, J.; Espin, D.: "A new system architecture for reliable transmission of oil well data", SPE Applied Technology Workshop on Reservoir, Drilling and Production Aspects of Smart Reservoirs and Wells, Puerto La Cruz-Venezuela, 2000.

7. Saputelli, L.; Memdoza, H.; Finol, J.J.; Rojas, L.; Lopez, E.; Bravo, H.; Buitrago, S.: "Monitoring Steamflood Performance Through Fiber Optic Temperature Sensing", SPE 49184, SPE Annual Technical Conference and Exhibition, New Orleans, Lousiana, USA, 27-30 September, 1998.

8. Mendoza, H.; Finol, J.J.; Butler, R.M.: "SAGD Pilot Test in Venezuela", SPE 53686, SPE Latin American and Caribbean Petroleum Engineering Conference, Caracas, Venezuela, 21-23 April, 1999.

9. Reis, J.C.: "A Steam-Assisted Gravity Drainage Model for Tar Sands: Liner Geometry", Journal of Canadian Petroleum Technology, Vol. 31, No 11, pp. 14-20, December 1992.

10. Closmann, P.J.: "A Simplified Gravity Drainage Oil Production Modelo for Mature Steamdrives", SPE 25790, pp. 143-154, 1994.

11. Vikas, S.; Kamath, V.A.: "Analytical Model for Steam-Assisted Gravity Drainage in Horizontal Wells", Symposium on Exploration, Characterizacion and Utilization of California Heavy Fossil Fuel Resources, pp. 886-900, 1992.

12. Prats, M.: *Procesos Térmicos de Extracción de Petróleo*, Ediciones tecnicas Intevep, Venezuela, 1987.

13. Buitrago, S.; Gammiero, A.; Llaguno, P.; Mora, G.; De Sousa, D.: "Drenaje Gravitacional Asistido por Vapor (SAGD) en PDVSA", to appear in Visión Tecnológica, Intevep S.A., 2001.

14. Rivas, O.R.: "Investigación y Desarrollo en Intevep Sobre los Métodos de Recuperación Mejorada de Petróleo", Revista Técnica Intevep, pp. 195-216, Julio-Diciembre 1989.

15. Yang, G.: Effects of Reservoir Heterogeneites on Heavy Oil Recovery by Steam Assisted Gravity Drainage, Aostra University Research Program, 1990.

16. Hamm, R.A.; Ong T.S.: "Enhanced Steam-assisted Gravity Drainage: A New Horizontal Well Recovery Process for Peace River, Canada", Journal of Canadian Petroleum Technology, Vol. 34, No 4, pp. 33-40, April 1995

17. Polikar, M.; Redford, D.A.: "Evolution of Steam-based Technology for the Recovery of Canadian Heavy Oil Reservoirs", Canada, Journal of Canadian Petroleum Technology, Vol.34, No 5, pp. 33-40, May 1995.

18. Singhal, A.K.; Das, S.K.; Leggitt, S.M.; Kasraie, M.; Ito, Y.: "Screening of Reservoirs for Explotation by Application of Steam Assisted Gravity Drainage/Vapex Processes", SPE 37144, pp. 867-876, 1996.

19. Falk, K.; Nzekwu, B.; Karpuk, B.; Pelensky, P.: "Concentric CT for Single-well", World Oil, pp. 85-94, July 1996.

TABLE 1

Data used in the analytical model

initial pressure	575 (psi)
reservoir temperature	95 (degree F)
porosity	0.35
stean quality	0.75
API	9.7
viscosity (SC)	21200 (cp)
initial oil saturation	0.74
initial water saturation	0.26
residual oil saturation	0.10
residual water saturation	0.26
effective permeability	1.75 (darcy)
WOR	0.79 (bl/bl)
volumetric formation heat capacity of the rock	32.2 (Btu / ft^3 degree F)
thermal diffusivity of reservoir	0.6566 (ft^2 / d)
oil formation volume factor	1.052
depth	700 - 850 (ft)
reservoir thickness	40 - 85 (ft)
horizontal section length	1381 (ft)
oil density	964.5 (Kg / m^2)
gravity	2.4016 10^{11} (ft / d^2)
thermal conductivity of the overburden	14.472 (Btu / d ft degree F)

TABLE 2

Heat losses (MMBtu) and steam injection rate (B/d)
calculated using the analytical model

Q_{CV}	Q_o	Q_{wi}	Q_{wc}	Q_L	Q_{MI}	steam injection rate
40621	7504	0	13878	3157	2069	930

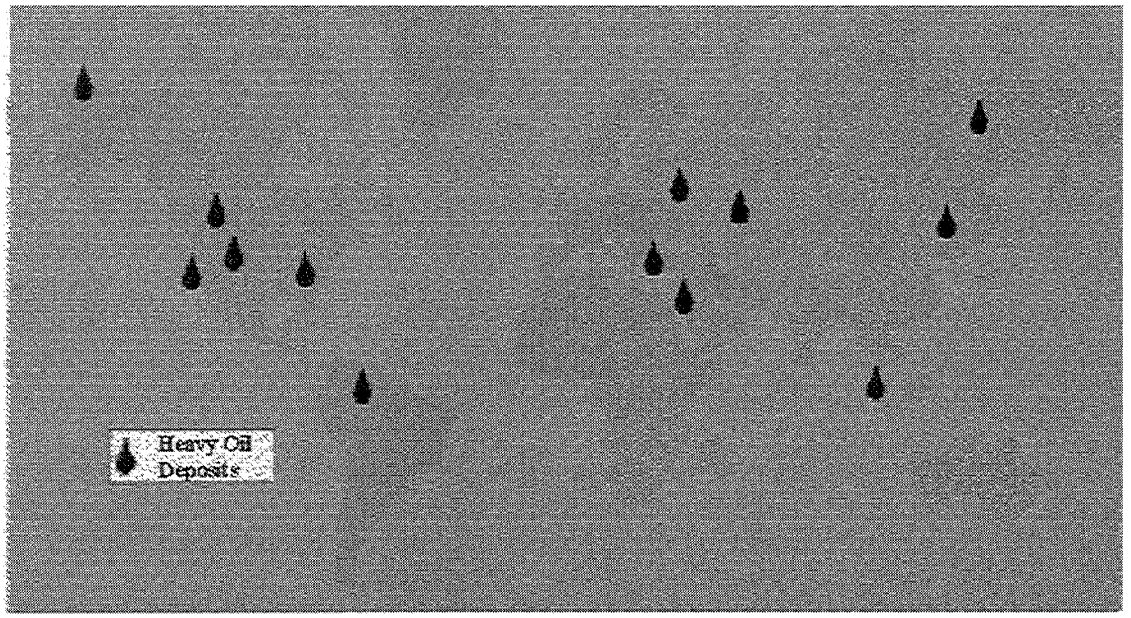

Fig.1 Main deposits of heavy oil in the world

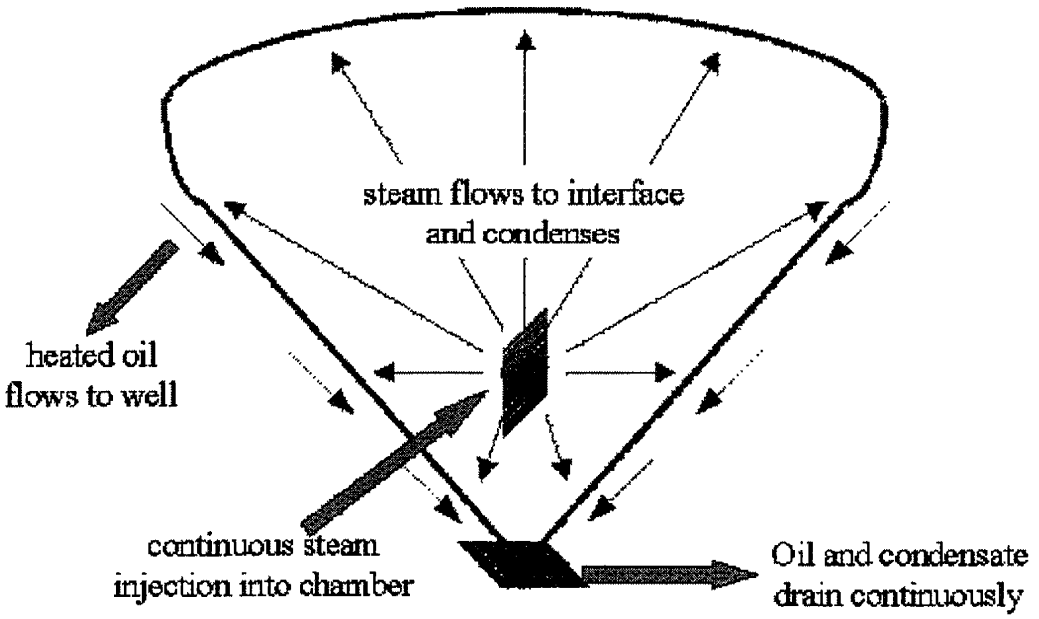

Fig.2 Diagram of the SAGD process. Mechanism: (a) steam condenses at interface, (b) oil and condensate drain to well at bottom, (c) flow is caused by gravity, (d) chamber grows upwards and sideways

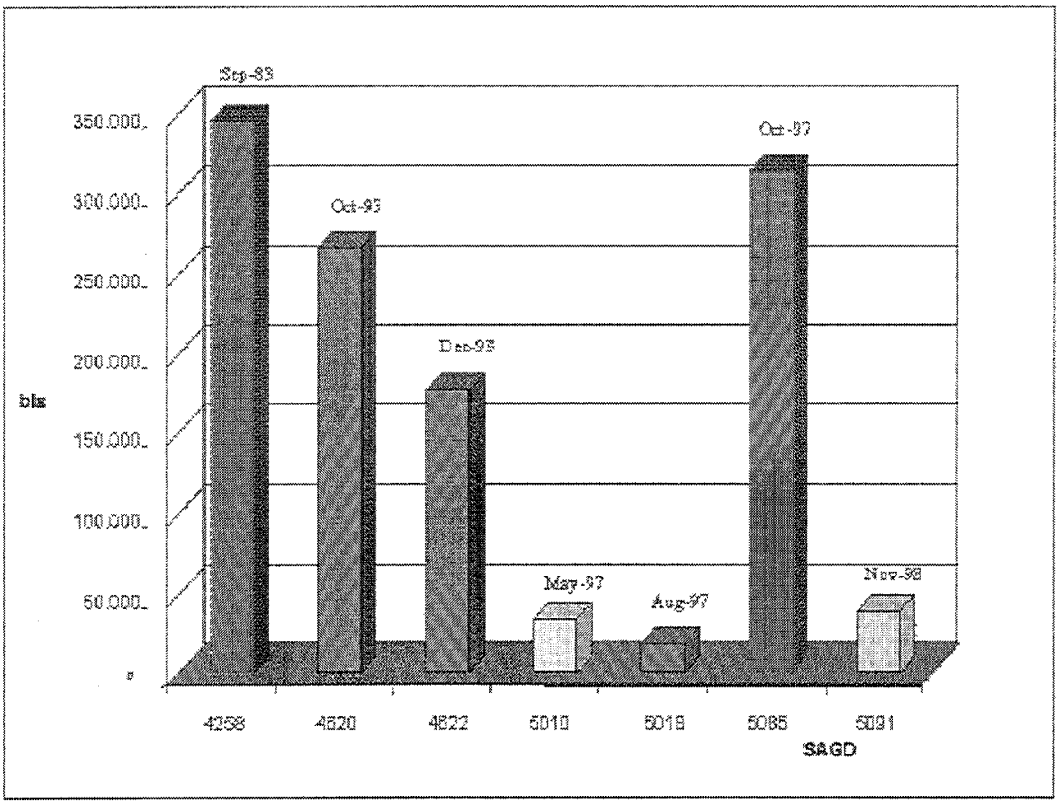

Fig.3 Comparison of the cumulative production of several wells under cyclic steam injection and the 2 SAGD pairs. The date on the top corresponds to the date when the production started.

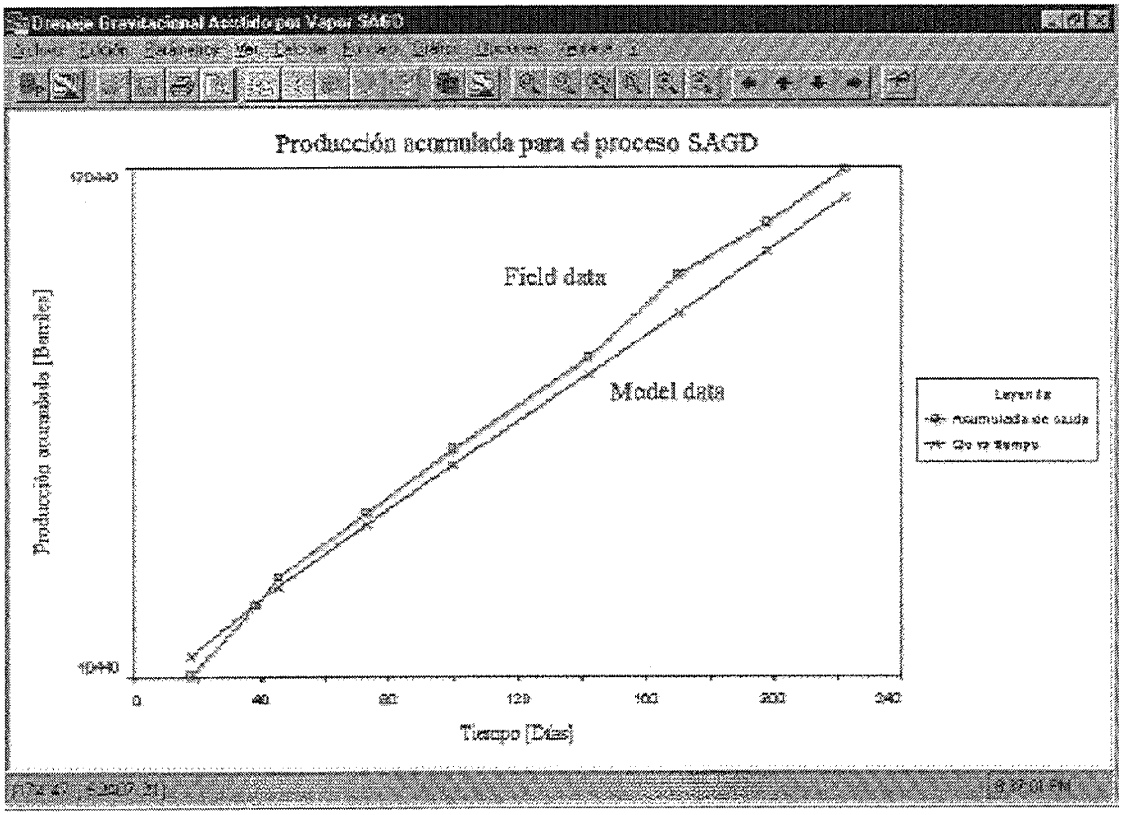

Fig.4 Field and calculated cumulative production for the SAGD pair

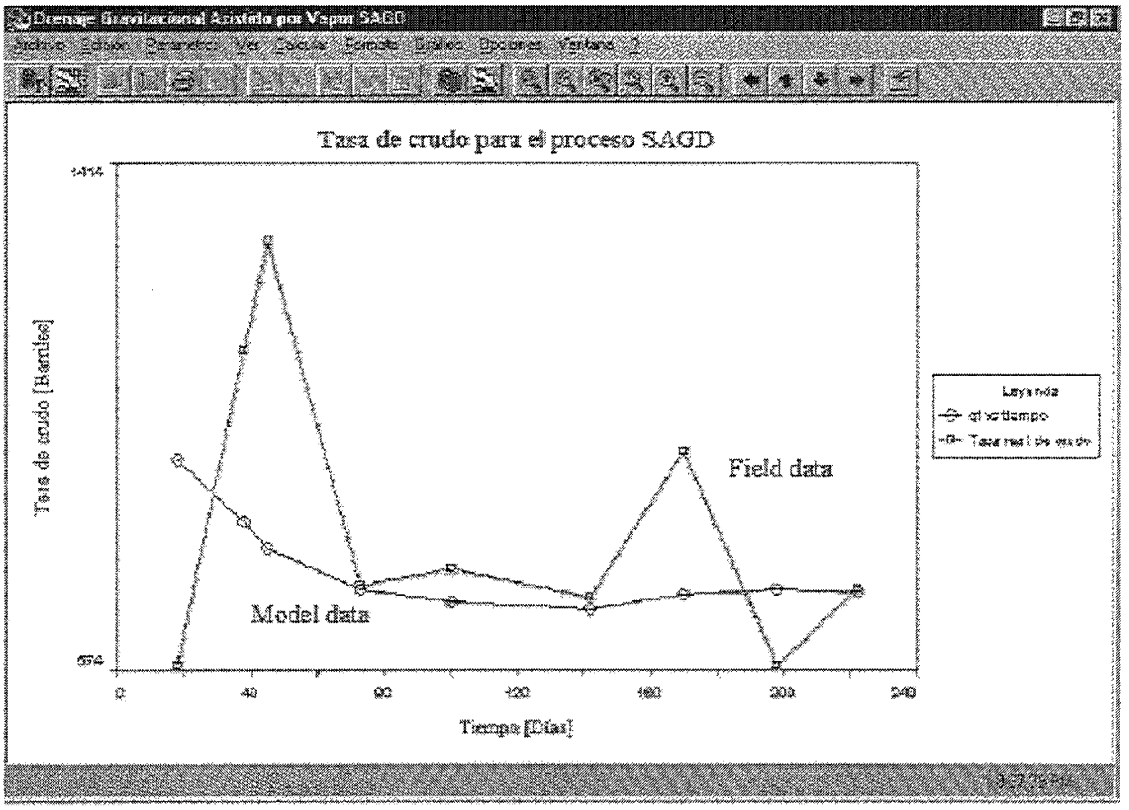

Fig.5 Field and calculated oil production rate for the SAGD pair

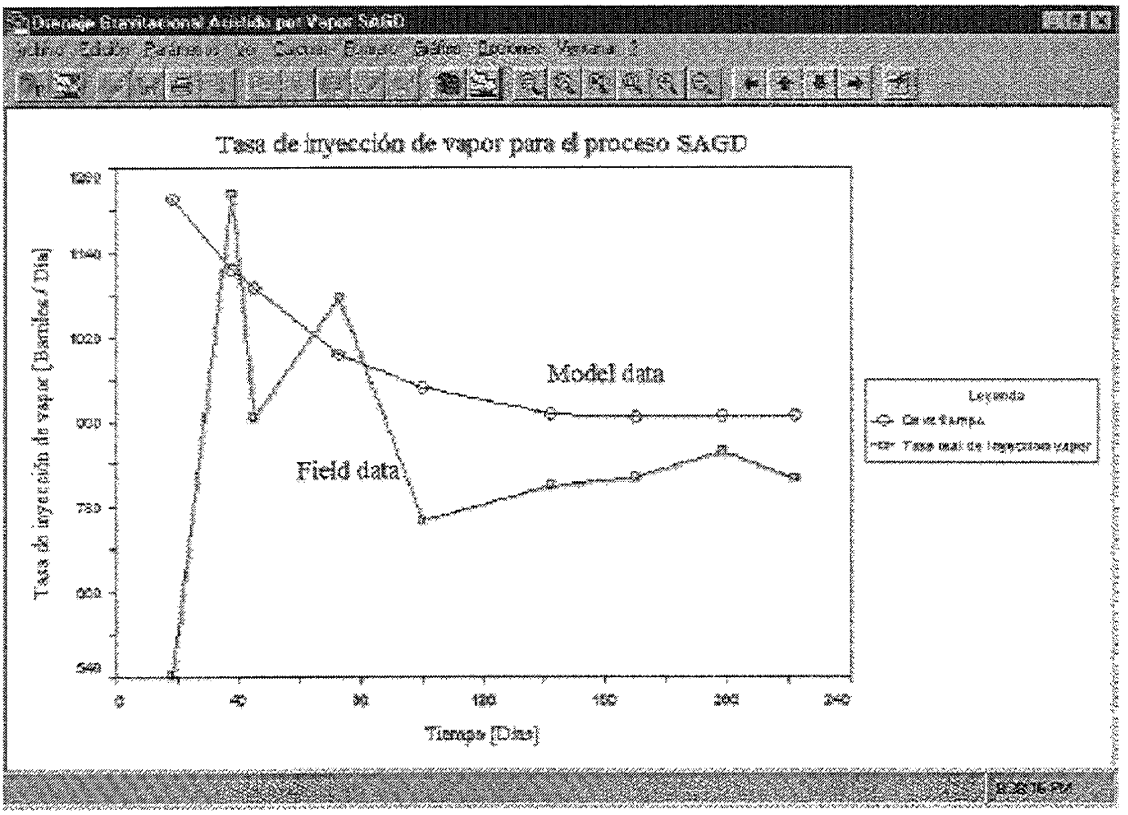

Fig.6 Field and calculated steam injection rate for the SAGD pair

Task 76 - DOE shall provide PDVSA Intevep with information on research undertaken by BDM Petroleum Technologies (now TRW Petroleum Technologies) to develop methods to economically recover heavy oil from the harsh arctic (North Slope, Alaska) environment.

Viscous Oil Recovery at Schrader Bluff, Alaska

Abstract

The purpose of this study was to establish the in-situ combustion behavior of Schrader Bluff crude oil on a restored-state Schrader Bluff core, and evaluate the sensitivity of the combustion behavior to various operating parameters. Prediction of oil recovery as a function of air injection rates and other parameters provides a better estimate of project potential. Two laboratory combustion tube runs were conducted with Schrader Bluff oil and restored state core to obtain kinetic coefficients, stabilized air and fuel requirements, and temperature profiles for high-temperature oxidation. Laboratory results from the tube runs combined with known reservoir rock, fluid, and geological parameters are needed to estimate oil recovery as a function of several operational conditions using state-of-the-art modeling tools. These conditions include air injection rate, air enrichment, cracking reaction kinetics, wet versus dry combustion, phase equilibrium constant, and well spacing.

Laboratory results showed good burn characteristics using Schrader Bluff oil and rock. A stable front can be maintained and recovery efficiencies are good. Wet combustion, a process combining in-situ combustion with water injection, appears to perform better than dry combustion provided the air injection rate is sufficiently high. A first estimate of air requirements, burn rates, etc., was determined. Results of a simulation sensitivity study of in-situ combustion were consistent with observed behavior in the laboratory. Extinction radius calculations indicated that to implement a successful 80 acre spacing in-situ combustion project, a minimum of 5 MMscf/D air injection rate was required. The simulation study suggests that in-situ combustion cannot be maintained in the low permeability sands (NC/ND, NE, and NF) at the minimum injection rate of 5 MMscf/D. No pronounced advantage in using high oxygen content air is predicted for the Schrader Bluff reservoir. Enriched air will accelerate peak oil production but has minimal effect on the overall oil recovery. The pre-exponential factor of the combustion kinetics has only marginal effect on predicted oil recovery. However, the phase equilibrium K values have significant impact on the predicted ultimate oil recovery. Wet combustion causes higher oil recovery and requires lower air/oil ratio (AOR) than that of dry combustion. AOR values for both dry and wet combustion are within the acceptable range. However, high water injection and/or low air injection rate may partially quench the combustion and reduce the recovery.

In conclusion, the in-situ combustion oil recovery process appears favorable for Schrader Bluff of Milne Point Unit, Alaska. The oil recovery process is efficient and the air and fuel requirements are good relative to other reservoirs tested. It is recommended that a detailed economic analysis be conducted using in-situ combustion at Schrader Bluff. Also, a relative measure of operational and environmental risk needs to be assessed for the arctic region. If found to be favorable, a field pilot test would be recommended. Because of the many limitations

---

This work was supported by the U.S. Department of Energy under contract DE-AD26-99FT00874 (GS-23LF-8079H) with TRW Petroleum Technologies.

of current laboratory and simulation tools, a good estimate of ultimate recovery efficiency can only be obtained from a properly designed field test.

Recovery by In-Situ Combustion

Background

Schrader Bluff reservoir, located at Milne Point Unit west of Prudhoe Bay field on the North Slope of Alaska, has been under development since 1991. Currently, Schrader Bluff is under waterflood and an active program to improve technical and economic performance is underway. TRW Petroleum Technologies has evaluated the potential to recover oil from Schrader Bluff using a variety of production methods, and have determined that many of the reservoir parameters are favorable for the in-situ combustion process. Thus, a more detailed study of in-situ combustion at Schrader Bluff was initiated.

In-situ combustion, or fireflooding as it is sometimes called, is the oldest member of the thermal oil recovery family. It is basically a gas injection process with gas being air to supply oxygen. The air sustains combustion of a portion of the reservoir oil for the purpose of generating heat in-situ and subsequently reducing the viscosity of the remaining oil. The combined effects of reduced fluid viscosity, increased oil swelling from generated carbon dioxide, and increased volume expansion from generated flue gases including steam, contribute to the enhanced recovery of oil.

Advantages over other advanced recovery methods include improved heat efficiency over steamfloods (no heat lost in wellbore during injection), more effective than steam injection in thin reservoirs, not limited by reservoir pressure, more robust with respect to variations in reservoir permeability, injection fluid (air) not limited by source location, less limited by well spacing as compared to other processes, and in general when successful is the most efficient thermal recovery process available. Furthermore in-situ combustion can be used to effectively recover a high percentage of oil in situations unsuitable for any other process.

Disadvantages include the requirement of expensive initial laboratory evaluation tests, increased economic uncertainties in prediction of field performance, implementation of more extensive field management practices, and in general all the disadvantages associated with implementation of a complex and sophisticated field project. The inability to reasonably predict field results for a given situation have led to many project failures. Subsequent analyses of these failures inevitably revealed that either the reservoir conditions, the process design, or the implementation particulars were not appropriate for the in-situ combustion process.

A number of past in-situ combustion field projects have been reviewed (Sarathi 1994; Sarathi 1995; Sarathi 1998). Nearly all of them were considered economically unsuccessful. The one successful project that was reviewed did not circumvent the planning steps discussed below and was carefully designed for operator contingencies. In general, in-situ combustion may enhance oil production by substantial amounts, provided the reservoir conditions are suitable and just as importantly, provided the project design is fully evaluated, well planned, and carefully implemented.

In order to determine if in-situ combustion can be effectively applied in a particular field, one must follow a prescribed scaling path. Other recovery processes have become more standard and often can circumvent some of these steps, but they are still required for in-situ combustion

to manage economic risks most effectively. Essentially, these steps in order are: (1) consider the favorable and unfavorable risk factors of the particular reservoir (reservoir screening), (2) conduct laboratory tube runs (laboratory scale burns), (3) evaluate the technical and economic sensitivities to project design factors, and (4) conduct a field pilot test. A field test is necessary to determine a reasonable estimate of field performance, and the precursor laboratory and simulation studies are needed to maximize the potential success of the field test.

Schrader Bluff Reservoir Properties

Schrader Bluff Reservoir Rock Properties

The Schrader Bluff consists of Late Cretaceous, near shore marine sand sequences, informally referred to as the "N" and "O" sands (Bidinger et al., 1995). The individual reservoir units are predominantly, very fine to fine grained, moderately sorted, unconsolidated quartz sands with varying amounts of accessory minerals, mainly rock fragments, mica and glauconite. The reservoir units are amalgamations of storm deposits redistributed, for the most part, below wave base. Bioturbation, and burrows are common in some intervals whereas, others display finely laminated bedding, suggesting more rapid sedimentation. Calcareous interbeds are locally common, often associated with concentrations of bivalve debris.

The upper "N" sands consist of multiple reservoir layers varying in thickness between 5 and 15 feet, with permeability's ranging between 5 millidarcies to 5 darcies. The lower "O" sands consist of two main sand bodies that although are finer grained than the "N" sands, are generally more massive and competent. These sands are more continuous and correlative across the North Slope than the thinner, more discontinuous "N" interval. The "O" sands thickness varies between 10 to 35 ft with permeabilities between 10 millidarcies and 1 darcy. The average porosity in all sand units varies between 25 to 28 percent.

The formation dips gently north-northeast at a rate of approximately 70 ft per mile. The resulting monocline is broken by numerous faults of variable displacement, most of which trend north-northeast and progressively downdrop the reservoir to the northeast. Depths range from 3500 feet to 4500 feet. Faults, with throws between 20 to 150 feet, compartmentalize the reservoir to some degree. This coupled with stratigraphic discontinuities, can hydraulically isolate individual reservoir units.

The fracture gradient is between 0.66-0.7 psi/ft with an overburden stress gradient of 0.85 psi/ft. The estimated net confining stress is between 1000 to 1300 psi.

Schrader Bluff Reservoir Fluid Properties

The Schrader Bluff Pool is undersaturated by about 500 psi and correspondingly has no gas cap. The initial average reservoir pressure was 1750 psig at 4000 ft true vertical depth subsea with an average reservoir temperature of 81° F. These pressures are only slightly higher than the local hydrostatic pressures. Currently, the average reservoir pressure is between 1400 and 1750 psi depending on the producing fault block. The geothermal gradient from surface to 2000 ft is 0.8° F/100 ft, due to the presence of a permafrost layer that extends to this depth (Fox & Earsley, 1998). From that point the geothermal gradient increases to 3° F/100 ft.

The hydrocarbon quality varies between the N and O sands, the deeper O sand containing a better-quality crude oil than the N sand (Smalley et al., 1996). The N sand oil gravities range from 14° to 19° API with live oil viscosities between 40 and 140 centipois (cP). The oil gravities and viscosities improve in the O sands, oil gravities typically falling between 18° to 21.5° API with viscosities from 30 to 45 cP.

In general, the PVT properties of the Schrader Bluff hydrocarbons bear a resemblance to conventional heavy oil systems, namely they have:

1. Low API gravities (14° to 22°)
2. Low gas oil ratio (GOR 100 to 200 scf/stb)
3. Low oil formation volume factor (1.04 to 1.08 bbl/stb)
4. High average viscosity (30 to 140 cP at reservoir conditions)

The "high average viscosity" for heavy oils is usually defined to be >100 cP at reservoir conditions. Clearly, the average oil viscosity of Schrader Bluff does not fit this criteria most of the time, and for this reason is more often called a viscous oil than a heavy oil. Even so, the viscosity is noticeably higher than typical light oils (<2 cP). Having such viscosity values adversely impacts production methods such as miscible gas injection, water injection, and even primary production (lower rates), which in combination with the harsh arctic environment can render oil recovery processes uneconomic as they are usually practiced.

The live oils of the Schrader Bluff are dominated by the C7+ fractions (ca. 67 mole). The small amount of C2-C6 intermediate hydrocarbons suggests high biodegradation. The gas composition is primarily methane, and contains no hydrogen sulfide, and very little quantities of carbon dioxide or nitrogen. The formation water contains approximately 27,000 ppm total dissolved solids, with an average salinity of 20,000 ppm NaCl equivalent.

In common with fluid systems from shallow and soft sands, the Schrader Bluff hydrocarbon properties exhibit significant variations across sand bodies. This variance is seen vertically, from sand to sand, and laterally within one sand as it is traced down dip. The mapped variance is poorly understood at this time. A summary of reservoir properties is provided in Table 1.

Similarities of Schrader Bluff Oil to Neighboring West Sak Oil

Composition of well E-20 Schrader Bluff oil is given in Table 2. Schrader Bluff crude oil is characterized by severe depletion of the light and medium light hydrocarbons (carbons 2 through 10) and by the presence of asphaltenes in the heavy ends. Asphaltenes are shown to be destabilized in high concentrations of some light solvents such as Prudhoe Bay MI and CO_2/NGL. Schrader Bluff gas is essentially methane, and at reservoir conditions the crude oil is undersaturated. Consequently, no gas cap was initially present and will not form until the reservoir pressure drops below the bubble point.

These characteristics result in increased oil viscosity, and at 92° F and saturation pressure the oil viscosity is 65 cP. To date, field practices have proven that Schrader Bluff oil can be produced,

but engineers remain challenged to improve the economic value of the project (McKean et al., 1999).

Also, the PVT studies showed that Schrader Bluff oil with high solvent concentrations (80 mole% Prudhoe Bay MI, 80 mole% CO_2/NGL) at reservoir conditions formed both a gas phase and 2 liquid hydrocarbon phases simultaneously. The lower more dense liquid phase contained greater amounts of the heavy ends and of the asphaltenes. The upper less dense liquid phase contained substantial amounts of hydrocarbon components but also contained a higher concentration of the solvent and essentially no asphaltenes. Although multiple phase systems have been observed elsewhere, fluid flow characterization of such complex phase systems are rare and commercial reservoir simulators are currently unable to manage all of these phases simultaneously (Okuyiga, 1992; Godbole et al., 1992; Fong et al., 1992; DeRuiter et al., 1990; Orr et al., 1980; Shelton & Yarborough, 1977)

The OA and OB sands of Schrader Bluff continue south and west into the Kuparuk River Unit, and are generally referred to in that region as West Sak. Fluid characterization studies of West Sak have also been published, and the oil characteristics are similar enough that a summary of these studies are included here (Okuyiga, 1992; Gondouin et al., 1991; DeRuiter et al., 1990; Sharma et al., 1989; MacAllister & DeRuiter, 1985). Although oil composition from well to well differs slightly, the average values are nearly identical to those of Schrader Bluff (Okuyiga, 1992). The gas composition is primarily methane and the light hydrocarbon components are severely depleted. Asphaltene content was determined to be 4.9 wt%. Oil gravity varies from 10° to 22° API and viscosity ranges from 20 to 5000 cP. Depth of the West Sak formation varies from 2000 ft to 4000 ft, and because the reservoir is more shallow, the reservoir temperatures are generally lower and viscosities are generally higher than that of Schrader Bluff.

Because properties of Schrader Bluff and West Sak oils are nearly the same and the reservoirs are in the same geographical proximity, production methods found successful for Schrader Bluff may similarly be successful for West Sak. While oil saturation values for Schrader Bluff is approximately 1.8 billion Bbl, estimates of oil saturation values for West Sak varies from 13 to 20 billion Bbl. The reservoir conditions are most favorable for Schrader Bluff, because the reservoir temperature is higher and the formation is well below the permafrost (downdip from West Sak). Thus, there is some advantage for evaluating the potential oil recovery at Schrader Bluff first using in-situ combustion. Successful production methods at Schrader Bluff may then be extended to West Sak with a much larger production target.

Favorable and Unfavorable Risks for In-situ Combustion

Table 3 summarizes the favorable and unfavorable risk factors for in-situ combustion processes. Evaluation of these factors is the first step and can be used to determine relatively quickly if the process is potentially suitable or not. Although not definitive (individual factors are not exclusive to success or failure), it is the basis for deciding whether to continue or not with more expensive laboratory studies.

The favorable risk factors for Schrader Bluff include, thin sand layers, high oil saturation, and good fluid transmissibility. Although unknown to the authors, overburden competence is expected to be good as well. None of the unfavorable risk factors listed in Table 3 appear to be

present for Schrader Bluff, although fractures and faulting are present and may be too high for some of the sands to ensure good lateral continuity. The degree of heterogeneity and faulting present at Schrader Bluff and the extent that the in-situ combustion process is unfavorably affected will need to be determined.

Since initial conditions appeared favorable, laboratory tube runs were conducted to determine the kinetic parameters of oil combustion at reservoir conditions. From this information minimum air requirements, ignition requirements, burn efficiency (air/fuel ratio), extinction radius, and overall favorability were further determined. These values can be used in simulation studies to develop estimates of potential recovery and economic costs. Sensitivities to ranges in project design parameters can be evaluated using simulation tools. However, full scalability is not possible and implementation of a field pilot project is ultimately required. The impact of heterogeneity, discontinuity, etc., can only be measured in such a pilot project, and burn front performance cannot be properly scaled in the laboratory. Furthermore, simulation techniques for in-situ combustion are not as reliable as that of other more commonly applied EOR processes, and simulation results will not be able to accurately predict in-situ combustion performance without prior field testing.

This report focuses on the evaluation results for in-situ combustion in Schrader Bluff. Based on the overall screening of EOR processes, in-situ combustion was among the methods considered potentially favorable. Laboratory scale tube runs were conducted followed by simulation sensitivity studies to determine if the kinetic parameters for the crude oil were favorable. Described in the following subsections are the results of (1) experimental tube runs, and (2) simulation sensitivity studies as related to in-situ combustion in Schrader Bluff. If all factors evaluated to this point appear favorable, conducting a field pilot test would then be recommended.

Laboratory Tube Run Tests

The purpose of conducting a laboratory tube run is to establish the in-situ combustion behavior of Schrader Bluff crude oil on a restored-state Schrader Bluff core. Tube run 1 is a dry combustion test and tube run 2 is a wet combustion test, where the latter evaluates the burn characteristics of co-injecting air and water. Where successful, wet combustion is more efficient since the injected water carries forward some of the heat from behind the burn front.

The primary information of interest from laboratory tube runs for specified operational conditions include: general burning characteristics, fuel requirement, air requirement, air/fuel ratio, peak combustion temperature, and hydrocarbons recovered from swept zone. However, because many of the operational conditions of a laboratory experiment of this type is not scaled to field conditions, results should be considered qualitative relative to field performance. Only certain specific combustion characteristics of the oil tested in the laboratory can be considered representative of a field operation.

In-situ Combustion Tube Run Number 1

Run 1 is a dry combustion test, and was performed at 1800 psig using normal air at a stable injection flux of 100.6 scf/ft^{2}h. Both oil and core material were from Schrader Bluff reservoir.

The core material was crushed and fired at 325° C to remove any residual hydrocarbons. Synthetic brine was used for the brine phase. The packing and saturation of Schrader Bluff materials were followed according to standard procedures and have been shown to reproduce performance at field conditions reasonably well. All phases of the laboratory tube run were conducted by the U. Calgary.

The core was initially preheated to 89° F and gas injection by helium was maintained until stabilized conditions are established. Helium gas was then replaced with air and injection rates were maintained throughout the run at 100.6 scf/ft^{2}h. Ignition heaters were activated to initiate the burn process.

A stable burn was maintained as expected at the designed injection rate. However some difficulties were encountered and the run was terminated early. The coreholder is divided into 12 zones (6 in long) with 12 thermocouples to monitor the front progression. When the front reached zone 8, the temperature never attained the optimal range and the burn appeared to die out. At 14 hr into the experiment, a stable burn could not be reestablished and the experiment was terminated.

A summary plot of the thermal gradient is shown in Figure 1. The progression of the front can be followed as the peak temperatures shift in time with distance (tube combustion zone). The collapse of the fire front is seen at about 12 hours, where the peak temperature is diminished in zone 8 and is not evident in subsequent zones.

Upon inspection of the system after the experiment was concluded, it was determined that the high pressures involved in the experiment resulted in the crushing of the downstream portion of the tube, and combined with high heat losses resulted in the quenching of the fire front. Even so, some results were obtained and are summarized in Table 4.

It was concluded that burn characteristics appeared favorable for Schrader Bluff oil and running a second tube run was recommended. Initial estimates of kinetic parameters are provided from these data for simulation sensitivity studies.

In-situ Combustion Tube Run Number 2

A second in-situ combustion tube run was conducted. The primary difference between run 2 and run 1 was the co-injection of water after a stable burn was established (wet combustion process). The primary purpose of injecting water is to carry more of the heat forward from behind the front to the oil ahead of the front via steam generation. Air is much less efficient for heat transfer processes relative to water. Although not always successful, when the burn allows for co-injection of water the oil recovery efficiency is improved. Tube run 2 was to test this method for Schrader Bluff.

All other conditions were the same as for tube run number 1. Injection of brine was initiated 0.5 hr after the burn was initiated. The test was terminated at the normal time of 15 hr. The overall results with Schrader Bluff oil appeared favorable for water injection with in-situ combustion.

Also, learning from the first run, care was taken to temporarily reduce injection rates (air, water) when system pressures reached high levels. For example, water injection was stopped

for about 5 hr (starting about 0.5 hr. after water injection was started), but once resumed was continued for the remainder of the run. The lower core permeability was also a factor leading to high system pressures. Results for run number 2 are given in Table 5.

Figure 2 shows the temperature profiles for tube run number 2. Unlike run 1, the burn front progresses through all zones of the tube and does not prematurely collapse. As can be seen in the Figure 2 and Table 5, high temperature oxidation was achieved and maintained throughout. The overall recovery was excellent and equal to nearly 100% of the original oil in place. Stabilized oxygen and fuel requirements determined from the tube runs are provided in Table 5 and can be used for further simulation sensitivity studies.

In conclusion, laboratory tube runs showed that the burn characteristics of Schrader Bluff oil in the reservoir matrix appear favorable. Wet combustion (co-injection of water and air) demonstrated an incremental increase in oil recovery, suggesting that wet combustion is effective. Additional sensitivity simulation studies are recommended, and the results of this study are discussed in the next section. Sensitivity studies will provide a more accurate estimate of operational requirements and ultimate oil recovery potential.

Simulation Sensitivity Studies

The purpose for conducting model sensitivity studies is to utilize all available information for estimating potential oil recovery rates, operation costs, capital investment requirements, parameter sensitivities, etc. From this information monetary exposure risks can be evaluated to determine whether the potential return on investment outweighs the financial risk. One must still conduct a field pilot project to determine the impact of field heterogeneity, burden of operations management, and other factors not easily predicted. However, a field pilot project is expensive, and simulation studies can help to eliminate poor candidates before initiating long and expensive field pilot projects.

For example, air injection rates are one of the most important controlling factors of the burn. Because these rates are directly linked to equipment design (e.g., size of compressors), air injection rate requirements directly impact both initial capital costs and ongoing operational costs. Sensitivity studies can be used to estimate what the expected recovery rates are as a function of air injection rates, and what are the ultimate potential return on investment.

Model Description and Data Input

Oil was divided into two components, a light fraction or light oil (CO_2, C_1-C_{16}) and a heavy fraction or heavy oil (C_{17}-C_{36+}). The simulator modeled these and other components with three phases: solid (coke), liquid (water, heavy oil, light oil) and gas (oxygen and inert gas) making a total of six components. Inert gas included all noncondensible gases other than oxygen. Its property was assumed to be that of nitrogen except molecular weight was assigned a value between that of nitrogen and carbon dioxide. The oil properties were molar average values derived from the individual component properties. The critical pressure, critical temperature, molecular weight, and component formula for the light oil were 526 psi, 372° F, 82 amu, and $C_{5.7}H_{13.6}$, respectively, while that for the heavy oil were 158 psi, 1092°F, 409 amu and $C_{29.1}H_{60.24}$,

respectively. Other properties, such as thermal expansion, fluid compressibility, and fluid heat capacity, are given in Table 6.

Four chemical reactions were included in the simulation. They were cracking of heavy oil and oxidation or burning of heavy oil, light oil, and coke. The stoichiometries were derived for the hydrogen, carbon, and oxygen separately, as shown in Table 7.

For combustion of the light oil, heat of reaction was assumed to be 948,000 Btu/lb-mole of oil, while that for the heavy oil was assumed to be 3,490,000 Btu/lb-mole. For the coke, heat of reaction was assumed to be 225,000 Btu/lb-mole of coke. These are average values found in published literature.

The reservoir was modeled based on a 36-layer model developed by BPX-Alaska. In our study, 36 layers were lumped into 14 layers to reduce computational time. Average values for initial water saturation, oil saturation, porosity, permeability, and compressibility were calculated based on the 36-layer model. In each layer properties are constant and pertinent data of the 36 and 14 layer properties, such as initial water and oil saturation, pay zone thickness, permeability, porosity, and compressibility are shown in Tables 8 and 9.

Capillary pressure was neglected and initial pressure (1981 psi) and temperature (88°F) were kept the same as in the BPX-Alaska 36-layer model. Relative permeabilities varied with different types of rock. In this simulation, 14 layers are classified as six types of rock and their relative permeabilities for each layer are listed in Table 10(a-f).

Pattern selection should be based on such considerations as well investment resources, well productivity, reservoir structure, etc. In this study, the injector was set in the center of four 20 acre squares surrounded by eight producers. This formed an 80-acre inverted 9-spot pattern. One-fourth of an 80 acre 9-spot pattern was used in our simulation, and initial oil, water, and pore volume in place are 2.3397E7 ft^3, 3.4001E7 ft^3, and 5.7399E7 ft^3, respectively.

Choosing a grid system is always one of the most critical tasks. A total of nine primary equations (six mass balances, one energy balance, and two mole-fraction constraints) need to be solved simultaneously at each node. Computer time rises dramatically as the total number of nodes increases. The number of nodes in the grid system was minimized without sacrificing simulation accuracy. The maximum grid number allowed for STARS (version STARS 96) is 13,440, and the product of block number and components is limited to 26,880. A 10x10x14 grid, with a block size of 93.338 ft x 93.338 ft x thickness, was utilized. For such large grid blocks the block temperature corresponds to the average temperature instead of the combustion front temperature. This resulted in failure of the block to ignite and caused unrealistically high heat losses in our early simulations.

To get around this simulation difficulty, the heat loss parameters were lowered sufficiently to enable average temperature to reach combustion temperature at the combustion front. Also, the activation energy was set to 0 to ensure that the burn front can be maintained. These assumptions are commonly done because of the inherent limitations of currently available simulators. However, as a consequence, heat losses are not accurately simulated and predicted burn front characteristics will be optimistic.

Sensitivity Studies and Results

Many parameters can influence the predicted performance. Gaining this information will help in the project design and economic evaluation. Our study focused on the operational parameters as well as the reservoir and fluid parameters such as, injection rate, air enrichment, cracking reaction kinetics, wet versus dry combustion, phase equilibrium constant, and well spacing.

The effect of injection rate on the recovery was investigated for three different values, 10 MMscf/D (11.48 scf/Dft^2), 7 MMscf/D (8.03 scf/Dft^2) and 5 MMscf/D (5.74 scf/Dft^2). Air was injected simultaneously into all 14 layers. The injection pressure was kept just above the reservoir pressure (1981 psi). Ignition time varied with the injection rate. In this study, external heat was provided for the first two years, long enough to ensure that ignition had been established. All simulation runs were limited to 10 years to avoid excessive run time.

The temperature distribution of plane Y=1 and Z=3 was captured in Figure 3. This figure shows the location of the combustion front at various times and injection rates. A higher injection rate results in a higher combustion front temperature due to greater oxygen availability. This greater availability of oxygen accelerated the burning rate of fuel. Since the combustion front cannot advance until all the fuel is consumed, accelerated consumption of fuel translated into higher predicted peak temperature and rapid advancement of combustion front through the reservoir.

In the eighth year the position of the combustion front for 5 MMscf/D is in grid block 7, while for 7 MMscf/D is in block 9, and for 10 MMscf/D is in block 10, indicating breakthrough. Note higher temperatures during the early time period in block 1 are caused by the external heat added into the block. Sharp temperature decrease in block 1 after two years was due to the heat loss to the cold injection air and the surrounding while external heaters were turned off.

Figure 4 presents the effect of injection rates on cumulative oil production, cumulative oil recovery and air/oil ratio (AOR). Higher injection rate accelerated the oil production. Oil recovery in this study refers to volumetric oil recovery expressed as a percentage of initial oil in place. As injection rate increases from 5 MMscf/D to 10 MMscf/D, the cumulative oil recovery increases from 19.6% to 32.9% over a 10 year period.

The accelerated oil production rate and increased oil recovery at higher injection rates are caused by: (1) the availability of large volumes of combustion gas to displace the oil from the pores, (2) greater distillation and cracking effect due to higher temperature, and (3) enhanced swelling and solvent effect resulting from the generation of large volumes of CO_2 and lighter ends. It is also believed that the higher temperature caused the water near the combustion front to vaporize much more rapidly, accelerating the build up of steam bank ahead of the combustion front and contributed to the increased recovery.

AOR values for all three runs were below 24 Mscf/bbl, the upper limit for economic purposes. However, 7 MMscf/D case had a much lower AOR compared to that of 10 MMscf/D case, and slightly higher AOR and 6.4% additional oil recovery than that of 5 MMscf/D case. No breakthrough occurred in the 10 year period run and this 7 MMscf/D case appeared to be the best case.

A test was made to see if altering the 14-layer model to reduce computational time affected the accuracy of the results. Air was injected only into the eight high permeability layers by shutting in the six low permeability layers (NE and NF layers plus four silt layers). The computation time was reduced by almost 40%, while ultimate oil recovery remained essentially the same as the 14-layer models (see Figure 5). Extinction radius calculation, which will be discussed later, also showed that these six layers couldn't maintain a combustion. This test suggests that the low permeability NE sands, NF sands, and 6 silt layers contribute very little toward the oil production.

Reduction of oxygen content from the injection gas can result in incomplete burn, promote Low Temperature Oxidation (LTO) reactions (promotes inefficient oil production), lower the peak temperature and lower recovery. Thus, enriching the injection air with oxygen was investigated and compared with normal air injection (21%) to evaluate project efficiency. For comparison on equal amount of oxygen basis, the air injection rates were adjusted to maintain the same total oxygen for both enriched air and normal air. The effect of enriched air was investigated by injecting 30% and 40% (by volume) oxygen content air separately and the results were compared with normal air injection.

Figure 6 shows the comparison among these three cases. Though the peak oil production was accelerated with enriched air injection (i.e. the peak daily production rates occurred 4 and 2 years earlier, respectively, compared to the normal air injection), the final cumulative oil recovery was only marginally higher. The slightly higher oil overall recovery with enriched air can be attributed to the somewhat higher CO_2 and steam production. The increased steam production is the result of more rapid evaporation of connate and produced water.

The kinetic model employed in the simulator is that of Arrhenius:

$$R_A = A \exp(-E/RT) \quad (1)$$

where A is pre-exponential factor, E is activation energy and R is universal gas constant. The value of E/RT is determined from the laboratory results, but the value of A is assumed in calculating the reaction rate. Thus, a sensitivity study was conducted on A to determine the relative error introduced by the assumed values. Increasing A values can accelerate the combustion reaction rates. Conducting this study can give us the insight of the role of the kinetics or reaction rate played in the combustion process. Three runs were made to evaluate the effect of pre-exponential factor on oil recovery. The cases studied were: A=1.0E5 (base case), A=1.0E8, and A=1.0E11. Figure 7 shows that the oil recovery rate in this study is not strongly controlled by variation on A and the resulting kinetics of the combustion or reaction rate. The pre-exponential factor increased by one thousand times over the base case had resulted in oil recovery 1.16% OIP decrease, while a million times increase in the pre-exponential factor resulted in only 0.93% decrease in oil recovery.

In terms of heat reaching the displacement front, the dry combustion process is less efficient because much of the heat released by the burning oil remains behind the combustion front. To improve this situation, water is injected simultaneously with the air after initial combustion has been established. Water, with a specific heat of approximately four times that of air, can recover part of the heat remaining behind the combustion zone and carry that heat forward beyond the combustion zone either as superheated or as saturated steam.

To evaluate the potential benefit, the following two cases were tested (7 and 10 MMscf/D). The same amount of water, (1000 stb/D) was simultaneously injected with the air at the end of two years dry combustion for both cases. Simulation results were compared with the corresponding dry combustion runs.

Figure 8 shows that at constant water injection rate, the oil recovery is a function of air injection rate. The recovery in both cases was superior to the corresponding dry combustion cases. The additional recovery due to wet combustion was determined to be about 3.5%. Higher recovery is the result of the more rapid combustion front movement, the increased utilization of energy, and increased volume of fluid injected.

Also, the air requirement is lower in wet combustion process because of the lower amount of coke deposited and lower amount of fuel consumed, which resulted in the lower AOR, as presented in Figure 9.

Contradictory behavior occurred when we lowered the air injection rate to 5 MMscf/D. The ultimate oil recovery dropped to 15.2% OIP, 4.4% lower than that of the corresponding dry combustion, as presented in Figure 10. Figure 11 captures the profile of the temperature distribution at the fifth year. The figure clearly shows that the combustion front moved much more slowly and temperature was much lower than that of dry combustion. Apparently this high water injection partially quenched the combustion, which resulted in the lower oil recovery rate. Figure 12 is a snapshot of the saturation profile at the same time. Note that oil saturation was zero in the burned zone. This distribution also indicated that less oil was produced in this high water injection case. Thus, there appears to be a minimum air injection rate for a given water injection rate, below which, the recovery is likely to decline.

Another parameter evaluated was crude oil component K-values, or equilibrium constants. This value determines the volatility of the oil components and affects the degree of vaporization at the fire front. More or less oil will be flashed leaving less or more to burn, depending on the K value settings.

Providing accurate phase equilibrium constants, K, is always troublesome. An initial attempt was made to calculate K-values by using CMG WINPROP. Unfortunately, the K-values converged in STARS to the trivial solution. To examine the effect of this K-value, studies were conducted by introducing two sets of K-values: one was generated by STARS (Base K values), the other was generated from Schrader Bluff crude oil composition and an equation of state (EOS), WINPROP. Table 11 shows the two sets of K-values for pressure 1915 psi and 2015 psi, and temperature from 77° F to 927° F with 50 degree intervals.

The EOS generated K values were much higher for the light oil and lower for the heavy oil than the base K values. In other words, the EOS made the oil lighter. This presumes that most light oil will evaporate before it burns. Thus, the amount of residual oil available for burning and cracking was lowered, the rate of advancement of combustion front was increased and oil recovery was higher.

Oil recoveries for each set of K-values are compared in Figure 13. The EOS generated K values resulted in an additional 4% oil recovery over the base K values, which clearly underscored the importance of estimating this parameter correctly. The Base K values were used in all other

simulations, since these values were tuned to field in-situ combustion cases using STARS. There is no basis of comparing the relevancy of these values to actual Schrader Bluff conditions, e.g., a field pilot project.

To study the effect of well spacing, the air injection rates were kept the same at 10 MMscf/D while the well spacings were arbitrarily changed to 40 and 160 acres, respectively. Smaller well spacing resulted in higher flux and correspondingly higher oil recovery. Figure 14 shows the comparison of oil recovery among three different well spacings. As expected, the highest oil recovery was predicted for 40 acre spacing.

Extinction Radius Calculations

The extinction radius is defined as the radial distance (from the injection well) beyond which it is no longer possible to support combustion. For a combustion process to succeed, the extinction radius at any given injection rate must exceed the spacing between the injector and producer. The extinction radius is a function of air injection rate and rock-fluid properties.

A spread sheet program was developed. Details are discussed below.

Four chemical reactions, cracking of heavy oil and oxidation of heavy oil, light oil, and coke, can be written as shown in Table 7.

Multiplying the last equation by 13.4 and adding to the summation of the first three equations, one can get

$$2C_{29.1}H_{60.24} + 88.3164O_2 \rightarrow 60.2372H_2O + 58.1978CO_2 + 9135792 \ \ Btu/lbmol \qquad (2)$$

Knowing the amount of oxygen consumption or heavy oil cracking enables the calculation of the total reaction heat, Q. This reaction heat is equal to the heat loss to the surrounding rock and heat absorbed by the mixture, which includes unoxidized oxygen, nitrogen, CO_2, H_2O (connate and produced), and oil (heavy and light oils). The energy balance equation is expressed as,

$$Q = \sum (nC_p)_i (T - T_0) + (T - T_0)t/(h/KA) \qquad (3)$$

where T_0 is initial reservoir temperature, t is the time, A is the area, and K is the rock conductivity. Reaction heat Q and mixture moles, n_i, are functions of time; C_p is specific heat (Btu/lb) and h is pay thickness (ft).

Since average radial velocity, U, is equal to

$$U = r/t = Q_1/(2\pi rh) = Q_0(P_0/P_1)(T_1/T_0)/(2\pi rh) \qquad (4)$$

where Q_0 P_0, P_1, T_1, T_0 and h is the injection rate, initial injection pressure, reservoir pressure, reservoir temperature, initial injection temperature and pay zone thickness, respectively. Rewriting this equation and expressing time t as a function of radius gives,

$$t = (2\pi r^2 h)/[Q_0(P_0/P_1)(T_1/T_0)] \qquad (5)$$

Substituting this equation into the energy balance equation and using a trial-and-error method, the extinction radius is calculated with assumed minimum supporting combustion temperature. The injection rate for each layer is assumed to be proportional to its permeability. Figure 15 shows the extinction radius in each layer as a function of injection rates. In each layer, a higher injection rate results in a higher extinction radius.

In this study, the injector was set in the center of four 20-acre squares surrounded by eight producers. Hence, the extinction radius should be greater than 934 feet. Figure 15 indicates that a minimum air injection rate of 5 MMscf/D must be maintained to implement the successful combustion. At 5 MMscf/D, the front will not reach the producer for the NC/ND, NE, and NF sands. The silt layers contain no oil, and therefore, no extinction radius is calculated for layers 2, 5, 7, and 12. At 10 MMscf/D, production by layer is given in Figure 16. Most of the oil produced came from sand layers NB and OA.

Summary

This CRADA project was conducted to identify the most promising recovery processes for Schrader Bluff Milne Point, Alaska. In-situ combustion was evaluated more extensively and results of this evaluation are discussed in this report. The following summarizes the results of this evaluation.

A laboratory study of in-situ combustion determined that Schrader Bluff crude oil has favorable burn characteristics. A stable front can be maintained and recovery efficiencies are good. Wet combustion, a process combining in-situ combustion with water injection, appears to perform better than dry combustion provided the air injection rate is sufficiently high. A first estimate of air requirements, burn rates, etc., were determined.

Results of a simulation sensitivity study of in-situ combustion were consistent with observed behavior in the laboratory.

Extinction radius calculations indicated that to implement a successful 80 acre spacing in-situ combustion project, a minimum of 5 MMscf/D air injection rate is required.

The simulation study suggests that in-situ combustion cannot be maintained in the low permeability sands (NC/ND, NE, and NF) at the minimum injection rate of 5 MMscf/D.

No pronounced advantage in using high oxygen content air is predicted for the Schrader Bluff reservoir. Enriched air will accelerate peak oil production but has minimal effect on the overall oil recovery.

The pre-exponential factor of the combustion kinetics has only marginal effect on predicted oil recovery. However, the phase equilibrium K values have significant impact on the predicted ultimate oil recovery. Results from a field pilot project is needed to improve the estimated K values.

Wet combustion causes higher oil recovery and requires lower AOR than that of dry combustion. AOR values for both dry and wet combustion are within the acceptable range for successful economical projects. However, high water injection and/or low air injection rate may partially quench the combustion and reduce the ultimate oil recovery.

REFERENCES

Bailey, H.R., and B.K. Larkin: "Conduction-Convection in Underground Combustion," AIME Petroleum Transactions, Vol. 219, pp. 320-331, 1960.

Bidinger, C.R. and J.F. Dillon: "Milne Point Schrader Bluff: Finding the Keys to Two Billion Barrels," SPE Paper 30289, Pres. Int. Heavy Oil Symposium, Calgary Canada, 19-21 June 1995.

Buchanan, L. and M. Raicar: "Sensitivity Study of Field Scale Combustion Simulation for a Lloydminster-Type Heavy Oil Reservoir," Petroleum Society of CIM, paper No. 83-34-47.

Chang, Y., G.A. Pope and K. Sepehrnoori: "A Higher-Order Finite Difference Compositional Simulator," J. Pet. Sci. Eng. No. 1, pp. 35-50, November 1990.

Coats, K.H.: "In-situ Combustion Model," Soc. Pet. Eng. J., Vol. 20(6), pp. 533-554, December 1980.

Craig, F. F., Jr., and D.R. Parrish: "A Multipilot Evaluation of the COFCAW Process," J. Pet. Tech. pp. 659-666, June 1974.

Crookston, R.B., W.E. Culham, and W.H. Chen: "A Numerical Simulation Model for Thermal Recovery Processes," SPE Paper 6724, 9-12 October 1977.

DeRuiter, R.A., L.J. Nash, and M.S. Wyrick: "Solubility and Displacement Behavior of Carbon Dioxide and Hydrocarbon Gases with a Viscous Crude Oil," SPE Paper 20523, Pres. SPE 65th Annual Technical Conference, New Orleans, LA, 23-26 September 1990.

Dingley, A.J.: "The Combustion Recovery Process -- Principles and Practice," J. Canadian Pet. Tech., pp. 196-205, October-December 1965.

Farouq Ali, S.M.: "Multiphase, Multidimensional Simulation of In-Situ Combustion," SPE Paper 6896, presented at SPE 52nd Annual Technical Conference and Exhibition, Denver, 9-12 October 1977.

Fox, J.B. and J.D. Earsley: "Application of Downhole Electric Heat Trace System in Arctic Completions," SPE Paper 49188, Pres. SPE Annual Technical Conference, New Orleans, Louisiana, 27-30 September 1998.

Gondouin, M. and J.M. Fox III: "The Challenge of West Sak Heavy Oil: Analysis of an Innovative Approach," SPE Paper 22077, Pres. Int. Arctic Technology Conf., Anchorage, AK, 29-31 May 1991.

Laureshen, C.J., S.A. Mehta, R.G. Moore, and M.G. Ursenbach: "Ramped Temperature Oxidation Characteristics of Alaska Crude Oil," report submitted by Dept. Chemical & Petroleum Eng., U. Calgary, 11 September 1998.

Laureshen, C.J., S.A. Mehta, R.G. Moore, N.E. Okazawa, and M.G. Ursenbach: "BDM Petroleum Technologies Combustion Tube Test No. 1 (Test No. 287), Alaska Reservoir," report submitted by Dept. Chemical & Petroleum Eng., U. Calgary, 10 December 1998.

Laureshen, C.J., S.A. Mehta, R.G. Moore, N.E. Okazawa, and M.G. Ursenbach: "BDM Petroleum Technologies Combustion Tube Test No. 2 (Test No. 287), Alaska Reservoir," report submitted by Dept. Chemical & Petroleum Eng., U. Calgary, 10 December 1998.

MacAllister, D.J. and R.A. DeRuiter: "Further Development and Application of Simulated Distillation for Enhanced Oil Recovery," SPE Paper 14335, Pres. SPE 60th Annual Technical Conf., Las Vegas, NV, 22-25 September 1985.

McKean, T.A.M., A.H. Thomas, J.R. Chesher, MC. Weggeland: "Schrader Bluff CO_2 EOR Evaluation," SPE Paper 54619, Pres. SPE Western Regional Meeting, Anchorage, Alaska, 26-28, May, 1999.

Moore, R.G., M.G. Ursenbach, C.J. Laureshen, J.D.M. Belgrave, and R. Mehta: "Ramped Temperature Oxidation Analysis of Athabasca Oil Sands Bitumen," Petroleum Society of CIM paper 95-23, pres. 46th Annual Technical Meeting, Banff, Alberta Canada, 14-17 May 1995.

Moore, R.G., C.J. Laureshen, M.G. Ursenbach, R. Mehta, and J.D.M. Belgrave: "Combustion/Oxidation Behavior of Athabasca Oil Sands Bitumen," SPE Paper 35392, pres. SPE/DOE Improved Oil Recovery Symposium, Tulsa, Oklahoma, 21-24 April 1996.

Okuyiga, M.O.: "Equation of State Characterization and Miscibility Development in a Multiple Phase Hydrocarbon System," SPE Paper 24937, Pres. SPE Annual Technical Conference, Washington D.C., 4-7 October 1992.

Parrish, D.R., and Craig, F. F.: "Laboratory Study of a Combination of Forward Combustion and Waterflooding," the COFCAW Process, J. Pet. Tech. pp. 753-761, June 1969.

Rubin, B. and W.L. Buchanan: "A General Purpose Thermal Model," SPE Paper 11713, presented at the 1983 California Regional Meeting, Ventura, California, 23-25 March 1983.

Sarathi, P.S. and D.K. Olsen: DOE Cost-Shared In-situ Combustion Projects Revisited," Paper ISC-4 Pres. at 1994 DOE/NIPER Conference, Tulsa, Oklahoma, April 21-22, 1994; Proceedings publ. in U.S. DOE Report NIPER/BDM-OK-0086 (DE95000116),. January 1995.

Sarathi, P.S. and D.K. Olsen (ed.): "Field Application of In Situ Combustion–Past Performance/Future Application, Symposium Proceedings," 1994 DOE/NIPER Conference, Tulsa, Oklahoma, April 21-22, 1994; Proceedings publ. in U.S. DOE Report NIPER/BDM-OK-0086 (DE95000116),. January 1995.

Sarathi, P.S.: "In-Situ Combustion Handbook–Principles and Practices," U.S. DOE Report DOE./PC/91008-0374, 401 pp., January 1999.

Sharma, A.K., S.L. Patil, V.A. Kamath, and G.D. Sharma: "Miscible Displacement of Heavy West Sak Crude by Solvents in Slim Tube," SPE Paper 18761, Pres. SPE California Regional Mtg., Bakersfield, California, 5-7 April 1989.

Smalley, P.C., N.S. Goodwin, J.F. Dillon, C.R. Bidinger, R.J. Drozd: "New Tools Target Oil Quality Sweetspots in Viscous Oil Accumulations," SPE Annual Technical Conference, Denver, Colorado, 6-9 October 1996.

Strycker, A., P. Sarathi, and S. Wang: "Evaluation of In-situ Combustion for Schrader Bluff," U.S. DOE Report TRWPT/CRADA-002-1, 46 pp., March 1999.

Wang, X., P.S. Sarathi, C.R. Bidinger: "Field Scale Combustion Simulation Studies–Investigation of Reservoir Fluid and Operational Parameters on Project Performance, Pres. Paper 1998.044 at the 7th UNITAR International Conference on Heavy Crude and Tar Sands, Beijing, China, 27-30 October 1998.

Youngren, G.K.: "Development and Application of an In-Situ Combustion Reservoir Simulator," Soc. Pet. Eng. J., pp. 39-51, February 1980.

Table 1. - Summary of reservoir parameters for Schrader Bluff Milne Point, Alaska

Property	Value
OOIP (MMbbl)	1800 (Milne Point Unit)
Recoverable (MMbbl)	250
Produced (MMbbl)	3 (as of 1996)
Areal Extent (Acres)	22,000 (Milne Point Unit)
Depth (ft)	4300 (ranges mostly from 3700-4800)
Temperature (°F)	90 (ranges mostly from 80-100)
Gross Pay (ft)	270 (ranges mostly from 30-40, individual sands)
Net Pay (ft)	75 (ranges mostly from 15-20, individual sands)
Porosity (fraction)	0.25 (ranges mostly from 0.25-0.30)
Permeability (mD)	250-1250 (ranges mostly from 50-3000)
Swi (fraction PV)	0.35 (ranges mostly from 0.35-0.55)
FVF (bbl/stb)	1.06
Gravity (°API)	19 (ranges mostly from 14-21)
Viscosity (reservoir conditions, live oil, cP)	37 (ranges mostly from 30-600)
GOR (scf/stb)	200 (ranges mostly from 100-200)
Initial Pressure (psi)	1900 (ranges mostly from 1900-2000)

Table 2. - Composition of Schrader Bluff crude oil

Component	Oil (mole%)	Component	Oil (mole%)	Component	Oil (mole%)
Nitrogen (N_2)	0.054	Nonanes (C9)	2.457	Tricosanes (C23)	1.692
Carbon Dioxide (CO_2)	0.221	Decanes (C10)	2.494	Tetracosanes (C24)	1.244
Methane (C1)	30.27	Undecanes (C11)	2.576	Pentacosanes (C25)	1.185
Ethane (C2)	0.275	Dodecanes (C12)	3.013	Hexacosanes (C26)	1.21
Propane (C3)	0.214	Tridecanes (C13)	3.393	Heptacosanes (C27)	0.931
Iso-Butane (iC4)	0.148	Tetradecanes (C14)	3.428	Octacosanes (C28)	1.054
n-Butane (nC4)	0.388	Pentadecanes (C15)	3.034	Nonacosanes (C29)	1.104
Iso-Pentane (iC5)	0.352	Hexadecanes (C16)	2.839	Triacontanes (C30)	0.821
n-Pentane (nC5)	0.374	Heptadecanes (C17)	2.677	C31	0.905
Hexanes (C6)	0.9	Octadecanes (C18)	2.739	C32	0.725
Benzene	0.028	Nonadecanes (C19)	2.134	C33	0.652
Heptanes (C7)	1.537	Eicosanes (C20)	2.357	C34	0.625
Toluene	0.186	Henicosanes (C21)	1.768	C35	0.595
Octanes (C8)	2.118	Docosanes (C22)	1.663	C36+	13.621

Table 3. - Summary of favorable and unfavorable risk factors for in-situ combustion

Favorable Risk Factors	Unfavorable Risk Factors
High reservoir temperature (≥150° F)	Extensive reservoir fractures and faults
Low vertical permeability	Large gas caps
Good lateral continuity	Strong water drive
Thin sand layers (≤50 ft)	Highly heterogeneous reservoir
High oil saturation (So*porosity≥0.1)	Low oil saturation
Good fluid transmissibility (permeability*thickness/viscosity≥20 md-ft/cp)	High oil viscosity (>5000 cp), low oil permeability in thin sands
Good overburden competence	
High dip	
Uniform permeability profile	

Table 4. - Summary of results for in-situ combustion tube run number 1

Core Porosity	0.436	Pre-Heat Temp.	89° F
Core Permeability	4.3 Darcy	Peak Temperature	1146° F
Pressure	1800 psig	Displ. Front Velocity	0.61 ft/hr
Inj. Air Flux	100 scf/ft^{2}hr	Air Requirement, Stabilized	166 l(ST)/l
Water/Air Ratio	0	Oxygen Requirement, Stabilized	35.7 l(ST)/l
Oil Sat., Initial	0.588	Fuel Requirement, Stabilized	1.04 lbm/ft^3
Water Sat., Initial	0.412	Air/Fuel Ratio, Stabilized	160 scf/lb
Overall recovery	0.845*	Oxygen Utilization, Stabilized	0.983

*Not comparative with Run 2, since only 60% of the core was burned.

Table 5. - Summary of results for in-situ combustion tube run number 2

Core Porosity	0.426	Pre-Heat Temp.	89° F
Core Permeability	0.5 Darcy	Peak Temperature	1053° F
Pressure	1800 psig	Displ. Front Velocity	0.48 ft/hr
Inj. Air Flux	100 scf/ft^{2}hr	Air Requirement, Stabilized	210 l(ST)/l
Water/Air Ratio	0.98 kg/l	Oxygen Requirement, Stabilized	41.2 l(ST)/l
Oil Sat., Initial	0.582	Fuel Requirement, Stabilized	1.40 lbm/ft^3
Water Sat., Initial	0.418	Air/Fuel Ratio, Stabilized	151 scf/lb
Overall recovery	0.921	Oxygen Utilization, Stabilized	0.985

Table 6. - Properties of heavy and light oil fractions in the simulation sensitivity study

	Heavy Fraction	Light Fraction
Molecular Weight (lbm/lbm mol)	409	82
Critical Pressure (psi)	158	526
Critical Temperature (°F)	1092	372
Gas-Phase Heat Capacities, $C_p=A+BT+CT^2+DT^3$ (Btu/(lbm mol-°F))		
A	-8.14	-1.89
B	0.549	0.1275
C	-1.68e-4	-3.9e-5
D	1.98e-8	4.6e-9
Compressibilities (psi^{-1})	5e-6	5e-6
Thermal Expansion Coefficient (°F^{-1})	1.496e-4	2.839e-4

Table 7. - Four chemical reactions defining in-situ combustion for Schrader Bluff crude oil

Reaction Type	Reaction Equation
Cracking	$C_{29.1}H_{60.24} \rightarrow 2.754\ C_{5.7}H_{13.6} + 13.4\ CH_{1.7} + 2.00 \times 10^4$ (Btu/lb-mole)
Heavy Oil Oxidation	$C_{29.1}H_{60.24} + 44.16\ O_2 \rightarrow 30.12\ H_2O + 29.1\ CO_2 + 3.49 \times 10^6$ (Btu/lb-mole)
Light Oil Oxidation	$C_{5.7}H_{13.6} + 9.1\ O_2 \rightarrow 6.8\ H_2O + 5.7\ CO_2 + 9.48 \times 10^5$ (Btu/lb-mole)
Coke Oxidation	$CH_{1.7} + 1.425\ O_2 \rightarrow 0.85\ H_2O + CO_2 + 2.25 \times 10^5$ (Btu/lb-mole)

Note: Reaction rate is proportional to A exp(-E/RT)

Table 8. - Schrader Bluff reservoir 36-layer model description

	36-Layer Model							14-Layer Model
Zone	Layer	Dz	netgrs	Por	Cr	Sw	Kx	Layer
NA	1	4	0.671	0.304	6.2E-5	0.5235	234	1
	2	4	0.762	0.319	5.6E-5	0.5235	445	
	3	4	0.963	0.306	4.6E-5	0.5235	343	
	4	4	0.42	0.235	3.8E-5	0.5235	23	
Silt	5	10.11	0.08	0.24	3.18E-4	1	0.7	2
NB	6	4.21	0.633	0.24	3.3E-5	0.4283	51	3
	7	4.21	0.76	0.3	5.0E-5	0.4283	261	
	8	4.21	0.76	0.324	5.2E-5	0.4283	501	
	9	4,21	0.76	0.316	3.8E-5	0.4283	409	4
	10	4.21	0.62	0.29	2.8E-5	0.4283	46	
	11	4.21	0.61	0.221	3.6E-5	0.4283	6	
Silt	12	11.24	0.08	0.23	1.96E-4	1	0.7	5
NC/ ND	13	1.07	0.923	0.304	4.6E-5	0.4	292	6
	14	1.07	0.624	0.328	6.7E-5	0.4	312	
	15	1.07	0.76	0.31	5.2E-5	0.4	358	
	16	1.07	0.868	0.231	2.6E-5	0.4	7	
Silt	17	9.43	0.08	0.24	2.04E-4	1	0.7	7
NE	18	48.01	0.549	0.262	2.04E-4	0.5511	20	8
NF	19	36.72	0.08	0.24	2.04E-4	0.5073	0.7	9
OA	20	3.75	0.687	0.238	5.5E-5	0.398	33	10
	21	3.75	0.946	0.315	6.7E-5	0.398	417	
	22	3.75	0.505	0.183	3.3E-5	0.398	27	
	23	3.75	0.946	0.262	5.0E-5	0.398	111	
	24	3.75	0.964	0.306	5.6E-5	0.398	246	11
	25	3.75	0.837	0.279	5.0E-5	0.398	159	
	26	3.75	0.711	0.225	3.1E-5	0.398	63	
	27	3.75	0.883	0.244	3.3E-5	0.398	84	
Silt	28	31.83	0.07	0.22	3.5E-4	1	0.7	12
OB	29	3.84	0.882	0.262	4.6E-5	0.4571	75	13
	30	3.84	0.943	0.285	5.3E-5	0.4571	135	
	31	3.84	0.941	0.29	4.5E-5	0.4571	186	
	32	3.84	0.941	0.307	4.6E-5	0.4571	279	
	33	3.84	0.836	0.274	4.0E-5	0.4571	129	14
	34	3.84	0.08	0.217	3.7E-5	0.4571	7	
	35	3.84	0.08	0.228	3.5E-5	0.4571	10	
	36	3.84	0.941	0.257	4.3E-5	0.4571	75	

Table 9. - Schrader Bluff reservoir 14-layer model description

	14-Layer Model						
Zone	**Layer**	**Dz**	**netgrs**	**Por**	**Cr**	**Sw**	**Kx**
NA	1	16.00	0.704	0.298	5.133E-5	0.5235	296.90
Silt	2	10.11	0.080	0.240	3.180E-4	1.0000	0.70
NB	3	12.63	0.718	0.291	4.571E-5	0.4283	283.98
	4	12.63	0.663	0.279	3.427E-5	0.4283	172.37
Silt	5	11.24	0.080	0.230	1.960E-4	1.0000	0.70
NC/ND	6	4.28	0.794	0.290	4.610E-5	0.4000	233.81
Silt	7	9.43	0.080	0.240	2.040E-4	1.0000	0.70
NE	8	48.01	0.549	0.262	2.040E-4	0.5511	20.00
NF	9	36.72	0.080	0.240	2.040E-4	0.5073	0.70
OA	10	15.00	0.771	0.260	5.354E-5	0.3980	173.73
	11	15.00	0.849	0.266	4.330E-5	0.3980	144.09
Silt	12	31.83	0.070	0.220	3.500E-4	1.0000	0.70
OB	13	15.36	0.927	0.286	4.753E-5	0.4571	170.22
	14	15.36	0.484	0.261	4.113E-5	0.4571	92.81

Dz = Layer Thickness, ft

Netgrs = Net-to-Gross Mulitplier

Por = Porosity, fraction

Cr = Compressibility, psi^{-1}

Sw = Water Saturation, fraction

Kx = Permeability in the X Direction, mD

Table 10 (a). - Liquid-gas and water-oil relative permeabilities for layers 1, 8 and 9, 14-layer model

Liquid-Gas Relative Permeabilities			Water-Oil Relative Permeabilities		
Liquid Saturation, Sl	Krg	Krog	Water Saturation, Sw	Krw	Krow
0.00	1.0000	0.0000	0.00	0.0000	1.0000
0.05	0.8563	0.0013	0.05	0.0061	0.909
0.10	0.7342	0.0046	0.10	0.0122	0.818
0.15	0.6378	0.0107	0.15	0.0204	0.7271
0.20	0.5627	0.0199	0.20	0.0294	0.6301
0.25	0.4794	0.0332	0.25	0.0387	0.5167
0.30	0.4171	0.0510	0.30	0.0482	0.4116
0.35	0.361	0.0735	0.35	0.0587	0.305
0.40	0.3081	0.1020	0.40	0.0703	0.2136
0.45	0.2567	0.1362	0.45	0.0815	0.1475
0.50	0.2042	0.1767	0.50	0.094	0.1048
0.55	0.1559	0.2236	0.55	0.1101	0.0759
0.60	0.1201	0.2773	0.60	0.1322	0.0569
0.65	0.0863	0.3383	0.65	0.1566	0.0385
0.70	0.067	0.4072	0.70	0.1928	0.0243
0.75	0.0517	0.4843	0.75	0.2397	0.0186
0.80	0.0398	0.5698	0.80	0.3006	0.0125
0.85	0.0299	0.6639	0.85	0.3915	0.0094
0.90	0.0199	0.7667	0.90	0.5106	0.0062
0.95	0.01	0.8788	0.95	0.6948	0.0031
1.00	0.0000	1.0000	1.00	1.0000	0.0000

Table 10(b). - Liquid-gas and water-oil relative permeabilities for layers 3 and 4, 14-layer model

Liquid-Gas Relative Permeabilities			Water-Oil Relative Permeabilities		
Sl	Krg	Krog	Sw	Krw	Krow
0.00	1.0000	0.0000	0.00	0.0000	1.0000
0.05	0.8563	0.0013	0.05	0.0045	0.8466
0.10	0.7342	0.0046	0.10	0.009	0.7489
0.15	0.6378	0.0107	0.15	0.0136	0.6588
0.20	0.5627	0.0199	0.20	0.0181	0.5768
0.25	0.4794	0.0332	0.25	0.0226	0.5144
0.30	0.4171	0.0510	0.30	0.0286	0.4494
0.35	0.361	0.0735	0.35	0.0355	0.3871
0.40	0.3081	0.1020	0.40	0.0446	0.3333
0.45	0.2567	0.1362	0.45	0.0574	0.2831
0.50	0.2042	0.1767	0.50	0.0743	0.2192
0.55	0.1559	0.2236	0.55	0.0965	0.1696
0.60	0.1201	0.2773	0.60	0.1254	0.128
0.65	0.0863	0.3383	0.65	0.1622	0.0929
0.70	0.067	0.4072	0.70	0.2104	0.0654
0.75	0.0517	0.4843	0.75	0.2736	0.0469
0.80	0.0398	0.5698	0.80	0.3544	0.0314
0.85	0.0299	0.6639	0.85	0.4588	0.0208
0.90	0.0199	0.7667	0.90	0.5971	0.0122
0.95	0.01	0.8788	0.95	0.7741	0.0056
1.00	0.0000	1.0000	1.00	1.0000	0.0000

Table 10(c). - Liquid-gas and water-oil relative permeabilities for layer 6, 14-layer model

Liquid-Gas Relative Permeabilities			Water-Oil Relative Permeabilities		
Sl	Krg	Krog	Sw	Krw	Krow
0.00	1.0000	0.0000	0.00	0.0000	1.0000
0.05	0.8563	0.0013	0.05	0.0038	0.8466
0.10	0.7342	0.0046	0.10	0.0075	0.7489
0.15	0.6378	0.0107	0.15	0.0113	0.6588
0.20	0.5627	0.0199	0.20	0.0151	0.5768
0.25	0.4794	0.0332	0.25	0.0189	0.5144
0.30	0.4171	0.0510	0.30	0.0243	0.4494
0.35	0.361	0.0735	0.35	0.0305	0.3871
0.40	0.3081	0.1020	0.40	0.0398	0.3333
0.45	0.2567	0.1362	0.45	0.0521	0.2831
0.50	0.2042	0.1767	0.50	0.0681	0.2192
0.55	0.1559	0.2236	0.55	0.0888	0.1696
0.60	0.1201	0.2773	0.60	0.1167	0.1280
0.65	0.0863	0.3383	0.65	0.153	0.0929
0.70	0.067	0.4072	0.70	0.2	0.0645
0.75	0.0517	0.4843	0.75	0.261	0.0469
0.80	0.0398	0.5698	0.80	0.3418	0.0314
0.85	0.0299	0.6639	0.85	0.4486	0.0208
0.90	0.0199	0.7667	0.90	0.5873	0.0122
0.95	0.01	0.8788	0.95	0.7672	0.0056
1.00	0.0000	1.0000	1.00	1.0000	0.0000

Table 10(d). - Liquid-gas and water-oil relative permeabilities for layers 10 and 11, 14-layer model

Liquid-Gas Relative Permeabilities			Water-Oil Relative Permeabilities		
Sl	Krg	Krog	Sw	Krw	Krow
0.00	1.0000	0.0000	0.00	0.0000	1.0000
0.05	0.8444	0.0013	0.05	0.0033	0.9209
0.10	0.7310	0.0046	0.10	0.006	0.8361
0.15	0.6464	0.0107	0.15	0.009	0.7427
0.20	0.5742	0.0199	0.20	0.0122	0.6413
0.25	0.4994	0.0332	0.25	0.0153	0.5369
0.30	0.4458	0.0510	0.30	0.0185	0.4261
0.35	0.3973	0.0735	0.35	0.0223	0.3342
0.40	0.3454	0.1020	0.40	0.0266	0.2581
0.45	0.2964	0.1362	0.45	0.0326	0.1919
0.50	0.2429	0.1767	0.50	0.0395	0.1411
0.55	0.2011	0.2236	0.55	0.0483	0.0999
0.60	0.1656	0.2773	0.60	0.0598	0.0648
0.65	0.1311	0.3383	0.65	0.0768	0.0464
0.70	0.0988	0.4072	0.70	0.1063	0.0318
0.75	0.0733	0.4843	0.75	0.1491	0.0229
0.80	0.0514	0.5698	0.80	0.2159	0.0143
0.85	0.0350	0.6639	0.85	0.3134	0.0107
0.90	0.0178	0.7667	0.90	0.4649	0.0071
0.95	0.0088	0.8788	0.95	0.6736	0.0036
1.00	0.0000	1.0000	1.00	1.0000	0.0000

Table 10(e). - Liquid-gas and water-oil relative permeabilities for layers 13 and 14, 14-layer model

Liquid-Gas Relative Permeabilities			Water-Oil Relative Permeabilities		
Sl	Krg	Krog	Sw	Krw	Krow
0.00	1.0000	0.0000	0.00	0.0000	1.0000
0.05	0.8444	0.0013	0.05	0.0025	0.8516
0.10	0.7310	0.0046	0.10	0.0049	0.7032
0.15	0.6464	0.0107	0.15	0.0074	0.5658
0.20	0.5742	0.0199	0.20	0.0098	0.4680
0.25	0.4994	0.0332	0.25	0.0118	0.3848
0.30	0.4458	0.0510	0.30	0.0153	0.3150
0.35	0.3973	0.0735	0.35	0.0195	0.2541
0.40	0.3454	0.1020	0.40	0.0267	0.2013
0.45	0.2964	0.1362	0.45	0.0372	0.1582
0.50	0.2429	0.1767	0.50	0.0512	0.1269
0.55	0.2011	0.2236	0.55	0.0696	0.0997
0.60	0.1656	0.2773	0.60	0.0954	0.0769
0.65	0.1311	0.3383	0.65	0.1289	0.0529
0.70	0.0988	0.4072	0.70	0.1696	0.0368
0.75	0.0733	0.4843	0.75	0.2288	0.0207
0.80	0.0514	0.5698	0.80	0.3069	0.0123
0.85	0.0350	0.6639	0.85	0.4140	0.0092
0.90	0.0178	0.7667	0.90	0.5620	0.0062
0.95	0.0088	0.8788	0.95	0.7625	0.0031
1.00	0.0000	1.0000	1.00	1.0000	0.0000

Table 10(f). - Liquid-gas and water-oil relative permeabilities for layers 2, 5, 7 and 12, 14-layer model

Liquid-Gas Relative Permeabilities			Water-Oil Relative Permeabilities		
Sl	Krg	Krog	Sw	Krw	Krow
0.00	0.7	0	0	0	0.7
1.00	0	0.7	1.00	0.7	0

Table 11. - Two sets of K values generated by CMG software

Base K Values (generated from STARS)				EOS K values (generated by WINPROP)			
Heavy Oil		Light Oil		Heavy Oil		Light Oil	
2.51e-9	2.39e-9	1.54e-4	1.46e-4	9.78e-20	8.89e-20	9.1030E-03	8.2680E-03
2.23e-8	2.12e-8	4.80e-4	4.56e-4	2.35e-16	2.14e-16	1.9943E-02	1.8115E-02
1.54e-7	1.46e-7	1.28E-03	1.22E-03	6.83e-14	6.21e-14	3.8548E-02	3.5013E-02
8.5e-7	8.08e-7	3.04E-03	2.89E-03	5.12e-12	4.65e-12	6.7585E-02	6.1388E-02
3.91e-6	3.72e-6	6.48E-03	6.16E-03	1.53e-10	1.39e-10	1.0968E-01	9.9618E-02
2.63e-5	2.50e-5	1.26E-02	1.20E-02	2.37e-9	2.15e-9	1.6721E-01	1.5188E-01
8.42e-5	8.00e-5	1.79E-02	1.70E-02	2.26e-8	2.06e-8	2.4224E-01	2.2003E-01
2.42e-4	2.30e-4	2.31E-02	2.20E-02	1.50e-7	1.37e-7	3.3639E-01	3.0554E-01
4.10e-4	3.90e-4	2.95E-02	2.80E-02	7.52e-7	6.83e-7	4.5086E-01	4.0951E-01
5.89e-4	5.60e-4	3.47E-02	3.30E-02	3.01e-6	2.73e-6	5.8641E-01	5.3263E-01
8.84e-4	8.40e-4	4.00E-02	3.80E-02	1.00e-5	9.12e-6	7.4341E-01	6.7524E-01
1.66E-03	1.58E-03	4.52E-02	4.30E-02	2.89e-5	2.63e-5	9.2191E-01	8.3737E-01
2.84E-03	2.70E-03	5.05E-02	4.80E-02	7.38e-5	6.70e-5	1.121608	1.018756
3.89E-03	3.70E-03	5.68E-02	5.40E-02	1.70E-04	1.54E-04	1.342004	1.218941
5.58E-03	5.30E-03	6.31E-02	6.00E-02	3.59E-04	3.26E-04	1.582379	1.437273
7.68E-03	7.30E-03	6.94E-02	6.60E-02	7.05E-04	6.41E-04	1.841869	1.672968
1.05E-02	1.00E-02	7.68E-02	7.30E-02	1.30E-03	1.18E-03	2.119497	1.925137
1.79E-02	1.70E-02	8.84E-02	8.40E-02	2.27E-03	2.06E-03	2.414210	2.192825

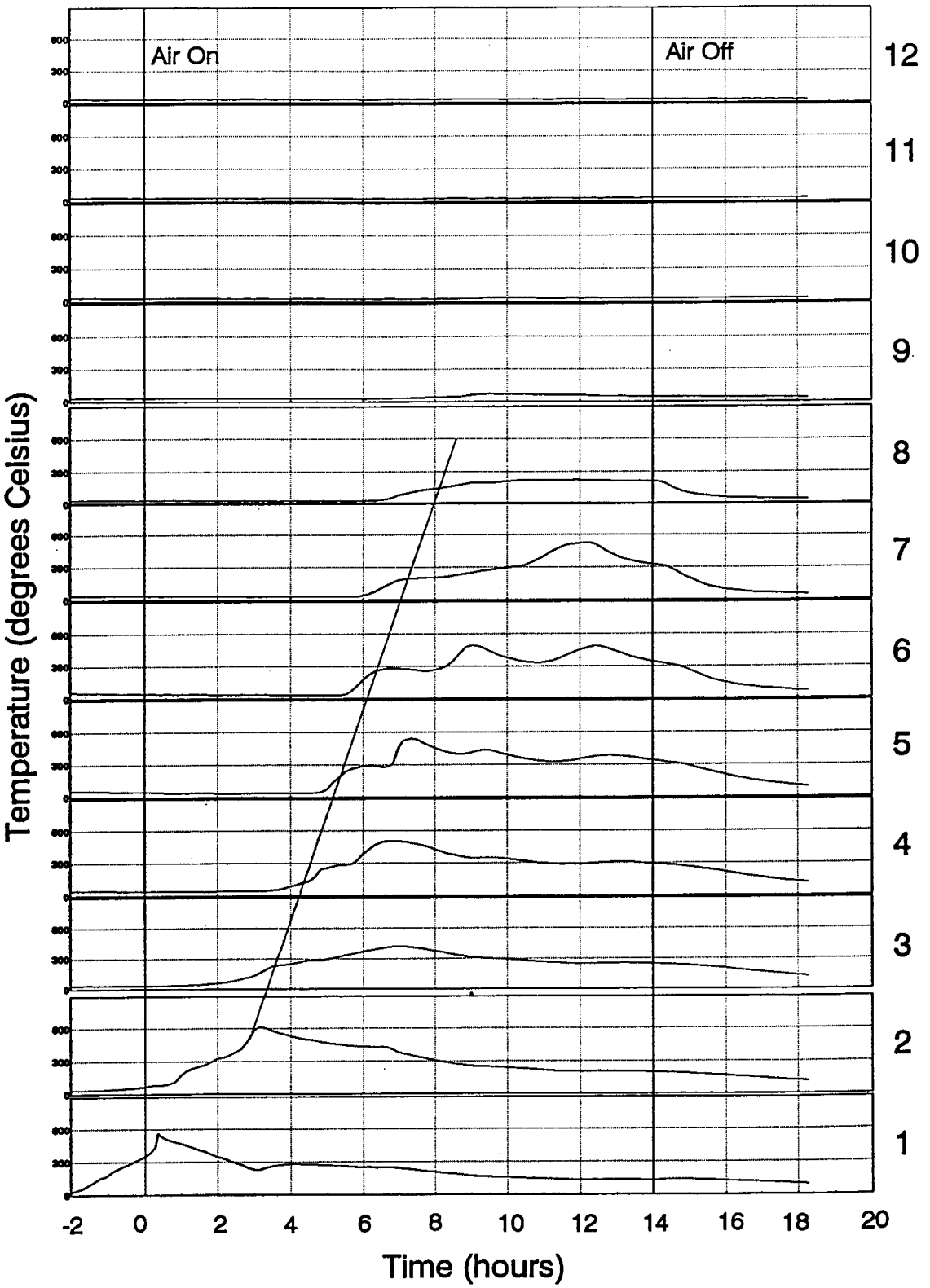

Figure 1. - Combustion zone temperature profiles for in-situ combustion tube test number 1

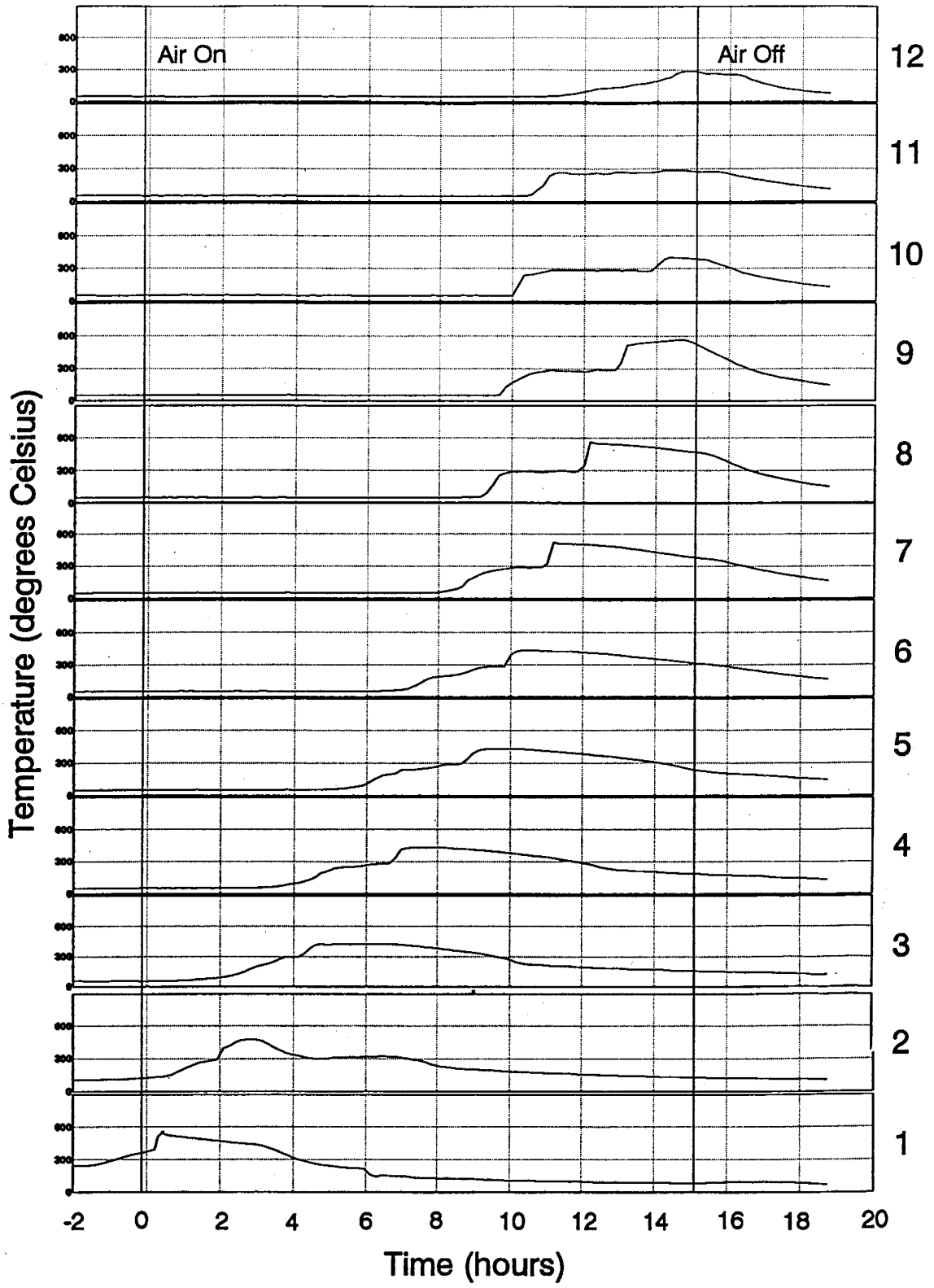

Figure 2. - Combustion zone temperature profiles for in-situ combustion tube test number 2

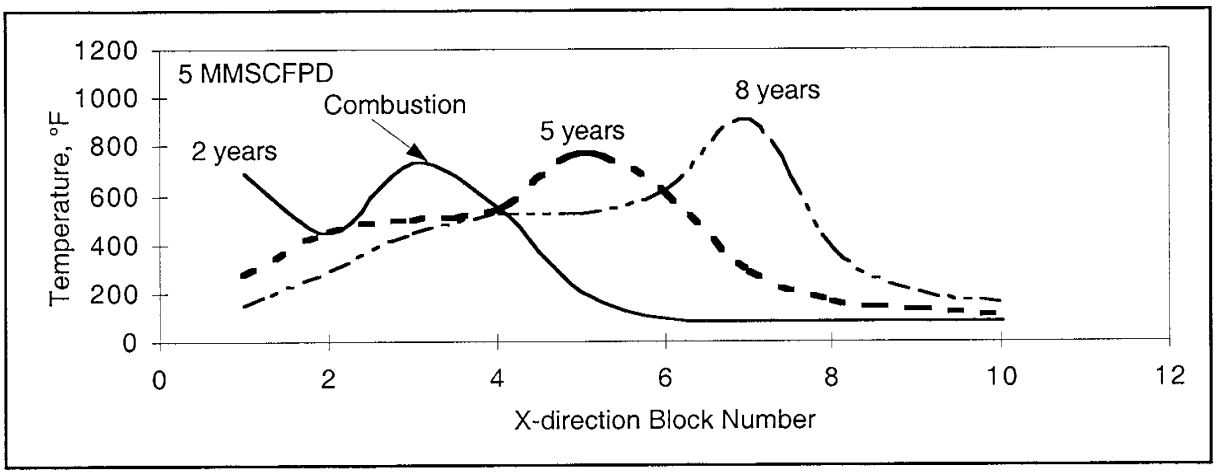

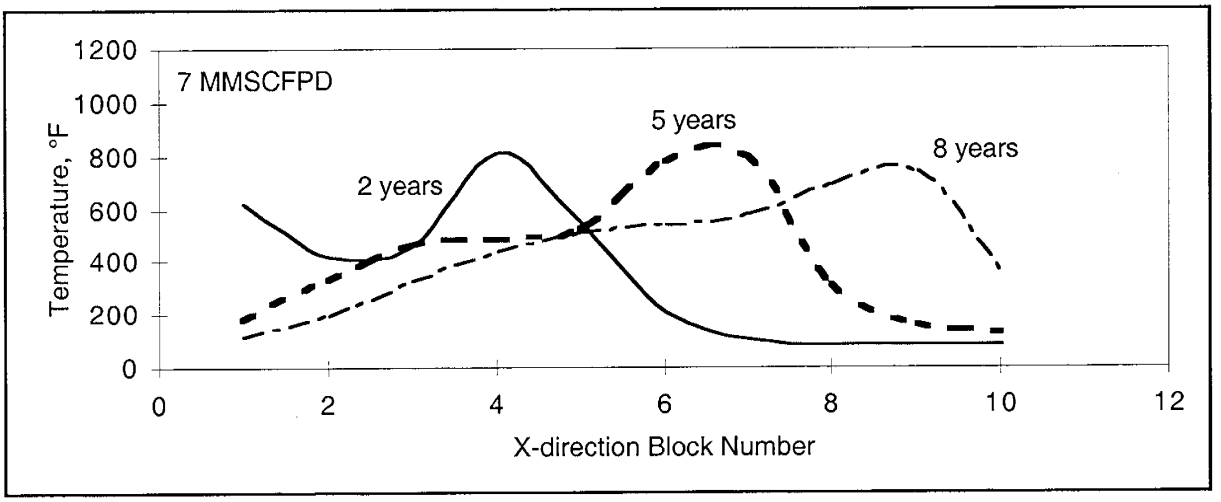

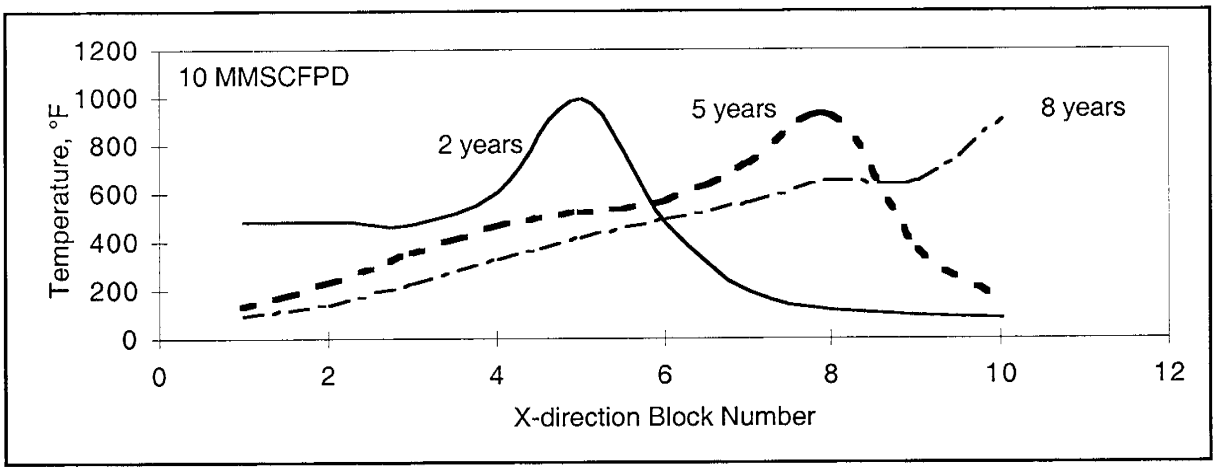

Figure 3. - Position of combustion front for various injection rates

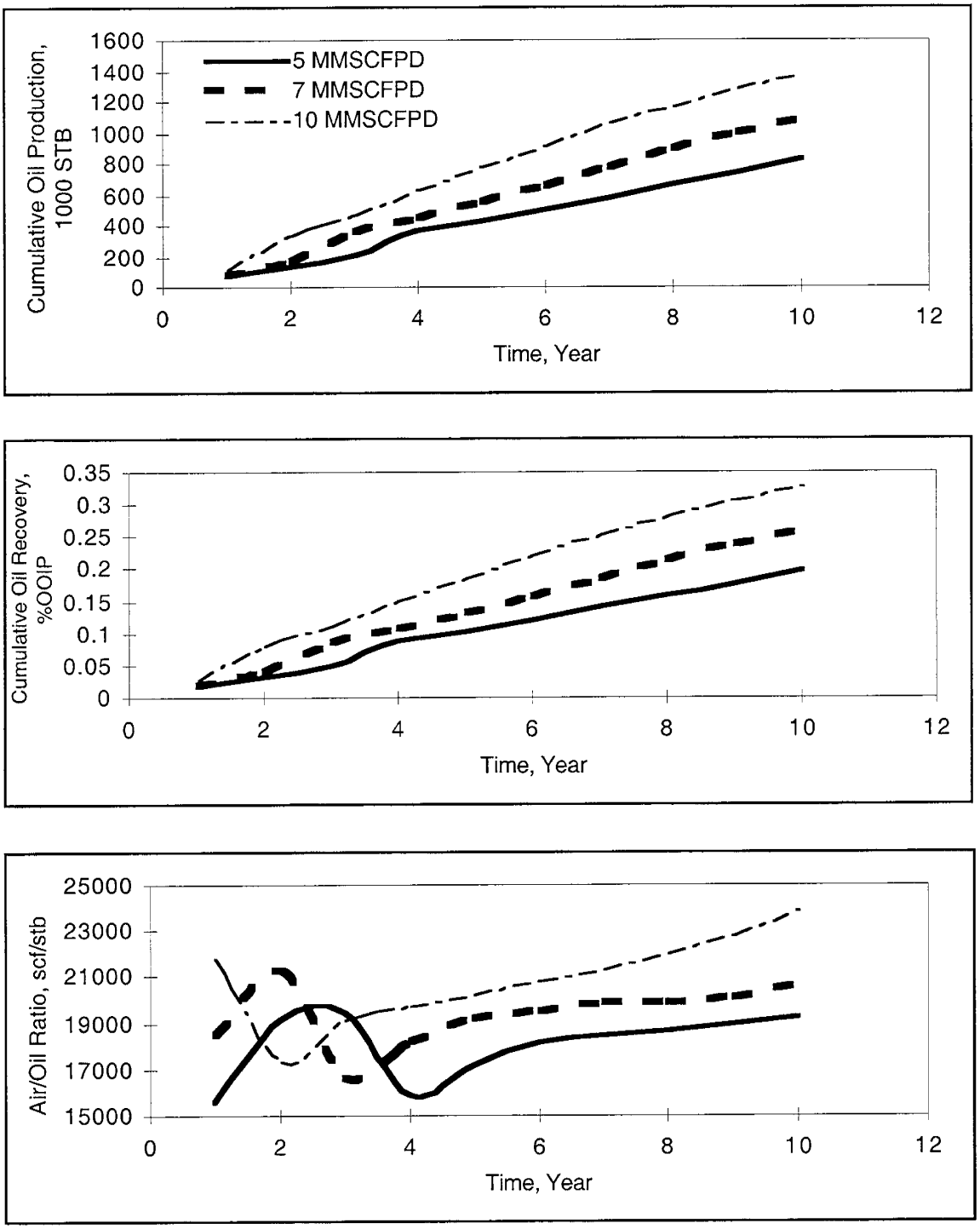

Figure 4. - Effect of injection rates on cumulative oil production, oil recovery and AOR

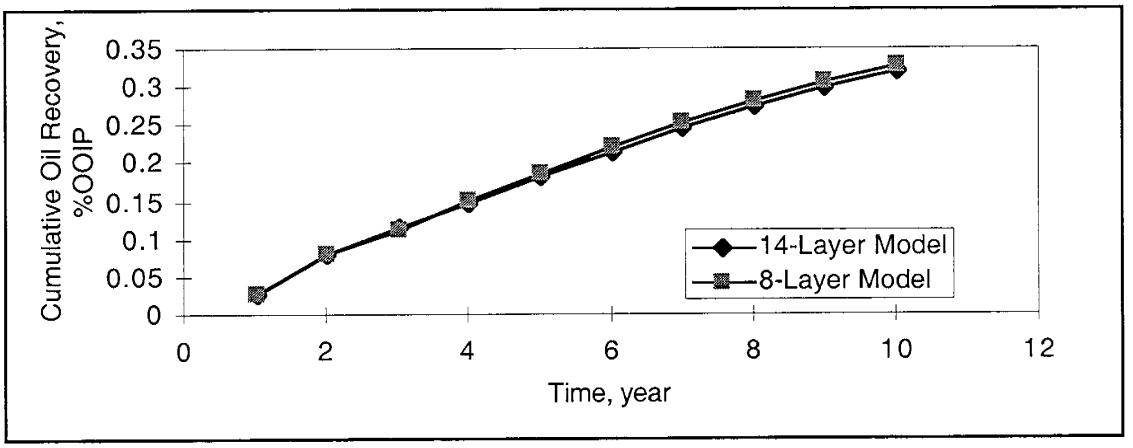

Figure 5. - Comparison of cumulative oil recovery–14-layer vs. 8-layer model (10 MMscf/D air inj.)

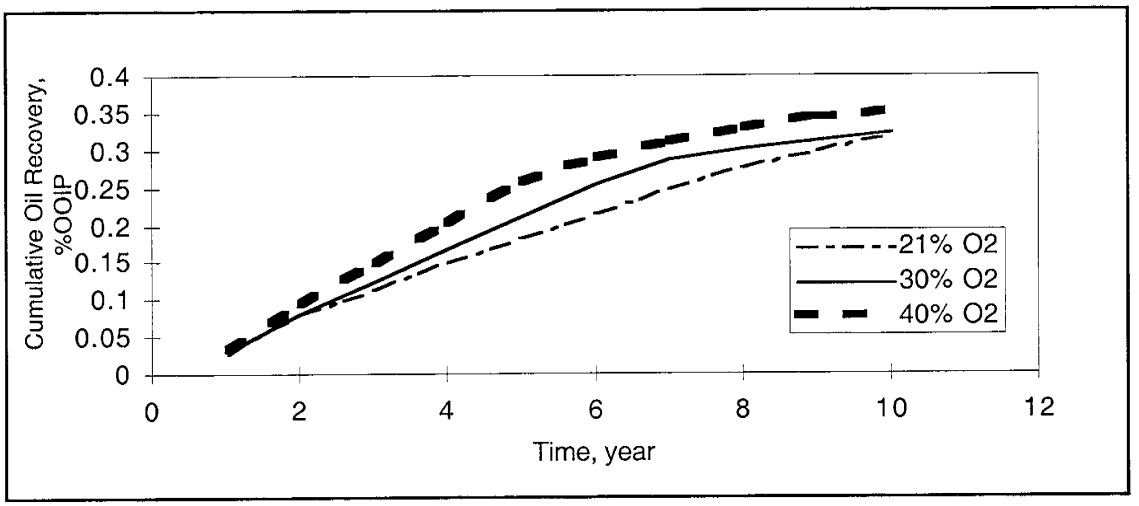

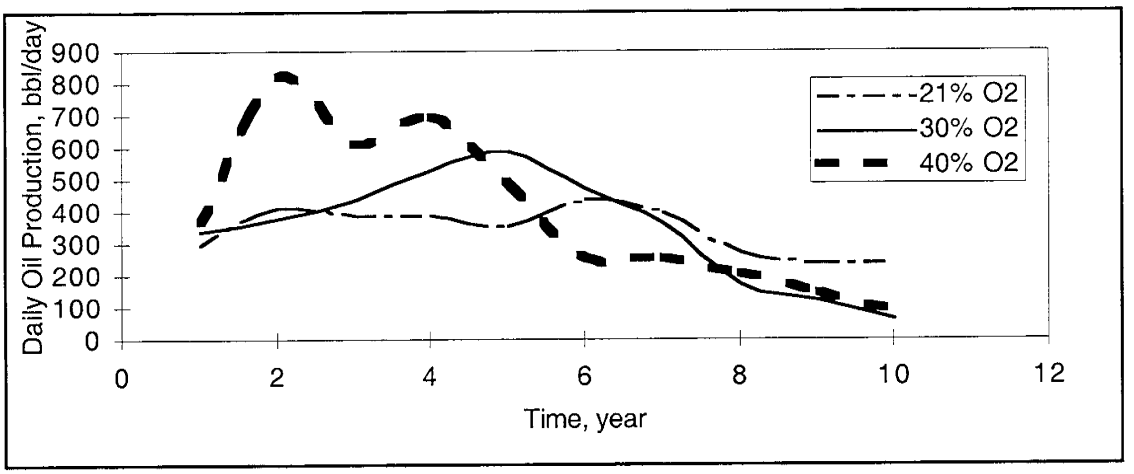

Figure 6. - Effect of enriched oxygen on daily oil production and cumulative oil recovery

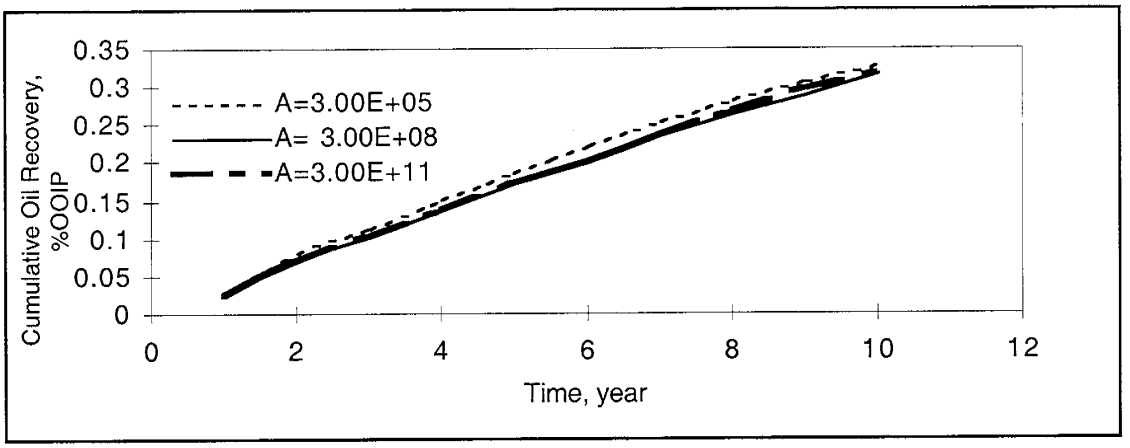

Figure 7. - Effect of kinetics of cracking reaction (10 MMscf/D air injection)

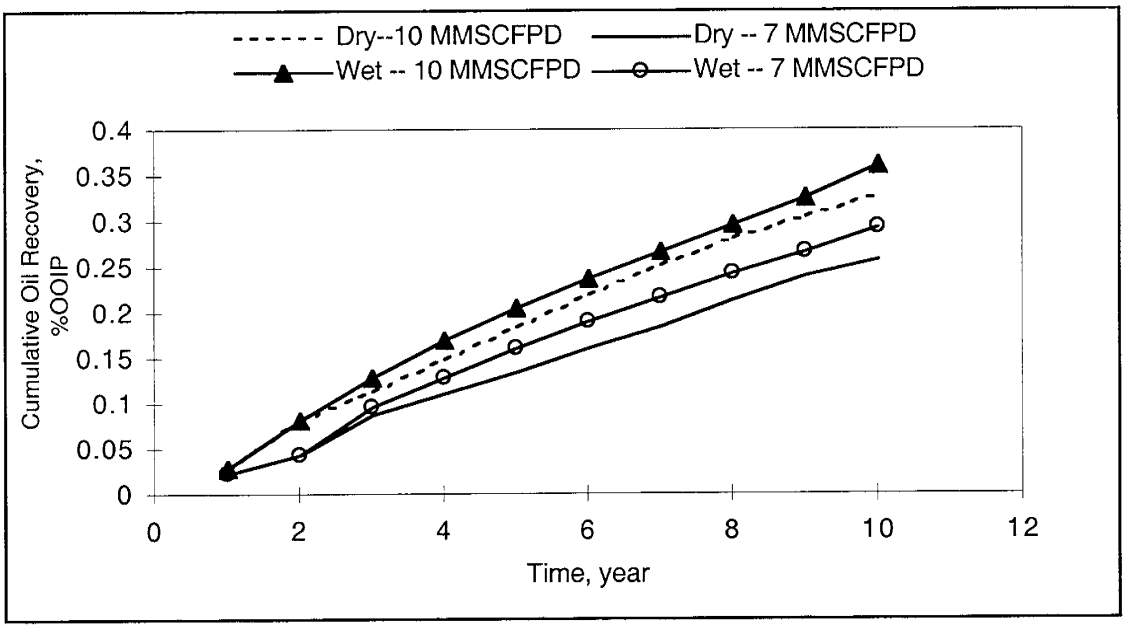

Figure 8. - Oil recovery in wet combustion is superior to the corresponding dry combustion

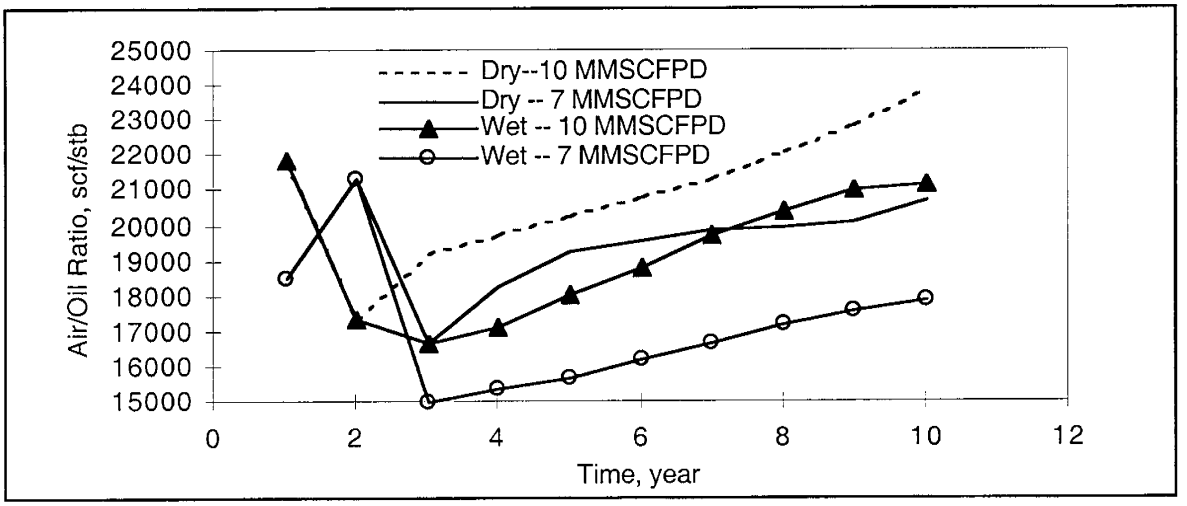

Figure 9. - Comparison of producing AOR for wet and dry combustion

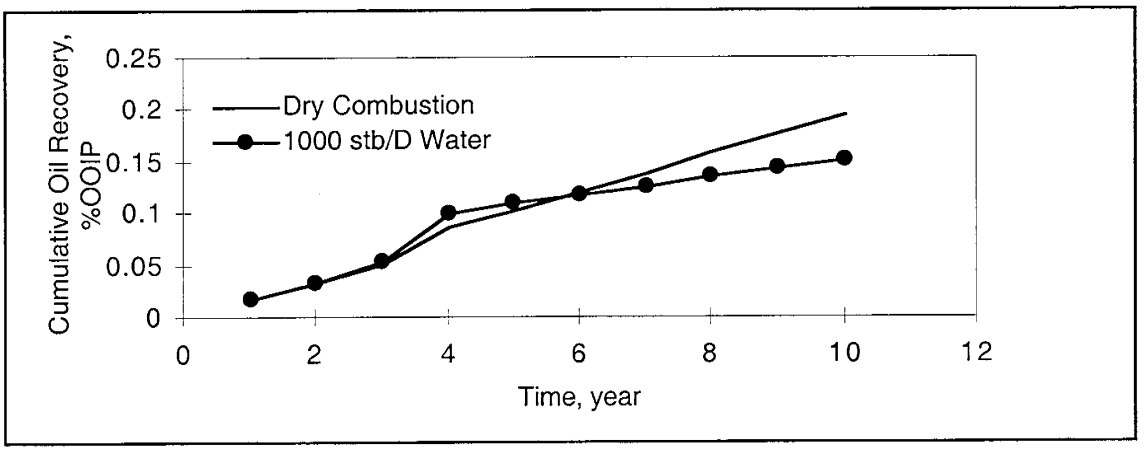

Figure 10. - Effect of water injection on oil recovery (5 MMscf/D air injection)

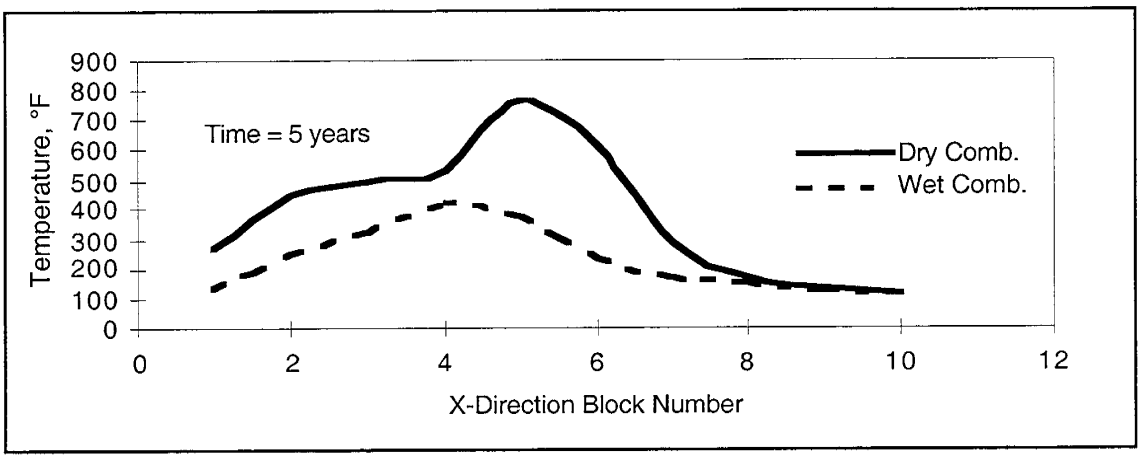

Figure 11. - Effect of wet combustion on temperature distribution (5 MMscf/D air injection)

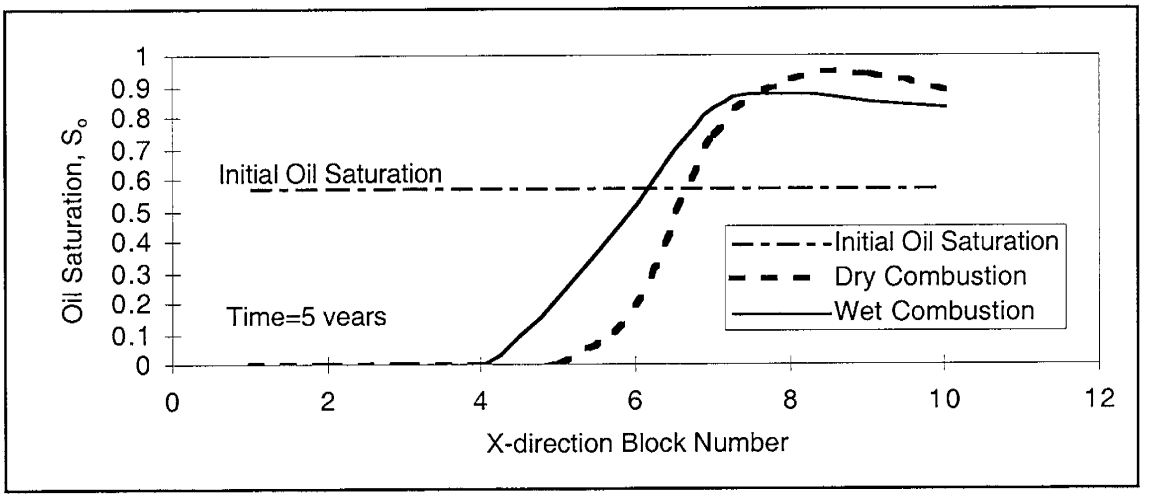

Figure 12. - Effect of wet combustion on oil saturation (5 MMscf/D air injection)

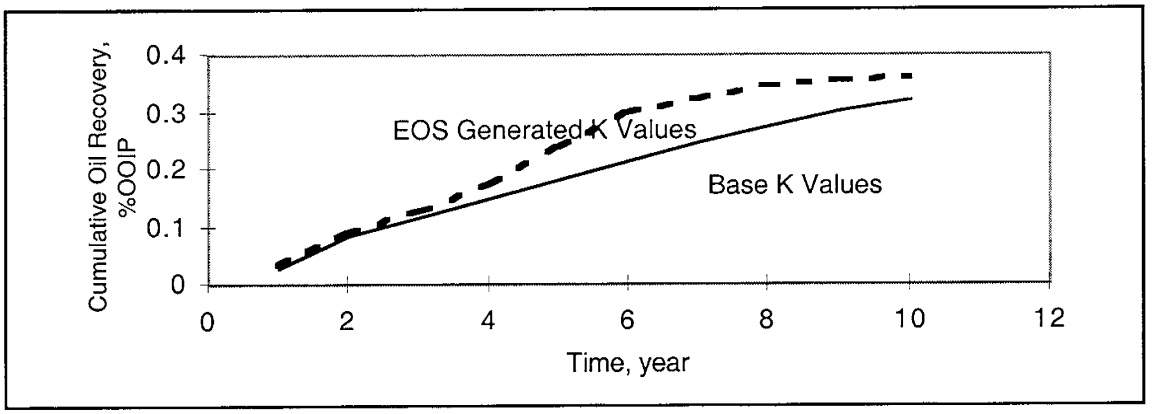

Figure 13. - Effect of phase equilibrium K-values on oil recovery (10 MMscf/D air injection)

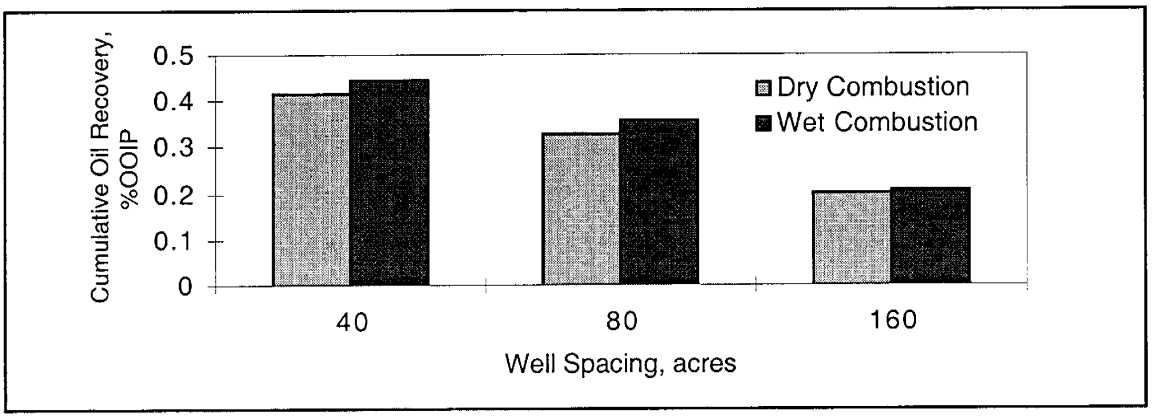

Figure 14. - Well spacing sensitivity study (10 MMscf/D air injection)

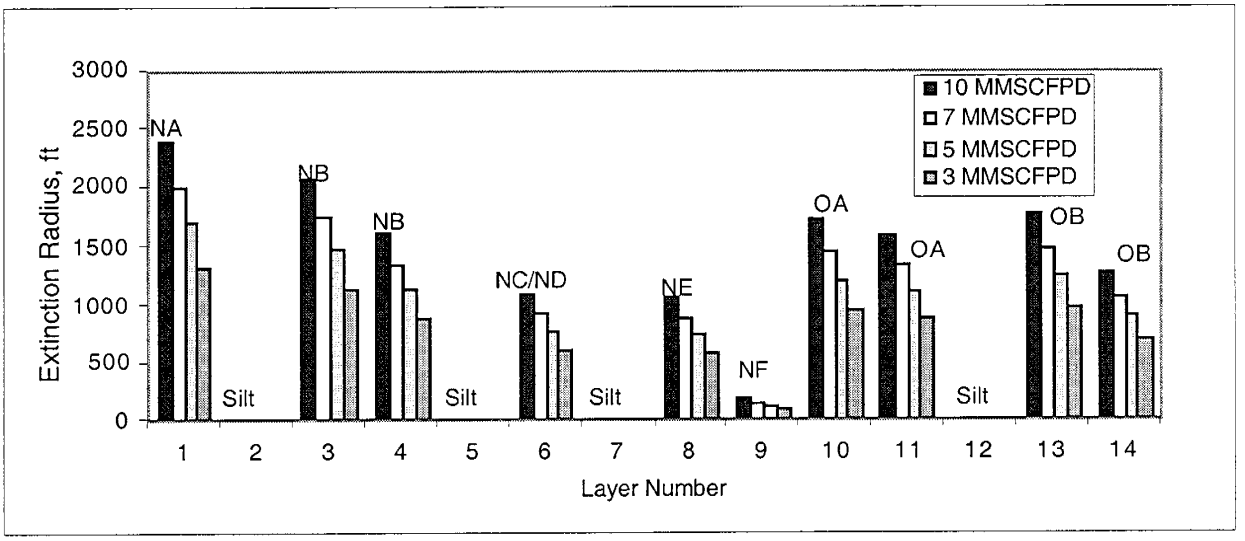

Figure 15. - Extinction radius calculation at various injection rates by layer

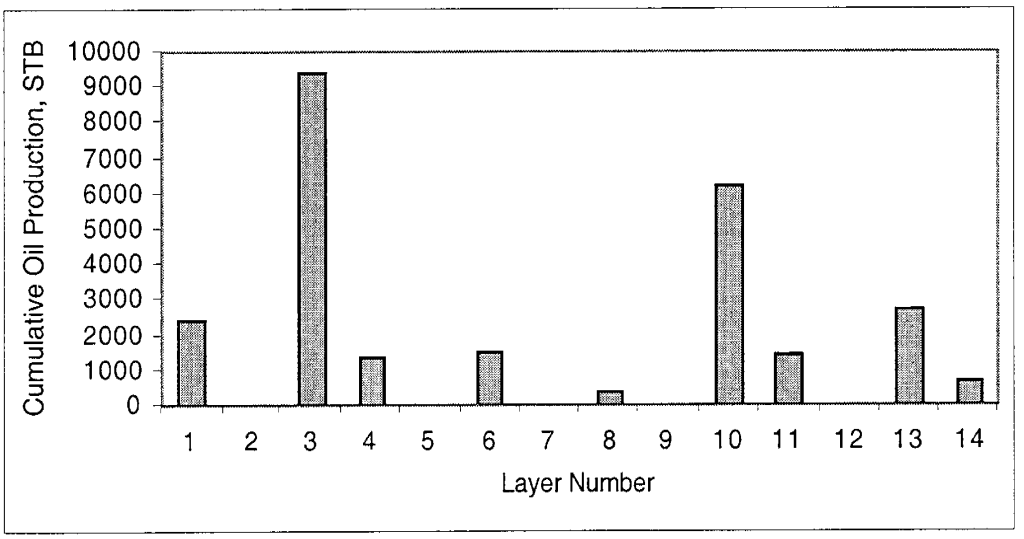

Figure 16. - Cumulative production by sand layer at 10 MMscf/D injected air for 10 years

Task 77 – PDVSA Intevep will provide DOE with information on the influence of coring and sampling procedures on geomechanical properties of unconsolidated materials to generate guidelines and procedures that guarantee field representatively in laboratory samples.

Mechanical Characterisation and Compaction Simulation in an idealised Orinoco Belt Reservoir

Parra Rosales, Jose Germán
PDVSA-INTEVEP

1. INTRODUCTION

One of the objectives of the research and development activities on heavy oil at INTEVEP is the study of compaction as a driving mechanism in the Faja del Orinoco (Orinoco Belt), and its relation with other driving mechanisms, namely: foamy oil behaviour and gas drive. The main reason for studying compaction in the Faja is the unconsolidated or uncemented nature of the productive sands. Unconsolidated sands have some peculiar mechanical properties that can profoundly affect the reservoir behaviour. The proper understanding of uncemented sand behaviour is fundamental for the assessment of the importance of compaction as a driving mechanism and would help to more effectively manage the reservoirs. Better recovery estimates would be obtained from a proper geomechanical characterisation of the sands. If compaction is an important driving mechanism, then some actions could be taken to further improve it and some pressure maintenance measures could be ineffective. Additionally, compaction studies are the basis for subsidence predictions, which could have a potentially large impact on the fragile Faja environment.

In this report a summary of some results on the simulation of compaction drive in an unconsolidated sand stratum is presented. The sand properties are based on a geomechanical characterisation of a certain Faja sand. The results of the characterisation are used in the simulations with the objective of studying the sensitivity of the compaction drive to the geomechanical properties of the reservoir. A discussion on the limitations of typical reservoir simulators to properly represent the behaviour of unconsolidated sands is given. Additionally, the effect of the sand behaviour on the variables that define the reservoir response to depletion are presented. At this stage, all these effects are evaluated by using specialised geomechanical simulators and no account is taken of the actual behaviour of the oil: a one-phase constant compressibility liquid is assumed.

2. SELECTION OF CONSTITUTIVE MODELS FOR COMPACTION STUDIES

The constitutive model is one of the key elements in the numerical treatment of any geotechnical or geomechanical problem. A constitutive model is a mathematical description of the relation between the stresses and strains in an elementary volume of material. In this report two kinds of constitutive models are used: an elastic isotropic model and an elastoplastic model. A brief description of each of those models, as well as their advantages and limitations, follows.

The simplest idealisation of the relation between the stresses and strains is provided by a linearly elastic model. If the elastic properties are assumed to be independent on the orientation in the material, the model is said to be isotropic. The main advantage of this model is that it is completely described by two constants. Among several choices it is common to use Young modulus (E) and Poisson ratio (ν) or Bulk modulus (K) and shear modulus (G). The later are preferred because they relate the main variables used to describe a triaxial test (appendix A for notation):

$\delta p' = K^* \delta \varepsilon p$ (in a fully saturated and drained sample) and $\delta q = 3G^* \delta \varepsilon q$

An additional advantage is the simplicity and robustness of the numerical algorithms used to analyse the stress and strain state of any problem. The main disadvantage of the elastic models is that they are incapable of describing the stress-strain relation of geomaterials over a significant strain interval, and over strain or stress reversals. In particular a material sample described by a linearly elastic model can be in stable equilibrium under any combination of applied stresses or strains, whereas a real geomaterial can be unstable or flow with unlimited strains under particular combinations of stresses. Another important disadvantage for the purpose of this study is that in an isotropic and elastic material volume changes are due only to changes in effective isotropic stress (p'), whereas an unconsolidated material can have volume changes even if subjected to pure shear stresses. This phenomenon (dilation or contraction) could have an important influence in the behaviour of a unconsolidated sand subjected to compaction.

An extension of the linearly-elastic models are provided by the elastoplastic models. Although there is an extensive family of such models, they all basically share the following elements: the strain increments may be decomposed in an elastic and a plastic part, there exists an

initial yield surface that limits the domain in which the material is linearly elastic, a plastic potential that describes how the plastic strains develop once the stress tensor reaches the yield surface, and a hardening rule which describes the way in which the yield surface changes upon plastic straining. Among the disadvantages of the elastoplastic models are the fact that much more laboratory tests are required to define their parameters and that they lead to more complex, more time consuming and less robust algorithms for the analysis of stress-strains distributions. The main advantage is that they allow to improve the description of the stress-strain relations and in particular to model the finite strength of geomaterials, and the coupling of volumetric strains to shear stresses. Due to the extremely complex and variable nature of geomaterials, no elastoplastic model currently available describes in detail all the aspects of their behaviour. On the other hand, depending on the nature of the problem, it could be possible to identify certain mechanisms or prevalent conditions that allow the use of simplified models with limited scope that are adjusted only for those particular conditions.

In this report all the numerical simulations were done with the FLAC3D and VISAGE programs [1,2], hence we are restricted in the selection of the elastoplastic models to those available in the simulation software. From those we selected the modified CAM-CLAY model [3,4] based on Critical State Mechanics concepts. A brief description of this model follows.

The CAM-CLAY model is an elastoplastic model originally developed for clays. The model has as a yield surface an ellipse in p′-q space. Inside the ellipse the material is considered linearly elastic and isotropic (although this last could be changed). The model is associated, hence the plastic potential is identical to the yield surface. The hardening rule is isotropic, meaning that subsequent yield surfaces have exactly the same shape. The 'size' of the yield surface changes only if there is a change in plastic volumetric strain (volumetric hardening). Changes in plastic shear strain produces no hardening. This is one important limitation of the CAM-CLAY model when applied to sands: hardening (change in yield surface size and or shape) is related to both volumetric and shear plastic strains. Although the CAM-CLAY model should not be used as a general model for sand behaviour, many of the patterns of response that this model predict are relevant to non-claylike materials [3,5]. In particular, the existence of critical states, the finite strength controlled by a friction angle, the importance of the void ratio and the isotropic stress level (p') in the dilatant or contractive behaviour could be approximately modelled for sands, although certainly under limited stress paths and strain intervals.

There are other simple elastoplastic models that could be more suitable to use with sands in a general application. Among them there are the Nor-Sand model [6] and the Lade two-cap model [5,7]. The Nor-Sand model is an elastoplastic model with isotropic hardening (similar to CAM-CLAY), specifically oriented for sands. The main difference with the CAM-CLAY is the formulation of the hardening rule, which is a function of the plastic shear strain increment and the relative distance of the current void ratio to the void ratio at the critical state under the same isotropic effective stress. This hardening rule seems to model more adequately the evolution from contractive to dilatant behaviour in samples subjected to moderate isotropic stresses (of the order of those encountered in applications to superficial geotechnical problems). For sands under high isotropic stresses (like those encountered in deep productive sands) this effect could not be so important because the behaviour would probably be contractive along the productive life of the reservoir. The Nor-Sand model is conceptually simple and uses a limited amount of parameters (similar to CAM-CLAY), yet is capable of simulating complex sand behaviour under monotonic and cyclic loads. Due to its relatively recent formulation there is not enough documented experience with its use.

The Lade model is a mixed associative and non-associative model that uses two surfaces for describing the yield locus [7]. The plastic strain increment is expressed as the sum of two components. One controlled by a non-associative flow rule and the other controlled by an associative rule. The Lade model is more difficult to implement in numerical analysis, but there is a larger data base of successful applications to sand modelling.

Both of these models (Nor-Sand and Lade models) could be used in further studies on the effect of compaction of uncemented sands in the production of oil. This will need the inclusion of them into a stress-strain-flow code, but up to date there is no commercial code known to the authors with those two models included.

2.1 Calibration of an elastoplastic constitutive model

In what follows an example of the quality of results that can be obtained from the calibration of the CAM-CLAY elastoplastic model applied to a Faja sand is presented. The sand analysed is an uncemented sand [8]. In geomechanical work applied to reservoir engineering the term unconsolidated sand is often used. In this report the term consolidated material is used to describe a material that have drained most of the excess of fluid pore pressure whereas the term uncemented means that there is no physical bond between the individual grains composing the sand. Macroscopically this means that a sand sample cannot sustain its shape if unconfined, or more formally, that it can withstand no tensile stress.

The mean size diameter of the sample sand is about 0.22 mm. If the USCS (Unified Soil Classification System), common in geotechnical work, is used, this sand would surely classify as silty-sand (SM). This means that the finer part (smaller than 200 sieve) would be probably silt rather than clay, but there was not enough data to verify this (there are simple tests used in soil mechanics to determine the nature of the finer part). This has important implications in the permeability and the nature of the stress-strain relations.

An attempt was made to fit a modified CAM-CLAY model to triaxial test data. A word of caution is necessary: what is expected is an approximation to the lab data in a strain interval similar to that expected in the field. The selected elastoplastic model implies a sudden transition from elastic to plastic behaviour with a drastic decrease in stiffness. In reality, as observed in the data, the transition is gradual, meaning that the choice of the plastic onset in rather arbitrary. Based on this, it was decided to define the plastic onset as a gross departure from an initial linear behaviour.

Alternatively, a better estimate of the initial elastic properties (at very small strains) could be obtained from loading-unloading tests or in-situ P or S wave speed. This would imply the use of more elaborate models with gradual transition from elastic to plastic behaviour such as the Bounded Plasticity [9] or multiple yield surface models [10,11]. Due to the software and time limitations this was not attempted.

2.1.1 Estimation of elastic properties

The initial elastic properties were estimated from the slopes of straight lines fitted to the p'-εp and q-εq plots (Figs. 2.1, 2.2) at stress levels of the order of those expected in situ (p'~1000 psi). If the sands were linear elastic and isotropic, all those plots would be straight lines with equal slope: K for p'-εp and 3G for q-εq. The deviation from such behaviour is evident, as can be seen in Figs. 2.1 and 2.2. A mean value of 224 MPa (32.5 Kpsi) for the bulk modulus and 197 MPa (28.6 Kpsi) for the shear modulus are used. They are equivalent to a Young modulus E=458 MPa and a Poisson ratio of 0.16.

2.1.2 Critical state line

The critical state line (CSL) is defined as the locus of point in v-p'-q space where unlimited plastic shear deformation is possible under constant volume (constant v) and constant effective stress. This line plays a fundamental role because any test with enough shear applied must end in a critical state point in this line. Also, the dilatant or contractive behaviour of a sand sample is known from the relative position of the initial state (p',q,v) with respect to the CSL. From the tests carried out on the sand, only the test n° 6 and the undrained test n° 7 (Fig. 2.4 for the stress paths) were likely to reach a critical state. The rest of the tests were carried out with a slope in the p'-q space not high enough to reach a critical state (Fig 2.3). The load path (effective) of the undrained tests (n° 7) did not reach a maximum shear strength, although it is moving along a line of constant mobilised friction angle. As can be seen in Fig. 2.9a, its behaviour changed from initially contractive (sharp increase in pore pressure) to dilatant (reduction in pore pressure), although the rate of dilatancy is small and it seems that it is not far from reaching a critical state. This behaviour has been observed in undrained tests under small confining pressures [11,12]: the effective stress path moves closely along the critical state line in the p'-q space, sometimes reversing its direction. From this it can be concluded that there is very limited information to confidently define the CSL. Accepting this, from the load paths of tests 6 and 7, the friction angle was estimated as 37° .

In the ln(p')-v space there is even more difficulty in locating the CSL. Test n° 7 for instance has a sudden volume change at the very beginning, which is probably due to some adjustments in the LVDT sensors. Test n° 6 is not close enough to the CSL. From results of different sands reported in the literature [13,14], the slope of the CSL in the high p' interval is

estimated to be λ=0.14 (a range between 0.11 and 0.15 is reported). In Fig. 2.3 a likely CSL is plotted. As can be seen, all the samples are contracting due to the combination of the high initial porosity (and hence, specific volume) and the high confining stresses. From λ=0.14 and a κ=0.029 (roughly 1/5 of λ, κ is the unloading-reloading modulus which is related to the K value) an initial value of λ-κ equal to 0.11 was assumed. The final estimate that provides the better fit in the stress interval of interest is λ-κ=0.07.

2.1.3 Initial yield surface and quality of fit.

In order to estimate p_0', the initial horizontal diameter of the elliptical yield surface (CAM CLAY), a MATLAB computer program was written to calculate the evolution of the drained triaxial tests with a CAM CLAY model. Observing the undrained test results (n° 7), it can be seen that starting with an initial p' equal to 1500 psi, the stress path starts to bend almost immediately with the application of shear. If the sand were elastic and isotropic, the effective stress path under this undrained test would be a straight vertical line, it would bend when plasticity is reached. From this it can be concluded that the initial value of po' should be close to 1500 psi. If this value is used to simulate the remaining tests, large discrepancies are observed. An attempt to minimise the differences between the measured and predicted stresses and strains was done, adjusting the value of p_0': a final value of 1700 psi was selected.

It is difficult to define a yield point for the tests, given the very gradual onset of plasticity. If an attempt to plot a yield surface is done, based only on the change in slope of the stress-strain plots, a distorted shape similar to an ellipse rotated about an axis with slope (dq/dp') roughly equal to 0.8 is obtained (Fig. 2.4). This shape is very much dependent on the assumption that the undrained test was started from a 'normally consolidated' state, i.e. in the border of the yield locus). This type of yield surface has been proposed in the literature [3], instead of an ellipse with axis along the q=0 line, as given by the CAM CLAY model. The problem with this choice is that it would fail completely in explaining the effective stress path for the undrained test (it would lead to a vertical stress path). Given that the used software only works with a horizontal ellipse, this alternative interpretation was not further explored.

It is observed that due to the limitations of the model (and to the number of stress paths tested) it was not possible to simultaneously match the volumetric and shear behaviour for all the tests.

In TABLE 1 a summary of the final values of the parameters for the CAM-CLAY model is given. In Figs. 2.5 to 2.11 the stress-strain relations measured and computed are compared.

TABLE 1. CAM-CLAY parameters for the analysed sand

Parameter	Description	Value
E	Young modulus	458 Mpa
ν	Poisson ration	0.16
v_0	Initial void ratio	Variable for each test
$\lambda-\kappa$	Slope of critical state line in v-ln(p') space minus slope of unloading-reloading line in v-ln(p') space	0.07
ϕ	Friction angle	37°
p'_0	Horizontal axis of the initial yield surface	1700 psi (11.74 Mpa)

2.2 General discussion on the limitations of the selected models

The quality of the constitutive model selected has to be analysed considering the final aim of the characterisation. In this work the model selected is going to be used for compaction studies, where a moderately small variation in strain and stresses is expected. This implies that a less rigorous but simpler model could be appropriate. The limitations of the CAM CLAY models have been highlighted in the previous discussion, but it is expected that useful results can be obtained from its use in compaction studies. A similar conclusion has been reached by other researchers working with sands of the Faja area [5]. On the contrary, if the purpose of the characterisation was the study of borehole stability, where very high and localised stresses and strains could be expected, then the use of a more refined and realistic model could be warranted.

Another fact supporting the use of not very refined models is the quality of the recovered samples. Although the sampling was done with the highest care and using advanced techniques to preserve the cores (freezing the samples), it is difficult to preserve the original structure of the

sand. The sampling and transport process from the reservoir to the surface produces a severe unloading of the sample, meaning that any weak cementation present in situ would be destroyed. The development of techniques for undisturbed sampling in sands is still very active, with no 'ideal' procedure available yet.

The stress strain properties given in this study are tied to the assumed constitutive model, and should give a reasonably good prediction of the stress strain behaviour from monotonic perturbations of the in situ original stress state. In particular, the elastic properties are 'best fit' of the observed laboratory results interpreted under the framework of classical plasticity theory. Analysing some unload-reload data available for the sand, the unload behaviour is not well represented by the elastic parameters chosen (the unload-reload is much stiffer than that obtained from the elastic parameters). A more complete plastic rule would be needed: for instance the one recommended in references [11, 15].

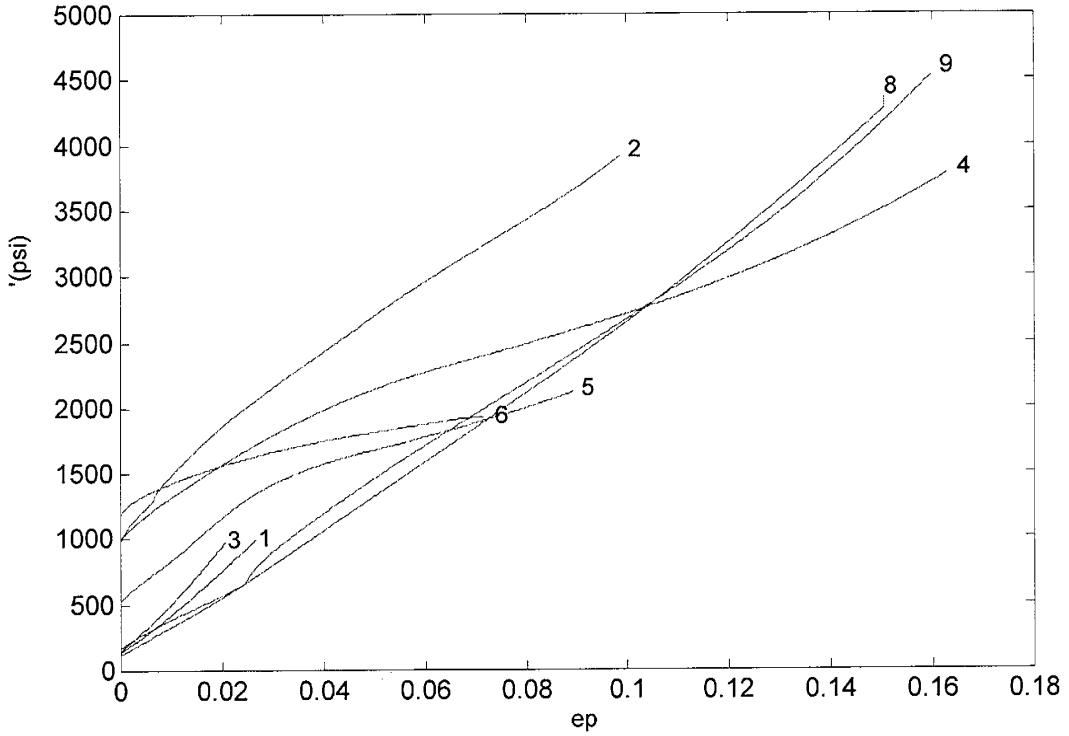
5000
4500
4000
3500
3000
2500
2000
1500
1000
500
0
'(psi)
0
0.02
0.04
0.06
0.08
0.1
0.12
0.14
0.16
0.18
ep
1
2
3
4
5
6
8
9

Fig. 2.1 ep-p'.

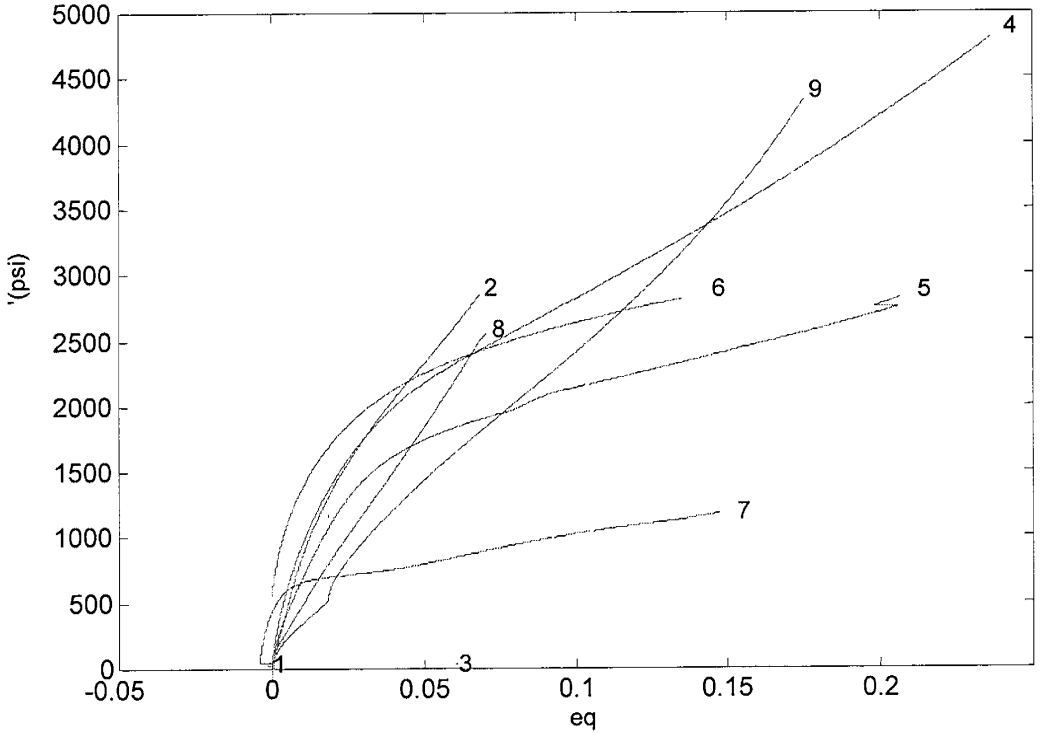

Fig. 2.2 eq-q plots.

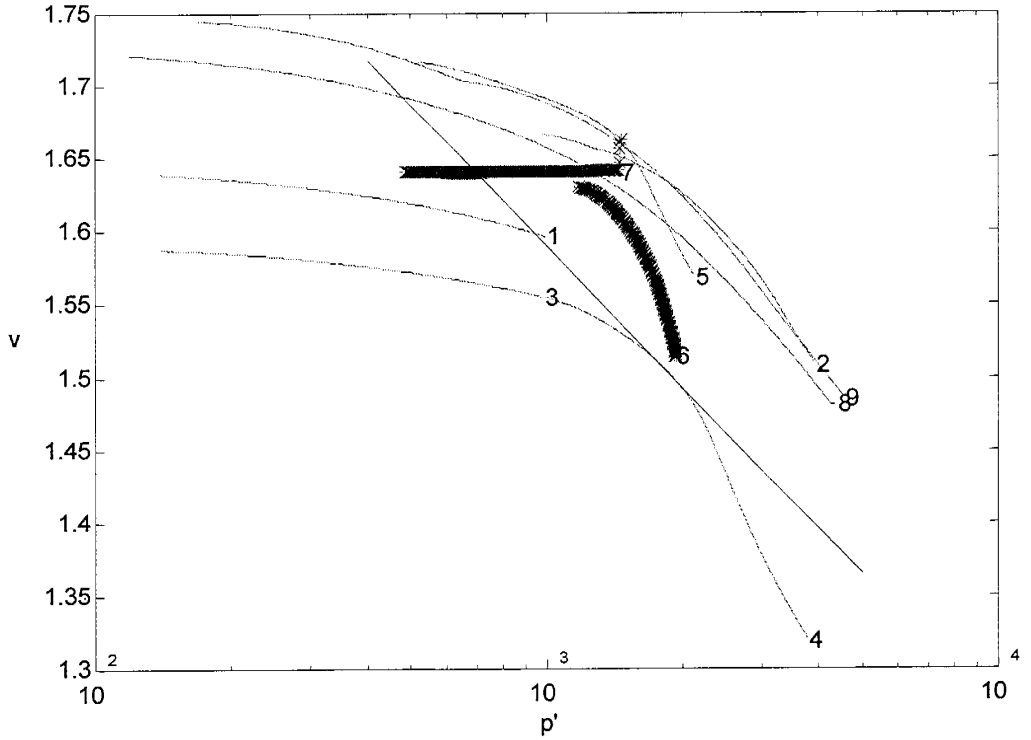

Fig. 2.3 A possible Critical State line in p'-v space

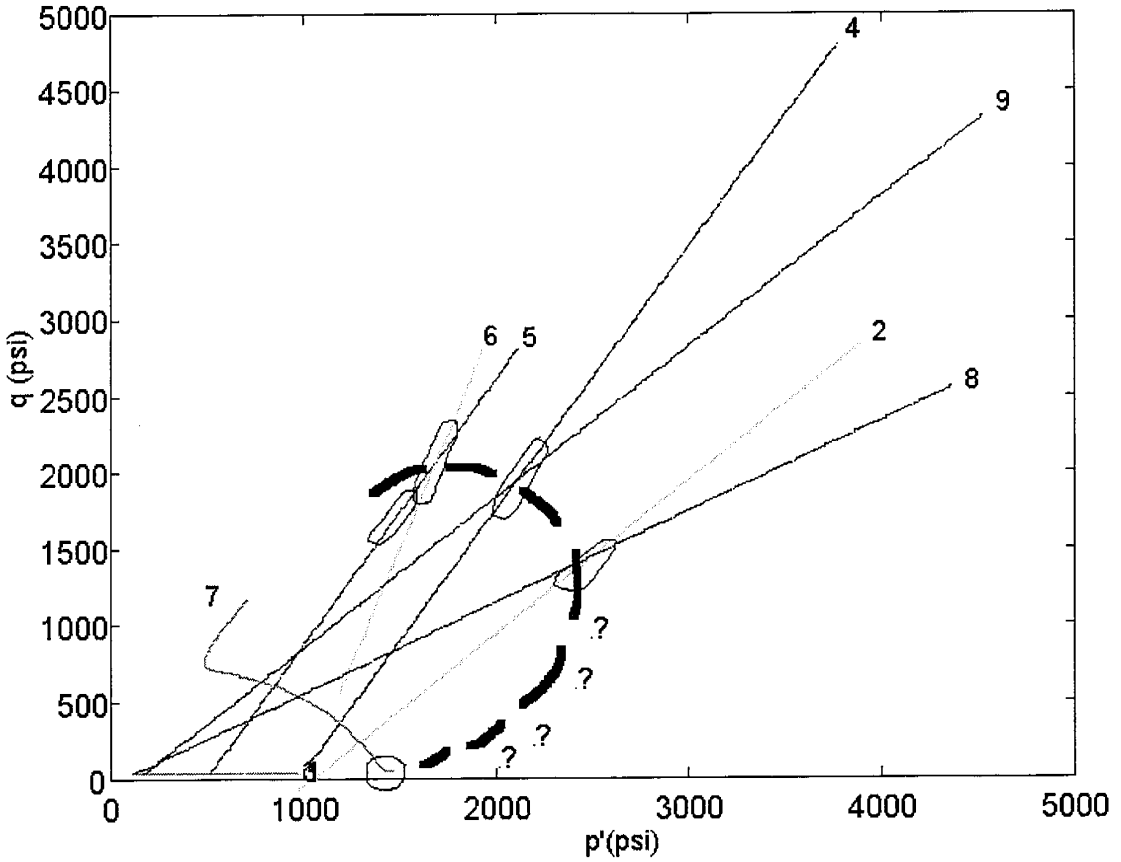

Fig. 2.4 A possible initial yield locus (fails to explain test 7)

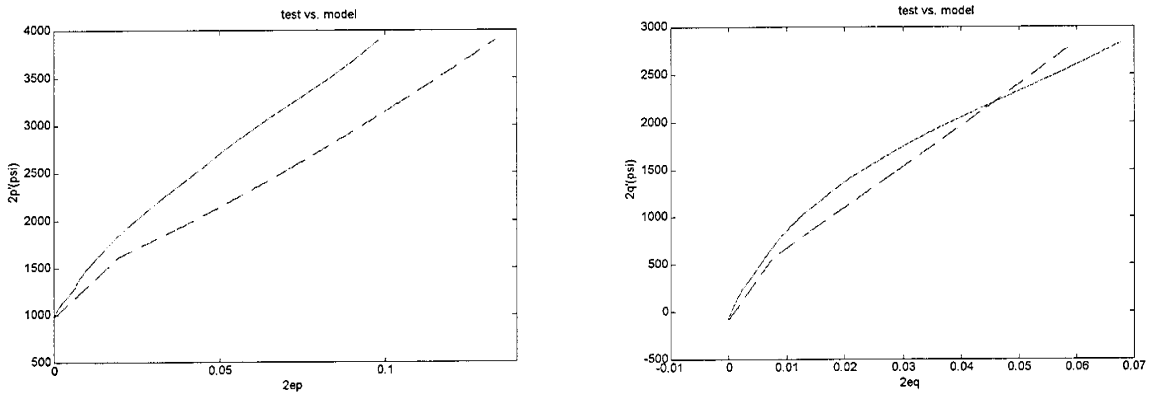

Fig. 2.5 Comparison test 2 vs. Cam-Clay model.

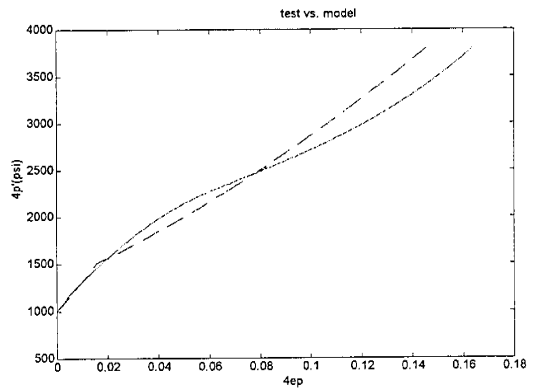

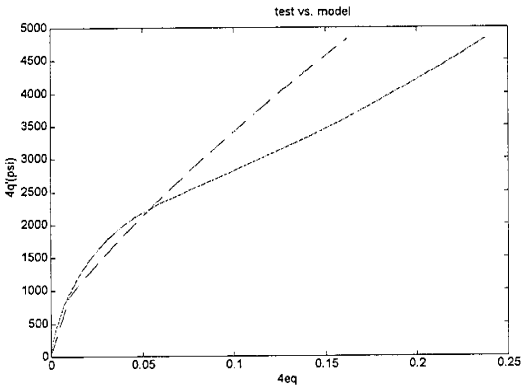

Fig. 2.6 Comparison test 4 vs. Cam-Clay model.

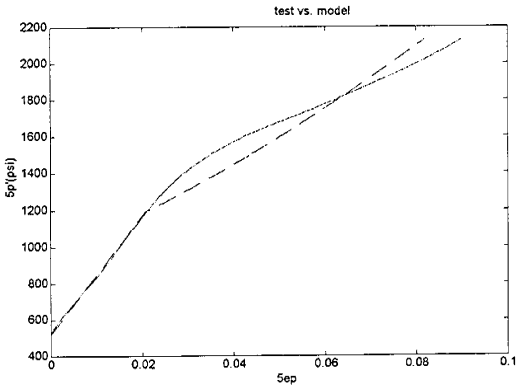

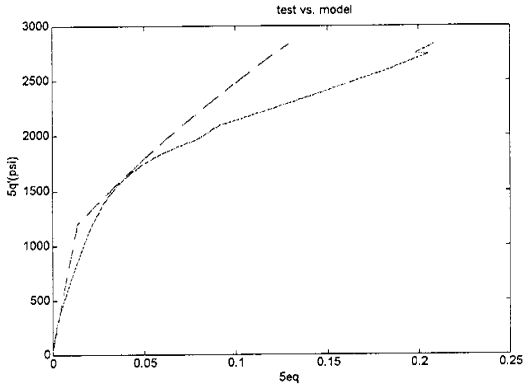

Fig. 2.7 Comparison test 5 vs. Cam-Clay model.

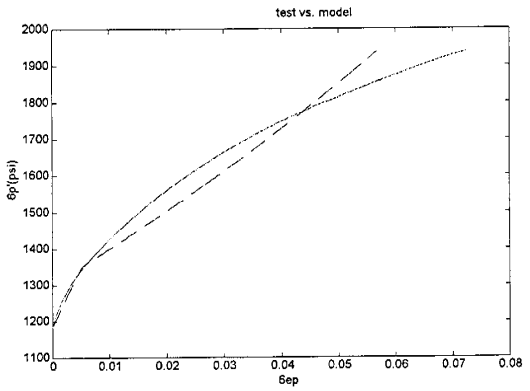

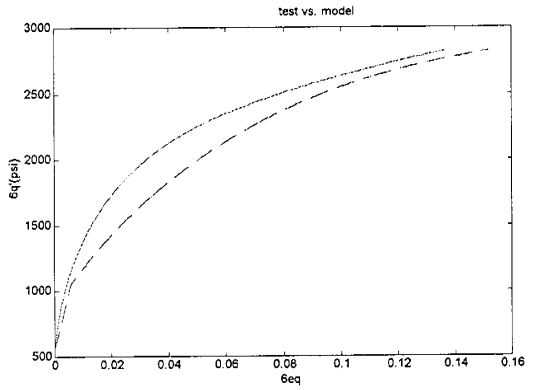

Fig. 2.8 Comparison test 6 vs. Cam-Clay model.

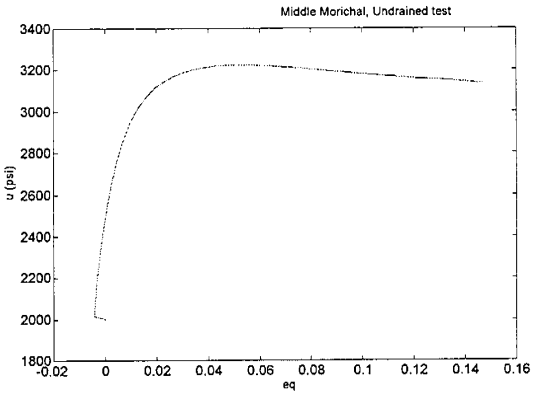

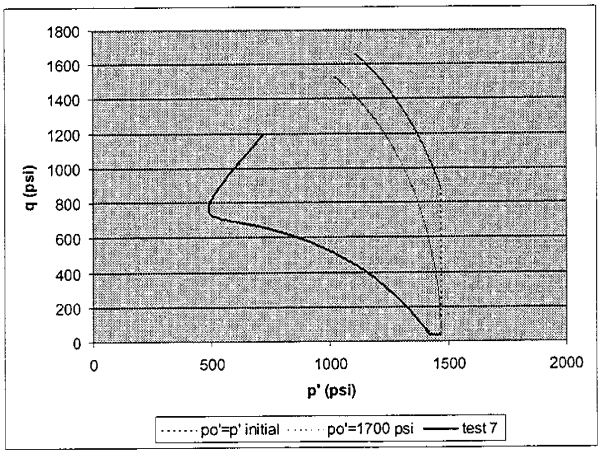

Fig. 2.9a Pore pressure vs shear strain. Test 7 undrained.

Fig. 2.9b Comparison test 7 vs. Cam-Clay model (effective stress paths compared).

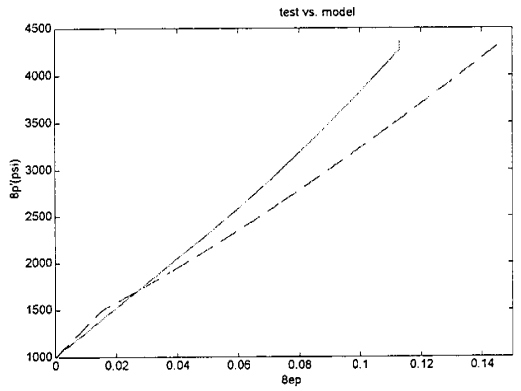

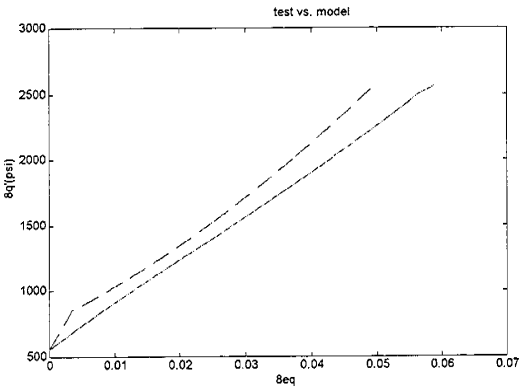

Fig. 2.10 Comparison test 8 vs. Cam-Clay model (p'>1000 psi).

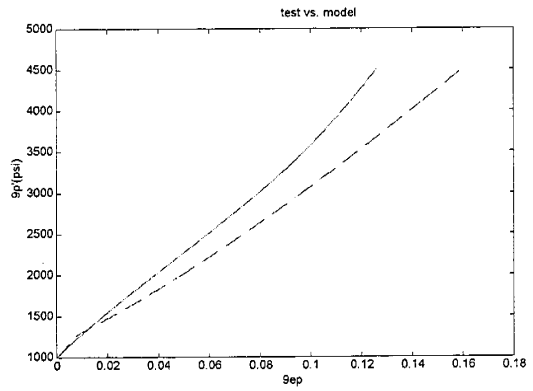

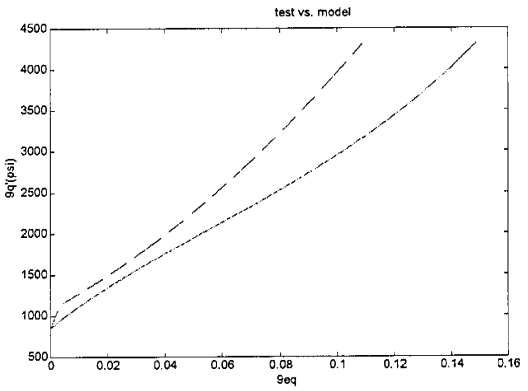

Fig. 2.11 Comparison test 9 vs. Cam-Clay model (p'>1000 psi).

3. SIMULATION OF COMPACTION

With the geomechanical characterisation of the sand previously presented, a set of simulations of compaction due to oil withdrawal on idealised production pads were attempted.

The objectives of the simulations are:

To study the effect of the constitutive model on the reservoir behaviour. In particular the effect on pressure decline with time, compaction rate, oil recovered, and displacements and strains in the solid matrix (sand).

To suggest approximate compressibility functions to be used in reservoir simulators.

The simulations were done with the geomechanical simulators FLAC3D and VISAGE. The main advantages and disadvantages of the simulators are briefly discussed in what follows.

3.1 Differences in the consideration of the behaviour of the solid matrix between reservoir and geomechanical simulators.

The classic formulation of reservoir simulators for the case of one-phase compressible flow in an incompressible solid matrix under isothermal condition is based on the application of the mass conservation principle, the Darcy law and the pressure-density relation for the liquid phase [16, 17]. If the compressibility of the liquid phase is small, the latter can be linearised as:

$$\rho = \rho_0\left(1 + C_f\left(p - p_0\right)\right) \qquad 3.1$$

where p_0 and ρ_0 are reference pressure and density, ρ is the density at pressure p, and Cf is the fluid compressibility (p is used for pressure instead of u). After some manipulations the relation that describes the pressure evolution in the reservoir reduces to the following diffusion type equation:

$$\frac{\partial p}{\partial t} = \frac{k}{\phi \mu C_f}\nabla^2 p \qquad 3.2$$

where k is the absolute permeability (length^2), ϕ the porosity, μ the viscosity of the fluid (Force*time/length^2), and t the time. The pressure evolution could then be calculated from the initial and boundary conditions and the (usually) numerical solution of 3.2.

If the solid matrix is not considered incompressible, then it is conventionally assumed in reservoir engineering that the solid matrix is an elastic material that follows a linear relation between changes in pore pressure and changes in pore volume:

$$\delta\varepsilon_p = -\phi C_s \delta p \qquad 3.3$$

where ε_p is the volumetric strain (positive in compression, appendix A) and C_s the 'solid compressibility'. After some manipulation, and using a modified expression for the conservation of mass, the following expression is obtained:

$$\frac{\partial p}{\partial t} = \frac{k}{\phi\mu\left(C_f + C_s\right)}\nabla^2 p \qquad 3.4$$

This is still a diffusion type equation, but with an equivalent compressibility for the fluid-solid matrix system. The pressure evolution could again be calculated from the initial and boundary conditions and the (usually) numerical solution of 3.4, which is identical in structure to 3.2. The volumetric strains could be calculated from 3.3 once the pressure distribution is known.

Many reservoir simulators consider the possibility of C_f and C_s as variable functions of pore pressure (p). The same conclusion applies with regard to the uncoupled nature of the equations.

From a mechanical point of view, there are several problems with the above formulation for the case of a deformable solid matrix. First of all, the formulation of the mass conservation principle has to take into account the fact that the control volume (solid matrix + fluid) suffers a deformation. Secondly and most important, the volume change in the solid phase cannot, in general, be expressed as a function of the change in pore pressure alone. If the first effect is considered in a rigorous manner the following expression is obtained [16, 18]:

$$C_f \frac{\partial p}{\partial t} - \frac{1}{\phi_o} \frac{\partial \varepsilon_p}{\partial t} = \frac{k}{\phi_o \mu} \nabla^2 p \qquad 3.5$$

In this expression the evolution of the pore pressure is coupled to the evolution of the volumetric strain (ε_p), and it cannot be obtained alone. The volumetric strain is linked to the stress state in the solid matrix through the effective stress relation:

$$\begin{aligned} \delta\varepsilon_p &= \sum \delta\varepsilon_{ii} \\ \delta\varepsilon_{ij} &= D_{ijkl}(\delta\sigma_{kl} - \alpha\delta p \delta_{kl}) \end{aligned} \qquad 3.6$$

where $\delta\varepsilon_p$ is the change in volumetric strain, $\delta\varepsilon_{ij}$ is the change in the strain tensor, $\delta\sigma_{kl}$ the change in the total stress tensor, δp the change in pore pressure, α the Biot constant, δ_{kl} the Kronecker delta and D_{ijkl} the incremental elastoplastic tensor (given by the constitutive law of the solid matrix). Expressed in words, Eq. 3.6 means that a change in the volumetric strain depends on the change in pore pressure (δp) and the change in total stress ($\delta\sigma_{kl}$). Hence the evolution of the pore pressure has to be obtained simultaneously with the evolution of the stress state. In other words, the compressibility of the solid matrix, as given by Eq. 3.3:

$$Cs = -\frac{1}{\phi} \frac{\delta\varepsilon_p}{\delta p} \qquad 3.3^a$$

is not a material property, but depends on the evolution of the stresses, strains and pore pressures.

Equation 3.5 cannot be solved without solving at the same time the stress and strain distribution, which requires the full consideration of the continuum mechanics equations (equilibrium and compatibility of strains) and the initial and boundary conditions not only in terms of pressures but also of displacements and total stresses.

Equation 3.5 can be written as:

$$\frac{\partial p}{\partial t} = \frac{k}{\phi_o \mu (Cf - \left\{ \frac{1}{\phi_o} \frac{\frac{\partial \varepsilon_p}{\partial t}}{\frac{\partial p}{\partial t}} \right\})} \nabla^2 p \qquad 3.7$$

The term in braces {} could be considered as an equivalent solid matrix compressibility, but its value in general will depend on the position in the reservoir, the time, the evolution of stresses and strains (stress path) and on the constitutive equation of the solid matrix (D_{ijkl}).

In this work, the 'equivalent compressibility' in a given point in a reservoir will be defined as:

$$C_s = -\frac{1}{\phi_o} \frac{\frac{\partial \varepsilon_p}{\partial t}}{\frac{\partial p}{\partial t}} \equiv -\frac{1}{\phi_o} \frac{\delta \varepsilon_p}{\delta p} \qquad 3.8$$

After the fully coupled problem is solved (using a geomechanical simulator), this compressibility could be computed for any point in the reservoir and expressed as a function of pore pressure. If its variation through the reservoir is moderate, the an average function could be defined as the best estimate of the 'compressibility function' C_s=f(p) to be used in a reservoir simulator.

3.2 Simulation of compaction in an idealised Faja reservoir.

3.2.1 Basic geometry

The idealised geometry on which the simulations are based is shown in Figs 3.1 and 3.2. It is assumed that the reservoir is horizontal, of infinite extent, homogeneous and of constant thickness. The sand is between 3200 and 3350 ft. The reservoir is producing through a series of long horizontal wells (length>1500 m) separated 600 m from each other (Fig. 3.2). If the pattern of horizontal wells is assumed to repeat itself an infinite number of times, then the sectorial symmetry could be used to reduce the problem to the analysis of a quarter of a pad (Fig. 3.3). The four vertical faces of this pad would be impermeable (because of the symmetry) and would have zero displacements in a direction normal to the face and unrestrained displacement in the plane

(hence the faces would be free of shear stresses). This condition would be approximately met by the production pads located around the centre of the field, but not by those located close to the boundaries.

Most of the flow will occur in vertical planes normal to the well axis, except in the zone close to the end points of the well. A reasonable approximation could be obtained by assuming that the flow and displacements are contained in these vertical planes normal to the well axis. Hence the problem could be considered approximately bidimensional (Fig. 3.3). From a mechanical point of view, this is equivalent to consider a plane-strain case (zero horizontal deformation normal to the plane of analysis). The final model would look as in Fig. 3.4.

An additional simplification could be obtained if extreme values for the stiffness of the overburden are considered. If the overburden is very stiff, then the imposed boundary condition at the top of the sand would be an equal vertical displacement condition. This can be modelled with an additional stiff layer (shale) with no flow in it. If the overburden is very soft, the condition would be a constant total vertical stress (Fig. 3.5). Both models were used in the simulations, with the one in Fig. 3.4 referred as the full 2D model and the one in Fig. 3.5 as the reduced 2D model.

3.2.2 Geomechanical and flow properties

The geomechanical properties of the sand are those given in Table 1, associated with the use of the Cam-Clay constitutive model. The initial porosity is assumed to be equal to 0.3. The absolute permeability is 10 darcys. The oil viscosity was taken as 3000 cp. The total density (solid matrix plus water) was taken as 2100 kg/m3.

3.2.3 Boundary and initial conditions

The whole domain of both models is assumed to be fully saturated with a fluid of density equal to that of the water (1000 kg/m3). This implies a normal gravity gradient for the pore pressure. For the 2D models the left and right boundaries are assumed impermeable due to sectorial symmetry. The bottom boundary is also assumed impermeable (shale basement). The upper boundary in the full 2D model (Fig. 3.4) has zero (atmospheric) pressure. The upper boundary in the reduced 2D model is an impervious boundary.

For the stress and displacements boundary conditions the left and right boundaries have zero horizontal displacement and unrestrained vertical displacement (shear free boundaries). The bottom boundary has zero horizontal and vertical displacement. The whole domain in both models has an initial total vertical stress given by a vertical gradient equal to the total unit weight (9.81*2100 N/m3). Hence the total stress in the upper boundary is zero for the full 2D model, and the value at the given depth for the reduced 2D model. The initial horizontal stresses are assumed equal in both directions (isotropic stress state in any horizontal plane). The magnitude of the effective horizontal stress is given as $Ko*\sigma'v$. A value of Ko=0.8 was assumed.

The hypothesis regarding the pore pressure gradient and total vertical stress gradient has been confirmed from field data in several reservoirs. In a few MINIFRAC tests, the minimum principal horizontal stress has been reported as low as an equivalent Ko_{min} ($\sigma'h_{min}/\sigma'vert$) equal to 0.32. The small value of the minimum horizontal effective stress could be due to the tectonic environment and deserves further verification. The large difference in the maximum and minimum horizontal stresses implies a higher deviator (q) and a lower effective isotropic stress (p'). Depending on their relative magnitude, this could lead to a delayed or early plastification of the sand compared to an initially isotropic state ($Ko_{max}=Ko_{min}=0.8$). Although most of the simulations were done with the initial isotropic state, a few results with the anisotropic case are presented in the following section.

With regards to the well modelling, a first option is to include its actual geometry (half a circle due to the symmetry). A second option is to apply the well condition at a node. At certain distance from the well, the difference between the two options is very small. The first option has the advantage of better representing what is happening close to the well, but it implies more computing time due to the finer mesh required for representing the well. As the objective of these simulations is the study of reservoir behaviour, the second option was used.

In the node representing the well two different conditions can be imposed: a flow per unit length (half of the actual value due to the symmetry) or a constant pressure drop. Both options could be used to study compaction, but the second was preferred as it is closer to what actually happens during production (the pumps create a pressure drop along the well). The pressure in the well was reduced 50% from its initial value, in order to induce flow. This pressure drop is somewhat too high, and it would surely lead to foamy behaviour or gas separation. It was used in order to ensure that plasticity would develop.

3.3 Results

The following results were mainly obtained by the use of the VISAGE simulator [1]. Some results were obtained from the FLAC3D simulator [2]. ***There is a very important caveat with regard to the interpretation of these results: the only driving mechanism that is studied is compaction. The fluid is considered as a one-phase medium with constant (zero???) compressibility. Hence most conclusions have to be considered preliminary: the combined effect of compaction and other driving mechanisms (foamy oil, gas drive) needs to be studied before final conclusions can be given.***

3.3.1 Approximate compressibility functions

As explained in section 3.1, the 'equivalent compressibility' that could be related to the compressibility used in reservoir simulators can be obtained from the evolution of the volumetric strain (ε_p) with the pore pressure (p) (Eq. 3.8). From the results of the simulations in the full 2D model and the reduced 2D model, it was verified that the strain path is close to oedometric, with the vertical strain at the end of the simulations (50 months) in the order of 100 to 1000 times larger than the horizontal in-plane strain (the out-of-plane horizontal strain is zero because of the 2D plane strain assumption). This is further discussed in section 3.3.2

As an independent check, the Cam Clay constitutive equations were numerically solved for one elementary reservoir volume, assuming an incompressible fluid, perfectly oedometric strain path, and a constant total vertical stress. A MATLAB computer program was written to integrate the Cam Clay equations and obtain the strain and stress evolution as a function of the reduction in pore pressure.

An example of the results is presented in Fig. 3.6. The stars (*) correspond to the results obtained from VISAGE at points located at 38.5, 71.85, and 141.7 meters from the well at the middle depth of the sand (998.3 m). The solid curve corresponds to the result calculated from the Cam Clay equations, starting with the stresses and pore pressures at 998.3 m. Finally, the dot-dashed curves correspond to the results from FLAC3D, using the implicit formulation. As expected, the slope of the curve (reading from right to left) is initially small, corresponding to the elastic phase, and then suddenly increases when the plastic yield envelope is reached. The Cam Clay model predicts a sudden change but in reality the sand shows this change more gradually.

It can also be observed that the VISAGE results and the calculated from the oedometric case are very close, whereas the FLAC3D results shows a systematic deviation, particularly after plasticity was reached. For the elastic case the FLAC3D formulation uses the non-linear elastic model originally proposed as part of the modified Cam Clay, as opposed to VISAGE which uses a linearly elastic model. The differences in the elastic domain are smaller than in the plastic one. For the plastic model the FLAC3D results show large 'noise' due to the sampling of the results (FLAC3D actually solves a sequence of uncoupled problems), and the mesh density used.

The 'equivalent' compressibility function is given in Fig. 3.7. The sand stratum shows an initial elastic phase with compressibility close to 50 μpsi^{-1}, followed by a drastic increase to about 100 μpsi^{-1}, when plasticity is initiated. The transition from elastic to plastic behaviour occurs when the depletion drops the pore pressure below 6.6 MPa (956 psi). As the initial pore pressure is in the order of 10MPa, a 30% decrease in pressure is needed to activate the plastic behaviour. These values cannot be generalised and depend on the particular reservoir that is studied.

It is important to remember that the previous comments apply to an idealised constitutive model fitted to the sands. In reality the increase in compressibility would be more gradual.

The combined effect of the plasticity in the sands and the foamy oil behaviour is not an objective for this report. Additionally, the properties of the foamy oil, and in particular its compressibility variation with pressure is still the subject of an ongoing research. In any case, and just to have a gross idea, in Fig. 3.8 a preliminary estimate of the compressibility of the mixture of oil and gas [8] is compared to the compressibility of the sand. As can be noticed (reading from right to left), for this particular oil and for pressures above 6 MPa (870 psi) the main driving mechanism would be compaction. Below 6 MPa the compressibility of the oil-gas mixture increases dramatically and it would dominate the reservoir behaviour. This conclusion has to be further verified with a proper reservoir simulation with a realistic model for the foamy oil.

Lastly, the effect of the initial stress state is studied. In all the previous simulations an isotropic horizontal effective stress state was assumed with Ko=0.8. From some limited MINIFRAC data, an extreme anisotropic state was assumed, with Komax=0.78 and Komin=0.32. Although this has to be further verified, if the initial stress state corresponds to this situation then for an oedometric depletion (and with a pressure drop of about 4MPa) the effective stress path would not cross the initial yield envelope (Fig. 3.9, VISAGE results). The reason for this is that

the lower Komin leads to a lower initial effective isotropic stress (and a higher deviator q) that pushes the initial state inside the assumed initial yield envelope. Hence the increase in compressibility associated with the onset of plasticity would not be observed. For this case the equivalent compressibility would be a constant value of 50 μpsi^{-1}. It can be concluded that the initial stress state is of utmost importance in the definition of the equivalent compressibility.

3.3.2 Stress and strain paths

As explained in the previous section, the sand follows closely an oedometric (zero lateral strain) path. In Fig. 3.10 the absolute value of the ratio of the vertical to the horizontal in-plane strain is plotted for three points at the same depth than the well. It can be seen how the ratio quickly tends toward a high (>10) value.

Regarding the stress path, it would be defined by the approximate oedometric condition. In Fig. 3.11 the stress paths in terms of p' and q are presented. If the condition were perfectly oedometric and the material elastic, all the paths would be straight lines. The deviation is due to the onset of plasticity and some small departures form the oedometric condition.

The slope of the stress path (dq/dp') is equal to 2.0. Although some paths, with a similar slope, were chosen in the laboratory tests, ideally more tests, following these paths would be needed to better characterise them. In particular, a set of oedometric tests with measurement of the lateral (horizontal) stress would be very useful.

3.3.3 Effect of plasticity development in compaction.

In Fig. 3.12 the evolution of the vertical strain for points at 137.9 m from the wells and at the same depth are shown. Two constitutive models are included: an elastic model and an elastoplastic model. The elastic properties for both models are the same.

As can be seen, once plasticity develops the rate of compaction increases, giving, after 50 months (and for a 50% initial pressure drop), a vertical strain that is about 30 to 40% larger in the actual elastoplastic case than in the elastic one.

The final vertical strain for the applied pressure drawdown (50% of initial value) is about 1.3%, hence the maximum expected subsidence is about 2 ft (0.6 m) for a 150' reservoir. This value can be considered as an upper bound because of the applied boundary conditions: infinite number of pads that leads to no possible 'bridging' effect from the overburden. Additionally, the applied drawdown is very high. If the geometry of the reservoir were such that the extent of the reservoir was similar or lower than its depth, then the expected value of compaction strain and the effect on the surface would be much lower. This deserves a sensitivity study.

3.3.4 Effect of plasticity development in the pressure decline.

In Fig. 3.13 the pressure decline (after an initial pressure drop of 50%) for the elastic and elastoplastic cases are compared. After 20 months the pressure in the elastoplastic case is 70% larger than in the elastic one, and after 30 months is about 100% larger. The increase in compressibility due to plasticity helps to decrease the rate of decline (improving recovery). These numbers are valid only if compaction is the only driving mechanism and if the permeability does not change significantly during compaction.

3.3.5 Effect of plasticity development in oil production.

The actual flow rates in the well produced by the applied pressure drawdown can only be roughly estimated for the kind of finite element model used in this report. As explained in section 3.2.3 the pressure drop was applied to a node (not to an actual semicircular geometry). This creates a singularity at the node and numerical inaccuracies in the velocity field close to it. Additionally, the magnitude of the initial drawdown is large (50% drop in pressure). In an attempt to estimate the effect of plasticity development in the flow rate, the velocity field was integrated along a rectangular neighbourhood around each node, with the upper an lower sides of the rectangle in the upper and lower faces of the sand, the left side of the rectangle on the left boundary of the model and the right side at about 10 m from the well. In Fig. 3.14 the flow variation is shown (the flow was assumed to be constant along the well). After 20 moths the flow for the actual elastoplastic case is 2.6 times that of the elastic one. After that, both flows diminish but the relative difference between the elastic and elastoplastic case increases.

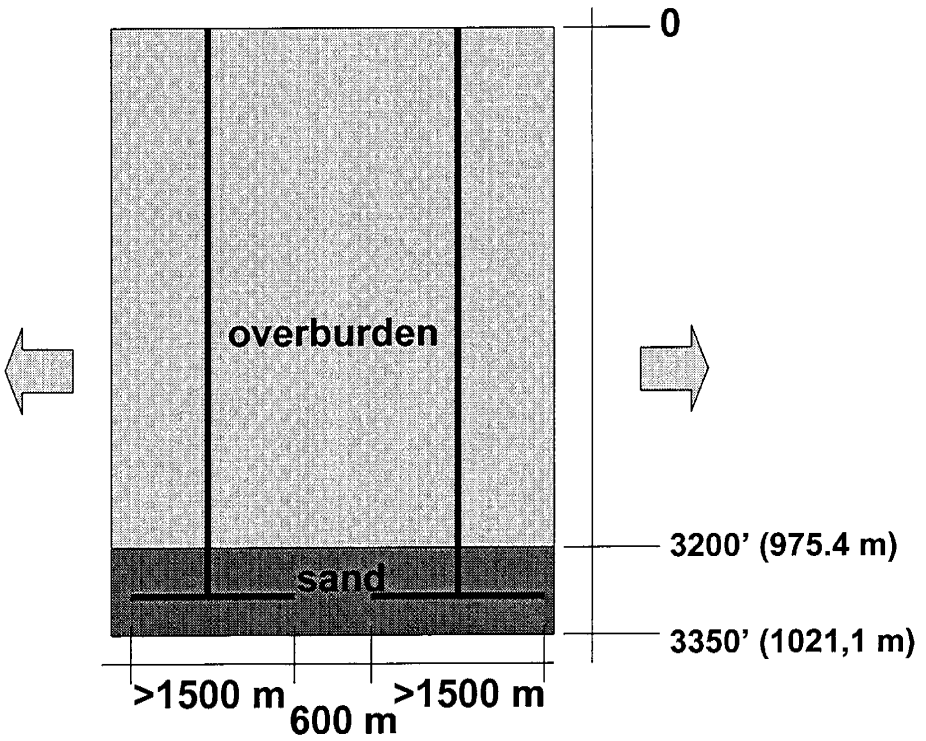

Fig.3.1 Idealised geomechanical model. Cross section.

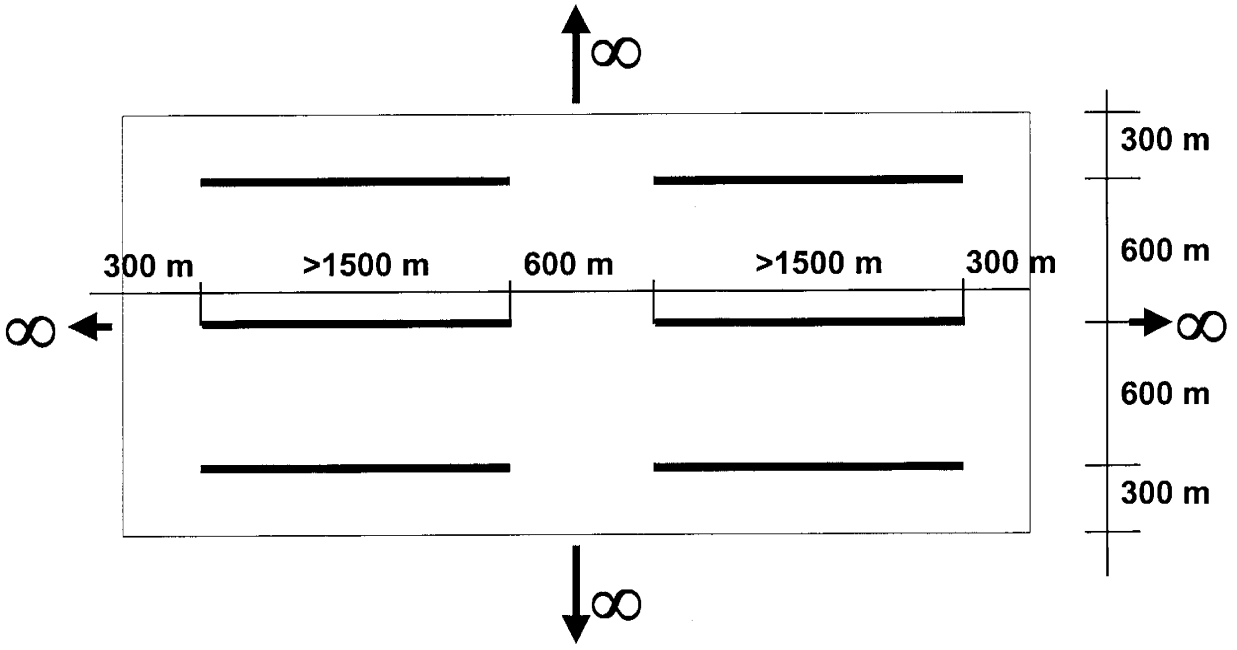

Fig. 3.2 Idealised geomechanical model. Plan view.

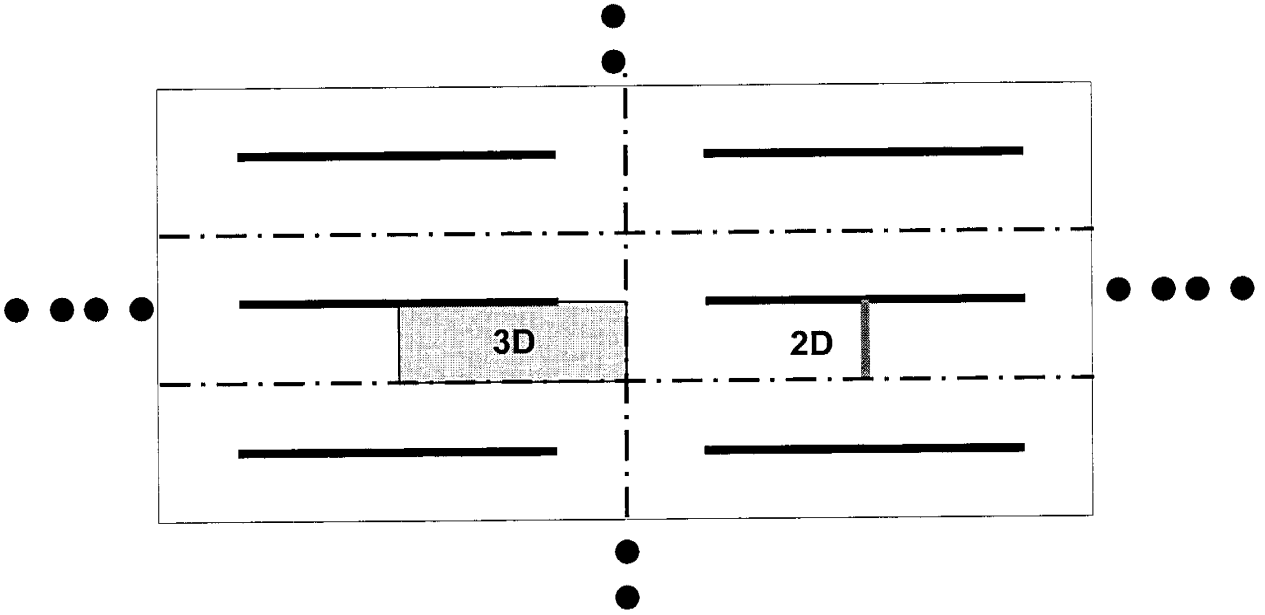

Fig. 3.3 Idealised geomechanical model. Sectorial symmetry: 3D and 2D models.

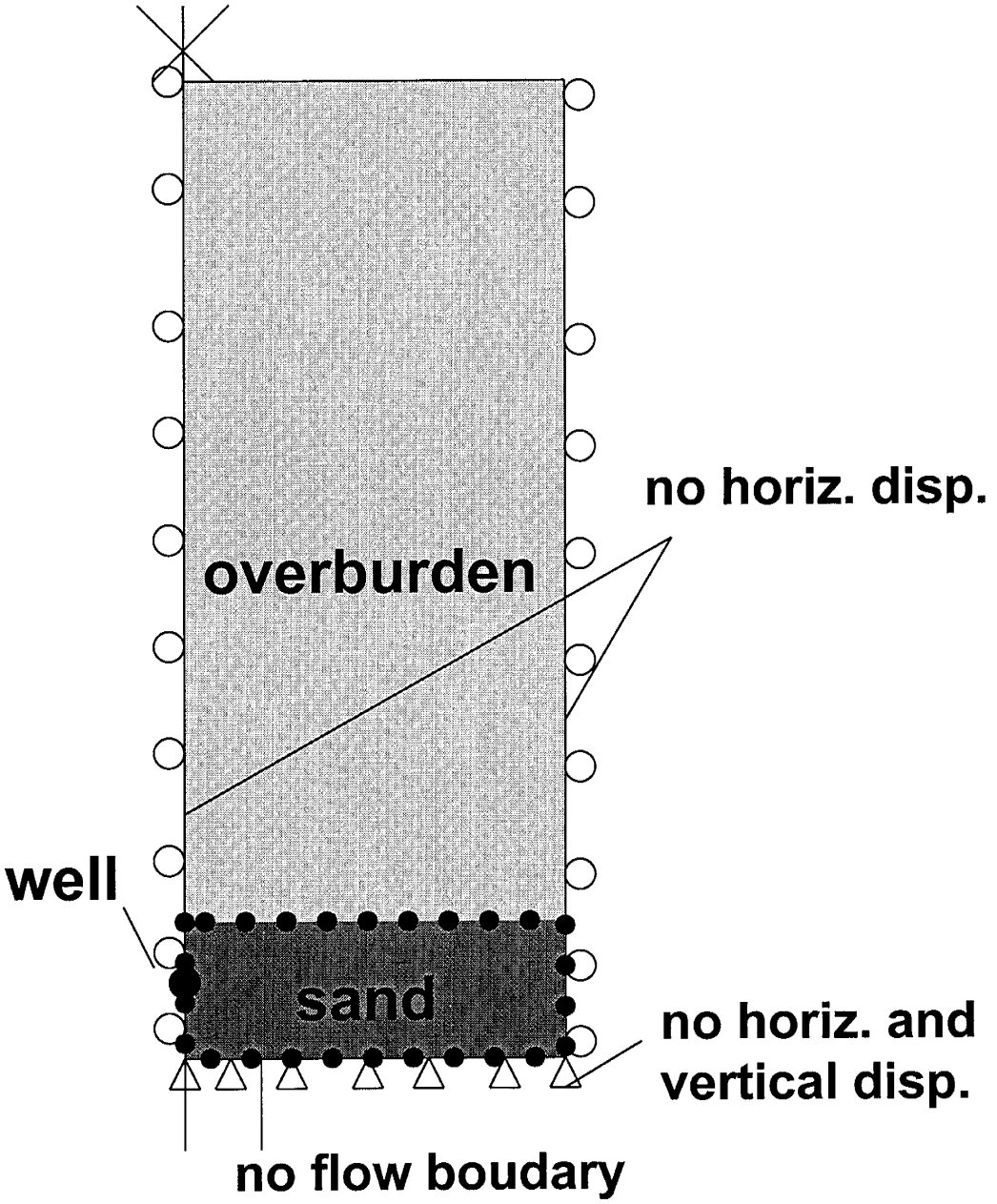

Fig. 3.4 Idealised 2D symmetrical model: Full overburden.

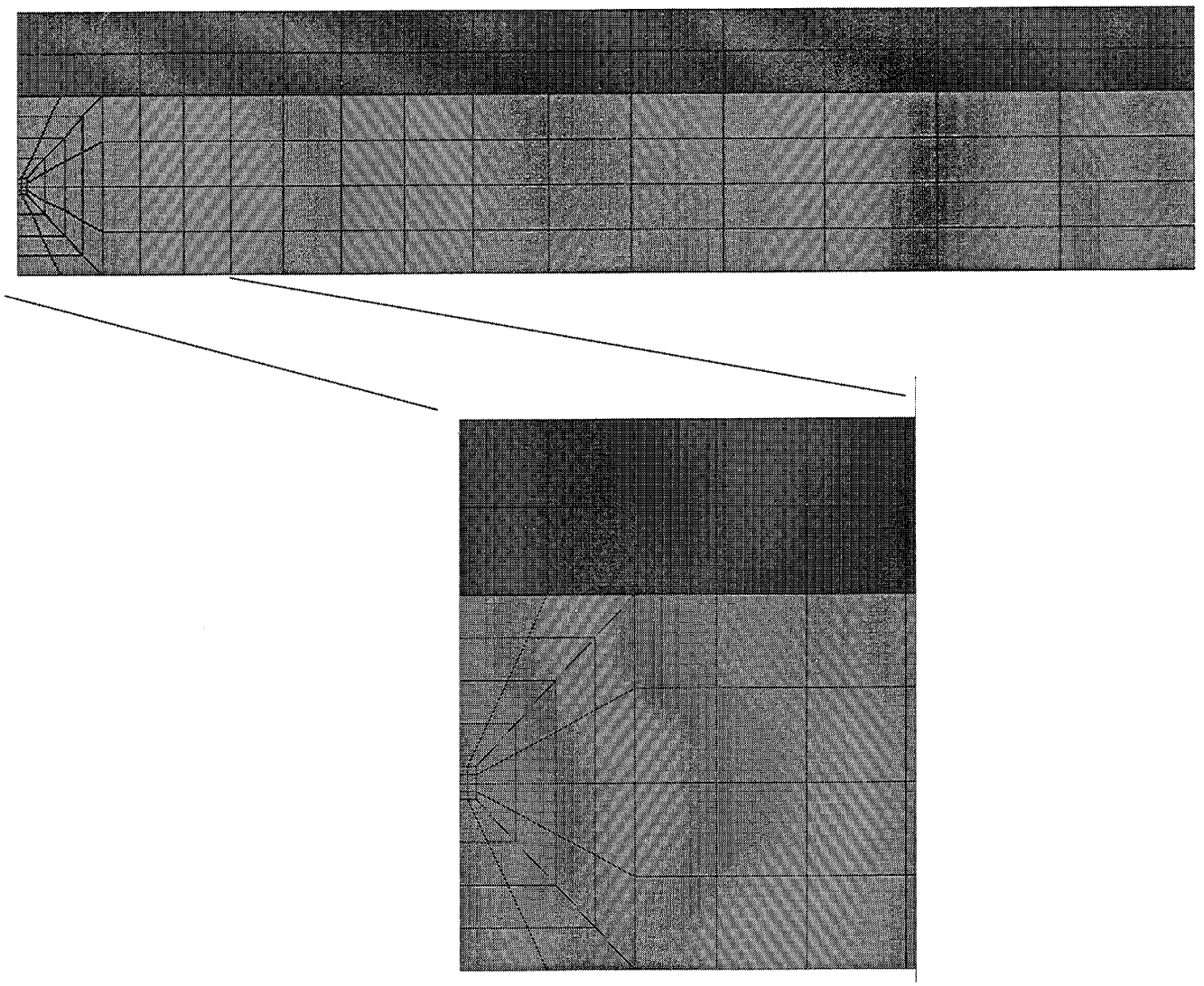

Fig. 3.5 Idealised 2D symmetrical model: limited overburden.

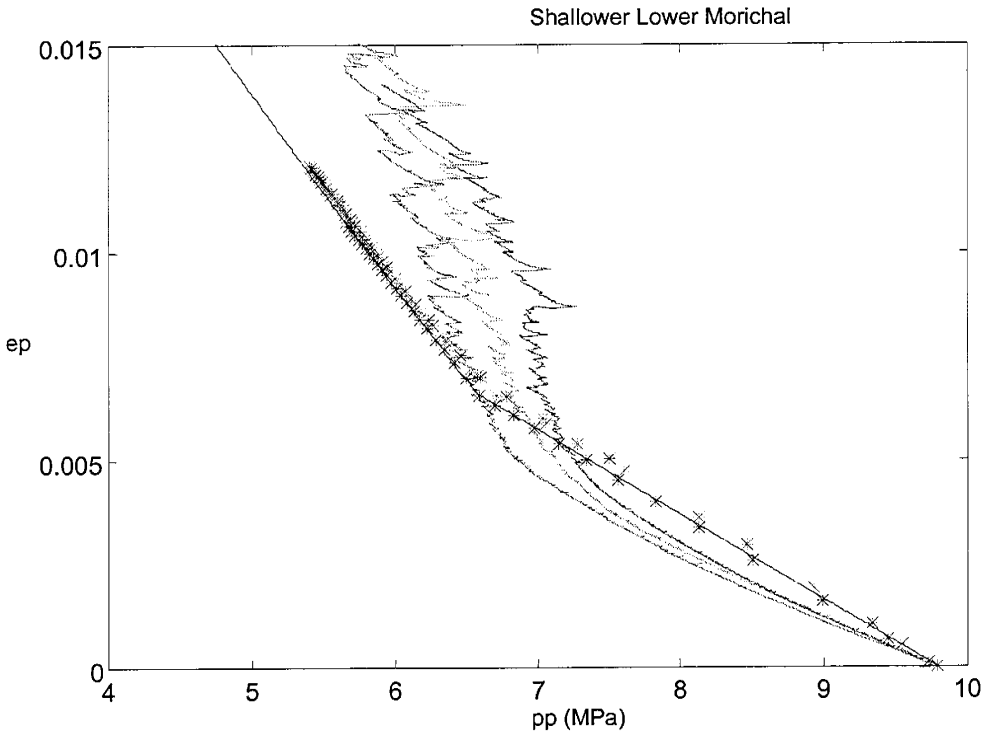

Fig. 3.6 Depletion curves.

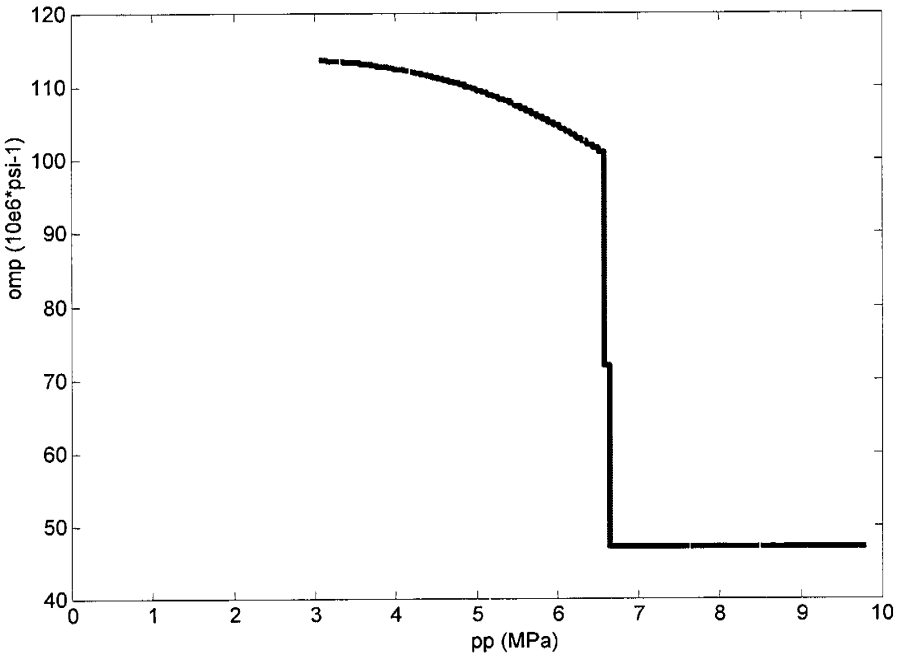

Fig. 3.7 Equivalent compressibility curve calculated from the oedometric hypothesis

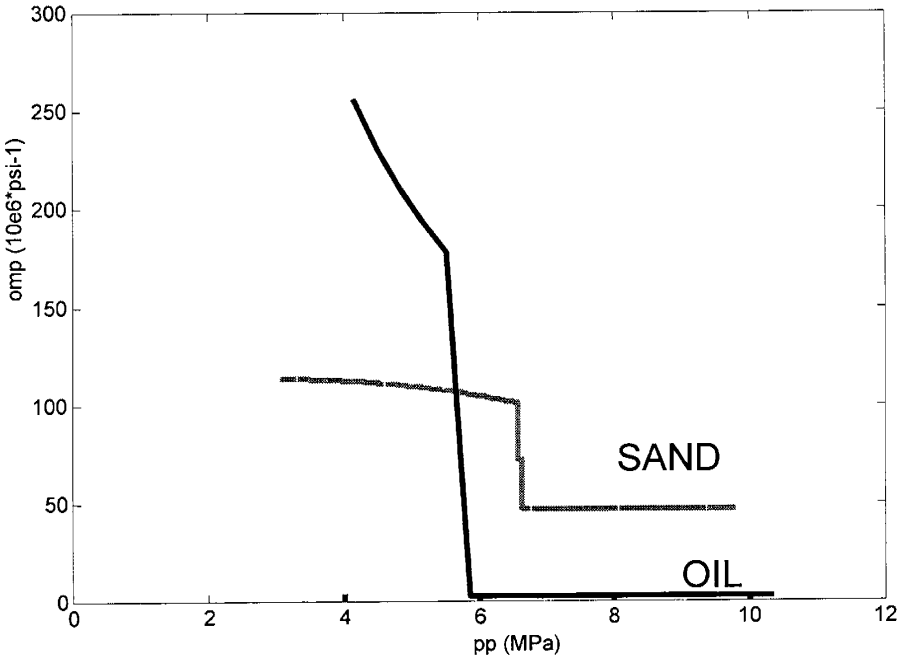

Fig. 3.8 Comparison between equivalent sand compressibility and foamy oil compressibility

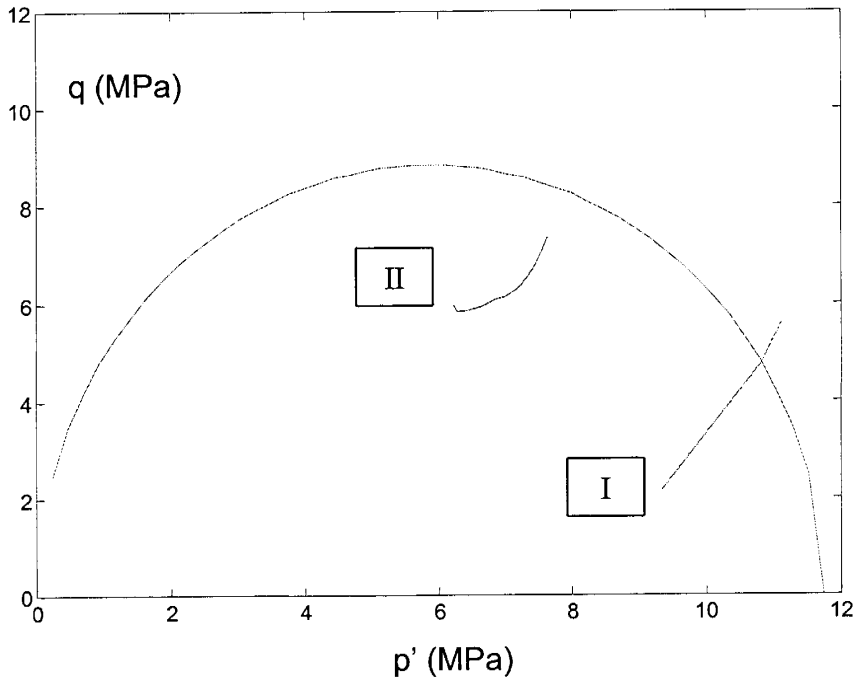

Fig. 3.9 Effective stress paths for two different initial stress states.
I: Komax=Komin=0.8; II: Komax=0.8, Komin=0.32.

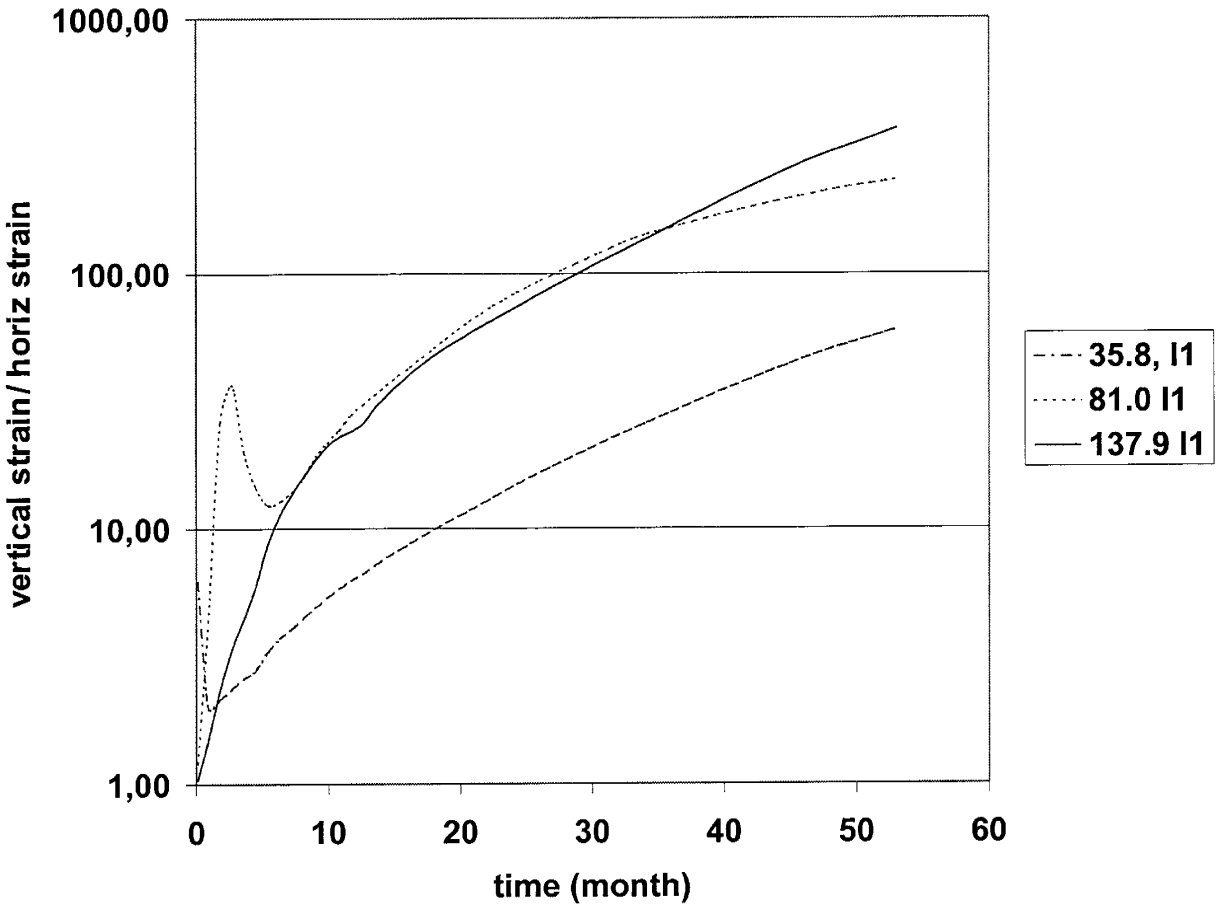

Fig. 3.10 Ratio of vertical to horizontal strains for three points at 35.8; 81.0; and 137.9 m from the well

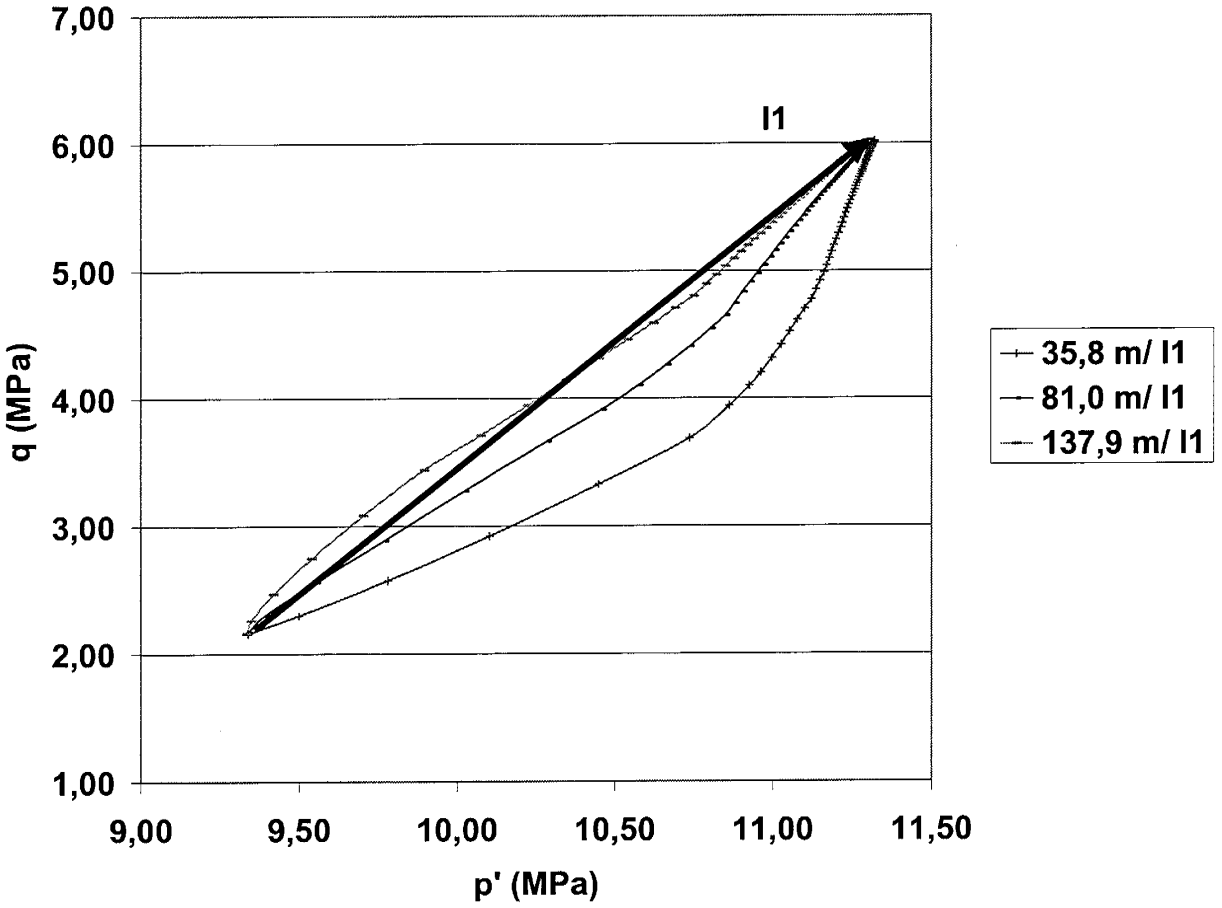

Fig. 3.11 Effective stress paths for three points at 35.8; 81.0; and 137.9 m from the well.

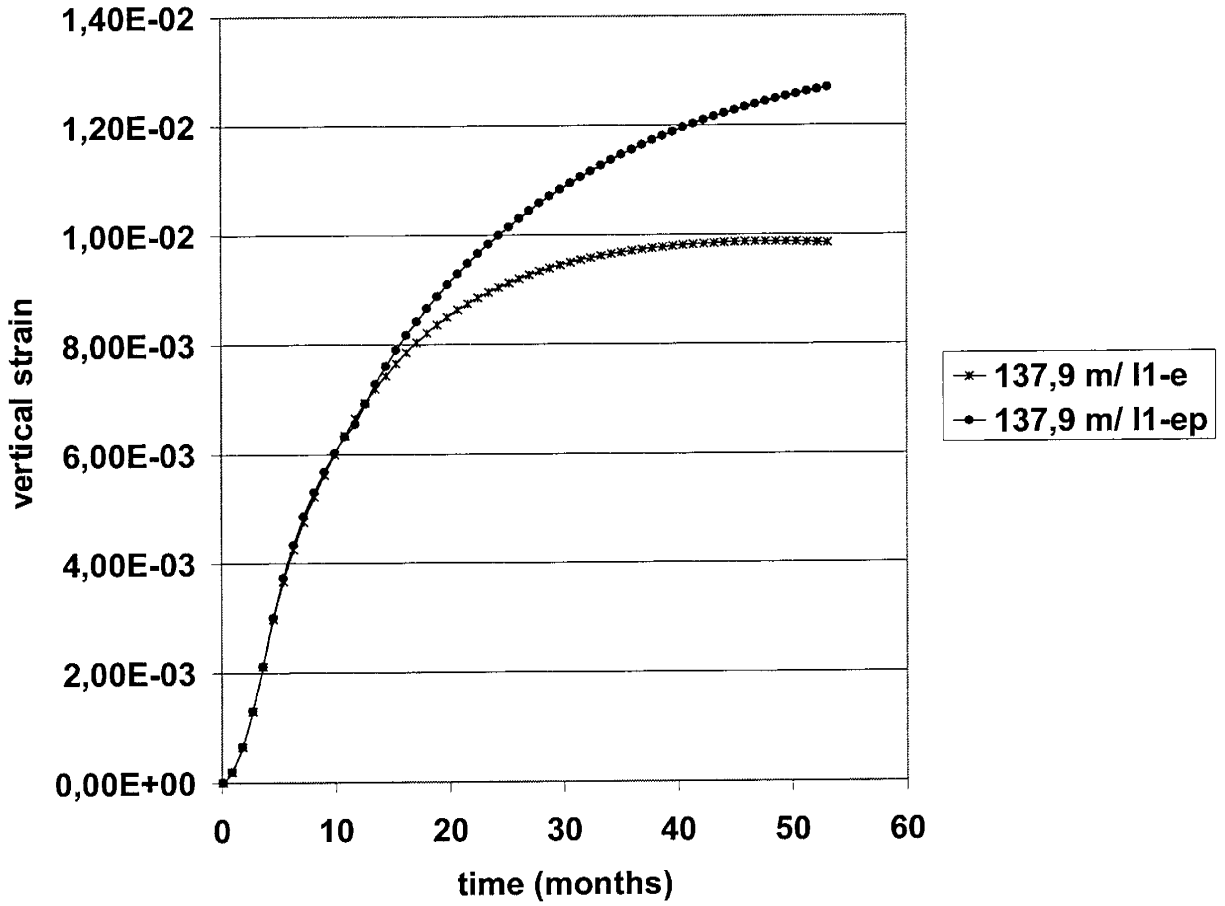

Fig. 3.12 Evolution of vertical strain for a 50% pressure drop applied at the well. Elastic (e) and Elasto-plastic (ep) constitutive models.

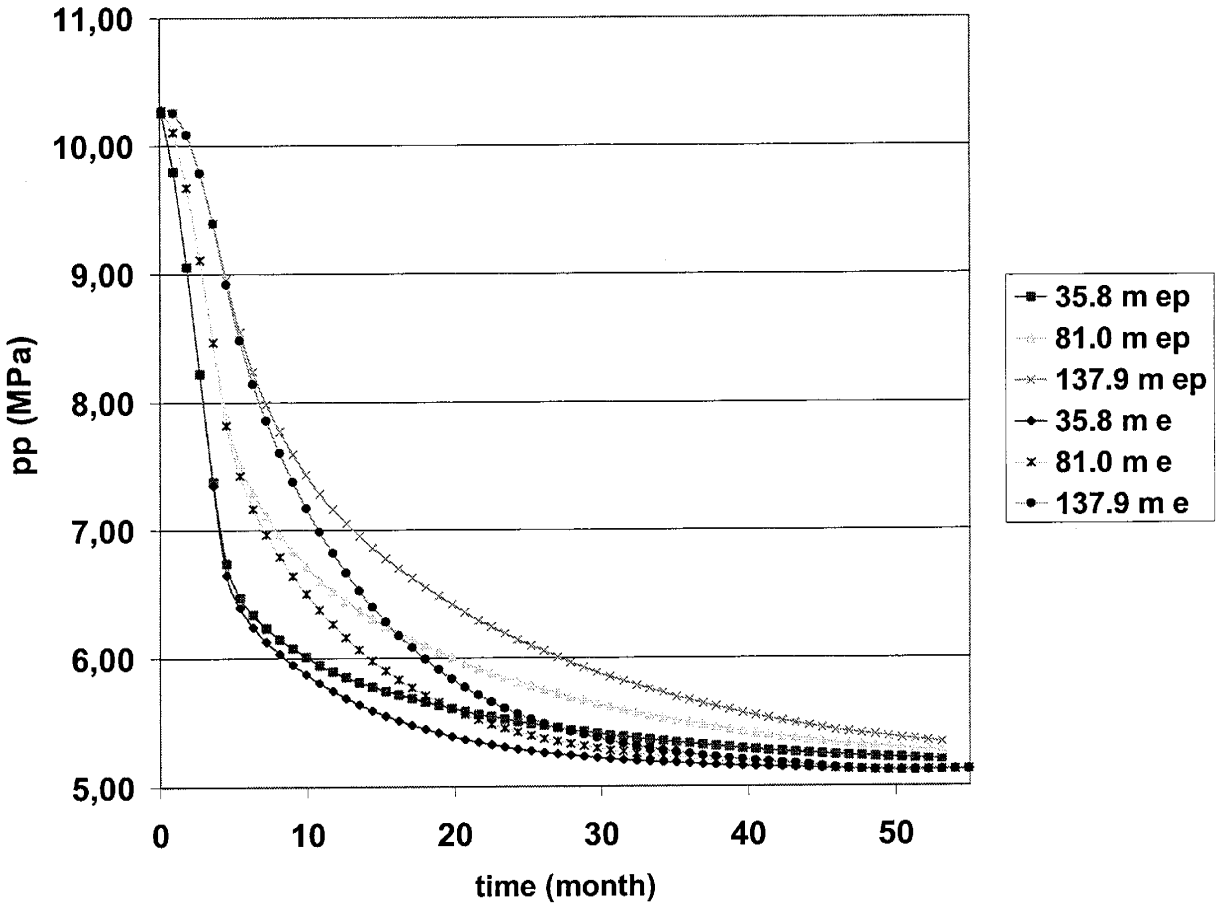

Fig. 3.13. Pressure decline: elastoplastic (ep) vs elastic (e) cases.

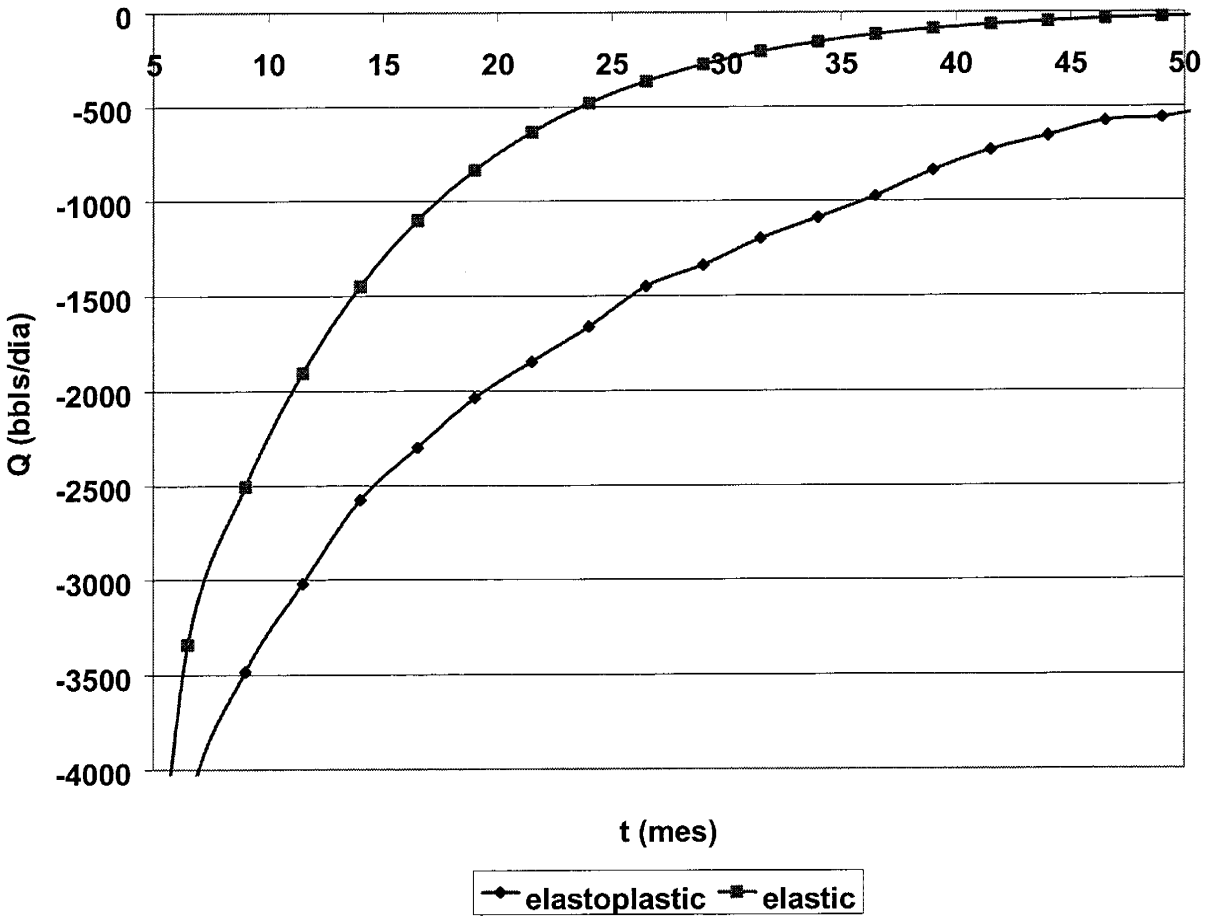

Fig. 3.14. Approximate oil flow. Elastoplastic and elastic cases.

4. CONCLUSIONS AND RECOMMENDATIONS

1.- An attempt to fit a Cam Clay model to the laboratory data from triaxial tests of a Faja del Orinoco sand (Orinoco Belt sand) is presented. Although the CAM CLAY model has limitations for the representation of the behaviour of uncemented sands, it could be appropriate for compaction studies, where a moderately small variation in strain and stresses is expected. The moderate deviations of the predicted behaviour to that measured can be reduced if a more realistic sand model is used. Some of the larger inconsistencies in the laboratory data cannot be explained even with more refined models, and are probably due to problems in the experimental set-up.

2. The strain paths followed by the productive sands under depletion are very close to the oedometric path: the horizontal strains are negligible. This conclusion is based on simplified 2D models, but is expected to hold for 3D models if the patterns of the pads is as shown in this study. The stress paths associated with this oedometric case were presented, and in general they are close to the paths used in the laboratory tests. The drawback of the use of these paths for characterisation of unconsolidated sands is that they do not allow to confidently define the critical state parameters: frictional angle and critical state line. If the characterisation is going to be used in problems where a higher strain or higher deviator stress are present (borehole stability for instance) then the laboratory data has to be complemented by additional tests under shear-dominated stress paths that take the sample to a critical state.

3. The possibility of using more refined sand models for compaction studies is limited by the availability of commercial geotechnical/geomechanical simulators with those models implemented. It could be convenient to discuss this possibility with the simulator developers. In any case, due to the fact that the strain path is basically oedometric for the case of the production pads analysed, the equations of more refined models could be solved under that hypothesis, at least for generating 'equivalent compressibility curves'. In particular it is recommended to study the use of the Nor-Sand [6] and the Pestana-Whittle [15] model.

4. If an initial isotropic horizontal stress state is assumed, with Ko=0.8, then the initial equivalent compressibility would be close to 47 μpsi^{-1}. When the pore pressure drops roughly 25%-30% from its initial value (a decrease in 2 to 3 MPa), then plasticity starts to act, and the equivalent compressibility increases to about 100 μpsi^{-1} and remains roughly constant for further realistic depletion. The CAM-CLAY model predicts a sudden transition whereas the sand shows

a more gradual change. The reason for the increase in the compressibility is that the shear stress would contribute to the volumetric strain: the sand experiences a contractive behaviour. If the initial horizontal stress state is anisotropic (Komax=0.8, Komin=0.32) then a pressure drop of up to 4MPa is not enough to activate plasticity. If this is the actual condition, then a constant equivalent compressibility of 47 μpsi^{-1} would be recommended.

6. The development of plasticity (for the Ko=0.8 case) and the corresponding higher compressibility would imply, in a one-phase oil, a lower decline rate and higher recovery as compared to the elastic case. Pressures 100% larger and oil production rates up to 160% larger would be expected from the effect of plasticity, ***if compaction were the only driving mechanism***. Preliminary estimates of the oil properties suggest that for the actual case, the foamy effect and gas drive would probably dominate when the pore pressure drops below 6 MPa. For pressures lower that this value the increase in the compressibility of the oil-gas mixture will override the compaction as a driving mechanism. If properties of the oil-gas foamy mixture are available, it is recommended to perform a set of geomechanical simulations with a one-phase liquid of variable compressibility, in order to study the actual interaction between the compaction and the foamy-oil drive.

7. For an extreme 50% drawdown, the maximum expected average vertical strain is 1,5%. If this compaction transmits to the surface, a final subsidence of the order of 0.6 m could be expected. The actual value depends on the geometry of the reservoir (and in particular its extent/depth ratio) and the mechanical properties and geological structure of the overburden. It is recommended to perform a sensitivity study with regard to the geomechanical boundary conditions in order to study the potential subsidence.

8. Further work is being carried on at PDVSA-INTEVEP. In particular: i) the addition of the foamy-oil effect to a geomechanical simulator through the use of a variable compressibility for a one phase fluid, ii) sensitivity analysis of the compaction and subsidence to reservoir geometry and geomechanical properties of the overburden and underlaying strata, and iii) the possibility of strain localisation in the form of compaction bands, which could dramatically modify the effect of compaction on primary recovery.

5. REFERENCES

1. VIPS. VISAGE User's Manual. Version 7.0 April, 1999.
2. ITASCA Consulting group. FLAC3D Version 2.0, User Manual. 1999.
3. WOOD, D. Soil Behaviour and Critical State Soil Mechanics. Cambridge University Press. 1990. 462 pages.
4. ROSCOE, K.; BURLAND, J. On the generalised stress-strain behaviour of 'wet' clay. In Engineering Plasticity, Heyman, J. And Leckie, F. (eds). 1968.
5. CHARLEZ, P. ROCK MECHANICS. Vol 2. PETROLEUM APPLICATIONS. Paris, Editions Technip, 1997. 661 p.
6. JEFFERIES, M. Nor-Sand: a simple critical state model for sand. Geotechnique. Vol 43, No. 1. 91-103. 1993.
7. LADE, P; NELSON, R.. Non-associated flow and stability of granular materials. Journal of Engineering Mechanics, ASCE. Vol 113. No. 9. 1302-1318. 1987.
8. YALE, D.; RODRIGUEZ, M. Personal communication to the author. Sep, 1998.
9. DAFALIAS, Y. Bounding surface plasticity. I: mathematical foundation and hypoplasticity. Journal of Engineering mechanics, ASCE. Vol 112, No. 9. 966-987. 1986.
10. PREVOST, J. A simple plasticity theory for frictional cohesionless soils. Soil Dynamics and Earthquake Engineering. Vol 4. No. 1. 9-17. 1985.
11 PARRA, E. Numerical modelling of liquefaction and lateral ground deformation including cyclic mobility and dilation response in soil systems. PhD thesis. Rensselaer Polythecnic Institute. 1996.
12. GONZALEZ, M; ECHEZURIA, H. Resistencia al corte y análisis de esfuerzos en los suelos de fundación del dique COLM. Inf. Técn. No. INT-TEIG-0044,94. INTEVEP, S.A. Los Teques, 1994.
13. BEEN, K.; JEFFERIES, M.; HACHEY, J. The critical state of sands. Geotechnique. Vol. 41, No 3. 365-381. 1991.
14. CROUCH, R.; WOLF, J.; DAFALIAS, Y. Unified critical-state bounding-surface plasticity model for soil. Journal of Engineering Mechanics, ASCE. Vol 120, No. 11, 2251-2270. 1994.
15 PESTANA, J.; WHITTLE, A. Compression model for cohesionless soils. Geotechnique. Vol 45, No. 4. 611-631. 1995.
16. CHARLEZ, P. ROCK MECHANICS. Vol 1. Theoretical Fundamentals. Paris, Editions Technip, 1991. 333 p.
17. ARONOFSKY, J. Flow through Porous Media. Chapter 88 in Handbook of Engineering Mechanics. Editado por: Flugge, W. Mc Graw Hill Company. 1982.

18. ZIENKIEWICZ, O.; CHAN, A.; PASTOR, M.; et al. Static and dynamic behaviour of soils: a rational approach to quantitative solutions. I: Fully saturated problems. Proceedings Royal Society of London. A 429. 285-309. 1990.

APPENDIX A
NOTATION

The main variables instrumented in a typical triaxial test are: change in length (δl), change in pore volume (δvp), total vertical stress (σv), total horizontal or radial stress (σh), and pore pressure (u). The results of the triaxial tests and numerical simulations are expressed in terms of the following stress variables [3]:

i) Isotropic component of total stress tensor: $p=(2*\sigma h+ \sigma v)/3$. Part of this stress is applied to the fluid phase (u) and the rest (p-u) is transmitted through the solid phase.

ii) Isotropic component of effective stress tensor: $p'=p-u$. In an ideal elastic isotropic material the change in pore volume of the sample is only function of the change in p'.

iii) Deviatoric component of the total or effective stress tensor $q=\sigma v-\sigma h$ (also referred to as the Von Mises component). In an ideal elastic isotropic material a change in q produces only change in shape (distortion) without change in volume.

In the previous expressions it is assumed that the compressibility of the material for the solid grains is much lower than the compressibility of the porous media, hence the Biot coefficient (α) would be equal to one. This approximation is usually valid for uncemmented sands.

The results are also given in terms of the following state and deformation variables:

iv) Specific volume (v): v=total (current) volume of the sample/volume of the solid phase. Based on the previous hypothesis, the volume of the solid phase is constant. The specific volume is related to the porosity (η): $\eta=(v-1)/v$. The use of specific volume lead to a very simple expression for the volumetric strain.

v) Volumetric deformation: $\delta\varepsilon p=\delta v/v$. Natural strains are used in this report, hence the volumetric strain would be the integration of the increments of strain, starting from the beginning of the test ($\varepsilon p=\sum \delta\varepsilon p$).

vi) Shear deformation: $\delta\varepsilon q = (1/3)\delta v/v - \delta l/l$. This expression is only valid if the sample remains roughly cylindrical during the test (condition of uniform strain in the sample). Serious errors can be committed if the sample develops localised deformation (failure planes). Natural strains are used in this report, hence the shear strain would be the integration of the increments of strain, starting from the beginning of the test ($\varepsilon q = \sum \delta\varepsilon q$). The shear deformation is a measure of the distortion of the sample as opposed to εp, which measures the change in volume.

Task 78 – DOE shall provide PDVSA Intevep information on resistivity imaging from cross-bore and surface-to-borehole electromagnetic induction methods developed by LLNL. The information will include acquisition system design, field methods, inversion algorithms, and field results. Field experiments will consist of EOR waterflood and steamflood front tracking in producing oil reservoirs. Information will be provided on research efforts to operate the receiver string in steel-cased boreholes.

Cross Borehole Electromagnetic Induction at an EOR site: A Joint Field – Laboratory Study

Barry Kirkendall, Jeffrey Roberts
Lawrence Livermore National Laboratory
Livermore, CA 94550
USA

Abstract

Interpretation of cross-borehole electromagnetic images acquired at heavy oil sites has traditionally proven to be qualitative and arbitrary due to the complex subsurface geology at such sites. This study is an attempt to develop a qualitative interpretation approach that uses field images and petrophysical results from laboratory analyses to assign accurate conductivity values for inversion images and to gain a clearer picture of the extent and effectiveness of EOR using water injection. We find behavior contrary to the intended waterflooding design with possible mechanisms for increasing the resistivity in this region including 1) increased oil content as injectate sweeps oil toward the plane of the observation wells; 2) lower conductance pore fluid displacing the high conductivity brine; 3) degradation of grain-to-grain contacts of the initially conductive matrix; and 4) artifact of the complicated resistivity/time history similar to that observed in the lab experiments. Additionally, we find a resistivity anomaly consistent with solid state conduction was clearly observed in the laboratory experimental results as evidenced by the resistivity dependence on effective pressure and the resistivity increase for some samples during brine injection. This solid state conduction mechanism would explain the contrary behavior we observe in the field images.

I. Introduction

Electromagnetic (EM) methods are predominately sensitive to the amount, state, and composition of subsurface fluids, while seismic methods provide information concerning subsurface structure. This sensitivity to EM suggests the application of borehole EM techniques towards characterizing subsurface resources and monitoring production and resource recovery processes. These techniques have numerous applications including the focus of this paper, enhanced oil recovery (EOR). The technique of cross-borehole EM induction uses kilohertz frequency EM fields to image the electrical conductivity structure in the plane intersecting two boreholes. Recent efforts to study and increase

borehole EM field and processing resolution (Alumbaugh et al., 2000), borehole EM inversion algorithm efficiency (Newman et al., 1997; Newman, 1995), and borehole ambient noise sources (Zhu et al., 1999) have resulted in advances in producing consistent cross borehole EM tomographic images. However, the interpretation of these tomographic EM images remains an undeveloped science.

Using cross-borehole EM induction imaging, we attempt to improve interpretation techniques by incorporating petrophysical analysis from core samples, formation fluids, and injection fluids obtained from the site. We account for resistivity values while saturated with both formation fluid and injection fluid, volume of oil moved through the sample during brine injection, and provide resistivity information concerning the core samples as a function of injection time. We develop a qualitative interpretation approach that uses field images and petrophysical results from laboratory analyses to assign accurate conductivity values for inversion images and to gain a clearer picture of the extent and effectiveness of EOR using water injection.

The site under investigation, defined as a heavy oil reservoir producing with an API index of 17, consists predominantly of high porosity and extremely low permeability diatomaceous deposits. EOR in the area has proven somewhat ineffective due to fracture induced injection flow dominating matrix flow. The ability to rapidly image the flow of water injection is therefore crucial to optimizing enhanced oil recovery and understanding the subsurface system. The purpose of this paper is to report field and laboratory results for an active, well-characterized EOR site and to demonstrate that interpretations that include analysis and consideration of physical properties determined by borehole and laboratory methods help obtain more in-depth understanding of injection and EOR processes. These methods can be applied to an arbitrary site.

II. Field Experiment

The Lost Hills oil field is located along the crest of the Lost Hills anticline in California's San Joaquin Valley. This anticline is the southernmost segment of a northwest-trending segmented antiform that includes the Kettleman Hills anticlines and the Coalinga anticline to the north. It is located on the western margin of the San Joaquin Basin and roughly parallels the trace of the San Andreas fault zone 20 miles to the west (Figure 1). The San Andreas fault system is thought to be the dominant control for structure in the western San Joaquin Valley oil fields (Miller et al., 1990).

The Lost Hills oil field was discovered in 1911, although substantial production did not occur until the 1960's. Presently, oil is produced via steam and waterflooding from a series of stacked oil sands ranging from the Miocene Monterey shales and diatomites to the Pleistocene Tulare sands. The Tulare Formation records the Pleistocene history of basin filling in the present-day San Joaquin valley. It is the first non-marine deposit to be preserved, unconformably overlying the marine Pliocene/Miocene Etchegoin Formation. The unconformity at the underlying units contains numerous normal faults while the Tulare is largely unfaulted and has apparently filled in the older faulted eroded surface.

Permeabilities range from a few hundred millidarcies in muddy sands to between 100 and 3000 millidarcies in the clean sands. For the samples used in this study, the permeabilities range between 1.3 and 39.4 millidarcies and the total porosity ranges from 44 to 63%. Oil saturations range between 35 and 75% with a weighted average of 65% (Wilt et al., 1996) and the oil ranges from 10 to 17 API index.

Induction borehole logs as shown in figure 4 show that only oil in the lower section near 1700 feet depth is affected by waterflooding. Preliminary images calculated in the field (Figures 5a and 5b) confirm this observation, which leads to the conclusion that the waterflood is not behaving as intended. At a minimum, changes denoting significant amounts of injection fluid should be present in the logs of OB-west (the observation borehole closest to the injector), but they are not. Therefore, we use laboratory measurements, in addition to our field images, to provide a time lapse history of area and study oil/water content over time. Specifically, we use laboratory sample behavior and field logs to better interpret the field images.

III. Field Data Processing

The technique of cross-borehole electromagnetic imaging, described in Kirkendall et. al (1999) and Wilt et al. (1995), is analogous to the technique of seismic borehole tomography (Ivansson, 1986 and Gustavsson, 1986). One specific difference is that EM induction continuously operates in the frequency domain with a kilohertz - frequency source signal. While the vertical dipole receiver antenna is stationary and the vertical dipole transmitter antenna is moved through the depth section of interest we record the scattered, or induced, field isolated from the primary source field using a frequency tuned phase lock loop with amplification. The scattered field is stacked for 300 ms, line filtered before isolation and sampled from the phase lock loop output at 1.0 Hz; this provides a stable data point every 0.15 meters.

The accuracy of the current crosswell system is estimated to be approximately 5% of well spacing – a factor dependent on well separation, instrument geometry, and source frequency. Decimation of the data is the first step in processing to reduce the computation time of the inversion process. Pre-processing also includes spike removal, cubic spline interpolation and resampling, correction of borehole deviation from gyroscopic logs, and removal of the field system transfer function using field calibration techniques and one-dimensional forward models.

Deep resistivity electromagnetic sounding (DRES) induction log data, also referred to as ILd, acquired from both boreholes, create a starting electrical resistivity model by extrapolating resistivity values into the plane intersecting the transmit and receive boreholes. Input to the inversion process uses this pre-injection DRES subsurface resistivity survey and resampled calibrated data; we invert for the electrical resistivity. The inversion code (Newman, 1998) is a two-dimensional Krylov algorithm using the quasi-minimum residual method, which is most appropriate when the inversion matrix eigenvalues are complex. Although this code is well characterized and considered a benchmark, sensitivity studies suggest limiting the number of iterations to between 5 and 10, as past experience suggests a tendency of this code to jump out of global minimum values in the process of smoothing the model to the data. Further information regarding this code should be referenced to Newman, 1995.

Inversion results are displayed using MATLAB scripts with the induction logs displayed on either side of the image to allow a general verification and comparison of the results. As shown in figures x5x – 6, the results provide a two-dimensional resistivity tomographic distribution in the plane between the two boreholes.

IV. Laboratory Experimental Techniques

A four-terminal pair, two-electrode lead configuration was used to measure the complex impedance as a function of frequency. Data were taken with an HP 4284A LCR meter. All instruments are high-input impedance devices that measure impedance magnitude $|Z|$, phase angle ϕ, resistance R, and capacitance C. The error of measurement varies according to frequency and resistance, but is generally less than 1% up to 100 k•, and within 5% at the highest impedance limits (>100 MΩ). The system was periodically checked for accuracy using a set of 1% tolerance resistors and capacitors and was found to yield consistent values.

V. Laboratory Experimental Measurement Procedures

This section discusses electrical measurements on oil and brine saturated samples at elevated pressure and temperature. Laboratory electrical measurements were performed at temperatures up to 50°C with separate confining and pore pressure control. The experimental apparatus consists of an externally-heated pressure vessel with separate pumps and controls for confining pressure and pore pressure on either side of the sample (Fig. 2). Pore pressure was controlled independently between 0.1 and 3.7 MPa, and for convenience the two systems are referred to as up- and down-stream pressure systems. The impedance bridge (HP 4284A) was used to continuously measure the resistance of the electrically isolated samples at 0.1, 1.0 and 10 kHz. Electrical resistivity was calculated from the resistance and geometry of the core. Calibration runs using Teflon blanks showed no current leakage through alternate electrical pathways.

Temperature was measured with type T thermocouples with an accuracy of ±2°C. Comparison of the thermocouples with calibrated standards indicated higher precision, on the order of ±0.2°C. Data collection was automated by use of a scanning unit and microcomputer. Pressures were measured using transducers with an accuracy of ±0.05 MPa. Confining pressure was typically held to 3.5 MPa, but ranged from 0.1 to 5.5 MPa during the course of the experiment. Pore pressure ranged from 0.1 MPa to 3.7 MPa, but was typically half that of the confining pressure.

The cylindrical sample having dimensions of 2.5 cm diameter and ~2.0 cm length is placed between two perforated Pt electrodes and Hastaloy endcaps. The endcaps have channels for the introduction of fluid and are welded to high pressure capillary tubing that serves as pore pressure lines. The entire assembly is jacketed with a high temperature polymer and the entire assembly is held together in a stainless steel frame to prevent separation of the electrodes from the sample during boiling events. Electrodes, thermocouples and pressure lines exit the pressure vessel through insulated conical fittings.

Samples were cut from teflon jacketed core plugs provided by Chevron. Samples were jacketed, assembled and placed in the experimental device. Confining pressure was increased to approximately 3.4 MPa followed by heating to the approximate temperature of the in situ sample according to borehole logs, between 30 and 50°C. After the experiment the resistivity data were corrected to the precise temperature of the sample's depth using the measured temperature dependence. Once the sample was finished heating and reached a stable resistivity, crude oil produced from the Lost Hills oil field was flowed through the sample. The electrical resistivity of the oil is greater than 7.7 x 10^4 ohm-m (σ = 0.013 μS/cm). The pore pressure required to force oil through the samples varied between approximately 1.0 and 2.8 MPa, depending on sample permeability. Oil was flowed through the sample until no water was observed in the exit

fluid that was collected and the resistivity again reached a stable value. This value is assumed to be the oil-saturated resistivity and is reported in Table 1, along with other sample parameters including temperature, reported permeability, brine saturated resistivity, and the resistivity ratio.

Once oil-saturated, the pore fluid was changed to a NaCl brine of resistivity 0.28 ohm-m ($\sigma = 3.57$ S/m). This solution was utilized because it has the same electrical conductivity as the brine, but was a cleaner solution that would not damage or contaminate the pumping system and reservoirs. The resistivity was continuously monitored while the brine pushed oil out of the sample. Both fluids were collected permitting estimates of the total volume of fluid flowed. The experiment was ended when the resistivity reached a stable, non-changing value.

VI. Field Results

Figures 5b is the two-dimensional electrical conductivity image acquired in November 1999, clearly showing the locations of high oil (higher resistivity red hue) and brine concentrations (lower resistivity blue hue). Contrasting depth intervals of this image are in between [1400' – 1600'] and [1600' – 1700'], where data would suggest EOR has mixed results. In the upper region, water injection has clearly swept the oil deposits, although in the lower region, EOR has not been effective. Permeability logs (4) suggest that the reason for this decrease in water movement is simply the increase in permeability, also shown in core samples (Table 1). Additionally, the majority of small scale flow as indicated by petrophysical measurements is through the rock matrix. As diatomite can be considered an unconsolidated formation, small scale fractures do not contribute towards significant amounts of flow. Hydraulic fracturing, however, is a cause of large scale fracture flow, and this large scale flow may be contributing to a significant volume of water leaving the injection area.

Figure 5a is the equivalent image acquired almost five months later in March 2000. The two distinct sections are clearly demarcated - the upper high permeability section and the lower low permeability section. Water appears to be moving in the upper section towards borehole OB-East, to the right of the image. In the lower section, we are seeing opposite movement towards OB-West, the left of the image. As noted above, image resolution is approximately 5% of well spacing, or about 3 – 4 feet, whereas figure 5a suggests movement of about 4 – 6 feet. In both images, EM induction well log images are plotted against each side for comparison.

Figure 6 is a comparison of Figures 5a and 5b shown simultaneously with the EM induction log acquired before water injection in December 1994 superimposed on the approximate location of the injector. Pre-injection oil deposits have for the most part not been significantly altered in low permeability regions, and as a result, swept oil has predominantly occurred in the lower section near OB-West. Figure 7 is the percent difference and fractional difference between the two time lapse images where the majority of change occurs near the bottom section of the image.

VII. Laboratory Results

Electrical resistivity as a function of effective pressure

The resistivity as a function of effective pressure (confining pressure-pore pressure) at 1 kHz is shown in Figure 8. These measurements were performed at the beginning of each sample run prior to heating. All samples displayed a similar behavior; decreasing resistivity with increasing effective (or confining) pressure. The two samples displayed, LH1803 and LH1886, are typical. One difference between the two samples is that the pressure increase for sample LH1803 (Fig. 8a) occurred after saturating the sample with oil and that for sample LH1886 (Fig. 8b) before the sample was saturated with oil. This trend is in conflict with the result of Walsh and Brace [1984] where an increase in confining pressure caused an increase in the resistivity of most porous rocks studied. Possible reasons for this behavior include the presence of a solid state conduction mechanism, such as a conducting film or conductive mineral phase, that is more conducting with better grain-to-grain contact as pressure is applied. Another possibility is that increasing the confining pressure crushes the sample, thereby increasing the permeability as well as enhancing electrical transport. Post-run sample characterization via optical and electron microscopy did not provide convincing evidence for one explanation over another.

Electrical resistivity during brine injection

Once the samples were at pressure and oil-saturated, the resistivity was monitored while brine was forced through the sample. These results are shown in Figures 3 a-h where resistivity is plotted as a function of time. For each sample a relatively constant oil-saturated resistivity was established followed by the injection of brine as indicated by the vertical dashed line. The confining pressure and pore-pressure gradient were typically 3.4 and1.7 MPa respectively, but both were higher for relatively impermeable samples. For all samples the final brine-filled resistivity value is lower than the initial oil-filled resistivity and the ratio of oil- to brine-saturated resistivity is listed in Table1. This ratio ranges between 1.8 and 6.7 and does not appear to correlate with either porosity or permeability as reported by Chevron.

Samples LH1329, LH1699, and LH1803 all show a period of decreasing resistivity after brine injection followed by an increase in resistivity again followed by a decrease in resistivity until a new lower resistivity value is reached. In the case of sample LH1803 the resistivity increases to a higher value than before brine injection began. The increase in resistivity occurs after water breakthrough, that is when brine was observed to exit the line downstream of the sample. Samples LH1446, LH1514, and possibly

LH1886 display an abrupt increase in resistivity after the onset of brine injection followed by an asymptotic decrease in resistivity. The final resistivity of the brine-saturated samples is lower because the higher conductivity brine displaces the high resistivity oil.

The increase in resistivity after brine injection is not yet explained but is another indication that a conducting film or solid state conductor might contribute significantly to overall conduction in these samples. Possible candidates include a conductive clay layer, a conducting carbon-rich or hydrocarbon coating, or a solid phase such as pyrite or ferrites, all of which are known to exist in these samples. It is not clear why brine injection would affect the conductivity of the solid phases unless the grains are pushed apart to make poorer electrical contact. Thus, a distributed phase is the favored explanation.

To interpret well-logs and cross-well induction sections it is important to consider that the initial response to brine injection is quite variable and that until sufficient amounts of water have flowed through the sample notable decreases in resistivity may not be evident. The implications of this variability will be discussed in more detail in the discussion section.

Water-rock ratios and oil recovery

Table 2 lists the total amount of brine flowed, the total amount of oil recovered, the percentage of oil recovered assuming the entire pore space was oil-filled, and the water/pore volume ratio. These values are estimates due to uncertainty in the total volume of the pressure lines and high-pressure fittings. Sample LH1699 indicates a greater amount of oil recovered than existing porosity. There is no clear explanation for this, however, the sample could have been fractured or contain an abnormal cavity or vug. Excepting sample LH1699, between approximately 33 and 91% of oil was recovered. There is no apparent relationship between the amount of oil recovered and either water/pore volume ratio or permeability.

Some of the samples were characterized using x-ray computed tomography. This method enables the non-destructive imaging of the samples before and after experimentation and is useful in determining the type of pore fluid, preferential flow pathways, and can possibly illustrate fracturing [i.e., Bonner et al., 1994], although imaging at pressure is not currently possible. X-rays of the sample were taken by translating the samples vertically through a 160 kVp linear source. X-rays passing through the sample were converted to a digital signal by a photo-diode array detector. Many views (angles) of the sample are taken and reconstructed into a series of tomographic slices. Figure 9 shows the reconstructed slices of LH1579 both after the experimental run (a) and as received

(b). The arbitrary color bar represents x-ray attenuation. A test showed that brine was more attenuating than oil, thus the white areas are assumed to be fluid-filled (brine) and the green and yellow areas, less attenuating, are assumed to be oil-filled. The interesting aspects of this imaging are the isolated islands and the band of medium to low-attenuating in figure (a), post-flow. These most likely represent regions of remaining oil not swept out by the brine flow. No such features are evident in the as received sample.

By comparing the ratios of green and white regions in the post-flow image a rough estimate of the amount of oil remaining can be obtained. This works out to about 35%, which is slightly less than the estimate of 46% using volume of oil recovered from the flow process. The white areas in Figure 9a could indicate that preferential flow channels have developed. Further analysis of samples with higher and lower oil recovery rates might reveal whether or not this is the case.

VIII. Discussion

The expected behavior is that as the injected water displaces the non-conducting oil, the resistivity will decrease. Water has been injected at the rate of 400 barrels of water per day (bwpd, 1 barrel = 158.98 liter) beginning in August 1995. The injectors were located at three depth intervals, 457.2, 489.2, and 522.7 m. The perforation holes are 1.2 cm diameter. Induction logs were taken in the observation holes, OB-west and OB-east (Fig. 1a) on December 1994, prior to water injection and again in August of 1999. At first glance we observe that resistivity does not change uniformly with water injection. Referring to Fig. 4 we observe that even over a period of 4.75 years the resistivity has decreased in some areas and remained fairly constant in others. In just a couple small regions the resistivity has increased by a small amount, i.e., ~1500 ft. depth. The results can be explained by examining in detail the cross-well section logs, by considering the possibilities of channelized and local flow paths, and by incorporating the laboratory results.

Another complicating factor is the difference in electrical resistivity of the produced versus injected water. The produced water has a resistivity of ~0.25 ohm-m (s = 4 S/m) and the injected water has a resistivity of ~0.8 ohm-m (s = 1.25 S/m). However, when compared to the resistivity of the displaced oil, 7.7 x 104 ohm-m (s = 13 mS/m), the contrast between the resistivity of oil and both aqueous fluids is sufficient to be readily observed.

The cross-well EM induction images taken November 1999 are in general agreement with the induction logs from August, 1999 (Fig. 5b). These snapshot images occurred over a period of time with continuous water injection. At these depths between the observation wells we might expect the most changes in resistivity. This is the case for the cross-well images displayed as differences in Fig. 7 a and b. However, the largest resistivity change is positive, toward more resistive pore fluids and slightly offset from the injector horizons. The question what does this resistivity increase represent?

Possible mechanisms for increasing the resistivity in this region include 1) increased oil content as injectate sweeps oil toward the plane of the observation wells; 2) lower conductance pore fluid displacing the high conductivity brine; 3) degradation of grain-to-grain contacts of the initially conductive matrix; and 4) artifact of the complicated resistivity/time history similar to that observed in the lab experiments.

The first mechanism, increased oil content due to EOR, can possibly be checked by examining production history of nearby wells. The second mechanism, changing pore

fluid conductivity is reasonable, because the highest observed resistivity change is slightly less than one ohm-m and the different fluids have a difference in resistivity of about 0.6 ohm-m. But, since the change is larger than this in at least some portion of the image plane, an additional or combination of mechanisms is likely. The third and fourth explanations are similar in that both involve some sort of solid state conduction mechanism. An resistivity anomaly consistent with solid state conduction was clearly observed in the laboratory experimental results as evidenced by the resistivity dependence on effective pressure and the resistivity increase for some samples during brine injection.

One observation we can make is the anomalous increase in resistivity occurs earliest times for the samples with the highest permeability. This complicates the interpretation of both well induction logs and the field images because different sample display different time-dependent resistivity changes; we don't expect equal injection along the plane of the image. However, an estimate of the maximum effect of the anomaly on measured field electrical properties can be accomplished by assuming equal and steady brine injection over the entire injection interval accompanied by uniform sweep of oil.

IX. References

Alumbaugh, D.L., Newman, G.A, 2000, *Image appraisal for 2-D and 3-D electromagnetic inversion*, Geophysics, v. 65 (5), pp. 1455 – 1467

Gustavsson, M., Ivansson, S., Moren, P., Pihl, J., 1986, Seismic Borehole Tomography – Measurement System and Field Studies, Proceedings of the IEEE, v. 74 (2), pp. 339 - 346

Ivansson, S., 1986, Seismic Borehole Tomography – Theory and Computational Methods, Proceeding of the IEEE, v. 74 (2), pp. 328 - 338

Kirkendall, B, Lewis, J.P., Hunter, S.L., Harben, P.E., 1999, *Progress in Crosswell Induction Imaging for EOR: Field System Design and Field Testing*, LLNL Internal Report UCRL-133468, 14 p. (http://www-r.llnl.gov/tid/lof/documents/pdf/235411.pdf)

Miller, D, McPherson, J.G., and Covington, T.E., 1990, *Fluvo-Deltaic Reservoir, South Belridge Field, San Joaquin Valley, California*, in Barwis, J.H., McPherson, J.G., and Studlick, J.R. (Editors), Sandstone Petroleum Reservoir, Springer-Verlag, New York, NY, pp. 109-130

Newman G.A., Alumbaugh D.L., 1997, Three-Dimensional Massively Parallel Electromagnetic Inversion – Theory, Geophysical Journal International, v. 128 (2), pp. 345 - 354

Newman, G.A., 1995, Crosswell Electromagnetic Inversion Using Integral and Differential Equations, Geophysics, v. 60 (3), pp. 899 - 911

Wessel, Paul and Smith, W.H.F., New Version of the Generic Mapping Tools Released, http://www.agu.org/eos_elec

Wilt, M.J., Lee, K.H., Morrison, H.F., Becker, A., Tseng, H.-W., Torres-Verdin, C., and Alumbaugh, D., 1995, Crosswell Electromagnetic Tomography: A New Technology for Oil Field Characterization, The Leading Edge, pp. 173 - 177

Zhu, Z.Y., Haartsen M.W., Toksoz M.N., 1999, Experimental studies of electrokinetic conversions in fluid-saturated borehole models, Geophysics, v. 64 (5), p. 1349 - 1356

X. Acknowledgements

This project was funded by the U.S. Department of Energy through Fossil Energy research under contract number W-7405-Eng-48. We gratefully acknowledge NPTO-DOE project manager Tom Reid for his continued support. We also acknowledge Mike Morea, Dale Julander, Qiang Zhou, Jim Copeland, and Kristin Castelucci of Chevron, Mike Hoversten of Lawrence Berkeley National Laboratory, Greg Newman of Sandia National Laboratory, Phil Harben, Steve Carlson, and Jennifer Swenson of Lawrence Livermore National Laboratory, and Mike Wilt and Ping Zhang of Electromagnetic Instruments Inc.

Table 1 Sample descriptions and measured properties.

Depth, ft	Porosity	Perm. (mD)	Oil filled resistivity (Ωm)	Brine filled resistivity (Ωm)	Ratio, Oil/brine	Activation energy, eV	Formation Temp. (°C)
1329.35	55.8	2.2	4.0	2.0	2.0	0.18	35.7
1446.20	44.7	39.4	4.0	2.3	1.7	0.18	37.6
1514.25	46.9	20.8	3.9	3.0	1.3	0.18	38.6
1579.70	47.4	10.8	4.8	3.7	1.3	0.17	39.2
1666.80	62.5	1.8	15.6	2.3	6.7	0.22	40.4
1699.00	47.9	2.4	5.1	2.8	1.8	0.17	40.9
1803.25	59.9	2.0	8.3	2.8	3.0	0.21	42.9
1886.20	58.3	1.3	5.6	1.7	3.3	0.20	44.1

Table 2 Fluid flow and oil recovery estimates (Nd = not determined)

Depth, ft	Descrip.	Total Flow (mL)	Water Flow (mL)	Oil Flow (mL)	%oil Recovered	Water/pore volume ratio
1329.35	Clayey	84	79	3.31	0.612	17.2
1446.20	Sandy	85	80	3.31	0.712	20.3
1514.25	Sandy	50	47	1.31	0.2043	11.9
1579.70	Clayey	12	8	2.81	0.535	1.9
1666.80	Clean	87	nd	nd		nd
1699.00	Clayey	40	33	5.31	1.228	8.4
1803.25	Clean	66	60	4.31	0.8031	12.6
1886.20	Clean	86	81.5	2.81	0.468	16.5

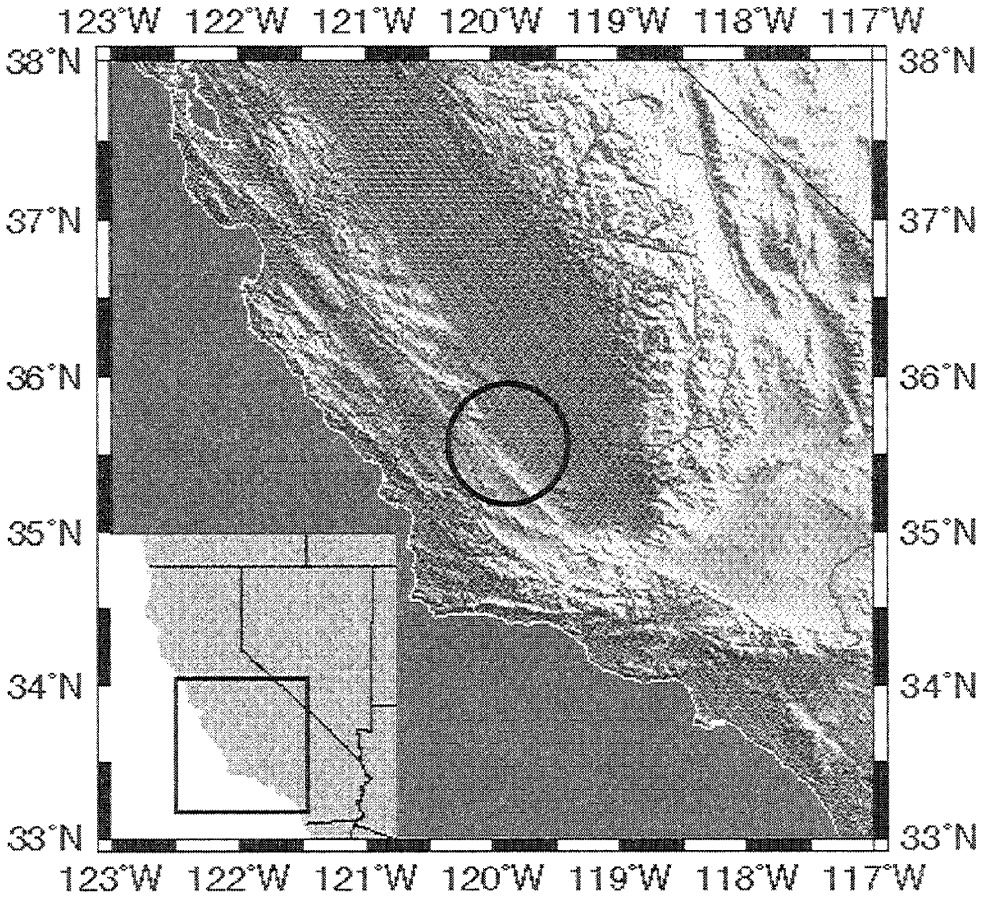

Figure 1 Location of field experiment in the San Joaquin Valley, California. The fields in this region are typically high porosity and low permeability, typical of diatomaceous deposits. Oil weight typically falls between 10 and 17 API, making this area a strong study in heavy oil EOR techniques.

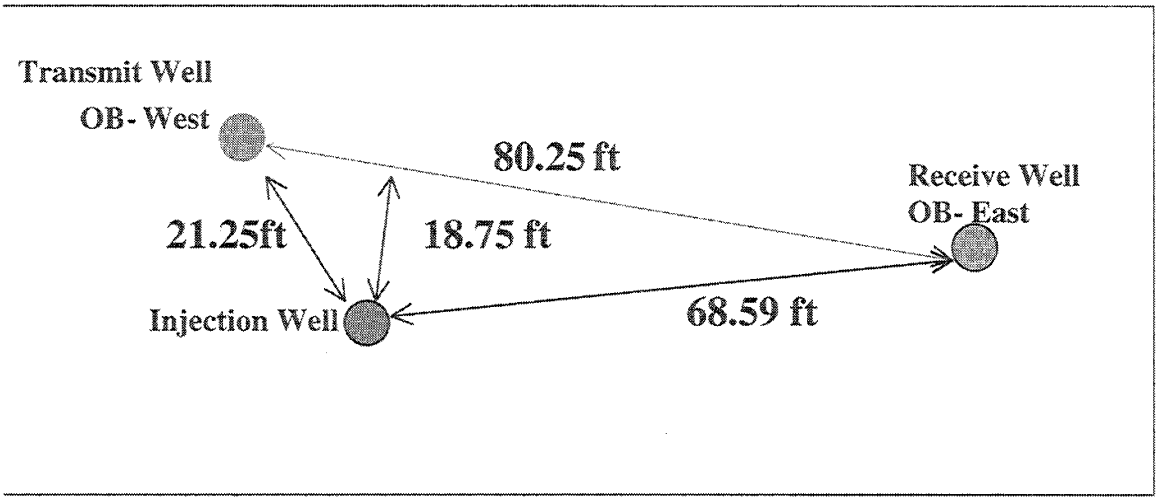

Figure 1a Planview of borehole geometry. OB-west and OB-east are non-conductive observation boreholes used to produce images 5a and 5b. The Injection well is displayed in figure 6 with the induction log at about 20 ft east of OB-west.

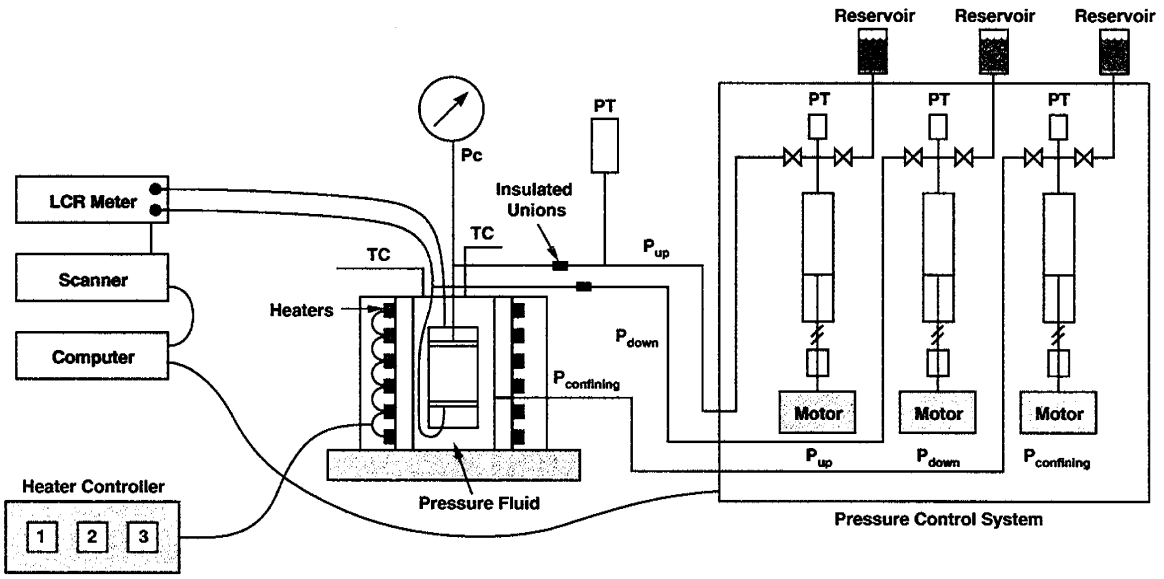

Figure 2 Schematic of device used to measure electrical properties at controlled temperature and pressure. There are three separate pressure control systems permitting the introduction and flow of various pore fluids. An additional press was used to introduce oil to the samples. Experimental parameters and data are collected with a computer data acquisition system.

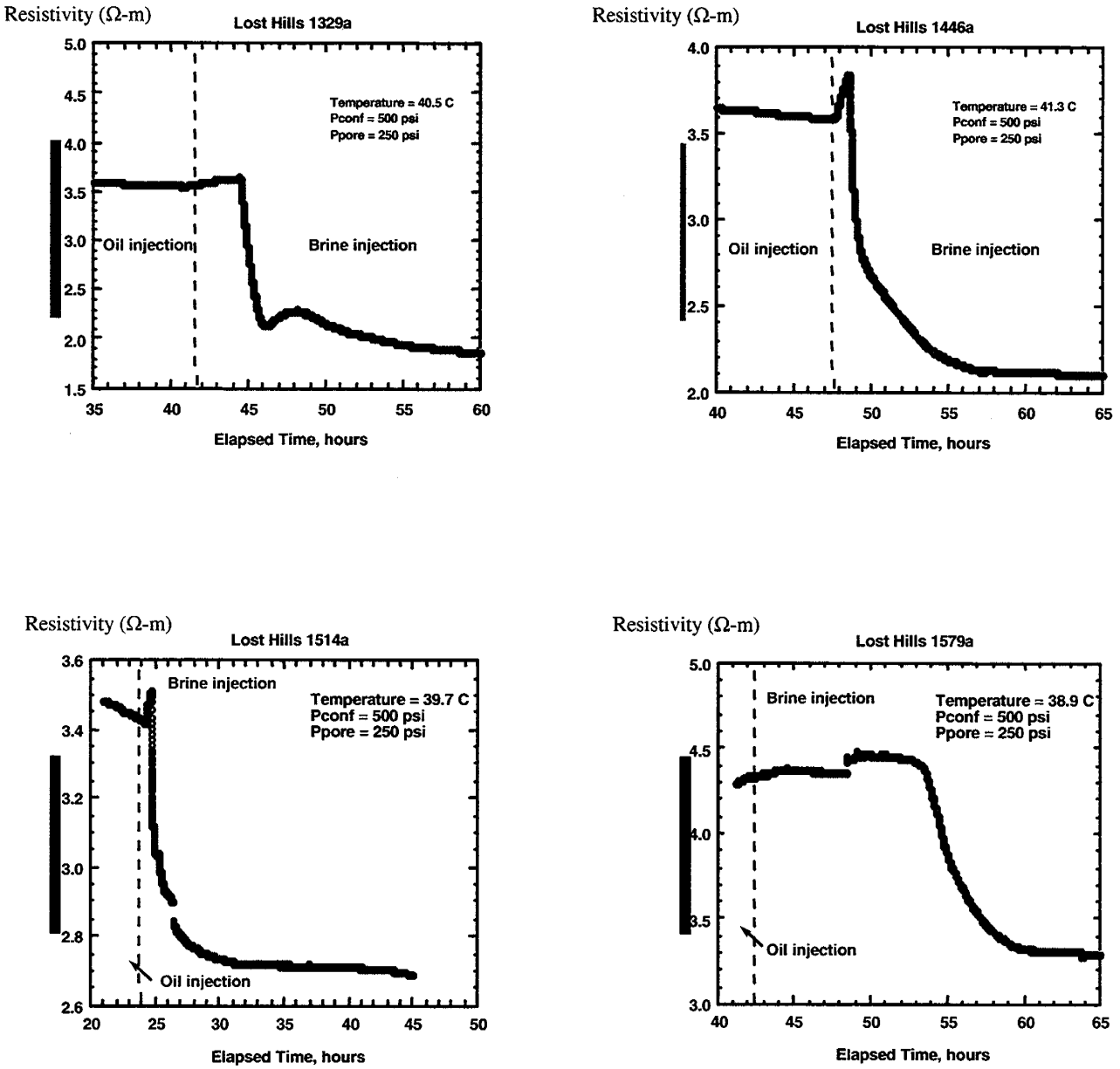

Figure 3 Slide I - Electrical resistivity measured at 1 kHz as a function of time for eight samples from Lost Hills, CA. Sample, temperature, confining and pore pressure of each run is listed on the individual plot. The vertical red-dashed line on each plot marks the change from oil to brine injection. In general, the oil-filled sample are more resistive than the brine-filled samples, however, there is some variation in resistivity as brine displaces oil. These variations are discussed in the text.

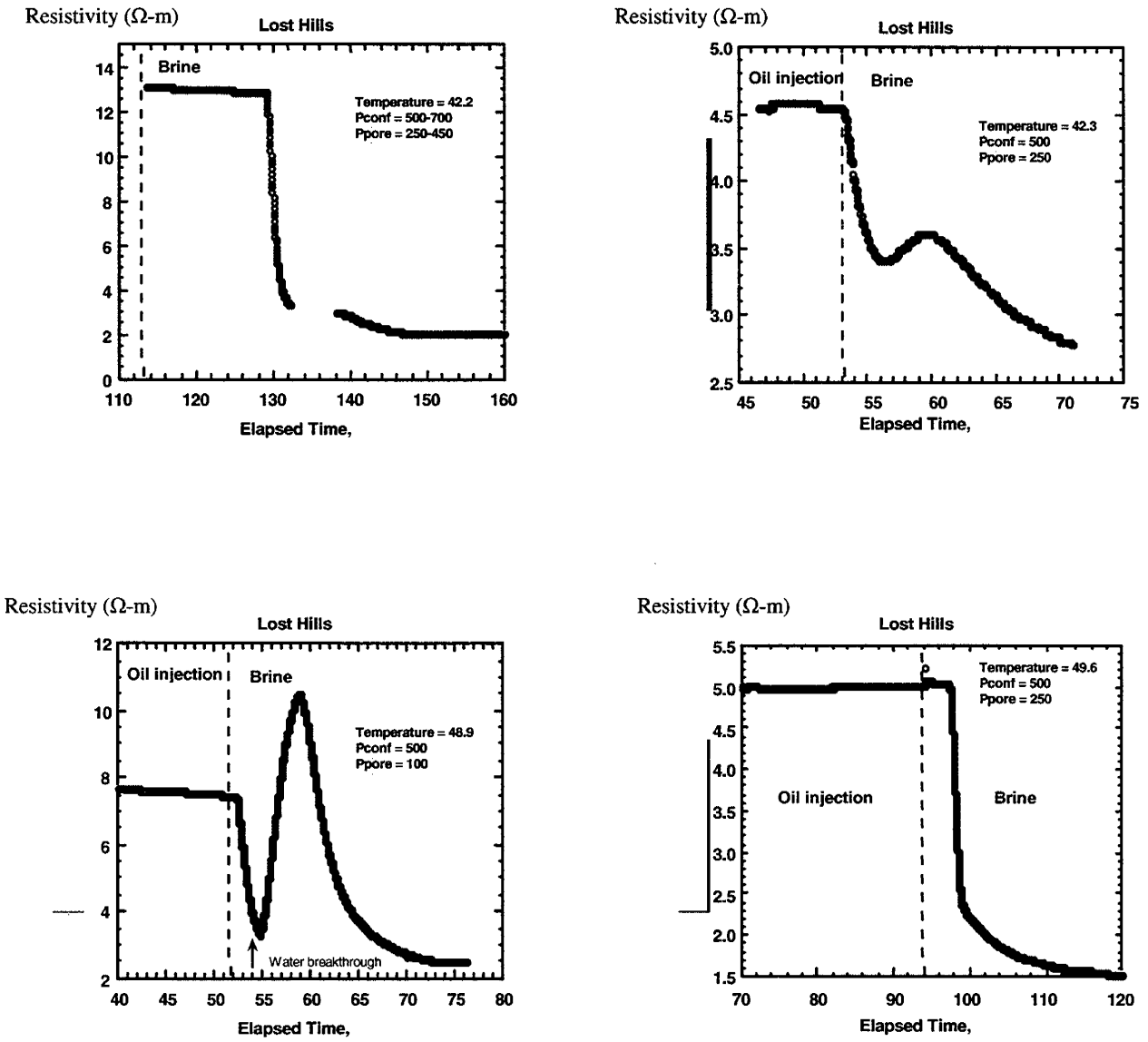

Figure 3 Slide II - Electrical resistivity measured at 1 kHz as a function of time for eight samples from Lost Hills, CA. Sample, temperature, confining and pore pressure of each run is listed on the individual plot. The vertical red-dashed line on each plot marks the change from oil to brine injection. In general, the oil-filled sample are more resistive than the brine-filled samples, however, there is some variation in resistivity as brine displaces oil. These variations are discussed in the text.

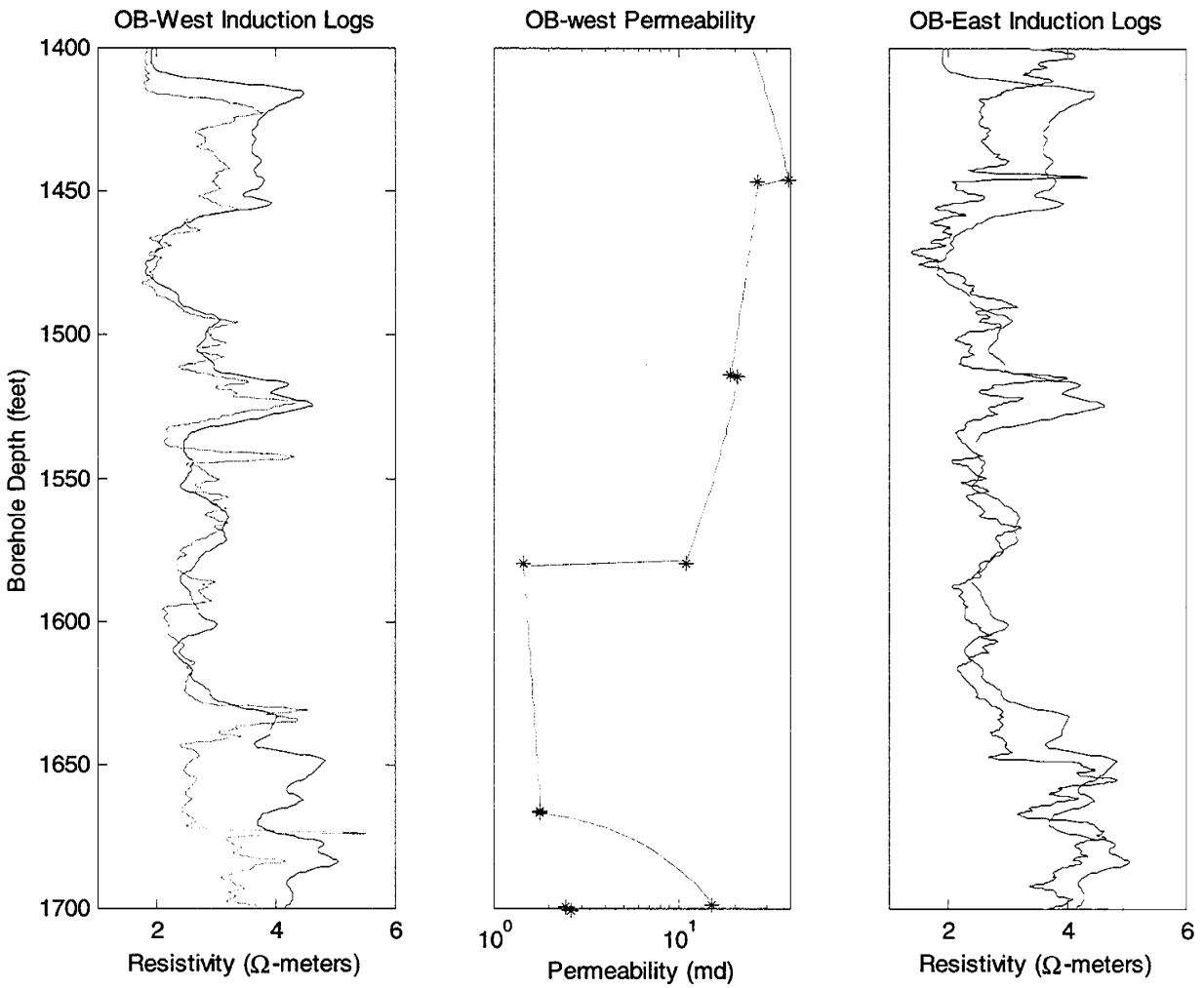

Figure 4 Induction logs and permeability log from waterflood site. Induction log plot (A) contrasts OB-west resistivity (green - acquired August, 1999) against the injector borehole resistivity (blue - acquired December, 1994). Slide (C) contrasts OB-east induction log resistivity (red - acquired August, 1999) against the injector borehole resistivity. Slide (B) is the interpolated logarithmic permeability distribution of borehole OB-west, acquired in August, 1999. Note the resistivity change at depth 1650' – 1700' is unique in borehole OB-west.

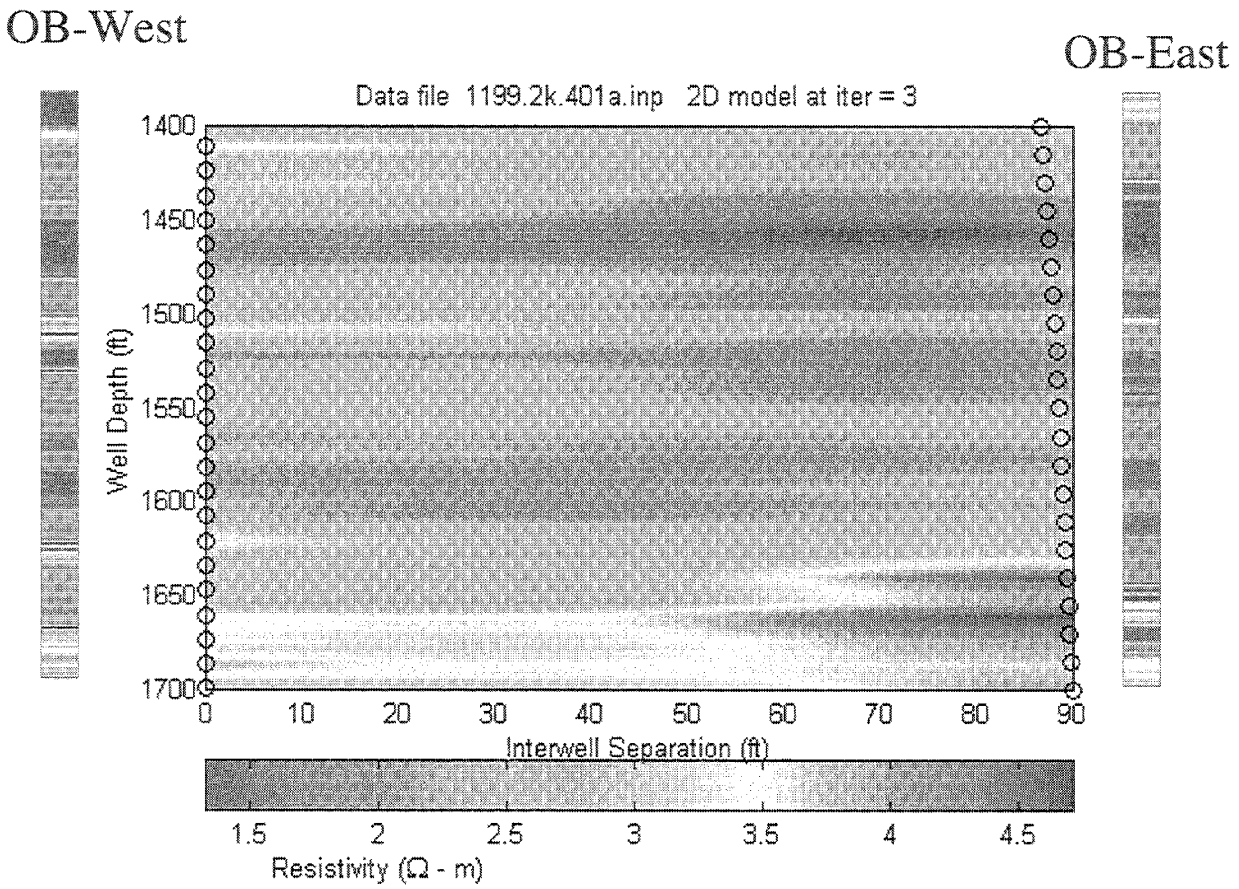

Figure 5b 2-D conductivity image acquired in November, 1999 between observation boreholes. All units are in feet and Ω-m. Induction logs from August, 1999 are placed on the sides for accuracy verification. Black circles represent the borehole – note the deviation of well OB-east. Formation fluid resistivity is approximately 4.0 Ω-m, while injection fluid resistivity is approximately 2.0 Ω-m.

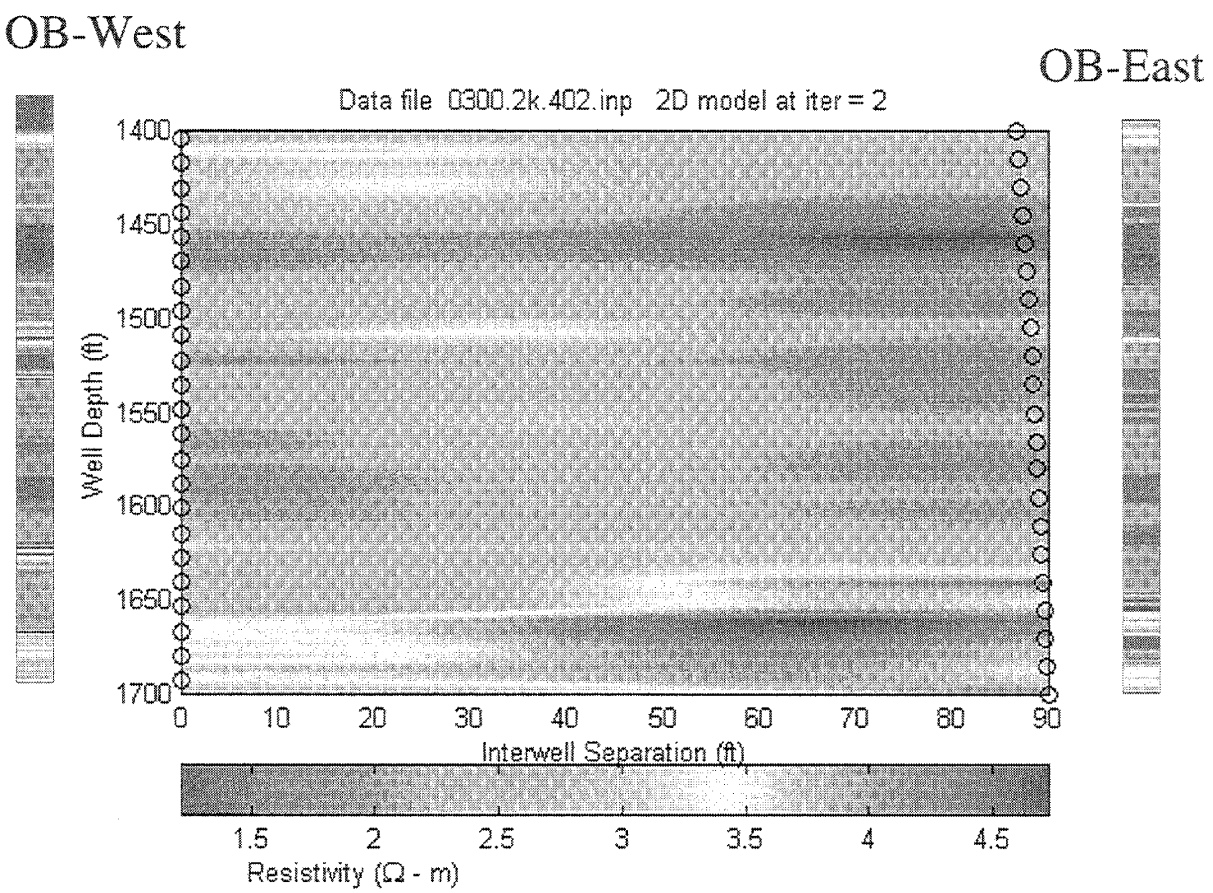

Figure 5a 2-D conductivity image acquired in March, 2000 between observation boreholes. All units are in feet and Ω-m. Induction logs from August, 1999 are placed on the sides for accuracy verification. Black circles represent the borehole – note the deviation of well OB-east. Formation fluid resistivity is approximately 4.0 Ω-m, while injection fluid resistivity is approximately 2.0 Ω-m.

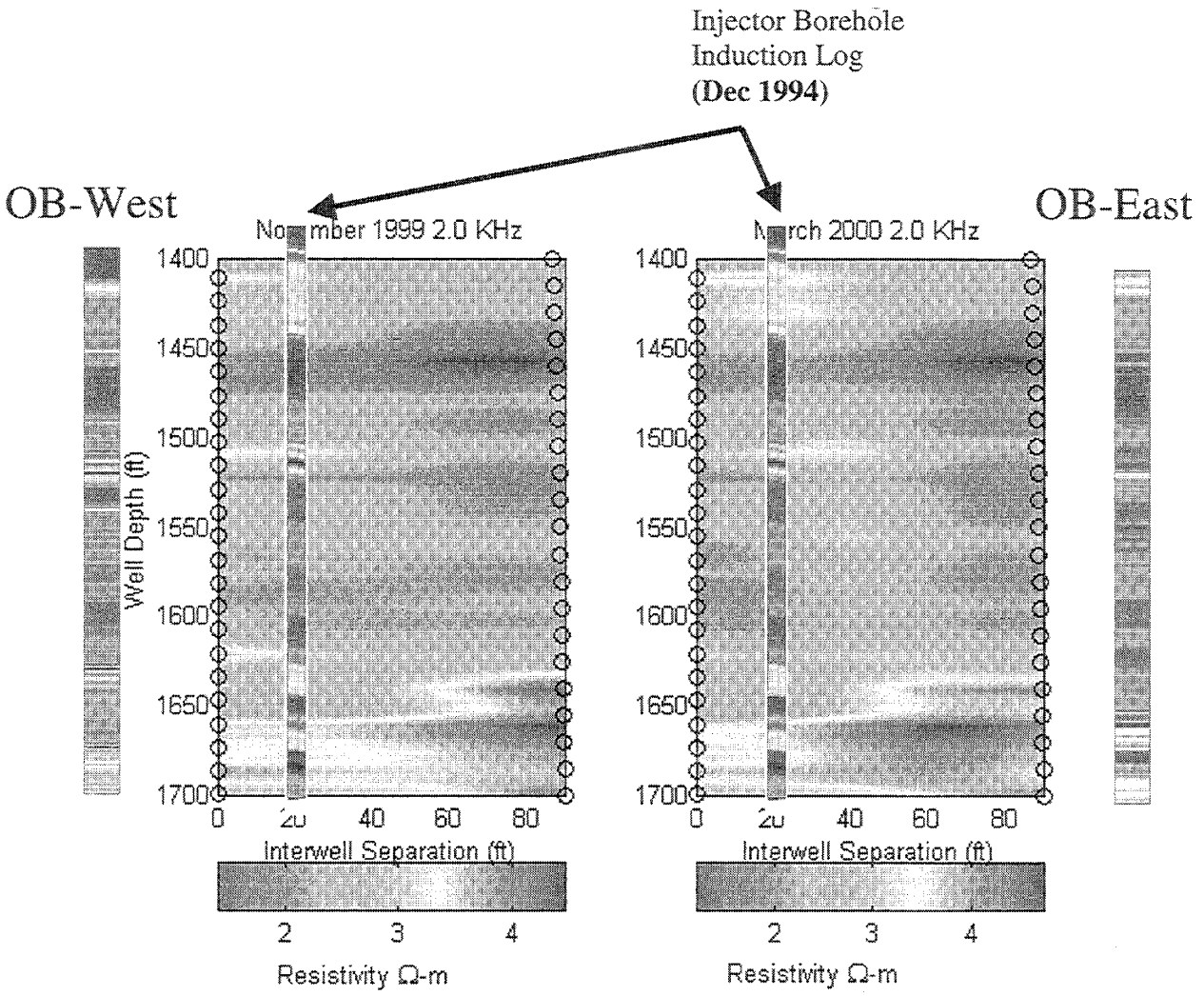

Figure 6 Comparison of figures 5a and 5b with injector borehole log (acquired in December 1994) added to show long term oil displacement. The behavior at depth 1650' shows the oil moved during waterflooding is limited to the west side of the images. Waterflooding appears to be ineffective in the lower section of the east side.

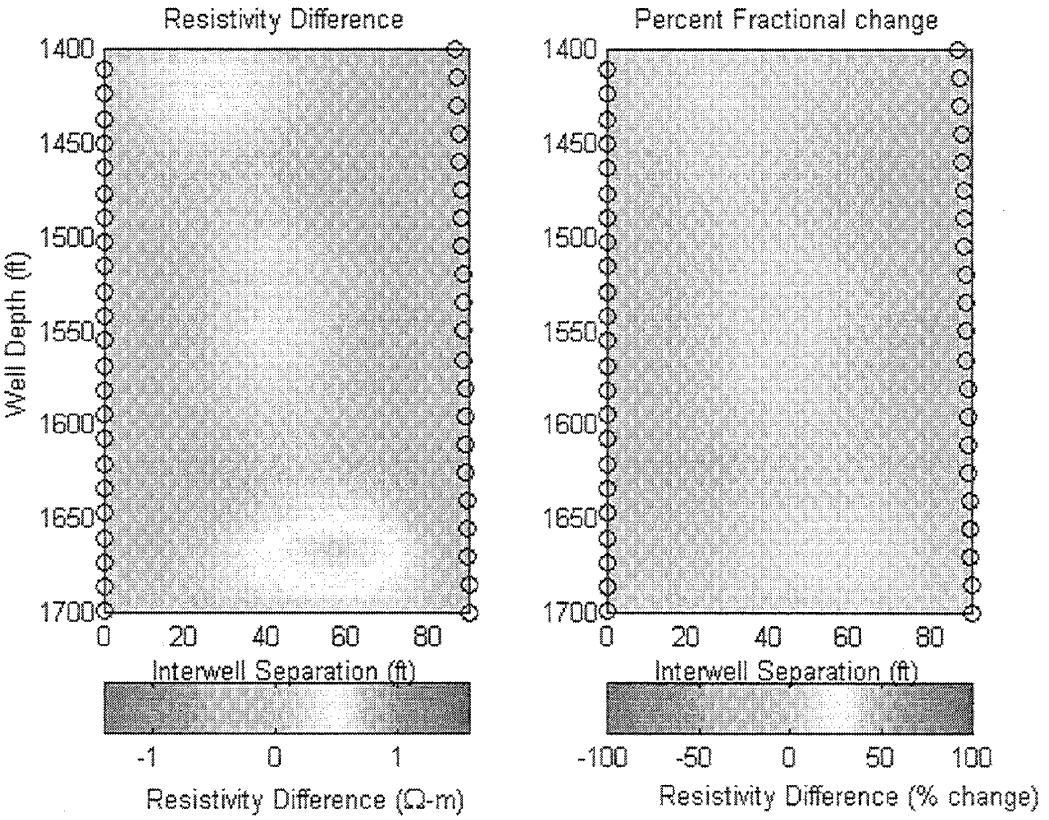

Figure 7 Resistivity Difference between images 5a and 5b (left slide). Yellow represents a positive change in resistivity, while cyan represents a negative difference. The percent fractional change slide (right) between 5a and 5b shows the resistivity difference between November 1999 and March 2000 as a percent change.

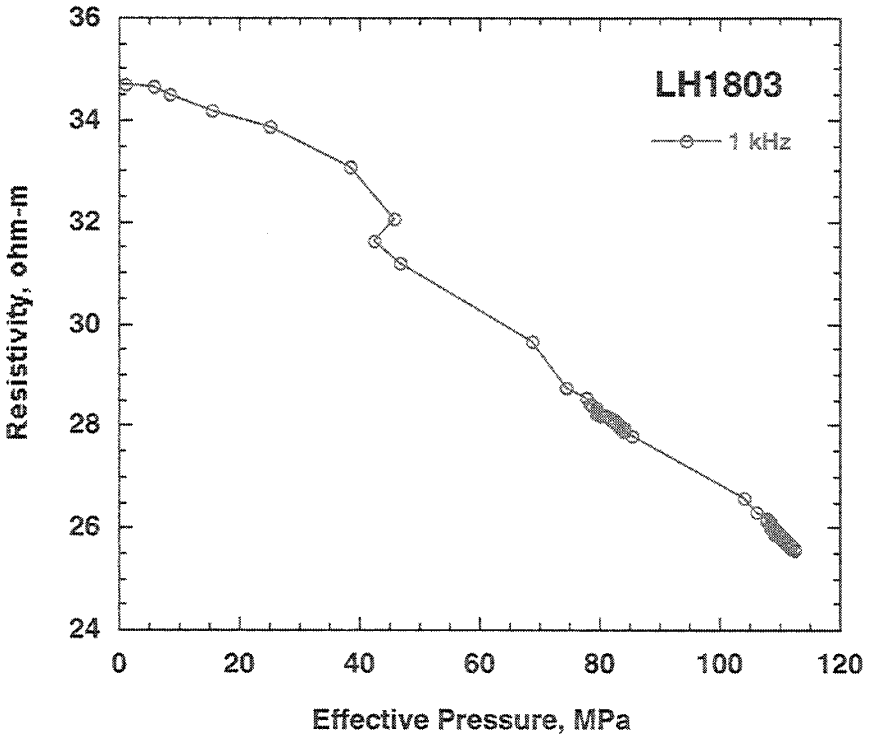

Figure 8 Slide I - Resistivity as a function of effective pressure for two samples, LH1803 (a) and LH1886 (b). All samples displayed similar behavior: a decreasing resistivity with increasing effective pressure. This indicates the dominant conduction mechanism is not aqueous diffusion through the pore space.

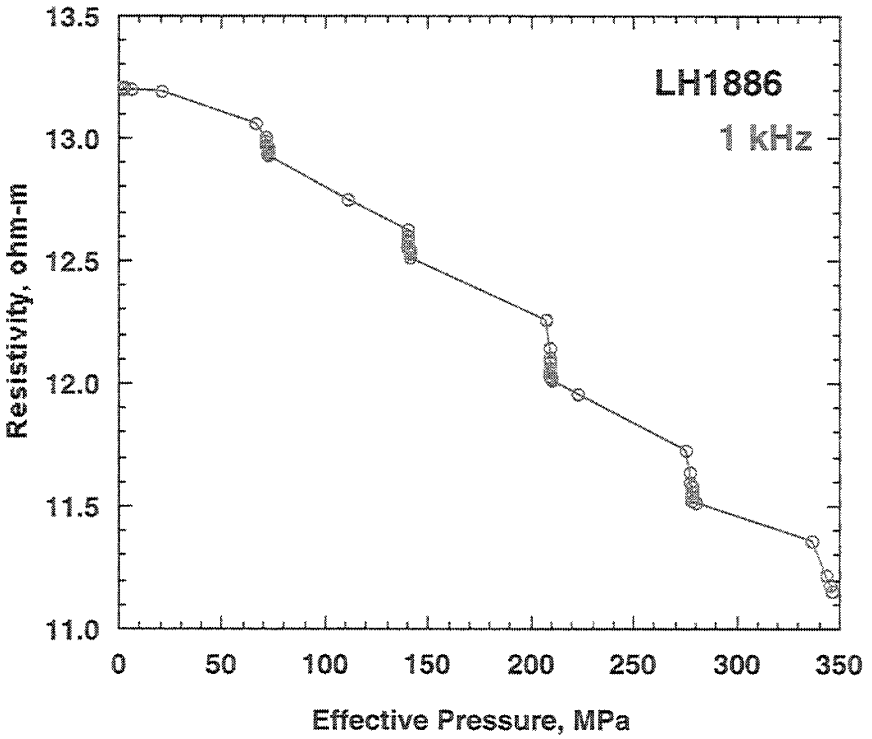

Figure 8 Slide II - Resistivity as a function of effective pressure for two samples, LH1803 (slide I) and LH1886 (slide II). All samples displayed similar behavior: a decreasing resistivity with increasing effective pressure. This indicates the dominant conduction mechanism is not aqueous diffusion through the pore space.

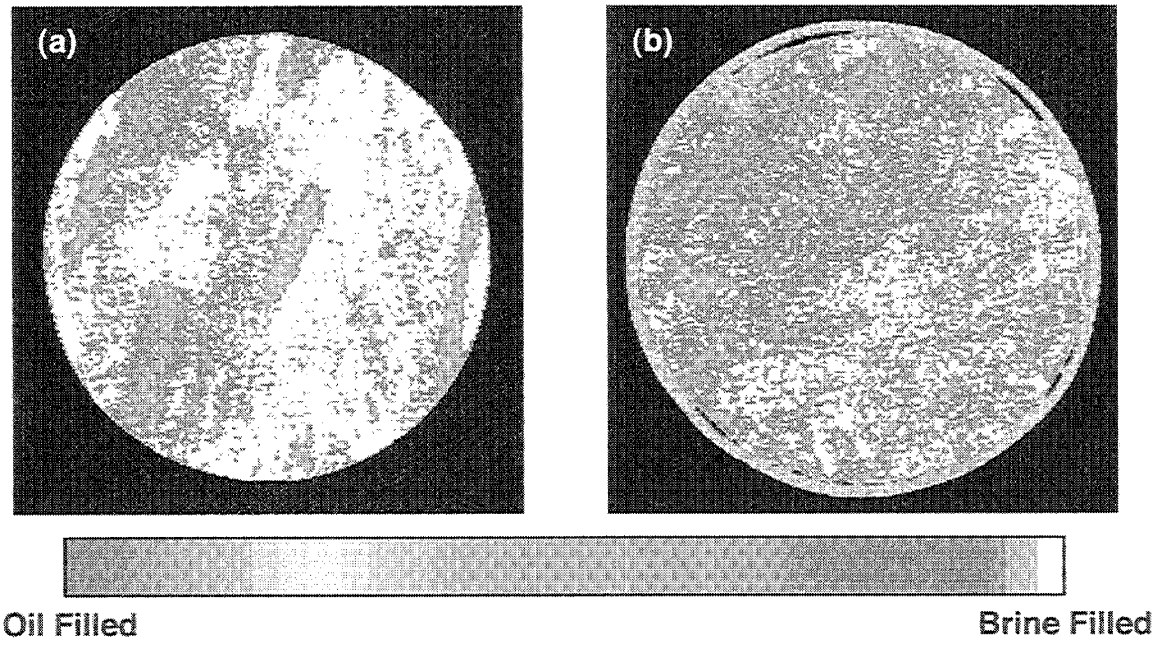

Figure 9 Computed x-ray tomographic slices of sample LH1579. Samples are 2.54 cm in diameter. The color bar at the bottom of the images is arbitrary, with warmer colors indicating lower x-ray attenuation and cooler colors and white indicating higher attenuation. A separate scan on oil and brine showed that oil was significantly less attenuating than the brine. (a) Sample after brine flow. Greenish areas indicate oil that remained in the sample. (b) Sample prior to the experimental run. The outer ring is the teflon core sleeve.

Task 79 – PDVSA Intevep will provide DOE with information on using seismic methods for monitoring reservoir production. This work deals with tracking a continuous thermal injection front in a pilot area, by means of comparing several 3D seismic surveys that are acquired in a time-lapsed fashion. The research effort will be focused in enhancing factors as repeatability of sources, repeatability of receiver, best approaches for upscaling issues. The research will include a determination of the economic value of the technology in monitoring thermal processes.

SEISMIC METHODS FOR MONITORING RESERVOIR PRODUCTION

(Cancelled due to funding adjustments)

APPENDIX A

Short text of the Eleventh Amendment to Annex IV of the Implementing Agreement Between the Department of Energy of the United States of America and the Ministry of Energy and Mines of the Republic of Venezuela in the Area of Enhanced Oil Recovery Thermal Processes signed by the Project Managers on September 30, 1998.

Eleventh Amendment and Extension to Annex IV
Enhanced Oil Recovery Thermal Processes
Agreement Between
Alejandro Izquierdo (PDVSA Intevep)
and
Thomas B. Reid (DOE)

Task 74 - DOE shall provide PDVSA Intevep with results of the SUPRI heavy oil mechanisms research program. This work includes studies of flow properties studies at heavy oil reservoirs conditions, in-situ combustion, steam with additives, formation evaluation and support of specific field experiments. Among the axis of research for the duration of this task are investigation of the "foamy oil" mechanism, of heat and fluid transfers in fractured media, better determination of flow parameters such as relative permeability and capillary pressure and effects of catalysts on in-situ combustion. In-situ upgrading methods will be investigated. Experiments will be conducted in micromodels and cores, with saturations measured by an X ray CT scanner.

Task 75 - PDVSA Intevep will provide DOE with information on the field results of monitoring the temperature profile along one pair of SAGD horizontal wells, as well as the modeling of the SAGD process using this information.

Task 76 - DOE shall provide PDVSA Intevep with information on research undertaken by BDM Petroleum Technologies to develop methods to economically recover heavy oil from the harsh arctic (North Slope, Alaska) environment.

Task 77 - PDVSA Intevep will provide DOE with information on the influence of coring and sampling procedures on geomechanical properties of unconsolidated materials to generate guidelines and procedures that guarantee field representatively in laboratory samples.

Task 78 - DOE shall provide PDVSA Intevep information on resistivity imaging from cross-bore and surface-to-borehole electromagnetic induction methods developed by LLNL. The information will include acquisition system design, field methods, inversion algorithms, and field results. Field experiments will consist of EOR waterflood and steamflood front tracking in producing oil reservoirs. Information will be provided on research efforts to operate the receiver string in steel-cased boreholes.

Task 79 - PDVSA Intevep will provide DOE with information on using seismic methods for monitoring reservoir production. This work deals with tracking a continuous thermal injection front in a pilot area, by means of comparing several 3D seismic surveys that are acquired in a time-lapsed fashion. The research effort will be focused in enhancing factors as repeatability of sources, repeatability of receiver, best approaches for upscaling issues. The research will include a determination of the economic value of the technology in monitoring thermal processes.

Thomas B. Reid
Project Manager, DOE

Alex Izquierdo
Project Manager, INTEVEP

APPENDIX B

Full text of tile Agreement For Energy Cooperation Between the Department of Energy of the United States of America and the Ministry of Energy arid Mines of the Republic of Venezuela, signed October 13, 1997.

AGREEMENT

FOR ENERGY COOPERATION

BETWEEN THE DEPARTMENT OF ENERGY OF

THE UNITED STATES OF AMERICA

AND

THE MINISTRY OF ENERGY AND MINES OF

THE REPUBLIC OF VENEZUELA

The Department of Energy of the United States of America (DOE) and the Ministry of Energy and Mmes of the Republic of Venezuela (MEM), hereinafter "the Parties":

CONSIDERING

The interest of the Parties in strengthening the bilateral cooperation for the development, application and sustainable use of conventional energy (especially fossil fuels), energy efficiency, and renewable energy;

The importance that the Parties, assign to the exchange of information, experiences, and points of view regarding the development and analysis of energy systems, the design and implementation of energy regulatory regimes, the dissemination of ,energy technology information, and the design, development and improvement of energy information systems;

The Parties desire to promote regional energy cooperation through information exchange, analysis and forecasting, and cooperative activities within the framework of hemispheric energy cooperation and integration

The importance the Parties assign to the contribution by conventional energy (especially fossil fuels), energy efficiency and renewable energy to increase the energy diversity and security of supply, to promoting sustainable development and opportunities for economic interaction, as well as to. the contribution of technology to the rational and ecologically acceptable development of all phases of energy activity, including evaluation of resources and energy production, transportation, processing distribution and end use;

The Agreement between the Government of the United States of America and the Government of the Republic of Venezuela for Scientific and Technological Cooperation signed October 13, 1997;

The Agreement between the Parties for Cooperation in the Field of Energy Research and Development signed March 6, 1980, and extended September 8, 1993 for a term of five years (hereinafter the Energy R&D Agreement), and the Parties interest in continuing certain Implementing Agreements under the Energy R&D Agreement (hereinafter referred to as "Project (Annexes") and undertaking new cooperative activities in the field of energy research and development.

Have agreed as follows: .

ARTICLE I
SCOPE AND OBJECTIVES

1. The purpose of this Agreement is to establish a framework for cooperation between the Parties in activities of mutual interest to promote the rational development and rise, of conventional energy (especially fossil fuels), energy efficiency and renewable energy, and such other topics as the Parties may agree.

2. Cooperative activities under this Agreement will be conducted on the basis of equality, reciprocity, and mutual benefit to the "Parties".

ARTICLE II
FORMS OF COOPERATION

Cooperation between the Parties under this Agreement may include, but need not be limited to the following activities:

A Exchange of information, analyses and forecasts pertaining to the Parties' energy sectors, including short-, medium-, and, long-term forecasts;

B. Development of joint studies and projects to facilitate energy planning, the formulation of policies related to energy production and end-use, the establishment of regulatory systems, and the promotion of trade and investment opportunities that foster greater productivity, sustainable, and reliability of energy supply and energy markets.

C. Design of training activities and educational materials for strengthening institutional capacities and promoting the cleaner and more rational use of conventional energy (especially fossil fuels), energy efficiency, and renewable energy;

D. Exchange of scientific and technical information, and results and methods of research and development on a periodic basis in a manner agreed to by the Joint Steering Committee established by Article 3 (D):

E. Organization of seminars and other meetings on agreed energy topics;

F. Survey visits by specialists to the agencies and facilities of the Parties;

G. Cooperation on the evaluation and development of renewable energy resources and on integrated planning of energy resources;

H. Conduct of program for the exchange and training of personnel from the Parties' energy sectors;

I. Exchange of information and collaboration to identify sources of Financial support for the development of studies, energy analyses and conduct of projects specifically intended to promote the rational and ecologically acceptable use of conventional energy (especially fossil fuels), energy efficiency and renewable energy;

J. Assistance in the purchase or loan of equipment needed to carry out specific activities undertaken under this Agreement;

K. Joint projects including experiments, test, design, analysis and other collaborative technical activities;

L. Exchange of materials, instruments, components, and equipment for testing and;

M. Such other activities as the Parties may agree in writing.

ARTICLE III
MANAGEMENT

A. The Secretary of Energy and of the United States of America and the Minister of Energy and Mines of the Republic of Venezuela each will designate senior Principal Coordinators, representing their respective countries, to coordinate activities under this Agreement. The Principle Coordinators will jointly plan and coordinate cooperative activities and report annually to the Minister and the Secretary, respectively. The Principal Coordinator may establish Joint Committees to assist them in the activities under this Agreement.

B. The Minister and the Secretary will review progress of the work under this Agreement when they meet. The Principal Coordinators, or the joint committees, will appoint Project Managers for each Project Annex established under Article 4.

C. The Principal Coordinators will meet annually, or as otherwise mutually agreed, alternatively in Venezuela and the United States. The Principal Coordinators may invite representatives of other organizations within their countries to attend the meetings and serve as advisers to assist in the planning and conduct of cooperative activities undertaken under this Agreement.

D. The Joint Steering Committee (JSC) established under the Energy R&D Agreement will continue supervising the implementation of the ongoing Annexes I, IV, X, XIV, XV, XVI and XVII under the Energy R&D Agreement and other new cooperative energy research and development activities.

ARTICLE IV
PROJECT ANNEXES

1. When the Parties agree to undertake a cooperative activity or an activity which may give rise to intellectual property, the Parties will execute a Project Annex. Each will include provisions for carrying out the activity as well as appropriate provisions pertaining to technical scope, intellectual property as defined in Annex A of this Agreement, management, total costs, cost sharing, schedule and other issues as appropriate.

2. The following Project Annexes which were entered into pursuant to the Energy R&D Agreement shall continue in effect until work undertaken is completed subject to the term and conditions of this Agreement or until this Agreement expires or is terminated in accordance with Article 12.

A. Project Annex I, Joint Characterization of Heavy Crude.

B. Project Annex IV, Enhanced oil Recovery Thermal Process.

C. Project Annex X, On-Site Training of Petroleum Engineers.

D. Project Annex XIV, Exchange of Energy Related Personnel.

E. Project Annex XV, Oil Recovery Information and Technology Transfer.

F. Project Annex XVI, Oil And Petrochemical Ecology and Environmental Research.

G. Project Annex XVII, Drilling Technology.

ARTICLE V
ASSIGNMENT OR EXCHANGE OF PERSONNEL

The following provisions shall apply concerning assignment or exchange of personnel under this Agreement:

A. Each Party will make best efforts to ensure that personnel to be assigned to or exchanged with the other Party. have the necessary qualifications skills and competence to perform the activities planned under this Agreement.

B . Each assignment or exchange of personnel will be agreed in writing.

C. Each Party will be responsible for the salaries, insurance, travel expenses, and allowances to be paid to its personnel.

D. Each Party will provide assistance to the personnel from the other Party (including accompanying relatives when appropriate) in matters such as lodging and administrative formalities related to the trips on mutually acceptable and reciprocal basis.

E. The personnel from each Party who are visiting the other Party will conduct themselves as agreed to in the specific assignment or exchange agreement.

ARTICLE VI
EXCHANGES OF EQUIPMENT

The following provisions shall apply concerning exchanges of equipment pursuant to this Agreement:

A. By mutual agreement, a Part may provide equipment to be utilized in a joint activity. In such case, the sending Party shall supply, as soon as possible, a detailed list of the equipment to be provided together with the relevant specifications and appropriate technical informational documentation related to the use, maintenance, and repair of the equipment.

B. Title to the equipment and necessary spare parts supplied by the sending Party for use in joint activities shall remain in the sending Party, and the property shall be returned to the sending Party upon completion of the joint activity, unless otherwise agreed in writing.

C. Equipment provided pursuant to this Agreement shall be brought into operation at the host established only by mutual agreement between the Parties.

D. The host establishment shall provide the necessary premises, shall provide for utilities such as electric power, water and gas, and normally shall provide materials to be tested, in accordance with the agreed technical requirements.

E.. The responsibility and expenses for the transport of the equipment and materials from the United States by plane or ship to an authorized port of entry in Venezuela convenient to the ultimate destination, and also the responsibility for its safekeeping and insurance en route shall rest with DOE.

F. The responsibility and expenses for the transport of the equipment and materials from Venezuela by plane or ship to an authorized port of entry in the United States convenient to the ultimate destination, and also the responsibility for its safekeeping and insurance en route shall rest with MEM

G. Equipment provided pursuant to this Agreement for use in joint activities shall be considered to be scientific, not having commercial character, and each Party shall make its best effort to obtain duty free entry

ARTICLE VII
EXCHANGES OF INFORMATION

The following provisions shall apply concerning exchanges of information pursuant to this Agreement: .

A. Each Party will, according to its legal authority, make available to the other the information which is relevant for complying with the activities in the Agreement and which can be made available in terms of the laws and regulations of each country as long as this information is reasonably accurate and is adequately documented. The Parties will not exchange business-confidential information of any nature unless agreed upon in writing. Information can be designated as business-confidential if the person or institution having the information may derive economic benefit or may obtain a competitive advantage over those who do not have it, the information is not generally known or publicly available from other sources, and the owner has not previously made the information available without imposing in a timely manner an obligation to keep it confidential. The Parties agree that exchange information which is not business-confidential as defined in this Article can be broadly disseminated.

B. The use and application of any information supplied, exchange, or developed by the Parties will be the responsibility of the receiving Party. The issuing Party does not guarantee, that the information is suitable for any purpose.

C. In the eventuality that any information which is generated, exchanged, or submitted under this Agreement is identified in a timely manner as business-confidential information, each Party and its participants will protect such information in view of the pertinent administrative laws, regulations, authorities and practices.

E. No provision in this Agreement can obligate the Parties to allow access to information that is restricted for any reason, or when one Party considers it essential for national security, the safeguard of national resources or the competitiveness for public or private companies, research centers, or laboratories.

F.

ARTICLE VIII
INTELLECTUAL PROPERTY

The provisions for the protection and transfer of intellectual property are established in Annex A to this Agreement, "Intellectual Property," which constitutes an integral part of this Agreement and is applicable to all cooperative activities performed under the Agreement.

ARTICLE IX
SECURITY OBLIGATIONS

The Parties agree that no information or equipment requiring protection in the interests of national defense or foreign relations of either Party and classified in accordance with the applicable national laws and regulations shall be provided under this Agreement, In the event that information or equipment which is known or believed to require such protection is' identified in the course of cooperative activities undertaken under this Agreement; it will be brought promptly to the attention of the appropriate. officials and the Parties will consult concerning the need for, and level of appropriate protection to be accorded such information or equipment

ARTICLE X
GENERAL PROVISIONS

A. Unless otherwise agreed by the Parties in writing, all expenses resulting from cooperative activities under this Agreement will be paid by the Party that incurs them,

B. Each Party will conduct the activities provided for in this Agreement subject to its respective laws and regulations and will provide financial resources subject to the availability of appropriated funds and personnel.

C. This Agreement shall, as of the date of , signature, supersede the Energy R&D Agreement, provided however that the Annexes (I, IV, X, XIV, XV, XVI and XVII) initiated under the Agreement are continued in effect and shall be subject to, and form an integral part of this Agreement.

ARTICLE X1
SOLUTION OF DISPUTES

All questions related to the interpretation of this Agreement will be solved by agreement of the Parties.

ARTICLE XII
ENTRY INTO FORCE, DURATION, MODIFICATION, AND TERMINATION

A This Agreement will enter into force upon signature and will remain in force for five (5) years unless it is modified or terminated pursuant to the terms established in this Agreement. Unless one of the Parties notifies the other Party in writing of its intention to terminate this Agreement at least six months before its expiration this Agreement will be automatically extended for an additional five-year Period.

B. This Agreement may be modified or extended by written. agreement of the Parties.

C. Either of the Parties may terminated this want upon ninety (90) days written notice to the other Party. The termination of thus Agreement will not affect the completion of' activities initiated but not completed during its term.

Done at the City of Caracas on the 13th day of the month of October, nineteen ninety-seven, in two versions in English and Spanish, both texts being equally authentic

BY THE DEPARTMENT OF ENERGY OF THE UNITED STATES OF AMERICA

Federico F. Pena
Secretary of Energy

BY THE MINISTRY OF ENERGY AND MINES OF THE REPUBLIC OF VENEZUELA

Erwin Jose' Arrieta Valera
Minister of Energy and Mmes

ANNEX A
INTELLECTUAL PROPERTY

A. The Parties shall ensure adequate and effective protection of intellectual property created or. furnished under this Agreement and relevant Project Annexes. The Parties agree to notify one another in a timely fashion of any inventions or copyrighted works arising under this Agreement and to seek protection for such intellectual property in a timely fashion. Rights to such intellectual property. shall be allocated as provided in this Annex. .

B. Scope

1. This Annex is applicable to all, cooperative activities undertaken pursuant to this Agreement, except as otherwise specifically agreed by the Parties or their designees.

2. For purposes of this Agreement, "intellectual property" shall have. the meaning found in Article 2 of the Convention Establishing the World Intellectual Property Organization, done at Stockholm, July 14, 1967.

3. This Annex addresses the allocation of rights and interests between the Parties. Each Party shall ensure that the other Party can obtain the rights to intellectual property allocated in accordance with this Annex, by obtaining those rights from its own participants through contracts or other legal means, if necessary. This Annex does not otherwise alter a prejudice the allocation between a Party and its nationals, which shall be determined by that Party's laws and practices.

4. Disputes concerning intellectual property arising under this Agreement should be resolved through discussions between the concerned participating institutions, or; if necessary, the Parties or their designees.. Upon mutual agreement of the Parties, a dispute shall be submitted to an arbitral tribunal for binding arbitration in accordance with the applicable rules of international law. Unless the Parties or their designees agree otherwise is writing the arbitration rules of the Untied Nations Commission on International Trade Law (UNCITRAL) shall govern. .

5. Termination or expiration of this Agreement shall not affect rights or obligations under this Annex.

6. Cooperative activities will not be entered into where the purposes of the activities is to produce inventions in the following areas, or where there is a possibility of producing inventions in the following areas, until such time as inventions in these areas are considered patentable subject matter by both Parties:

1. drinks and food products for humans and animals;
2. medicine of all kinds, and

3. pharmaceutical and chemical preparations, reactions and compounds.

C. Allocation of Rights

1. Each Party shall be entitled to a nonexclusive, irrevocable, royalty free license in all countries to translate, reproduce, and publicly distribute scientific and technical journals articles, reports and books directly arising from cooperation under this Agreement. All publicly distributed copies of a copyrighted work prepared under this provision shall indicate the names of the authors of the work unless an author explicitly declines to be names

2. Rights to all forms of intellectual property, other than those described in Paragraph C.1 above shall be allocated as follows:

   (i) Visiting researchers for example scientists visiting primarily in furtherance of their education, shall receive intellectual property rights under the policies of the host institution. In addition, each visiting researcher named as an inventor shall be entitled to national treatment with regard to awards, bonuses, benefits, or any other rewards, in accordance with the policies of the host institution.

   (ii) (a) For intellectual property created during joint research, for example, when the Parties, participating institutions, or participating personnel have agreed in advance on the scope of work; each Party shall be entitled to obtain all rights and interests in its own country. Rights and interests ins third countries will be determined in Project Annexes. If research is not designated as "joint research" in the relevant Project Annexes, rights to intellectual property arising from the research will be allocated in accordance with paragraph C.2(i) above. In addition, each person named as an inventor shall be entitled to national treatment with regard to awards, bonuses, benefits or any other rewards in accordance with the policies of the participating institutions.

   (b) Notwithstanding paragraph C.2(ii)(a) above, if a type of intellectual property is available under the laws of one party but not the other Party, the Party whose laws provide for this type of protection shall be entitled to all rights, and interests worldwide. Persons named as inventors of the property shall nonetheless be entitled to national treatment with regard to awards, bonuses, benefits, or any other rewards in accordance with the policies of the participating institutions of the Party obtaining the rights.

D. Business-confidential Information

In the event that information identified in a timely fashion as business-confidential is furnished or created under this Agreement, each Party and its participants shall protect such information in accordance with applicable laws, regulations, and administrative practices. Information may be identified as "business-confidential" if a person having the information may derive economic benefits from it or may obtain a competitive advantage over those who do not have it, the information is not

generally known or publicly available from other sources, and the owner has not previously made the information available without imposing in a timely manner an obligation to keep it confidential.